TESIS DOCTORAL/DOKTOREGO TESIA
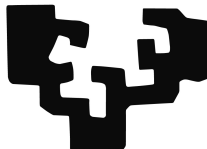
Probabilistic Modelling of Classical and Quantum Systems

Autor/Egilea:
Simone RUSCONI

Directores/Zuzendariak:
Prof. Elena AKHMATSKAYA
Prof. Dmitri SOKOLOVSKI

Bilbao, 2018

eman ta zabal zazu

Universidad   Euskal Herriko
del País Vasco   Unibertsitatea

DOCTORAL THESIS

Probabilistic Modelling of Classical and Quantum Systems

Author:

Simone RUSCONI

Supervisors:

Prof. Elena AKHMATSKAYA

Prof. Dmitri SOKOLOVSKI

Bilbao, 2018

bcam
basque center for applied mathematics

EXCELENCIA
SEVERO
OCHOA

Abstract

While probabilistic modelling has been widely used in the last decades, the quantitative prediction in stochastic modelling of real physical problems remains a great challenge and requires sophisticated mathematical models and advanced numerical algorithms.

In this study, we developed the mathematical tools for solving three long-standing problems in Polymer Science and Quantum Measurement theory.

The question, "Why kinetic models cannot reproduce experimental observations in Controlled Radical Polymerization (CRP)?" has been answered by introducing in the kinetic model a delay and treating CRP as a non-Markovian process. The efficient stochastic simulation (SS) approach allowing for an accurate description of CRP has been formulated, theoretically grounded and tested using experimental data and the less advanced SS algorithms.

An accurate prediction of a morphology development in multi-phase polymers is vital for synthesis of new materials but still not feasible due to its complexity. We proposed a Population Balance Equations (PBE)-based model and derived a conceptually new and computationally tractable numerical approach for its solution in order to provide a systematic tool for a morphology prediction in composite polymers.

Finally, we designed a stochastic simulation framework for continuous measurements performed on quantum systems of theoretical and experimental interest, which helped us to re-examine the "fuzzy continuous measurements" theory by Audretsch and Mensky (1997) and expose some of its deficiencies, while making amendments where necessary.

All developed modelling approaches are general enough to be applied to the broad range of physical applications and thus ultimately to contribute to the understanding and prediction of complex chemical and physical processes.

Contents

List of Figures

List of Tables

List of Algorithms

Summary

Natural phenomena and physical systems usually involve processes, characterised by randomness. Probabilistic modelling is a powerful tool, providing a rich description of such processes. The underlying randomness in a probabilistic model is represented by the means of a probability distribution function, which maps any possible outcome of a given event to its occurrence probability.

The set of all possible outcomes of the observed phenomenon is known as the sample space. A probability distribution function must be non-negative and return the total probability, if the entire sample space is considered. Then, the shape of the function indicates the way the probability is distributed over the various outcomes.

The objective of probabilistic modelling consists in inferring the probability distributions governing the considered systems. Such description gives the full range of probabilities for any state of the system, accounting for the inherent randomness.

In this Thesis, we focus on the time evolution of the probability distributions describing various physical and chemical processes in classical and quantum systems. We develop novel modelling approaches, which ultimately will contribute to understanding and prediction of such processes. In particular, the Thesis investigates probabilistic models and simulations techniques addressing the following applications: (i) Controlled Radical Polymerization, (ii) Multi-phase Polymers Morphology and (iii) Continuous Fuzzy Measurements made of elementary quantum systems.

Controlled Radical Polymerization (CRP) is a chain-growth process that proceeds by addition of monomer units to a growing polymer chain. CRP is a special type of polymerization which is conducted in the presence of an additional chemical reagent known as a control agent. The presence of such agent allows one to control the molecular weight of the polymer chain.

The available experimental data show that the introduction of control agents in Radical Polymerization can change the relative frequencies of the competitive reactions, resulting in a significant reduction of the polymers branching. The interest in new modelling arises from the reported contradiction between experimental evidences and classical modelling of chemical kinetics.

The **Multi-phase Polymers Morphology (MPM)** can be defined as the pattern of phase-separated domains comprising a multi-phase polymers particle. Properties of such a particle strongly depend on its morphology, and thus the control of particle morphology is a key factor for success in producing high quality polymers materials.

The synthesis of new morphologies is time and resources consuming, as it largely relies on heuristic knowledge. Therefore, the predictive modelling of such processes is of great interest to the practitioners. No general methodology is currently available for predicting the morphology of realistic multi-phase systems. Several modelling approaches, describing the dynamics of the morphology of a single particle, have been suggested in the last few years (ref. in Section 2.1.1). However, the single-particle approaches only provide a partial view of realistic systems, containing many particles. Furthermore, such models are computationally demanding even with the use of High Performance Computers.

Continuous Fuzzy Measurements (CFM) consist of observations performed on quantum systems of experimental and theoretical interests. In contrast to the classical case, quantum measurements have to perturb the system evolution, or no information can, in general, be gathered. In other words, accurate observations can be only obtained at the price of a strong influence on the free dynamics of the studied system.

In the nineties of the last century, Mensky reconsidered the need for a compromise between the ac-

curacy and the perturbation incurred. His proposal consisted in using a sequence of less accurate (fuzzy) meters, employed ever frequently, ultimately tending to a continuous limit. We will refer to this technique as Continuous Fuzzy Measurements (CFM). For such a regime, Audretsch and Mensky (1997) predicted the possibility to detect the system state by direct inspection of the meter outcomes, eventually aligning with one of the eigenvalues of the measured quantity. We notice that this is not what happens even if a system is prepared in an eigenstate, in which it will then remain at all times. This observation motivated our interest in the re-examination of the Mensky's theory of the CFM, using the techniques of probabilistic modelling.

The objective of this Thesis is to shed light on some of the questions mentioned above. For that, we propose to develop probabilistic frameworks for (*i*) the quantitative modelling of Controlled Radical Polymerization, which would agree with the experimental evidence, (*ii*) the on-the-fly prediction of Multi-phase Polymers Morphology for systems of many particles and (*iii*) the modelling and analysis of Continuous Fuzzy Measurements for the re-examination of the Mensky's theory.

Probabilistic models and simulation algorithms advanced dramatically over the past few decades. Today one of the major challenges is to turn the mathematical methods into practical tools. Such tools should be fast, accurate and made suitable for integration into the modern technological processes. The algorithms being implemented in the original software package should provide the level of accuracy and efficiency required for the study of real-world processes.

With these goals in mind, we have chosen two probabilistic modelling frameworks: (*a*) **Stochastic Simulations (SS)** and (*b*) **Population Balance Equations (PBE)**.

(a) Research Lines of SS Framework.

(b) Research Lines of PBE Framework.
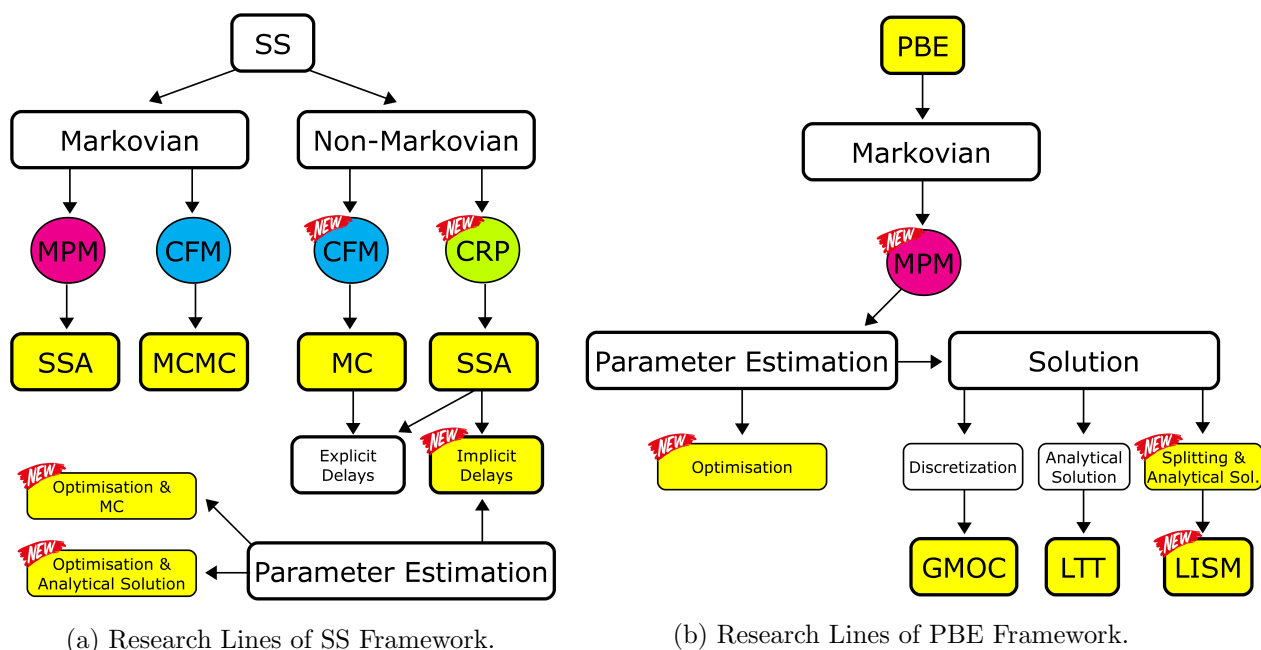
Figure S.1: Probabilistic modelling frameworks proposed in this study: (*a*) Stochastic Simulations (SS) and (*b*) Population Balance Equations (PBE). Known features and well-established techniques are shown in white, while novel formulations and implementations are highlighted in yellow. The icon "New" indicates conceptually new ideas.

While **Stochastic Simulations** strategy is employed in all considered studies, i.e. for the CRP, MPM and CFM, the **Population Balance Equations**-based model was only proposed for the prediction of the development of multi-phase morphologies, i.e. for the MPM.

We consider **Stochastic Simulations models** in two regimes: Markovian (for the MPM, CFM) and non-Markovian (for the CRP, CFM). The development of non-Markovian models was crucial for reproducing the delays, present in chemical reactions of Controlled Radical Polymerization, and for a reconstruction of non-Markovian, in general, behaviour of meter readings in the CFM. On the other hand, the evolution of the particles morphology development in the MPM, and highly accurate measurements in the CFM, are pure Markovian processes, and can be fully described by Markovian

models.

Several different formulations and implementations of the Monte Carlo algorithm, e.g. Markov Chain Monte Carlo (MCMC), Stochastic Simulation Algorithm (SSA), random walk Monte Carlo (MC), have been proposed for the use in Stochastic Simulations within this Thesis, in order to achieve the best accuracy and performance for each specific application. In addition, the advanced optimisation procedures, combined with either Monte Carlo or a novel analytical approach, have been developed for tuning parameters of probability density functions in non-Markovian models.

Figure S.1a summarises the Stochastic Simulations (SS) framework developed, implemented and applied within this Thesis. The applications of specific components are labelled by an encircled application name. The known features and well-established techniques are shown in white, whereas the novel formulations, derivations or implementations are highlighted in yellow. An icon "New" indicates where conceptually new ideas have been proposed.

One of such ideas is to assume non-Markovian kinetics, and introduce delays among the competitive processes of Controlled Radical Polymerization. This assumption, and a thorough analysis of the statistics of the polymers chains growth in the presence of delays, have led us to yet another two new findings. First, we identified the effective way to implicitly define a probability distribution function in a stochastic simulation of delayed processes, even if the precise amount of delay is unknown. Then, the optimisation algorithm, which secures such identification, has been dramatically improved by replacing its Monte Carlo core with an analytical solution.

The **Population Balance Equations (PBE)-based framework** for prediction of the Multi-phase Polymers Morphology development in multiple particles systems is explained in Figure S.1b. The notations similar to those in Figure S.1a are used.

In contrast to currently available computationally expensive and restricted single-particle approaches, the proposed PBE-based model provides a view of the whole population of polymers particles, taking into account Physics and Chemistry behind the morphology formation. The novel model has been presented in dimensionless and computationally tractable variables using our new optimisation algorithm. In addition to the Stochastic Simulation Algorithm (SSA) falling into Stochastic Simulations framework, we developed three original numerical methods for solving the PBE model for MPM: the discretization based Generalised Method Of Characteristics (GMOC), the Laplace Transform Technique (LTT), which analytically derives the Laplace transforms of the PBE solutions, and the Laplace Induced Splitting Method (LISM). The latter is based on the idea, which, to our knowledge, has never been explored in numerical methods for PBE. More specifically, we combine a splitting integration scheme with Laplace induced analytical solutions derived for the simplified PBEs, which together compose the PBE of interest.

In the following we provide further details about the proposed solutions for each application under consideration, i.e. CRP, MPM and CFM, while in Table S.1 we outline the objectives, state-of-the-art, new ideas and major achievements specific to those applications.

Chapter 1 focuses on the quantitative modelling of Controlled Radical Polymerization (CRP). As stated before, experimental evidence indicates that the introduction of control agents can change the relative frequencies of the competitive reactions, resulting in a significant reduction of the polymer's branching. However, no theoretical or modelling / simulation proofs were presented to date in the support of this claim. In this study, we suggest that classical kinetics theories cannot predict the observed reduction, because of the underlying hypothesis of memoryless dynamics. In Chapter 1, we show that such a reduction can be explained by assuming the non-Markovian kinetics, accounting for the delays caused by the chemical reactions.

To prove this idea, we select the probabilistic framework of the Stochastic Simulation Algorithm (SSA), because it can account for the constraints characterising the CRP reaction. In addition, it can potentially estimate any quantity of interest by the computation of the corresponding statistics. However, the formulation of SSA requires the choice of the distributions of inter-event times.

Based on the above, we provide the analytical representation of distributions modelling polymerization reactions with delaying events. We propose mathematical models for Markovian and non-Markovian growth of a polymer chain, showing that the introduction of delays significantly changes the statistics of the grown polymer. Our analysis also results in (*i*) the functional expression of suitable distribu-

	Chapter 1	CRP	Chapter 2	MPM	Chapter 3	CFM
Application	Controlled Radical Polymerization (CRP)		Multi-phase Polymers Morphology (MPM)		Continuous Fuzzy Measurements (CFM)	
Objective	Quantitative Modelling of CRP		On-the-fly Prediction of MPM		Modelling & Analysis of CFM	
State-of-the-art	Kinetic Modelling disagree with Experiments		Morphology Prediction for a Single Particle		Mensky's Theory on CFM	
Fresh Ideas	CRP is a non-Markovian Process with Delays		Calculate the Distribution of Morphologies for the Whole Population		Some Statements in Mensky's Theory are Incorrect	
Results	Stochastic Approach for Modelling CRP in Agreement with Experiments		Computationally Efficient Modelling Framework for Prediction of MPM		Re-examination of Mensky's Theory	

Table S.1: Outline of the Thesis.

tions to embed the required delays and (ii) the SSA-based methodology to simulate the polymerization reactions of interest.

Since our objective is to explain the reduction in relative frequencies of the competitive reactions, we then apply the simulation methodology to the computation of relative frequencies of constrained events. In particular, we design a Monte Carlo (MC) method for evaluation of the quantities of interest. We also derive the corresponding analytical approach, providing a formula for the rate of polymers branching in CRP of acrylic monomers.

We demonstrate in Chapter 1 that our analytical procedure is free of statistical errors, and thus guarantees more accurate estimations, than those provided by an MC simulation. In addition, the method is significantly (an order of the sample size $\geq 10^4$) faster than the MC approach.

The analytical and Monte Carlo procedures are used as a core of the optimisation routine designed for refining the parameters of the delayed distributions with the help of available experimental data. The delayed density functions, with the optimised parameters, complete the formulation of our stochastic approach for modelling the CRP reaction in agreement with experimental observations. The simulated branching levels correctly reproduce the available data, as shown in Chapter 1.

The goal of Chapter 2 is to develop a modelling framework allowing a fast and accurate prediction of Multi-phase Polymers Morphology (MPM). The speed of the predictive simulations technique should be high enough for enabling on-the-fly recommendations for technological conditions in the synthesis of new multi-phase morphologies.

Contrarily to the available single-particle approaches, we propose to calculate the distribution of morphologies for the whole population of polymer particles, taking into account the relevant kinetic and thermodynamic effects.

We start with the derivation of a model describing the physics of the process through the distribution of the expected size of polymers agglomerates. The model is formulated in terms of integro-differential equations known as Population Balance Equations (PBE). The PBE model accounts for the mechanisms of the considered reaction: aggregation, growth, nucleation and phase transition.

We propose an original procedure for the automatic scaling of the PBE model to dimensionless and computationally tractable variables. The technique relies on the optimisation routine for finding proper scaling factors, embedding the information carried by experimental rates expressed in physical units. We demonstrate that for the latex polymers, the scaling procedure results in reducing the ratio between maximal and minimal parameters values from 10^{57} (original) to 10^5 (dimensionless).

We also perform an analysis of the derived model, showing the non-negativity of the unknown solution, characterising its first-orders moments, and studying its asymptotic behaviour.

We develop four approaches for integrating the PBE model: Stochastic Simulation Algorithm (SSA), Generalised Method Of Characteristics (GMOC), Laplace Transform Technique (LTT) and Laplace Induced Splitting Method (LISM). The features of each method are analysed in Chapter 2, outlining benefits and drawbacks.

Although LTT provides high levels of precision and speed for the tested models, its applicability is limited by the required assumptions. The numerical experiments show that SSA is a robust integration technique, but computational inefficiencies make the approach not competitive for solving the addressed PBE model. In the performed experiments, GMOC ensures good accuracy and efficiency of simulation. However, LISM outperforms GMOC in computational speed by up to a factor of two orders of magnitude, while guaranteeing the same accuracy for the tested cases.

On the basis of the performed experiments, we conclude that the developed LISM methodology is a promising technique for prediction of multi-phase polymers morphology in systems of many particles.

Chapter 3 aims to model and analyse the behaviour of measurements performed on quantum systems. In particular, we consider frequent observations, continuous in the limit, such as Continuous Fuzzy Measurements (CFM).

By their very nature, continuous quantum measurements are not amenable to an analytical treatment, but are well suited for numerical simulations. Thus, we propose a stochastic model and a Monte Carlo (MC) method to study the dynamics of the observations. The measurements behaviour is described through the knowledge of the distribution of their outcomes.

The developed MC algorithm allows estimating the outcomes of the performed measurements and the density matrix, describing the state of the monitored quantum system. We validate the accuracy and the expected convergence rate of the designed MC method, comparing it with the analytical solutions, whenever these are available. In particular, we obtain an analytical expression for the expectation of the first meter reading, valid for any level of accuracy of the performed measurements. In addition, the analytical solution for the density matrix is available, if the taken observations are accurate enough. In such a case, the meter readings behave like a Markov chain, whose transition probability matrix is readily derived.

Different regimes of the taken observations are characterised by their accuracy and the corresponding influence on the system dynamics. In particular, accurate measurements lead to the Markovian behaviour of the meters, but affect the natural dynamics of the quantum system. On the other hand, infrequent imprecise observations result in the non-Markovian regime of the meters. The natural evolution is unaltered, but very little is known about the actual state of the system. We provide the proof and the validating tests for the Markovian and non-Markovian behaviour of the quantum measurements. Both regimes can be successfully simulated using the designed MC method.

The Monte Carlo technique helped us to re-examine the theory by Audretsch and Mensky (1997) on CFM, often seen as a universal model-free approach to continuous quantum measurements. In particular, we demonstrate that a Gaussian restriction, resulting in a sequence of many highly inaccurate measurements, is not sufficiently strong to ensure proximity between the observations and the Feynman paths along which the monitored system evolves. In the continuous limit, the variations of a typical measurement become much larger than the separation between the eigenvalues of the measured quantity. Therefore, we revise the statements of the Mensky's theory, proposing a different mechanism for the decoherence in a free system and the Zeno effect in a driven system, when its Rabi oscillations are quenched by monitoring.

In summary, the methodologies developed within this Thesis have been inspired by several particular applications and unresolved issues. However, the proposed novel approaches, such as, the mathematical analysis of delayed reactions, the parameter estimation procedure with the analytical core, the scaling technique to computationally tractable variables, the Laplace induced splitting integration method, the stochastic model for quantum observations or the revised theory of Continuous Fuzzy Measurements, can be applied to a broader range of problems in physics, chemistry, and biology. Our results have been presented in four scientific papers published in the high impact journals [1, 2, 3, 4].

Resumen

Los fenómenos naturales y los sistemas físicos suelen implicar procesos caracterizados por su aleatoriedad. La modelización probabilística es una herramienta potente que proporciona una rica descripción de tales procesos. En un modelo probabilístico, la aleatoriedad subyacente se representa por medio de una función de distribución de probabilidad, que realiza un mapa de todos los resultados posibles de un evento dado en función de la probabilidad de sus ocurrencias.

El conjunto de todos los resultados posibles del fenómeno observado se conoce como "espacio muestral". Una función de distribución de probabilidad debe ser no negativa y reflejar la probabilidad total si se toma en consideración todo el espacio muestral. En ese caso, la forma de la función indica la manera en que se distribuye la probabilidad entre los distintos resultados.

El objetivo de la modelización probabilística consiste en inferir las distribuciones de probabilidad que rigen los sistemas considerados. Esta descripción proporciona la gama completa de probabilidades para cualquier estado del sistema, teniendo en cuenta la aleatoriedad inherente.

En esta Tesis nos centramos en la evolución en el tiempo de las distribuciones de probabilidades que describen varios procesos químicos y físicos en sistemas clásicos y cuánticos. Desarrollamos enfoques de modelización novedosos, que, en última instancia, contribuirán al entendimiento y predicción de dichos procesos. En concreto, la Tesis investiga modelos probabilísticos y técnicas de simulaciones que tratan las siguientes aplicaciones: (*i*) Controlled Radical Polymerization, (*ii*) Multi-phase Polymers Morphology y (*iii*) Continuous Fuzzy Measurements realizadas sobre sistemas cuánticos elementales.

Controlled Radical Polymerization (CRP) es un proceso de crecimiento en cadena que actúa mediante adición de unidades monoméricas a una cadena de polímeros en crecimiento. CRP es un tipo especial de polimerización que se realiza en presencia de un reactivo químico adicional conocido como agente de control. La presencia de dicho agente permite que se controle el peso molecular de la cadena de polímeros.

Los datos experimentales disponibles muestran que la introducción de agentes de control en el proceso de polimerización puede cambiar las frecuencias relativas de las reacciones competitivas, lo que da como resultado una reducción significativa de la ramificación de polímeros. El interés por nuevas modelizaciones deriva de la contradicción observada entre las evidencias experimentales y la modelización clásica de la cinética química.

Multi-phase Polymers Morphology (MPM) puede definirse como el patrón de dominios separados por fases que incluye una partícula de polímeros multifásicos. Las propiedades de dicha partícula dependen en gran medida de su morfología y, por tanto, el control de la morfología de las partículas es un factor clave para el éxito en la producción de materiales poliméricos de alta calidad.

La síntesis de nuevas morfologías consume tiempo y recursos, puesto que se basa en gran medida en el conocimiento heurístico. Por tanto, la modelización predictiva de dichos procesos es de gran interés. En la actualidad, no existe una metodología general para predecir la morfología de sistemas multifásicos realistas. En los últimos años, se han sugerido varios métodos de modelización que describen la dinámica de la morfología de una única partícula (ref. en Section 2.1.1). No obstante, los métodos que enfocan una única partícula solo proporcionan una visión parcial de los sistemas reales, que contienen muchas partículas. Además, dichos modelos son computacionalmente exigentes, incluso con el uso de ordenadores de alto rendimiento.

Continuous Fuzzy Measurements (CFM) consisten en observaciones realizadas en sistemas cuánticos con interés experimental y teórico. En contraposición al caso clásico, las mediciones cuánticas tienen que perturbar la evolución del sistema o, por lo general, no se puede compilar información. En

otras palabras, solo se pueden obtener observaciones precisas a costa de una fuerte influencia sobre la dinámica libre del sistema estudiado.

En los años noventa del siglo pasado, Mensky reconsideró la necesidad de un compromiso entre la precisión y la perturbación incurrida. Su propuesta consistía en el uso de una secuencia de mediciones menos precisas (fuzzy) empleada con frecuencia y que en última instancia tendía a un límite continuo. Nos referiremos a esta técnica como Continuous Fuzzy Measurements (CFM). Para dicho régimen, Audretsch y Mensky (1997) predijeron la posibilidad de detectar el estado del sistema mediante inspección directa de los resultados de medición, que convergerían a uno de los autovalores de la cantidad medida. Apreciamos que esto no es lo que ocurre aunque se prepare el sistema en un estado propio, en el que después permanecerá en todo momento. Esta observación motivó nuestro interés en el examen de la teoría de Mensky sobre las CFM con el uso de las técnicas de modelización probabilística.

El objetivo de esta Tesis es el de aportar luz sobre algunas de las cuestiones mencionadas anteriormente. Para ello, proponemos desarrollar marcos probabilísticos para (i) la modelización cuantitativa de CRP, que estarían de acuerdo con la evidencia experimental, (ii) la predicción sobre la marcha de MPM para sistemas de muchas partículas y (iii) la modelización y análisis de CFM para el reexamen de la teoría de Mensky.

Los modelos probabilísticos y los algoritmos de simulación han avanzado muchísimo en las últimas décadas. En la actualidad, uno de los principales retos consiste en convertir los métodos matemáticos en herramientas prácticas. Dichas herramientas deberían ser rápidas, precisas y aptas para su integración en los modernos procesos tecnológicos. Los algoritmos que se implementan en los paquetes de software deberían proporcionar el grado de precisión y eficiencia que se requiere para el estudio de procesos reales.

Con estos objetivos en mente, hemos elegido dos marcos de modelización probabilística: (a) **Stochastic Simulations (SS)** y (b) **Population Balance Equations (PBE)**.
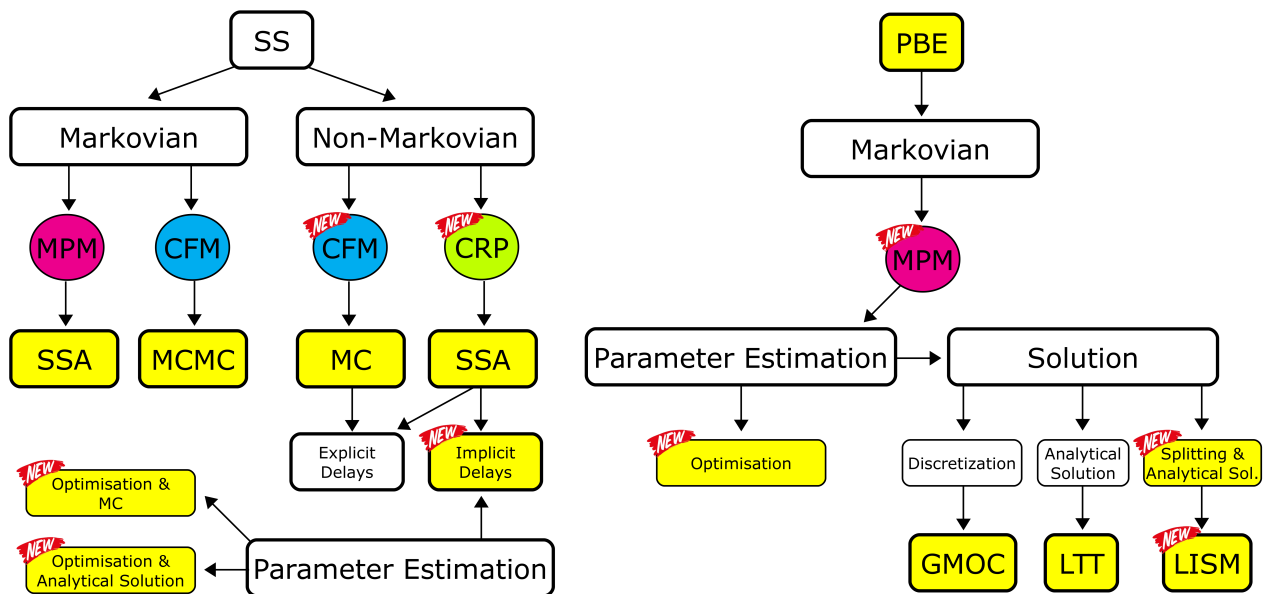
(a) Líneas de Investigación del Marco SS.　(b) Líneas de Investigación del Marco PBE.

Figure R.1: Marcos de modelización probabilística propuestos en este estudio: (a) Stochastic Simulations (SS) y (b) Population Balance Equations (PBE). Las características conocidas y las técnicas consolidadas se muestran en blanco, mientras que las formulaciones e implantaciones novedosas se destacan en amarillo. El icono "New" indica ideas conceptualmente nuevas.

Si bien la estrategia de **Stochastic Simulations** se emplea en todos los estudios considerados, i.e. para CRP, MPM y CFM, el modelo basado en **Population Balance Equations** únicamente se propuso para la predicción del desarrollo de morfologías multifásicas, i.e. para MPM.

Consideramos los modelos de **Stochastic Simulations** en dos regímenes: markoviano (para MPM, CFM) y no markoviano (para CRP, CFM). El desarrollo de modelos no markovianos fue crucial

para reproducir los retrasos, presentes en reacciones químicas de CRP, y para reconstruir del comportamiento no markoviano, en general, de las mediciones en CFM. Por otro lado, la evolución del desarrollo de la morfología de partículas en MPM y las mediciones sumamente precisas de CFM son procesos markovianos puros y pueden describirse completamente mediante modelos markovianos.

Se han propuesto varias formulaciones e implantaciones diferentes del algoritmo Monte Carlo, e.g., Markov Chain Monte Carlo (MCMC), Stochastic Simulation Algorithm (SSA), random walk Monte Carlo (MC), para el uso en el marco SS de esta Tesis con el fin de optimizar la precisión y rendimiento para cada aplicación específica. Además, se han desarrollado procedimientos avanzados de optimización, combinados con un enfoque Monte Carlo o un novedoso enfoque analítico, para ajustar los parámetros de funciones de densidad de probabilidades en modelos no markovianos.

Figure R.1a resume el marco de Stochastic Simulations (SS) desarrollado, implementado y aplicado en esta Tesis. Las aplicaciones de componentes específicos se etiquetan con un nombre de aplicación rodeado por un círculo. Las características conocidas y las técnicas consolidadas se muestran en blanco, mientras que las formulaciones, derivaciones e implementaciones novedosas se destacan en amarillo. Un icono "New" indica dónde se han propuesto ideas conceptualmente nuevas.

Una de dichas ideas consiste en asumir la cinética no markoviana e introducir retrasos entre los procesos competitivos de CRP. Esta asunción y un análisis de las estadísticas del crecimiento de las cadenas de polímeros en presencia de retrasos nos ha llevado a otros dos nuevos hallazgos. En primer lugar, hemos identificado la forma efectiva de definir implícitamente una función de distribución de probabilidades en una simulación estocástica de procesos retrasados, incluso aunque la cantidad precisa de retraso sea desconocida. Así pues, el algoritmo de optimización, que garantiza dicha identificación, ha mejorado mucho con el reemplazo de su núcleo Monte Carlo por una solución analítica.

El marco basado en **Population Balance Equations (PBE)** para la predicción del desarrollo de la morfología de polímeros multifásicos en sistemas de múltiples partículas se explica en Figure R.1b. Se usan notaciones similares a las de Figure R.1a.

Como contraposición a los enfoques actuales, caros desde el punto de vista computacional y restringidos a una única partícula, el modelo propuesto de PBE proporciona una visión de toda la población de partículas de polímeros, teniendo en cuenta los aspectos físicos y químicos subyacentes a la formación morfológica. Este novedoso modelo se ha presentado en variables sin dimensión y computacionalmente rastreables, puesto que se ha aplicado nuestro nuevo algoritmo de optimización. Además del Stochastic Simulation Algorithm (SSA), que recae dentro del marco SS, hemos desarrollado tres métodos numéricos originales para resolver el modelo PBE para MPM: Generalised Method Of Characteristics (GMOC), basado en discretización, Laplace Transform Technique (LTT), que deriva analíticamente las transformadas de Laplace de las soluciones de PBE, y Laplace Induced Splitting Method (LISM). El último se basa en la idea de que, a nuestro saber, nunca se ha explorado en métodos numéricos para PBE. Más específicamente, combinamos un método de integración de "splitting" con soluciones analíticas inducidas por las transformadas de Laplace de PBEs simplificadas, que en conjunto componen la PBE de interés.

A continuación, damos más detalles sobre las soluciones propuestas para cada aplicación considerada, i.e. CRP, MPM y CFM, mientras que en Table R.1 describimos los objetivos, estado actual, nuevas ideas y principales logros específicos para tales aplicaciones.

Chapter 1 se centra en la modelización cuantitativa de Controlled Radical Polymerization (CRP). Como se ha indicado anteriormente, la evidencia experimental muestra que la introducción de agentes de control puede cambiar las frecuencias relativas de las reacciones competitivas, lo que da como resultado una reducción significativa de la ramificación de polímeros. No obstante, no se han presentado hasta la fecha pruebas teóricas o de modelización/simulación que apoyen de esta afirmación. En este estudio, sugerimos que las teorías cinéticas clásicas no pueden predecir la reducción observada a causa de la hipótesis subyacente de dinámicas sin memoria. En Chapter 1, mostramos que dicha reducción puede explicarse asumiendo la cinética no markoviana, que tiene en cuenta los retrasos ocasionados por las reacciones químicas.

Para demostrar esta idea, seleccionamos el marco probabilístico de Stochastic Simulation Algorithm (SSA), porque puede dar cuenta de las restricciónes que caracterizan a la reacción CRP. Además, puede calcular potencialmente cualquier cantidad de interés a través de la computación de las estadísticas

	Chapter 1	CRP	Chapter 2	MPM	Chapter 3	CFM
Aplicación	Controlled Radical Polymerization (CRP)		Multi-phase Polymers Morphology (MPM)		Continuous Fuzzy Measurements (CFM)	
Objetivo	Modelización Cuantitativa de CRP		Predicción sobre la Marcha de MPM		Modelización y Análisis de CFM	
Estado Actual	Disconformidad de la Modelización Cinética con los Experimentos		Predicción Morfológica para una Única Partícula		Teoría de Mensky sobre CFM	
Ideas Nuevas	CRP es un Proceso Markoviano con Retrasos		Calcular la Distribución de Morfologías para Toda la Población		Algunos Resultados de la Teoría de Mensky son Incorrectos	
Resultados	Enfoque Estocástico para Modelización de CRP Conforme a los Experimentos		Marco de Modelización Computacionalmente Eficiente para Predicción de MPM		Reexamen de la Teoría de Mensky	

Table R.1: Descripción de la Tesis.

correspondientes. No obstante, la formulación de SSA requiere la elección de las distribuciones de los tiempos transcurridos entre eventos.

Basándonos en lo anterior, proporcionamos la representación analítica de distribuciones que modelizan reacciones de polimerización con eventos retardantes. Proponemos modelos matemáticos para crecimiento markoviano y no markoviano de una cadena de polímeros, lo que demuestra que la introducción de retrasos modifica significativamente las estadísticas del polímero desarrollado. Nuestro análisis también da como resultado (i) la expresión funcional de distribuciones adecuadas para incrustar los retrasos requeridos y (ii) la metodología basada en SSA para simular las reacciones de polimerización de interés.

Dado que nuestro objetivo es explicar la reducción en frecuencias relativas de las reacciones competitivas, aplicamos la metodología de simulación a la computación de frecuencias relativas de eventos constreñidos. En concreto, diseñamos un método Monte Carlo (MC) para la evaluación de las cantidades de interés. También derivamos el método analítico correspondiente, proporcionando una fórmula para la tasa de ramificación de polímeros en CRP de monómeros acrílicos.

Demostramos en Chapter 1 que nuestro procedimiento analítico está libre de errores estadísticos y, por tanto, garantiza estimaciones más precisas que las proporcionadas por simulaciónes MC. Además, el método es significativamente más rápido (en orden del tamaño de muestra $\geq 10^4$) que el enfoque MC.

Los procedimientos analítico y Monte Carlo se usan como núcleo de la rutina de optimización diseñada para refinar los parámetros de las distribuciones retrasadas con la ayuda de datos experimentales disponibles.

Las funciones de densidad retrasadas, con los parámetros optimizados, competan la formulación de nuestro enfoque estocástico para modelizar la reacción CRP de conformidad con las observaciones experimentales. Los niveles de ramificación simulados reproducen correctamente los datos disponibles, como se muestran en Chapter 1.

El objetivo de Chapter 2 es desarrollar un marco de modelización que permita una predicción rápida y precisa de Multi-phase Polymers Morphology (MPM). La velocidad de la técnica de simulacion predictiva debería ser lo suficientemente alta para permitir recomendaciones sobre la marcha de condiciones tecnológicas en la síntesis de nuevas morfologías multifase.

Contrariamente a los enfoques actuales de partícula única, proponemos calcular la distribución de

morfologías para toda la población de partículas de polímeros, teniendo en cuenta los efectos cinéticos y termodinámicos relevantes.

Comenzamos con la derivación de un modelo que describe la física del proceso a través de la distribución del tamaño previsto para los aglomerados de polímeros. El modelo se formula en términos de ecuaciones integro-diferenciales conocidas como Population Balance Equations (PBE). El modelo PBE da cuenta de los mecanismos de la reacción considerada: agregación, crecimiento, nucleación y transición de fases.

Proponemos un procedimiento original para escalar automáticamente el modelo PBE en variables sin dimensiones y computacionalmente rastreables. La técnica se basa en la rutina de optimización para encontrar factores de escalado adecuados, incrustando la información proporcionada por parámetros experimentales expresados en unidades físicas. Demostramos que, para los polímeros de látex, el procedimiento de escalado da como resultado la reducción de la relación entre los valores máximos y mínimos de los parámetros desde 10^{57} (original) hasta 10^{5} (sin dimensión).

También realizamos un análisis del modelo derivado, que muestra la no negatividad de la solución, caracteriza sus momentos de los dos primeros órdenes y estudia su comportamiento asintótico.

Desarrollamos cuatro enfoques para integrar el modelo PBE: Stochastic Simulation Algorithm (SSA), Generalised Method Of Characteristics (GMOC), Laplace Transform Technique (LTT) y Laplace Induced Splitting Method (LISM). Las características de cada método se analizan en Chapter 2, describiendo sus ventajas e inconvenientes.

A pesar de que LTT proporciona altos niveles de precisión y velocidad para los modelos probados, su aplicabilidad está limitada por las condiciones requeridas. Los experimentos numéricos muestran que SSA es una técnica de integración sólida, pero las ineficiencias computacionales hacen que el enfoque no resulte competitivo para resolver el modelo PBE tratado. En los experimentos realizados, GMOC garantiza una buena precisión y eficiencia de simulación. No obstante, LISM supera a GMOC en rapidez computacional en hasta dos órdenes de magnitud, garantizando la misma precisión para los casos probados.

A partir de los experimentos realizados, concluimos que la desarrollada metodología LISM es una técnica prometedora para la predicción de la morfología de polímeros multifásicos en sistemas de muchas partículas.

Chapter 3 tiene por objeto modelizar y analizar el comportamiento de mediciones realizadas en sistemas cuánticos. En particular, consideramos observaciones frecuentes, continuas en el límite, tales como Continuous Fuzzy Measurements (CFM).

Por su naturaleza, las mediciones cuánticas continuas no son aptas para un tratamiento analítico, pero se pueden describir a través de simulaciones numéricas. Por tanto, proponemos un modelo estocástico y un método Monte Carlo (MC) para estudiar la dinámica de las observaciones. El comportamiento de las mediciones se describe a través del conocimiento de la distribución de sus resultados.

El algoritmo MC desarrollado permite calcular los resultados de las mediciones realizadas y la matriz de densidad, que describe el estado del sistema cuántico de interés. Validamos la precisión y la tasa de convergencia esperada del método MC diseñado, comparándolo con las soluciones analíticas disponibles. En concreto, obtenemos una expresión analítica para la previsión de la primera lectura de mediciones, válida para cualquier nivel de precisión de las mediciones realizadas. Además, se dispone de la solución analítica para la matriz de densidad si las observaciones realizadas son los suficientemente precisas. En tal caso, las lecturas de mediciones se comportan como una cadena de Markov, cuya matriz de probabilidad de transición es derivada.

Diferentes regímenes de las observaciones realizadas se caracterizan por su precisión y la influencia correspondiente en la dinámica de el sistema. En concreto, mediciones precisas llevan al comportamiento markoviano de las mediciones, pero afectan a la dinámica natural del sistema cuántico. Por otro lado, observaciones imprecisas dan como resultado el régimen no markoviano de las mediciones. La evolución natural no se ve alterada, pero se sabe muy poco sobre el estado real del sistema. Proporcionamos las pruebas y los ensayos de validación para el comportamiento markoviano y no markoviano de las mediciones cuánticas. Ambos regímenes pueden simularse con éxito usando el método MC diseñado.

La técnica Monte Carlo nos ayudó a reexaminar la teoría de Audretsch y Mensky (1997) sobre CFM,

entendida con frecuencia como un enfoque universal para realizar mediciones cuánticas continuas. En concreto, demostramos que una restricción gaussiana, que da como resultado una secuencia de muchas mediciones altamente imprecisas, no es suficiente para garantizar proximidad entre las observaciones y las rutas (Feynman paths) a través de las que avanza el sistema de interés. En el límite continuo, las variaciones de una medición típica resultan mucho más grandes que la separación entre los valores propios de la cantidad medida. Por tanto, revisamos las afirmaciones de la teoría de Mensky, proponiendo un mecanismo diferente para la decoherencia cuántica y el efecto Zeno.

En resumen, las metodologías desarrolladas en esta Tesis se inspiran en varias aplicaciones particulares y cuestiones sin resolver. No obstante, los enfoques novedosos propuestos, tales como el análisis matemático de reacciones retardadas, el procedimiento de estimación de parámetros con el núcleo analtico, la técnica de escalado para variables computacionalmente rastreables, el método de integración de splitting inducido por transformadas de Laplace, el modelo estocástico para observaciones cuánticas o la teoría revisada sobre CFM, pueden aplicarse a otros problemas de física, química y biología. Nuestros resultados se han presentado en cuatro estudios científicos publicados en revistas de gran difusión [1, 2, 3, 4].

Chapter 1

Stochastic Modelling of Polymerization Reactions with Delays

1.1 Motivation

1.1.1 Controlled Radical Polymerization: Unresolved Issues

A substantial part of the polymer market is produced by free radical polymerization (FRP). This is a chain-growth process that proceeds by addition of monomer units to a growing polymer chain. The addition of monomer units is called *propagation*. In radical polymerization of monomers, each propagation outcome regenerates the active radical species at the chain end, and the chain continues to grow, forming high molecular weight polymer molecules. Chain growth may be terminated by bimolecular reaction of two growing chains and by transfer of the radical to monomer or to polymer [5].

Alternatively, the reactive radical at the end of the chain can be transferred to a carbon atom within the chain, thus generating a so called mid-chain radical. It occurs via a process known as *backbiting* [6]. Due to the specific molecular configuration required for the backbiting to occur, at least three propagation outcomes must take place before the next backbiting outcome occurs. Hence, the reactive radical is transferred from the polymer chain tail to a monomer unit located at least two positions behind.

The mid-chain radical formed by backbiting may (*i*) react with a monomer, thus continuing the chain growth [6, 7], (*ii*) migrate along the chain [8], (*iii*) undergo a beta-scission [9], i.e. a conversion of the mid-chain radical into a free radical by splitting a carbon-carbon bond [10], and (*iv*) react with other species present in the medium [11]. The addition of monomer units to the mid-chain radical, which is formed by backbiting, generates a branched structure. The reactions of propagation and backbiting, with the formation of the branched structure, are schematically illustrated in Figure 1.1.

In the last two decades, Controlled Radical Polymerization (CRP) of monomers [12] has revolutionised FRP, allowing an unprecedented control of the polymer micro-structure. Controlled Radical Polymerization is a special type of radical polymerization which is conducted in the presence of an additional chemical reagent known as a *control agent*. In CRP, the reactive radical chain end is subjected to frequent deactivation and reactivation steps, allowing one to control the molecular weight of the polymer chain. *Reversible deactivation* of the reactive chain end is an outcome which occurs in competition with propagation and backbiting.

Obtaining information about the kinetics of the process as well as predicting relative rates of reactions between backbiting and propagation are important for understanding polymerization of monomers. The ratio of the two competitive outcomes has a strong impact on the micro-structure and mechanical properties of the resulting polymer. It can be measured by evaluating the *branching fraction*, which is determined experimentally as the ratio of the number of branches to the number of propagation outcomes that have occurred.

In a conventional radical polymerization there exists a competition between several potential kinetic events a growing propagating radical can undergo. The most notable ones are propagation, termina-
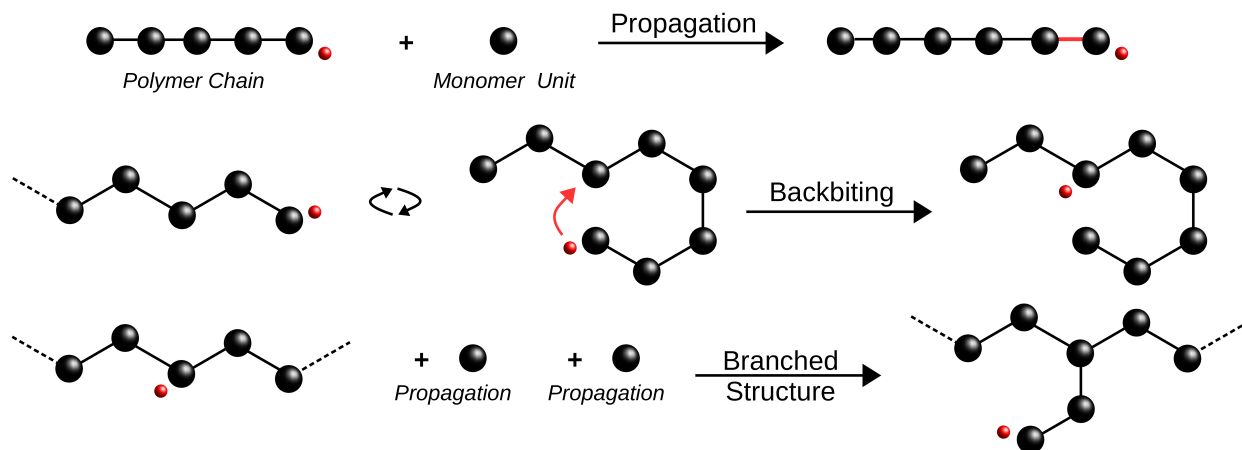
Figure 1.1: The *propagation* process consists in the addition of a *monomer unit* (black sphere) to a *polymer chain*. The radical (red sphere) located at the chain end creates the bond (red line) between the polymer chain and the added monomer. The propagation reaction also regenerates the active radical (red sphere) at the new tail of the chain. The *backbiting* reaction can occur after the polymer chain starts rolling. The bend allows the radical (red sphere) being transferred to a monomer unit within the polymer chain, producing the *mid-chain radical*. Successive propagations from the mid-chain radical result in the formation of a *branched structure*.

tion and backbiting. The characteristic time for termination is much longer than that of propagation and backbiting, and therefore is not expected to affect the relative number of backbitings and propagations. On the other hand, the introduction of an intermittent deactivation stage in controlled radical polymerization, imposes an additional event taking place at a time scale similar to that of backbiting and propagation. Although classical chemical reaction kinetics dictates that the imposition of the additional competitive process should not impact the ratio of backbitings to propagations, experimental evidences have shown that there is a strong reduction in branching fraction under CRP conditions [13, 14]. Furthermore, it has been reported that the rate of backbiting and the branching fraction may be affected by the presence of polar solvents [15] and high concentrations of chain transfer agent [14, 16].

The kinetics of radical polymerization have been systematically studied for nearly a century and in general are well understood. However, in light of recent developments in controlled radical polymerization many kinetic anomalies have arisen. One of such unexplained results, namely, a decrease of the branching level in CRP observed in multiple experiments but not understood theoretically or predicted by simulations has prompted a lively debate on the causes of such findings.

Initially, it was suggested that the change in branching fraction in controlled radical polymerization is caused by differences in the concentrations of highly reactive short chain radicals between controlled and conventional radical polymerization [13]. However, both stochastic [17] and deterministic models [18] have shown that the chain-length-dependent rate constants have a minimal effect on the branching fraction. The authors of these studies have nominated three possible causes for the reduction in branching such as (*i*) a decrease in the backbiting reaction under controlled radical polymerization conditions, (*ii*) a fast and virtually irreversible deactivation of the tertiary radical formed by backbiting, or (*iii*) a combination of the above.

Reyes and Asua [17] suggested that the reduction in branching fraction may be caused by a decrease in the backbiting reaction because the time scale for deactivation of the active radical is faster than the time scale for backbiting. However, the stochastic modelling assuming the Gaussian distributions for the probability density functions of the different reactions did not confirm this hypothesis and led to the conclusion that backbiting can never occur.

Konkolewicz et al. [18] studied the decrease of branching fraction in atom transfer radical polymerization (ATRP) of acrylates. Choosing in their model the probability function to be an exponential function they observed no variation in the backbiting relative to propagation and thus concluded that

the decrease in branching fraction was caused by irreversible deactivation of some tertiary radicals. This hypothesis, however, has been disproved by experiments of Ballard et al. [14] who demonstrated that the irreversible capping of the mid-chain radical is not the reason for the branching reduction in ATRP. This left a reduction in the backbiting relative to propagation to be the only factor responsible for the lower branching in ATRP and arose the question why such reduction is not confirmed by the study of Konkolewicz et al. [18].

The reduction in branching fraction for high chain transfer agent (CTA) concentrations [14, 16] was attributed to a patching mechanism in which the tertiary radical tends to undergo chain transfer to CTA instead of propagation [19, 20, 21]. This hypothesis also has been refuted by Agirre et al. [16] who demonstrated a significant reduction in branching fraction compared to a conventional radical polymerization in the presence of large amounts of CBr_4 as a chain transfer agent, with no patched structure found. Therefore, similar to the case of ATRP, the only possible reason for lower branching can be a smaller backbiting/propagation ratio, but this is not confirmed by the conventional stochastic and deterministic simulations.

Therefore, although many experiments indicate that in controlled radical polymerization reduction in branching fraction must be due to reduction in the rate of backbiting with respect to propagation, no theoretical or modelling-simulation proofs were presented to date in the support of this claim.

1.1.2 Modelling Controlled Radical Polymerization: A Proposed Solution

The discussed above studies are based on an intrinsic assumption that the CRP process is memoryless, and hence the probability density functions, that are the distributions of possible reaction times, follow an exponential decay. We argue that in radical polymerizations, particularly in controlled radical polymerization, where the leading reaction, i.e. backbiting, depends on the preceding events, and the radical intermediate is intermittently deactivated, models without memory cannot explain the observed kinetic anomalies. Instead, the memory models should be developed. More precisely, we will show that the reduction of the branching level in radical polymerization can be explained by assuming a non-Markovian kinetics and introducing delays among the competitive processes.

The objective of this chapter is to (i) propose a stochastic model for the polymerization reactions with delays, (ii) provide the efficient methods for solving such a model for a broad range of applications and (iii) implement the developed model to a study of the branching reduction in CRP of acrylic monomers.

Keeping this in mind, we organise the chapter as follows.

Section 1.2 reviews the Stochastic Simulation Algorithm (SSA) [22, 23] as a possible modelling framework for the simulation of polymerization reactions with delays. SSA is a natural method of choice for the simulation of systems characterised by competitive processes, such as the considered chemical reactions. Its flexibility will allow us to introduce non-Markovian kinetics either through the modification of the inter-event time distribution or by the addition of constraints among the possible events in an SSA algorithm.

In Section 1.3, the mathematical models for Markovian and non-Markovian growth of a polymer chain are discussed. We provide the mathematical grounds for derivation of probability density functions modelling polymerization reactions with delaying events. We show that the introduction of delays significantly changes the statistics of polymer chain growth. Furthermore, we explain how to simulate the given processes by introducing delays in the formulation of SSA.

In Section 1.4, the delayed SSA provides the Monte Carlo (MC) framework to compute the relative frequencies of constrained events in stochastic processes. The proposed technique can be applied to any system with well-posed constraints. In particular, it is suitable for explaining the reduction in relative frequencies of propagations and backbitings experimentally observed in CRP.

Section 1.5 derives the analytical alternative to the MC method for the computation of the relative frequencies of constrained events in stochastic processes. The approach is free of statistical errors affecting MC methods and faster by a factor of the MC sample size. The derivation is valid for any stochastic process with well-posed constraints among the possible events, making the method useful for various applications. Then, the result is formulated for the prediction of the branching fraction in CRP of acrylic monomers. The proposed analytical approach also helps to prove that memoryless

models are not able to explain the observed reduction of the branching fraction, and thus only models with delays should be applied for study of CRP.

For this reason, Section 1.6 focuses on the delayed densities suitable for the prediction of branching fractions in Controlled Radical Polymerization. In particular, the Monte Carlo method and the analytical approach are specifically formulated for the estimation of the branching fraction in CRP of acrylic monomers. A fitting scheme is designed for refining the parameters of the proposed probability density functions using the available experimental data. Finally, the SSA routine for modelling CRP of acrylic monomers is proposed.

In Section 1.7, we test the accuracy and efficiency of the developed methodologies on the computation of the branching fraction in Controlled Radical Polymerization of acrylic monomers.

Section 1.8 provides conclusions and discussion.

1.2 Stochastic Simulation Algorithm

Stochastic Simulation Algorithm (SSA) [22, 23] is one of the most common approaches for study of stochastic processes describing the evolution of various phenomena in natural and human-made systems. It relies on the knowledge of inter-event probability density functions, and on the information about dependencies between all possible events. SSA is a Monte Carlo based method: it draws multiple realisations of the process and then computes statistics on them. The conventional SSA is based on the assumption that the studied system is well-mixed and memoryless. These assumptions lead to independent exponentially distributed inter-event times. As intuition suggests, this set of hypothesis does not hold for all phenomena of practical interest. One such example is a constrained stochastic process, where the occurrence of some events may depend on the previous history of the process [24]. In these cases, the SSA algorithm can be easily adapted in such a way that the dependencies are realised either *explicitly* by introducing constraints in the SSA algorithm, or *implicitly*, through a modification of inter-event times probability distributions.

In this work, we have chosen to use the SSA method for simulation of polymerization reactions with delays due to its ability to follow the kinetics of competitive processes and to deal with non-Markovian dynamics in the evolution of the system. Section 1.2.1 provides a revision of SSA methods and discusses the Stochastic Simulation Algorithm as a possible methodology for the simulation of polymerization reactions with delays.

1.2.1 SSA Review

Let us consider a well-mixed and thermally equilibrated chemical system of $N \geq 1$ species $\{S_1, .., S_N\}$, which interact through $M \geq 1$ chemical reactions $\{R_1, .., R_M\}$. The purpose of the Stochastic Simulation Algorithm (SSA) is to estimate the state vector

$$\mathbf{X}(t) \equiv [X_1(t), .., X_N(t)] \in \mathbb{N}^N, \tag{1.1}$$

where $X_i(t)$ is the number of molecules of the species S_i at time t, $\forall i = 1, .., N$. Each chemical reaction R_j is characterised by the state-change vector $\nu_j \in \mathbb{Z}^N$ and the propensity function $p_j(\mathbf{x}) \geq 0$, with $j = 1, .., M$. The state-change vector ν_j is defined as the variation of the system state $\mathbf{x}$ caused by one occurrence of the reaction R_j, i.e.

$$\mathbf{x} \xrightarrow{R_j} \mathbf{x} + \nu_j, \quad \forall j = 1, .., M. \tag{1.2}$$

The propensity function $p_j(\mathbf{x})$ corresponds to the occurrence rate of the reaction R_j, given $\mathbf{X}(t) = \mathbf{x}$. In other words, the function $p_j(\mathbf{x})$ is defined so that

$$p_j(\mathbf{x})\, dt \equiv \text{the probability that one } R_j \text{ reaction will occur during}$$
$$\text{the infinitesimal interval } [t, t + dt], \text{ given } \mathbf{X}(t) = \mathbf{x}. \tag{1.3}$$

Having the system state and all possible reactions defined, one might be interested in inferring the probability $\mathbb{P}(\mathbf{x}, t|\mathbf{x}_0, t_0)$ to find the system in the state $\mathbf{X}(t) = \mathbf{x}$ at time t, given $\mathbf{X}(t_0) = \mathbf{x}_0$ at the initial time t_0. The time-evolution equation for $\mathbb{P}(\mathbf{x}, t|\mathbf{x}_0, t_0)$ relies on the definition (1.3) and has been derived in [22]:

$$\frac{\partial \mathbb{P}(\mathbf{x}, t|\mathbf{x}_0, t_0)}{\partial t} = \sum_{j=1}^{M} \left[p_j(\mathbf{x} - \nu_j) \mathbb{P}(\mathbf{x} - \nu_j, t|\mathbf{x}_0, t_0) - p_j(\mathbf{x}) \mathbb{P}(\mathbf{x}, t|\mathbf{x}_0, t_0) \right]. \tag{1.4}$$

Equation (1.4) is known as the Chemical Master Equation (CME).

The CME equation can also serve as a starting point in estimating the average of a given function h of the system state $\mathbf{X}(t)$, i.e. $\langle h(\mathbf{X}(t)) \rangle \equiv \sum_{\mathbf{x}} h(\mathbf{x}) \mathbb{P}(\mathbf{x}, t|\mathbf{x}_0, t_0)$. For example, the time derivative of the expected system state $\langle \mathbf{X}(t) \rangle$ can be obtained by summing (1.4), multiplied by $\mathbf{x}$, over all possible system states $\mathbf{x}$:

$$\frac{d\langle \mathbf{X}(t) \rangle}{dt} = \sum_{j=1}^{M} \nu_j \langle p_j(\mathbf{X}(t)) \rangle. \tag{1.5}$$

In the hypothetical case, random fluctuations can be neglected, i.e. $\langle h(\mathbf{X}(t)) \rangle = h(\mathbf{X}(t))$ for any function h, and thus (1.5) leads to the Reaction Rate Equation (RRE):

$$\frac{d\mathbf{X}(t)}{dt} = \sum_{j=1}^{M} \nu_j \, p_j(\mathbf{X}(t)). \tag{1.6}$$

Analytical solutions of (1.4) and (1.6) are rarely available and numerical methods are needed to estimate the state vector $\mathbf{X}(t)$. SSA is one of such methods, which provides realisations of $\mathbf{X}(t)$ with time t evolving. Any quantity of interest $\langle h(\mathbf{X}(t)) \rangle$ can be then estimated by averaging the accumulated samples.

The key means of the SSA algorithm is the joint probability distribution $P(\tau, j|\mathbf{x}, t)$ of two random variables: the time $\tau > 0$ needed for the next reaction to occur and the label $j = 1, .., M$ of the next occurring reaction, given $\mathbf{X}(t) = \mathbf{x}$. As shown in [22], the definition (1.3) yields:

$$P(\tau, j|\mathbf{x}, t) = p_j(\mathbf{x}) \exp\left(-p_0(\mathbf{x})\tau\right), \quad p_0(\mathbf{x}) \equiv \sum_{j=1}^{M} p_j(\mathbf{x}). \tag{1.7}$$

Equation (1.7) implies (i) τ and j to be statistically independent, (ii) the time τ to be an exponential random variable with mean (and standard deviation) $1/p_0(\mathbf{x})$ and (iii) the reaction label j to be chosen with probability $p_j(\mathbf{x})/p_0(\mathbf{x})$.

The introduced in such a way $P(\tau, j|\mathbf{x}, t)$ suggests the SSA procedure [22] reported in Algorithm 1.1 for generating a single trajectory of the system state $\mathbf{x}$, starting from the initial condition $\mathbf{X}(t_0) = \mathbf{x}_0$.

Algorithm 1.1: The Stochastic Simulation Algorithm (SSA) for simulating the state $\mathbf{X}(t)$ (1.1) of a well-mixed and thermally equilibrated chemical system. The procedure generates a single trajectory of $\mathbf{X}(t) = \mathbf{x}$ during the time interval $[t_0, t_{\max}]$, starting from $\mathbf{X}(t_0) = \mathbf{x}_0$.

1 Assign the state-change vector ν_j (1.2) for each reaction R_j, $j = 1, .., M$;
2 Assign the occurrence rate $p_j(\mathbf{x})$ (1.3) for each reaction R_j, given $\mathbf{X}(t) = \mathbf{x}$;
3 Initialise the time $t = t_0$ and the system state $\mathbf{x} = \mathbf{x}_0$;
4 while $t < t_{\max}$ **do**
5   Draw $\tau \in \mathbb{R}^+$ from an exponential distribution with mean $1/p_0(\mathbf{x})$, $p_0(\mathbf{x}) \equiv \sum_{j=1}^{M} p_j(\mathbf{x})$;
6   Select the index j with probability $p_j(\mathbf{x})/p_0(\mathbf{x})$, for $j = 1, .., M$;
7   Update the time $t \leftarrow t + \tau$ and the system state $\mathbf{x} \leftarrow \mathbf{x} + \nu_j$;
8 end

SSA numerically simulates chemical systems by stepping in time to consecutive events, randomly chosen according to (1.7). As explained above, the distribution (1.7) arises from the same premise

(1.3) that gave rise to the CME (1.4). This guarantees the exactness of the proposed sampling.

An equivalent elaboration of SSA was introduced in [25] and it is known as the First Reaction Method. The procedure to generate trajectories of the system state is explained in Algorithm 1.2. It can be proved that Algorithms 1.1 and 1.2 are equivalent, generating values for τ and j in agreement with the joint density function (1.7). However, if the system has many reaction channels, the First Reaction Method will be computationally less efficient than the procedure given in Algorithm 1.1.

Algorithm 1.2: The First Reaction Method for simulating the state $\mathbf{X}(t)$ (1.1) of a well-mixed and thermally equilibrated chemical system. The procedure generates a single trajectory of $\mathbf{X}(t) = \mathbf{x}$ during the time interval $[t_0, t_{\max}]$, starting from $\mathbf{X}(t_0) = \mathbf{x}_0$.

1 Assign the state-change vector ν_j (1.2) for each reaction R_j, $j = 1, .., M$;

2 Assign the occurrence rate $p_j(\mathbf{x})$ (1.3) for each reaction R_j, given $\mathbf{X}(t) = \mathbf{x}$;

3 Initialise the time $t = t_0$ and the system state $\mathbf{x} = \mathbf{x}_0$;

4 **while** $t < t_{\max}$ **do**

5   Draw $\tau_j \in \mathbb{R}^+$ from an exponential distribution with mean $1/p_j(\mathbf{x})$, for all $j = 1, .., M$;

6   Select the index j_m corresponding to the smallest τ_j for $j = 1, .., M$;

7   Update the time $t \leftarrow t + \tau_{j_m}$ and the system state $\mathbf{x} \leftarrow \mathbf{x} + \nu_{j_m}$;

8 **end**

More advanced formulations of the presented above algorithms have been proposed in [26], [27]. Despite the computational improvements offered in these works, the generation of every reaction event remains often too slow for practical simulations of realistic systems, no matter how efficiently it is done. For this reason, we revise further developments of the SSA methods, proposed with the aim either to speed up the simulations (tau-leaping procedure) or to deal with stiff systems.

Tau-leaping. In order to speed up the simulation, it might be possible to sacrifice some of the exactness of SSA and follow approximated methods, such as the *tau-leaping* procedure [28]. For any time t, it considers the time interval with the preselected length $\tau > 0$, such that the rates remain essentially constant during $[t, t + \tau)$. The firing of all possible reactions is performed for $[t, t + \tau)$, without updating the propensity functions. The number of occurred reactions is distributed as a Poisson random variable. The less frequent computation of the rate functions may allow for more efficient simulations, especially in the case of complex systems. If the number of occurrences during the preselected interval is big enough, the Poisson random numbers are well approximated by Normal random numbers, leading to the Chemical Langevin Equation (CLE), corresponding to a differential equation driven by zero-mean Gaussian noise [29]. In the limit, when the species populations and the system volume approach infinity, which result in constant species concentrations, the noise terms in the CLE can be neglected and the CLE reduces to the RRE (1.6).

The *tau-leaping* approximation leads to the following updating scheme for the system state $\mathbf{X}(t) = \mathbf{x} \in \mathbb{N}^N$ (1.1):

$$\mathbf{X}(t + \tau) = \mathbf{x} + \sum_{j=1}^{M} \mathcal{P}_j(p_j(\mathbf{x})\tau)\nu_j, \tag{1.8}$$

where $\mathcal{P}_j(m_j) \in \mathbb{N}$ is an independent Poisson random variable with mean (and variance) m_j, ν_j is the state-change vector (1.2) and $p_j(\mathbf{x})$ is the propensity function (1.3). The time step size $\tau > 0$ corresponds to the preselected length of the interval between updates of the system state. Some practical issues should be resolved to implement the scheme (1.8). First, one should explain how to select the largest value of τ such that the rates $p_j(\mathbf{x})$ remain essentially constant during $[t, t+\tau)$. Then, large values of the drawn Poisson random numbers $\mathcal{P}_j$ may lead to negative values of the populations $\mathbf{X}(t)$. Consequently, care has to be taken of guaranteeing non-negative values for the state $\mathbf{X}(t)$ for any drawn random number $\mathcal{P}_j$.

A fast and accurate strategy for the estimation of τ is suggested in [30]. It computes the largest value of τ, for which the estimated fractional change in each propensity function during $[t, t + \tau)$ is bounded by a user-specified accuracy-control parameter. Then, [31] discusses a procedure to ensure non-negative values of the state $\mathbf{X}(t)$ for any drawn Poisson random number. Given a user-specified integer $N_c \geq 1$, it labels as critical (or currently in danger of exhausting any of its reactants) all those reactions for which the maximum number of permitted firings during τ is not exceeding N_c. The distribution (1.7) is used to draw the required time τ_c and the index j_c of the next critical reaction. The time step size τ_n for the non-critical reactions is computed as described in [30]. If $\tau_c < \tau_n$, the critical reaction R_{j_c} fires at time $t + \tau$, $\tau \equiv \tau_c$, and the system state is updated accordingly. Otherwise, the scheme (1.8) is used to update the reactant populations of the non-critical reactions, with the time step size $\tau \equiv \tau_n$. As a result, at most one occurrence of any critical reaction is possible during $[t, t + \tau)$ and the reactant populations are guaranteed to be non-negative. Numerical tests in [30] indicate the ability of the tau-leaping technique to simulate faster than SSA with only a slight loss of accuracy, especially in the case of large species populations.

Stiff systems. Finally, we review some techniques to deal with stiff systems, characterised by well-separated fast and slow dynamical modes. The SSA simulation of successive reactions is only able to reproduce properly the fast dynamics of a stiff system, leaving unexplored the slow dynamics. In the light of deterministic approaches, stiff systems can be treated by implementing implicit updating schemes, as proposed in [32]. In addition, the slow-scale SSA (ssSSA) [33] provides a novel strategy to deal with stiff systems. The reactions are labelled as fast or slow, according to the order of magnitude of the respective rate functions. If changed by a fast reaction, the species populations are classified as fast, otherwise as slow. Under some stiffness conditions [33], the ssSSA allows us to ignore the fast reactions and to simulate the system state $\mathbf{X}(t)$ through only the slow reactions, with modified propensity functions. In other words, the ssSSA only simulates the slow reactions following Algorithm 1.1 with modified rate functions. The fast reactions are ignored and the populations of the fast species can be recovered by Monte Carlo sampling from the corresponding distributions. The applications provided in [33] show an increase in the simulation speed over the exact SSA with no perceptible loss of accuracy.

The methodology presented in the following sections is primarily aimed to study the Controlled Radical Polymerization, which, we argue, can be fully described by a very few (not exceeding three) competitive reactions. For this purpose, we choose to use the Stochastic Simulation Algorithm presented in Algorithm 1.2. For more complex processes involving many reaction channels the advanced methods, such as tau-leaping or ssSSA should be applied. The ideas presented in this chapter can be extended to those methods but this is beyond the scope of this study.

1.3   Non-Markovian Models of the Growth of a Polymer Chain

In this section we provide the mathematical grounds for modelling polymerization reactions with delays. In particular, we describe the non-Markovian growth of a polymer chain. In Section 1.3.1, we define the probabilities for different growth scenarios. In Section 1.3.2, we briefly review growth without a delay, leading to Markovian master equations for the probabilities of interest. In Section 1.3.3, we consider linear growth with a fixed downtime introduced after each attachment of a monomer. We show that such a delay leads to a non-Poisson distribution of the polymer length, and a set of time-delayed differential equations for the relevant probabilities. In Section 1.3.4, we study the short- and long-time limits of the mean length of the grown polymer. In Section 1.3.5, we explain how to numerically simulate the delayed growth, by formulating three suitable implementations of the Stochastic Simulation Algorithm (SSA), reviewed in Section 1.2.1. The accuracy and efficiency of the proposed methods are compared. Finally, Section 1.3.6 discusses the presented results and puts them in the context of the applications considered in the following sections of the chapter.

1.3.1 Linear Growth

Consider the growth of a linear polymer which proceeds by attaching monomers to, say, its right end at discreet times $t_j = jdt$. We begin with a single monomer. At each t_j an extra monomer is added with the probability p_j, or else nothing happens with the probability $1 - p_j$. Thus, the probability to add a monomer after $J - 1$ unsuccessful attempts is $f(t_J) = p_J \prod_{j=1}^{J-1}(1 - p_j)$, while the probability for not adding a monomer up to and including t_J, is $g(t_J) = \prod_{j=1}^{J}(1 - p_j)$. In general, we may start the process at some t_i and let the probabilities depend on both t_j and t_i, $p = p_{j,i}$. In the continuum limit, we should send $dt \to 0$ and introduce the growth rate $c(t_j, t_i)dt \equiv p_{j,i}$, assuming c to be a slowly varying function. The probability to add nothing for $t' \leq t'' \leq t$ is then given by

$$g(t, t') = \exp\left[-\int_{t'}^{t} c(t'', t') \, dt''\right], \tag{1.9}$$

while for the probability density function (PDF) to start at t', and add the first monomer in the interval $[t, t + dt]$, we have

$$f(t, t') = c(t, t') \exp\left[-\int_{t'}^{t} c(t'', t') \, dt''\right] = -\partial_t g(t, t'). \tag{1.10}$$

By a given t, the monomer is either attached or not, so the two corresponding probabilities add to one,

$$\int_{t'}^{t} f(t'', t') \, dt'' + g(t, t') = 1. \tag{1.11}$$

With many monomers able to join the polymer chain between t' and t, we are looking for the probability $P(n, t, t')$ to have n new additions by the time t. This is just the probability for adding monomers at $t' \leq t_1 \leq t_2 \leq .. \leq t_n \leq t$, multiplied by the probability that no more monomers are added between t_n and t, and summed over all t_i, $i = 1, 2, ..n$,

$$\left.\begin{aligned}
P(n, t, t') &= \int_{t'}^{t} dt_n .. \int_{t'}^{t_2} dt_1 \, g(t, t_n) \, f(t_n, t_{n-1}) .. f(t_1, t'), \quad n \geq 1, \\
P(0, t, t') &= g(t, t').
\end{aligned}\right\} \tag{1.12}$$

One can check that Equation (1.11) ensures the correct normalisation of the probabilities $P(n, t, t')$, $\sum_{n=0}^{\infty} P(n, t, t') = 1$. Another useful quantity is the probability density $W(n, t, t')$ for n monomers to be attached in the interval $[t', t]$, with the last of them added in $[t, t + dt]$,

$$W(n, t, t') = \int_{t'}^{t} dt_{n-1} .. \int_{t'}^{t_2} dt_1 \, f(t, t_{n-1}) .. f(t_1, t'), \quad n \geq 1, \tag{1.13}$$

in terms of which $P(n, t, t')$ is expressed as

$$P(n, t, t') = \int_{t'}^{t} dt'' \, g(t, t'') \, W(n, t'', t'), \quad n \geq 1. \tag{1.14}$$

The quantities $W(n, t, t')$ have the advantage that they satisfy the simple evolution equations,

$$\partial_t W(n, t, t') = f(t, t) W(n - 1, t, t') + \int_{t'}^{t} dt'' \, \partial_t f(t, t'') \, W(n - 1, t'', t'). \tag{1.15}$$

Their use will be described below. At least three cases need to be distinguished.

A. The growth rate depends only on the current time, and not on the previous history of the chain,

$$c(t, t') = c(t), \quad f(t, t') = c(t) \exp\left[-\int_{t'}^{t} c(t'') \, dt''\right]. \tag{1.16}$$

This is the *Markovian* case we will briefly review in Section 1.3.2.
B. The growth rate depends only on the chain's past, and is not manipulated externally.

$$c(t,t') = c(t-t'), \quad f(t,t') = f(t-t') = c(t-t') \exp\left[-\int_0^{t-t'} c(t'') \, dt''\right]. \tag{1.17}$$

Here one may think that after each time a monomer is added, some additional time is needed before the next monomer can be attached. This the *non-Markovian* case is the main subject of this chapter. **C.** Finally, the growth rate, which depends on the polymer's history in the sense outlined above, may also be manipulated externally. In this case c is a function of both t and t', and the process is also non-Markovian.

1.3.2 Markovian Growth

Consider the case when there is an unlimited supply of monomers to be added to the chain, and the probability to add one at a given time is modified externally, e.g. by varying the temperature at which the process takes place. The growth begins at some t', and we are interested in the length of a polymer at a time t. The probability for adding a monomer in $[t, t+dt]$ is $c(t)dt$, and the function g and the PDF f in (1.9) and (1.10) are of the form

$$g(t,t') = \exp\left[-\int_{t'}^t c(t'') \, dt''\right], \quad f(t,t') = c(t) \exp\left[-\int_{t'}^t c(t'') \, dt''\right]. \tag{1.18}$$

Inserting (1.18) into (1.12), and recalling that $\int_{t'}^t dt_n .. \int_{t'}^{t_2} dt_1 \, c(t_n) .. c(t_1) = [\int_{t'}^t c(t'') \, dt'']^n/n!$, we recover a Poisson distribution [34] (the subscript M stand for Markovian),

$$\left.\begin{array}{l} P_M(n,t,t') = \dfrac{I(t)^n}{n!} \exp(-I(t)), \quad n \geq 1, \\[2mm] P_M(0,t,t') = \exp(-I(t)), \end{array}\right\} \tag{1.19}$$

where

$$I(t) = \int_{t'}^t c(t'') \, dt''. \tag{1.20}$$

From (1.19)-(1.20), it follows that the mean length of the chain,

$$\langle n(t) \rangle = \bar{c}(t,t') \, (t-t'), \tag{1.21}$$

where $\bar{c}(t,t') = (t-t')^{-1} \int_{t'}^t c(t'') \, dt''$ is the average of the growth rate over the growth period. If the external conditions remain unchanged, $c(t) = c$, the growth is linear with time, $\langle n(t) \rangle = c \, (t-t')$. Differentiation of (1.19) yields a closed master equation for the probabilities $P_M(n,t,t')$

$$\left.\begin{array}{l} \partial_t P_M(n,t,t') = c(t) \left[P_M(n-1,t,t') - P_M(n,t,t')\right], \quad n \geq 1 \\[2mm] \partial_t P_M(0,t,t') = -c(t) P_M(0,t,t'), \end{array}\right\} \tag{1.22}$$

to be solved with the initial condition

$$P_M(n,t',t') = \delta_{n0}, \tag{1.23}$$

where δ_{nm} is the Kronecker delta. Equations (1.22) are obviously Markovian, as the rate at which a $P_M(n,t,t')$ changes depends only on the current state of the system, $\{P_M(n,t,t')\}_{n \in \mathbb{N}}$.

1.3.3 Non-Markovian Growth with Delays

Suppose next that, as in the previous Section, there is an unlimited supply of monomers, and the external conditions remain unchanged. But each added monomer, except the first, now needs a time τ to properly settle into the chain structure, only after which the chain is ready to attach again, with the same constant growth rate c. The process is now explicitly non-Markovian: to check whether a monomer can be added, one needs to know the history of the chain. Accordingly, the rate $c(t)$ depends

not on the time elapsed since t', but on the time elapsed since the last monomer was added. In (1.9) we, therefore have $c(t, t') = c(t - t')$. Explicitly, we obtain (NM stands for Non-Markovian)

$$c(t - t') = \begin{cases} 0, & 0 \le t - t' < \tau, \\ c, & t - t' \ge \tau, \end{cases} \tag{1.24}$$

and

$$g_{NM}(t, t') = g_{NM}(t - t') = \begin{cases} 1, & 0 \le t - t' < \tau, \\ \exp[-c(t - t' - \tau)], & t - t' \ge \tau. \end{cases} \tag{1.25}$$

From (1.10) we also have

$$f_{NM}(t, t') = f_{NM}(t - t') = c\,\theta(t - t' - \tau)\,\exp[-c(t - t' - \tau)], \tag{1.26}$$

where $\theta(z) = 1$ for $z \ge 0$ and 0 otherwise. In the case of the monomer initiating the polymer chain, the value of $\tau = 0$ must be imposed in (1.24)-(1.26), since no settling time is required. The physical background of (1.24)-(1.26) is as follows. In classical kinetics, the pseudo-first order processes are considered purely stochastic, i.e., described by an exponential probability distribution function. However, this is intuitively difficult to justify because the probability density that a reaction occurs at $t = 0$ should be 0, since instantaneous reactions do not occur. This concept will be used to analyse the competitive processes occurring in CRP and to explain the reduction of branching in CRP of acrylic monomers. Equation (1.26) can be considered a simplification of the linear-exponential distribution we proposed for CRP, as explained in Section 1.6.2.

Returning to (1.13) and putting $t' = 0$, we note that the probability $W(n, t, t' = 0) \equiv W(n, t)$ is the same as for growth with a constant c, but for a shorter time. The effective time of growth, t_{eff}, is, therefore, the elapsed time t minus the total time the growth was shut down due to adding $n - 1$ monomers, i.e., $t_{eff} = t - (n-1)\tau$. Should $(n-1)\tau$ exceed t, the process is not possible, and the corresponding probability is zero. From (1.13) and (1.26) we easily find

$$\left. \begin{aligned} W_{NM}(n, t|\tau) &= c\,\frac{[I_n(t, \tau)]^{n-1}}{(n-1)!}\,\exp[-I_n(t, \tau)], \quad n \ge 1, \quad (n-1)\tau < t, \\ I_n(t, \tau) &= c\,[t - (n-1)\tau]. \end{aligned} \right\} \tag{1.27}$$

The physical probabilities $P(n, t, t' = 0) \equiv P(n, t)$ are no longer given by a Poisson distribution, but can be obtained as quadratures using (1.14), (1.25) and (1.27)

$$\left. \begin{aligned} P_{NM}(n, t|\tau) &= \int_0^{t-\tau} \exp[-c(t - t' - \tau)]\,W_{NM}(n, t'|\tau)\,dt' \\ &\quad + \int_{t-\tau}^{t} W_{NM}(n, t'|\tau)\,dt', \quad n \ge 1, \\ P_{NM}(0, t|\tau) &= \exp(-ct). \end{aligned} \right\} \tag{1.28}$$

It is instructive to look at the evolution equations (EE) satisfied by the probabilities. There are no simple EE, similar to (1.22), for $P_{NM}(n, t|\tau)$ in (1.28). There are, however, EE (1.15) which, as $\partial_t f(t) = c\delta(t - \tau) - cf(t)$, read

$$\left. \begin{aligned} \partial_t W_{NM}(n, t|\tau) &= c\,[W_{NM}(n - 1, t - \tau|\tau) - W_{NM}(n, t|\tau)], \\ n &\ge 2, \quad 0 < (n-1)\tau < t, \\ W_{NM}(1, t) &= c\exp(-ct). \end{aligned} \right\} \tag{1.29}$$

Unlike (1.22) in the Markovian case, equations (1.29) depend on the state of the system in the past through $W_{NM}(n - 1, t - \tau|\tau)$ and their properties may differ significantly from those of (1.22), as will be illustrated in Section 1.3.4.

1.3.4 Mean Chain Length for a Delayed Growth

One quantity of practical interest is the mean length of the chain grown in the presence of a delay,

$$\langle n(t,\tau)\rangle_{NM} = \sum_{n=1}^{\infty} n P_{NM}(n,t|\tau), \qquad (1.30)$$

shown in Figure 1.2a for various values of the parameters $c\tau$. We note that $c\tau < 1$ implies that the delay is shorter than the average reaction time. Similarly, $c\tau \geq 1$ indicates that the delay is longer, or equal, than the average reaction time. As $c\tau \to 0$ we recover the Poisson distribution (1.19), and for $ct \ll 1$, $\langle n(t,\tau)\rangle_{NM}$ grows linearly at the rate close to c. In the opposite limit, $c\tau \gg 1$, the behaviour is more interesting with the curves showing a steplike variation at short times before settling into a linear behaviour later. This has a simple physical explanation. The time it takes the chain to add one monomer at a constant growth rate c, t_{add}, is approximately $1/c$. If $c\tau \gg 1$, a monomer is added quickly, but then the system has to wait long until another one can be attached. Thus, for $t_{add} < t < \tau$, it behaves as if the delay were infinite, i.e. as if the only two possible outcomes were one or none monomers added, with the probabilities $P(\text{one}) = 1 - \exp(-ct)$ and $P(\text{none}) = \exp(-ct)$, respectively. The mean length

$$\langle n(t,\tau)\rangle_{NM} \approx 1 - \exp(-ct), \quad t_{add} < t < \tau \qquad (1.31)$$

reaches the value of 1, and remains unity until $t \approx \tau$, when the system recalls that the delay is not infinite after all. A second monomer is added quickly, and $\langle n(t,\tau)\rangle_{NM}$ remains flat and close to 2 until $t \approx 2\tau$, and so on. This behaviour can be expected from the way we have constructed our model. As $t/\tau \to \infty$ the steps are smoothed out, and the mean length of the polymer grows linearly with time (K is a positive constant),

$$\langle n(t,\tau)\rangle_{NM} \approx \tilde{c}t + K, \quad t \to \infty, \qquad (1.32)$$

at a constant rate $\tilde{c} > 0$. The value of $\tilde{c}$ is found by recalling that in our model adding $\langle n(t)\rangle$ monomers is accompanied by switching off the growth for a duration of approximately $\langle n(t)\rangle\tau - \tau/2$. The last addition may occur close to t, so its delay is, on average, shorter. Thus, the growth is similar to the growth without delay over a time $[t - \langle n(t)\rangle\tau + \tau/2]$ at the rate c. Equating $\langle n(t)\rangle$ to $c[t - \langle n(t)\rangle\tau + \tau/2]$ yields

$$\tilde{c} = \frac{c}{1+c\tau}, \quad K = \frac{c\tau}{2(1+c\tau)}. \qquad (1.33)$$

The two limiting cases, (1.31) and (1.32), are illustrated in Figure 1.2b.

1.3.5 Stochastic Simulation of Delayed Growth

Next, we consider the delay in backbiting, caused by the fact that in order to form the six-membered ring required for the backbiting reaction, a minimum of $n_0 = 3$ monomer units is needed in a linear segment of the chain. It is assumed that the backbiting reaction, which forms branches, occurs at a constant rate c_{branch} but can only happen if at least n_0 monomer units have been previously added. For growth occurring at a constant rate c_{add}, the probability to add n_0 monomers within a time τ is

$$w_{n_0}(\tau) = \int_0^{\tau} d\tau_{n_0-1} .. \int_0^{\tau_2} d\tau_1 \, f_{add}(\tau - \tau_{n_0-1}) .. f_{add}(\tau_1)$$

$$= c_{add}^{n_0} \frac{\tau^{n_0-1}}{(n_0-1)!} \exp(-c_{add}\tau), \qquad (1.34)$$

where we have used $f_{add}(t) = c_{add}\exp[-c_{add}t]$. Next we average the delayed PDF for branching,

$$f_{branch}(t,\tau) \equiv c_{branch}\,\theta(t-\tau)\,\exp[-c_{branch}(t-\tau)], \qquad (1.35)$$

(a) Mean Length Behaviour.

(b) Short- and Long-Time Limits.
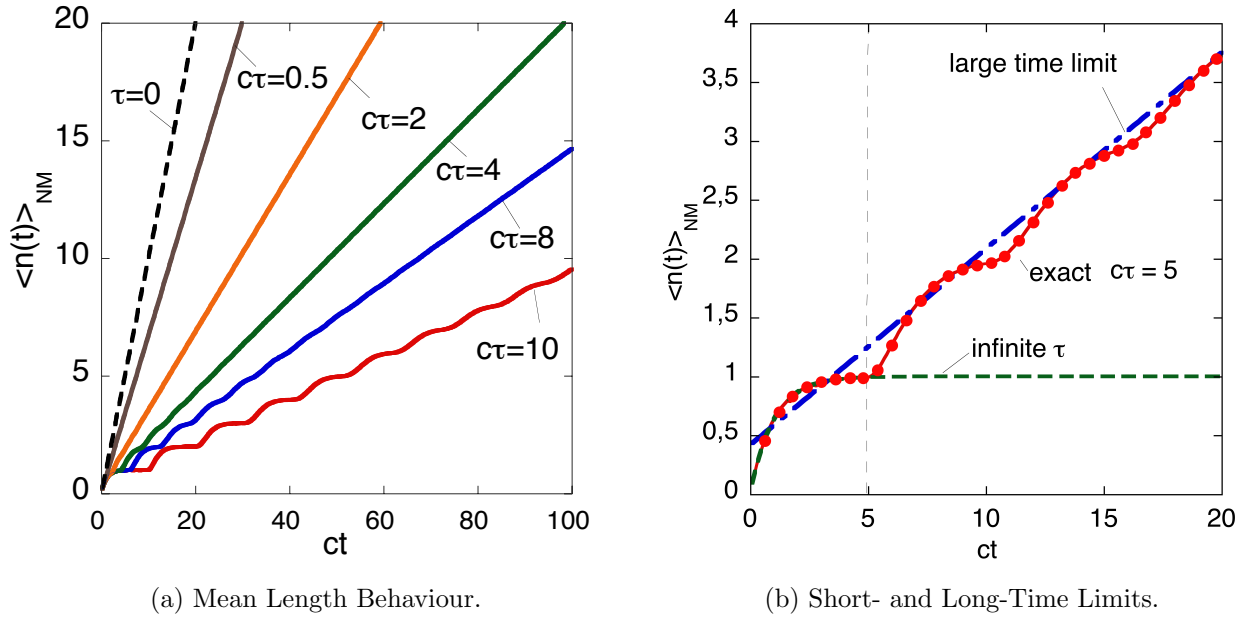
Figure 1.2: Figure (a) shows the mean length of the polymer chain versus time for different values of the delay τ. Figure (b) shows the short time limit (1.31) for infinite τ and the large time limit (1.32) of the mean length of the polymer chain.

over all possible delays, thus obtaining

$$
\begin{aligned}
\bar{f}_{branch}(t, n_0) &\equiv \int_0^\infty w_{n_0}(\tau)\, f_{branch}(t, \tau)\, d\tau = \\
&= \frac{c_{branch} c_{add}^{n_0}}{(n_0 - 1)!}\, \exp(-c_{branch} t)\, \frac{d^{n_0-1}}{d\beta^{n_0-1}} \left[\frac{\exp(\beta t) - 1}{\beta} \right]_{\beta = c_{branch} - c_{add}}.
\end{aligned}
\tag{1.36}
$$

Then we replace f in the equation (1.13) with $\bar{f}_{branch}$ and use it to generate the statistics for branching events. As no simple analytic solution is available for the resulting non-Markovian equations, we consider a numerical stochastic algorithm, namely SSA.

Two equivalent formulations of the SSA method are possible to simulate the delayed branching of a polymer chain due to the alternative occurrence of monomer additions and backbiting reactions. In particular, the delay can be either implicitly or explicitly introduced in the simulated systems. The modification of the inter-event time distribution implicitly accounts for the required delay. In Section 1.3.5.1, we discuss the implicit approach, considering a single delayed process, with the delay built into the corresponding probability density function. Alternatively, it is possible to add the explicit constraints among the possible events. The explicit method simulating two Poisson processes with an additional constraint, accounting for the required delay is described in Section 1.3.5.2. The equivalence of the discussed methods is proven in Section 1.3.5.3. In Section 1.3.5.4, an approximated simulation method is proposed and all three suggested approaches are compared in accuracy and efficiency.

1.3.5.1   Stochastic Simulation of a Single Delayed Process

Following Algorithm 1.1, a random number generator is prepared, so that it draws a random number t_j, $j = 1, 2, ... K$ with a probability

$$
\omega_j = f(t_j)\, dt,
\tag{1.37}
$$

where $f(t) \equiv \bar{f}_{branch}(t, n_0)$ (1.36), for a given $n_0 \in \mathbb{N}$. The number of branches is set to zero, and then the first value t_1 is drawn. If it lies between 0 and the time t at which the growth is stopped, the number of branches is increased by 1, and t_1 becomes the new starting time. This step is repeated

until the k-th step yields $t_k > t$, at which point the drawing stops, and the vector $\hat{t} = (t_1, t_2, ..., t_{k-1})$ corresponding to this particular realisation of the system's history is stored. Repeating the simulation a large number of times N, one obtains a collection of histories, from which the probability of any particular property can be obtained as the relative frequency with which the property occurs. For example, the probability to have n branches by a time t is given by

$$P(n, t) = N_n/N, \tag{1.38}$$

where N_n the number of realisations with exactly n events. The accuracy and efficiency of the approach for the PDF (1.36) are presented in Figure 1.4 and Figure 1.5.

1.3.5.2 Stochastic Simulation of two Poisson Processes with an Additional Constraint

Based on the formulation of SSA given in Algorithm 1.2, one can perform a simulation of two simultaneous Poisson processes with their respective PDFs defined as follows:

$$f_{add}(t) = c_{add} \exp(-c_{add}t), \quad \text{and} \quad f_{branch}(t) = c_{branch} \exp(-c_{branch}t), \tag{1.39}$$

and impose an additional constraint that a branching can only occur after n_0 monomers have been added previously. Without such a constraint the processes are independent, and the ratio of the mean number of branchings to the mean length of a polymer is a constant equal to c_{branch}/c_{add} at all times. Now in each step of the simulation, one draws random values of t_k^{add} and t_k^{branch} from the probability distributions f_{add} and f_{branch} in (1.39), respectively. If $t_k^{add} < t_k^{branch}$, a growth event is recorded at $t_k = t_{k-1} + t_k^{add}$. Otherwise the recorded event is the branching of the chain appearing at $t_k = t_{k-1} + t_k^{branch}$. The step is repeated until t_k is found to be greater than t, and a history consisting of branching events interspersed among acts of growth is stored. With many histories collected, average values of observables are evaluated as in Section 1.3.5.1. The comparison shown in Figure 1.4 demonstrates a good agreement between the single- and two-processes simulations of branching events. However, the approach of Section 1.3.5.1 is more efficient than the straightforward algorithm described here, since it reduces the number of simulated processes to one. The computational cost is compared in Figure 1.5.

1.3.5.3 Equivalence Proof

The aim of this section is to prove that stochastic simulation of two explicitly constrained Poisson processes (Section 1.3.5.2) is equivalent to simulating a single delayed process (Section 1.3.5.1), with the delay built into the probability density function (1.36).

Let us consider two competing Poisson processes, an addition and a branching, which occur at constant rates c_{add} and c_{branch} respectively, with a branching event possible only after at least n_0 additions. We are interested in the time $\bar{T}_{branch}$ needed for the next branching event to happen, whose distribution $\bar{g}_{branch}(t, n_0)$ we want to establish. With n_0 initial additions required, $\bar{T}_{branch}$ has the form

$$\bar{T}_{branch} = \sum_{i=1}^{n_0} T_{add}^i + T_{branch}, \tag{1.40}$$

where $T_{add}^1, T_{add}^2, .., T_{add}^{n_0}$ are the times required for the $1^{st}, 2^{nd}, .., n_0^{th}$ addition respectively and T_{branch} is a time for the next branching event to occur if no delay is imposed.

First, we derive the corresponding PDFs for each term of the r.h.s of (1.40) and then find the resulting PDF for the sum of random variables in equation (1.40).

As addition is a Poisson process, its probability density function is

$$f_{add}^{T_{add}^i}(t) = c_{add} \exp(-c_{add}t)\, \theta(t) = g(t; 1, c_{add}), \quad \forall i = 1, .., n_0, \tag{1.41}$$

where $g(t; \alpha, \beta) = (\beta^\alpha/\Gamma(\alpha))\, t^{\alpha-1} \exp(-\beta t)\, \theta(t)$ is the density of the Gamma distribution $\text{Gamma}(\alpha, \beta)$, $\Gamma(\alpha)$ is the gamma function, with $\Gamma(\alpha) = (\alpha - 1)!$ if $\alpha \in \mathbb{N}$, and $\theta(t)$ is 1 if $t \geq 0$, and 0 otherwise.

The moment generating functions (mgf) of m independent random variables $T_i \overset{\text{ind.}}{\sim} \text{Gamma}(\alpha_i, \beta)$, $i = 1, .., m$, are given by

$$\psi_{T_i}(\lambda) \equiv \int_0^{+\infty} \exp(\lambda t) \frac{\beta^{\alpha_i}}{\Gamma(\alpha_i)} t^{\alpha_i - 1} \exp(-\beta t) \, dt = \left(1 - \frac{\lambda}{\beta}\right)^{-\alpha_i}, \quad \forall i = 1, .., m. \tag{1.42}$$

The product $\prod_{i=1}^m \psi_{T_i}(\lambda)$ yields the mgf $\psi_T(\lambda)$ for the sum $T \equiv \sum_{i=1}^m T_i$, i.e. $\psi_T(\lambda) = (1 - \lambda/\beta)^{-\sum_i \alpha_i}$. Comparing again with (1.42), we have $T \sim \text{Gamma}\left(\sum_{i=1}^m \alpha_i, \beta\right)$. It follows that the sum $\sum_{i=1}^{n_0} T_{add}^i$ in (1.40) is distributed as

$$f_{add}^{\sum_{i=1}^{n_0} T_{add}^i}(t) = g(t; n_0, c_{add}) = \frac{c_{add}^{n_0}}{(n_0 - 1)!} t^{n_0 - 1} \exp(-c_{add} t) \, \theta(t). \tag{1.43}$$

Once the required minimal number n_0 of additions is achieved, branching is also a Poisson process, and T_{branch} is distributed as

$$f_{branch}(t) = c_{branch} \exp(-c_{branch} t) \, \theta(t). \tag{1.44}$$

The density $\bar{g}_{branch}(t, n_0)$ of $\bar{T}_{branch}$ (1.40) can now be found as the convolution of the distributions of its constituent parts:

$$\begin{aligned}
\bar{g}_{branch}(t, n_0) &\equiv \int_0^{+\infty} f_{add}^{\sum_{i=1}^{n_0} T_{add}^i}(\tau) \, f_{branch}(t - \tau) \, d\tau = \\
&= \frac{c_{branch} \, c_{add}^{n_0}}{(n_0 - 1)!} \exp(-c_{branch} t) \int_0^t \tau^{n_0 - 1} \exp[(c_{branch} - c_{add})\tau] \, d\tau = \\
&= \frac{c_{branch} \, c_{add}^{n_0}}{(n_0 - 1)!} \exp(-c_{branch} t) \frac{d^{n_0 - 1}}{d\beta^{n_0 - 1}} \left[\frac{\exp(\beta t) - 1}{\beta}\right]_{\beta = c_{branch} - c_{add}}.
\end{aligned} \tag{1.45}$$

Since the distributions $\bar{g}_{branch}(t, n_0)$ (1.45) and $\bar{f}_{branch}(t, n_0)$ (1.36) are identical, we can conclude that the simulation of the two explicitly constrained Poisson processes is equivalent to simulating a single delayed process with the modified density (1.36).

1.3.5.4 Stochastic Simulation of Delayed Processes with an Approximated PDF

The algorithm outlined in Section 1.3.5.1 suggests an efficient way of simulating delayed processes, if the amount of delay is known *a priori*. In practice, however, it is often not the case. If so, one may use a set of experimental data to tune the distributions parameters taking an appropriate optimisation route, as will be discussed later in Section 1.6.2. Optimisation is most easily achieved for distributions having simple analytical representations and depending only on a small number of parameters. Here we propose to use a simple two-parametric analytical PDF broadly similar to (1.36) for simulating delayed processes with the unknown amount of delay:

$$\bar{f}_{branch}^{LE}(t) = \begin{cases} kt & \text{for } 0 \leq t < b, \\ kb \exp\left[-\frac{(t-b)}{\tau}\right] & \text{for } t \geq b, \\ 0 & \text{otherwise,} \end{cases} \tag{1.46}$$

where $t = b$ corresponds to the argument of the maximum of $\bar{f}_{branch}(t, n_0)$ in (1.36), $k = \bar{f}_{branch}(b, n_0)/b$ and $\tau = (1 - kb^2/2)/kb$. From now on we will refer to such distribution as linear-exponential (LE). Figure 1.3 compares the probability density function $\bar{f}_{branch}(t, n_0)$ (1.36) with its LE approximation (1.46) for two values of the ratio c_{branch}/c_{add} and $n_0 = 3$, while Figure 1.4 illustrates the level of accuracy achieved by the approximated distribution (1.46) in computation of the branching fraction. The LE approximation accurately reproduces the short time behaviour of the branching fraction curve, while in the long time limit it underestimates its value by less than 8%.

Finally, the comparison of computational efficiency of three simulation approaches proposed in Section 1.3.5.1, Section 1.3.5.2 and Section 1.3.5.4 is presented in Figure 1.5. The approximated approach

outperforms two other proposed methods by up to two orders of magnitude, which will become more dramatic with increasing size and complexity of simulated processes.
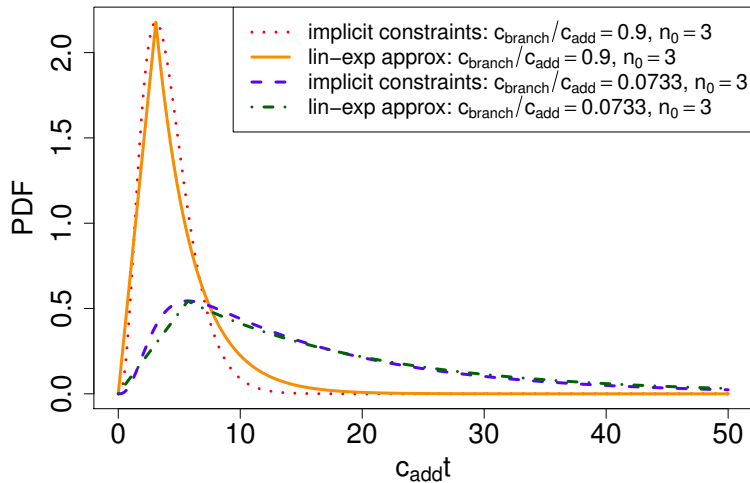
Figure 1.3: Comparison of the delayed PDF $\bar{f}_{branch}(t, n_0)$ (1.36) (implicit constraints) with its linear-exponential approximation $\bar{f}_{branch}^{LE}(t)$ (1.46) for two values of the ratio c_{branch}/c_{add} and $n_0 = 3$.
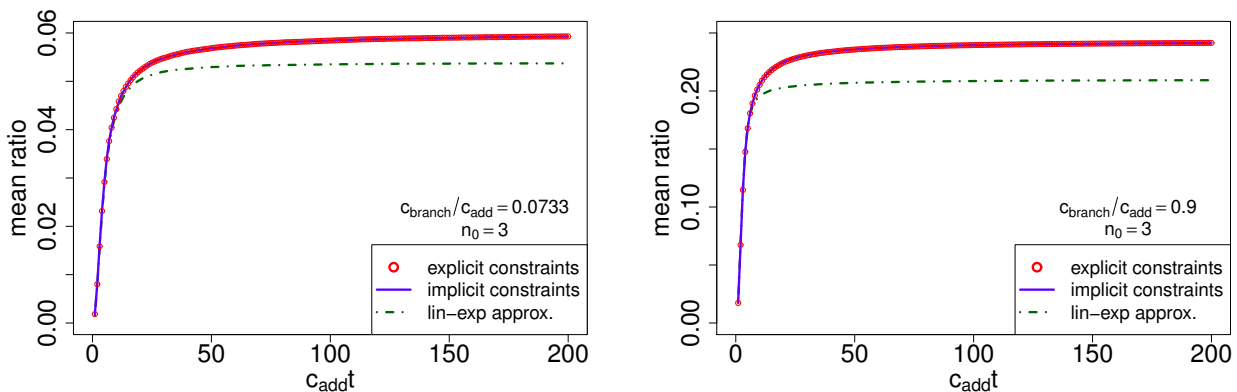
Figure 1.4: The ratio of the mean number of branches to the mean total length of the chain (the branching fraction) simulated using the algorithms presented in Section 1.3.5.1 (solid line), Section 1.3.5.2 (circles) and Section 1.3.5.4 (dashed line) for two values of the ratio c_{branch}/c_{add} and $n_0 = 3$.

1.3.6   Summary

We proposed the mathematical models of the growth of a polymer chain for two different regimes, Markovian and non-Markovian, and derived the evolution equations for the probability distributions modelling the growth process in both scenarios. We proved that the equations and the statistics characterising the Markovian growth differ significantly from those describing a non-Markovian regime. The predicted time evolution of the mean lengths of the grown chain for different amounts of delay clearly demonstrate such differences. While in the Markovian case, the mean length is linear in time, the presence of delays may force the growth to show step-like variations at short times before settling into a linear behaviour later.

Further we explained how to simulate the delayed growth by formulating two suitable implementations of the Stochastic Simulation Algorithm (SSA). The first approach simulates a single delayed process, with the delay built into the probability density function as was proposed for the non-Markovian growth model. The second methodology corresponds to the stochastic simulation of two Poisson
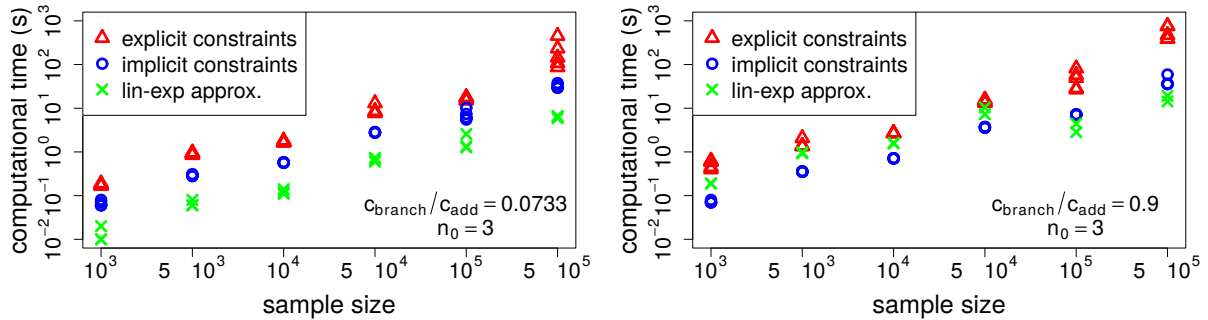
Figure 1.5: Computational cost of simulation approaches discussed in Section 1.3.5.1 (circles), Section 1.3.5.2 (triangles) and Section 1.3.5.4 (crosses) for two values of the ratio c_{branch}/c_{add} and $n_0 = 3$. The approximated method given in Section 1.3.5.4 is the most computationally efficient, especially for big sample sizes.

processes. The delay is introduced by adding explicit constraints among the possible events. We proved the equivalence of two proposed techniques but found the first approach computationally more sound. We also proposed the approximated distribution (1.46) for modelling non-Markovian processes and compared accuracy and efficiency of all designed approaches. The comparison revealed that the approximated method enhances the simulation speed, especially for big sample sizes while maintaining a proper accuracy.

We published the results presented in this section in [2].

In the next sections, we show how the proposed mathematical framework can be applied in practice. In particular, in Section 1.4 and Section 1.5 we develop a Monte Carlo and analytical methods, respectively, for computation of the relative frequencies of constrained events in stochastic processes. Both methodologies arise from the approaches discussed in this section for the simulation of stochastic processes with the additional constraints among the possible events.

1.4 Relative Frequencies of Constrained Events in Stochastic Processes: A Monte Carlo Approach

Our intention now is to demonstrate how the proposed analysis of the non-Markovian processes can be applied in practice. Since, as stated above, our objective is to explain the reduction in relative frequencies of propagations and backbitings experimentally observed in the Controlled Radical Polymerization, we concentrate on simulation of relative frequencies of constrained events. In this section we discuss a Monte Carlo approach for evaluation of relative frequencies of constrained events in stochastic processes.

First, in Section 1.4.1 we formulate the SSA procedure for calculating the quantity of interest by using explicit constraints among the possible events, as suggested in Section 1.3.5.2.

Then, Section 1.4.2 presents a formulation of SSA for the computation of the relative frequencies, where the constraints are implicitly built in the density functions, as proposed in Section 1.3.5.1.

Finally, Section 1.4.3 discusses the presented methodologies and provides the motivation for the following sections of this chapter.

1.4.1 SSA Algorithm with Explicit Constraints

We consider a stochastic process during the time interval $[t_0, t_{\max}]$. The realisations of the random variables building the stochastic process correspond to the events occurring during $[t_0, t_{\max}]$. Each event may have N possible outcomes. The outcome $i = 1, .., N$ corresponds to a possible value assumed by the random variables. The outcomes are constrained, i.e.

the outcome $i = 1, .., N$ can occur if and only if at least $c_{ij} \in \mathbb{N}$ outcomes $j = 1, .., N$

have already occurred after the previous occurrence of the outcome i. $\quad\quad$ (1.47)

If the outcome i is possible, the required time $T_i = \tau$ for its occurrence is distributed according to the known probability density function (PDF)

$$f_i(\tau), \quad \tau \in \mathbb{R}^+, \quad i = 1, .., N. \tag{1.48}$$

The objective is to compute the ratio between final numbers n_{i_1} and n_{i_2} of occurred outcomes i_1 and $i_2 \in \{1, .., N\}$.

It is worth noting that there are the conditions the system needs to satisfy in order to be able to evolve its state. First, each outcome must not be constrained by itself, or

$$c_{ii} = 0, \quad \forall i = 1, .., N, \tag{1.49}$$

and second, there is at least one outcome free to occur, or (s.t. is a shorthand for "such that")

$$\exists i \in \{1, .., N\} \quad \text{s.t.} \quad c_{ij} = 0, \forall j = 1, .., N. \tag{1.50}$$

Otherwise, if $c_{ij} \neq 0$ for all i, j, none of the events are possible.

Given a well-posed set of constraints (1.47), Algorithm 1.3 presents a Monte Carlo (MC) procedure for computing a single realisation of the relative frequency of the outcomes i_1 and i_2. The constraints are explicitly accounted during the evolution of the process, as suggested in Section 1.3.5.2.

Algorithm 1.3: The MC procedure for computing a single realisation of the relative frequency n_{i_1}/n_{i_2} of the outcomes i_1 and $i_2 \in \{1, .., N\}$ during the time interval $[t_0, t_{\max}]$. The algorithm explicitly accounts for the constraints (1.47) (s.t. stands for "such that").

---
1 Define the initial time $t = t_0$ and final time $t_{\max} > t_0$;
2 Given $N \in \mathbb{N}$, set the number of occurred outcomes $n_i = 0$, $\forall i = 1, .., N$;
3 Initialise the label $j_i = 0$ for the possible occurrence of the outcome i, $\forall i = 1, .., N$;
4 Assign the constraints $c_{ij} \in \mathbb{N}$, $\forall i, j = 1, .., N$;
5 **while** $t < t_{\max}$ **do**
6 $\quad$ Reset $j_i = 0$, $\forall i = 1, .., N$;
7 $\quad$ **for** $i = 1, .., N$ **do**
8 $\quad\quad$ **if** outcome i satisfies all the constraints (1.47) **then**
9 $\quad\quad\quad$ Set the label $j_i = 1$;
10 $\quad\quad\quad$ Draw a realization τ_i from $T_i \sim f_i(\tau)$ (1.48), with $\tau \in \mathbb{R}^+$;
11 $\quad\quad$ **end**
12 $\quad$ **end**
13 $\quad$ Select the outcome $i_0 \in \{1, .., N\}$ such that $\tau_{i_0} = \min_{i=1,..,N \text{ s.t. } j_i=1} \tau_i$;
14 $\quad$ Update the time $t \leftarrow t + \tau_{i_0}$;
15 $\quad$ Update the occurred outcomes $n_{i_0} \leftarrow n_{i_0} + 1$;
16 **end**
17 Return the final ratio n_{i_1}/n_{i_2};

1.4.2 SSA Algorithm with Implicit Constraints

We consider the stochastic process described in Section 1.4.1, addressing the relative frequency of the occurred outcomes i_1 and $i_2 \in \{1, .., N\}$.

Given the constraints (1.47) and the PDF (1.48), we define the distribution

$$\bar{f}_{i_k}\left(\tau; \{c_{ij}, f_i(\cdot)\}_{i,j=1,..,N}\right), \quad \tau \in \mathbb{R}^+, \quad k = 1, 2, \tag{1.51}$$

of the values $\bar{T}_{i_k} = \tau$ of the required time for the occurrence of the outcome i_k, $k = 1, 2$, accounting for all the possible events with the relative constraints. An illustrative example for (1.51) is given by the density (1.36) for the constrained branching presented in Section 1.3.5.

Following Section 1.3.5.1, Algorithm 1.4 describes an MC procedure for computing a single realisation of the relative frequency of the outcomes i_1 and i_2. The PDF (1.51) implicitly accounts for the constraints (1.47) and the distributions (1.48).

Algorithm 1.4: The MC procedure for computing a single realisation of the relative frequency n_{i_1}/n_{i_2} of the outcomes i_1 and $i_2 \in \{1, .., N\}$ during the time interval $[t_0, t_{\max}]$. The density $\bar{f}_{i_k}$ (1.51) implicitly accounts for the constraints among the possible events and their required times.

---

1 Define the initial times $t_1 = t_2 = t_0$ and final time $t_{\max} > t_0$;
2 Set the number of occurred outcomes $n_{i_1} = n_{i_2} = 0$;
3 for $k = 1, 2$ **do**
4 **while** $t_k < t_{\max}$ **do**
5   Draw a realization τ_k from $\bar{T}_{i_k} \sim \bar{f}_{i_k}$ (1.51);
6   Update the time $t_k \leftarrow t_k + \tau_k$;
7   Update the occurred outcomes $n_{i_k} \leftarrow n_{i_k} + 1$;
8 **end**
9 end
10 Return the final ratio n_{i_1}/n_{i_2};

1.4.3 Summary

In this section we have formulated SSA-based algorithms for calculating relative frequencies of constrained events in stochastic processes. The algorithms can be applied in any study where relative frequencies of constrained events are of interest.

The constraints among the possible events can be introduced either explicitly (Algorithm 1.3) or implicitly (Algorithm 1.4). In the general case, it looks difficult to show the equivalence among the presented algorithms. Once the constraints (1.47) and the PDF (1.48) are specified, the equivalence can be shown by recovering the density (1.51) from the procedure given in Algorithm 1.3, as discussed in Section 1.3.5.3. Figure 1.4 verifies the agreement between the two approaches in the computation of the branching fraction.

Algorithm 1.4 (implicit constraints) is expected to improve the computational efficiency of Algorithm 1.3 (explicit constraints). If the number N of outcomes is very large, Algorithm 1.4 requires a significantly smaller number of random generations and conditional statements than Algorithm 1.3 does. The enhanced efficiency of the implicit approach is confirmed in Figure 1.5. However, it may be not always possible, or convenient, to apply Algorithm 1.4. Indeed, it requires samples drawn from the density (1.51). Particular shapes of the PDF (1.48) and complex structures of the constraints (1.47) may lead to non-closed form expressions of (1.51) and expensive procedures for the samples drawing. Regardless of the distinctiveness, both MC algorithms 1.3 and 1.4 suffer from the same drawback: they are computationally expensive. For this reason, we show in Section 1.5 how to directly solve the dynamics of the system without having to resort to any MC method. In particular, we derive a significantly more effective analytical approach for computing relative frequencies of constrained events in stochastic processes. The analytical formula is obtained in the same terms as Monte Carlo routine is defined, ensuring the equivalence of the two methodologies.

1.5 Relative Frequencies of Constrained Events in Stochastic Processes: An Analytical Approach

In Section 1.4, we suggested Monte Carlo (MC) based approaches for study of constrained stochastic processes. Such methodologies, however, are computationally demanding. The aim of this section is

to show that it is possible to replace heavy MC methods with the analytical expression for the asymptotic relative frequencies of constrained events. The replacement not only provides more accurate estimation of the properties of the process, but also reduces the simulation time by a factor of order of the sample size (at least $\approx 10^4$). The method is validated using the exactly solvable model introduced in Section 1.3 and then applied to the evaluation of branching fractions in Controlled Radical Polymerization (CRP) of acrylic monomers. The proposed method does not depend on a choice of a PDF or properties of a constrained system and thus is suitable for the wide range of applications (see [24] for examples of constrained systems).

The section is organised as follows. In Section 1.5.1, we derive the analytical expression for the relative asymptotic frequency of constrained events in general stochastic processes. The result is tested in Section 1.5.2 for the exactly solvable case of a process with a single constraint. The comparison with the MC method from Section 1.3.5.2 validates the obtained formula. Following the ideas described in Section 1.5.1, we derive in Section 1.5.3 the analytical expression for the asymptotic branching fraction in CRP of acrylic monomers. Section 1.5.4 discusses the presented results and provides the connections with the rest of the chapter.

1.5.1 Relative Asymptotic Frequencies of Constrained Events in Stochastic Processes

Consider a stochastic process with a given total number of events $n_T \gg 1$. These events correspond to the realizations of the random variables building the stochastic process. Each event may have N possible outcomes. A particular outcome is given by a possible value assumed by the random variables. The outcomes are constrained (1.47): the outcome $i = 1, .., N$ can occur if and only if at least $c_{ij} \in \mathbb{N}$ outcomes $j = 1, .., N$ have already occurred after the previous occurrence of the outcome i. As specified in Section 1.4.1, the system needs to satisfy the conditions (1.49) and (1.50) in order to be able to evolve its state. Our objective is to compute ratios between asymptotic numbers n_i and n_j of occurred outcomes i and j.

The n_T events can be partitioned as follows. Let us divide all events into 2^N non-overlapping subsets labelled $(j_1, j_2, .., j_N)$, where $j_k = 0, 1$ and $k = 1, 2, .., N$. $j_k = 1$ means that the k-th outcome is possible, whereas if $j_k = 0$ it is not possible due to constraints. Let $n(j_1, j_2, .., j_N)$ be the number of events in a subset, e.g. $n(1, 0, ..., 0)$ is the number of events for which the outcome $i = 1$ is possible, but the rest of them are not. Obviously

$$\sum_{j_1, .., j_N = 0, 1} n(j_1, j_2, .., j_N) = n_T. \tag{1.52}$$

Let $n_i(j_1, j_2, .., j_N)$ be the number of outcomes of a kind i in the subset $(j_1, j_2, .., j_N)$. The assumption is that the events belonging to each subset $(j_1, j_2, .., j_N)$ are independent (unconstrained). Such an assumption does not lead to loss of generality because the constraints used in building different subsets can contain the information about the dependencies between events.

Then if $n(j_1, j_2, .., j_N) \to +\infty$, the probability $\mathbb{P}_i(j_1, j_2, .., j_N)$ for the i-th outcome to occur in the set $(j_1, j_2, .., j_N)$ corresponds to the limit of frequency of the i-th outcome, i.e.

$$\mathbb{P}_i(j_1, j_2, .., j_N) = \frac{n_i(j_1, j_2, .., j_N)}{n(j_1, j_2, .., j_N)}, \quad \forall i \in \{1, .., N\}. \tag{1.53}$$

A formulation of the Gillespie Stochastic Simulation Algorithm (SSA) [25] can be used to define the probability $\mathbb{P}_i(j_1, j_2, .., j_N)$. Let independent random variables $T_1, T_2, .., T_N$ be the times required for the next occurrence of the respective outcome, if it is possible. SSA suggests to pick the outcome that realizes the minimal occurrence time among the possible ones, as summarised in Algorithm 1.2. In other words,

$$\mathbb{P}_i(j_1, j_2, .., j_N) = \begin{cases} 0 & \text{if } j_i = 0, \\ \mathbb{P}\left(T_i < T_k : \forall k \neq i \text{ s.t. } j_k = 1\right) & \text{if } j_i = 1 \wedge \exists k \neq i \text{ s.t. } j_k = 1, \\ 1 & \text{if } j_i = 1 \wedge j_k = 0, \forall k \neq i. \end{cases} \tag{1.54}$$

Equations (1.53) and (1.54) offer the way for calculation of the asymptotic numbers of outcomes of a kind i, n_i, for any i:

$$n_i = \sum_{j_1,..,j_N} \mathbb{P}_i(j_1, j_2, .., j_N) n(j_1, j_2, .., j_N), \quad \forall i \in \{1, .., N\}. \tag{1.55}$$

The ratio between n_i and n_j for any i and j can be immediately obtained from (1.55) and (1.54). The number of possible outcomes N should not be crucial for the proposed approach. In particular, the proposed solution holds for big values of N. More important for the applicability of the method are the possible dependencies between different events. In general, complex dependencies between different subsets may lead to non-converged asymptotic behaviour of the ratios of interest. However, when the constraints are limited and well defined, as in the examples presented in the following sections, the ratios of interest can be evaluated exactly for any value of N.

1.5.2   A Process with a Single Constraint

The analytical approach of Section 1.5.1 can be tested on the simple model introduced in [2]. We consider the case of a stochastic process with only two possible outcomes, 1 and 2. The first one is free to occur with the occurrence rate c_1, but the second one must wait till at least n_0 occurrences of kind 1 after its own previous occurrence. Its occurrence rate is c_2. There are only two possible subsets in this case (the order of events is preserved as described above):

$$(1, 0), (1, 1). \tag{1.56}$$

The corresponding probabilities are given by

$$\begin{aligned} \mathbb{P}_1(1, 0) &= 1, & \mathbb{P}_1(1, 1) &= \mathbb{P}(T_1 < T_2), \\ \mathbb{P}_2(1, 0) &= 0, & \mathbb{P}_2(1, 1) &= \mathbb{P}(T_2 < T_1). \end{aligned} \tag{1.57}$$

The total number of events $n(1, 0)$ in the subset $(1, 0)$ is given by n_0 outcomes 1 for each occurrence of the outcome 2:

$$n(1, 0) = n_2 n_0, \tag{1.58}$$

where n_2 is the asymptotic total number of outcomes 2. The total number of events in the complementary subset $n(1, 1)$ can be computed by subtraction:

$$n(1, 1) = n_T - n_2 n_0. \tag{1.59}$$

Equation (1.55) gives

$$n_1 = n_2 n_0 + \mathbb{P}(T_1 < T_2)(n_T - n_2 n_0), \tag{1.60}$$

$$n_2 = \mathbb{P}(T_2 < T_1)(n_T - n_2 n_0), \tag{1.61}$$

where T_i is the time required to fire the next occurrence of kind $i = 1, 2$ (if possible). Equations (1.60) and (1.61) can be rewritten as

$$n_1 = \frac{\mathbb{P}(T_1 < T_2) + n_0 \mathbb{P}(T_2 < T_1)}{1 + n_0 \mathbb{P}(T_2 < T_1)} n_T, \tag{1.62}$$

$$n_2 = \frac{\mathbb{P}(T_2 < T_1)}{1 + n_0 \mathbb{P}(T_2 < T_1)} n_T. \tag{1.63}$$

Equations (1.62) and (1.63) show that, as $n_T \to \infty$, the asymptotic fraction n_2/n_1 reaches the fixed asymptotic value. In particular

$$\frac{n_2}{n_1} = \frac{\mathbb{P}(T_2 < T_1)}{\mathbb{P}(T_1 < T_2) + n_0 \mathbb{P}(T_2 < T_1)}. \tag{1.64}$$

Following [25], we assign independent exponentially distributed probability density functions $f_i(t)$ to the random variables T_i, $i = 1, 2$:

$$f_i(t) = c_i \exp(-c_i t), \quad t, c_i \in \mathbb{R}^+, \quad i = 1, 2. \tag{1.65}$$

The probabilities in (1.64) can be computed as

$$\mathbb{P}(T_1 < T_2) = \int_0^{+\infty} f_1(t) \left[1 - \int_0^t f_2(\tau) \, d\tau \right] dt = \frac{c_1}{c_1 + c_2}. \tag{1.66}$$

Thus, the asymptotic ratio between the number of outcomes 2 and the number of outcomes 1 becomes

$$\frac{n_2}{n_1} = \frac{c_2}{c_1 + n_0 c_2}. \tag{1.67}$$

This result is in good agreement with the data obtained using the Monte Carlo method proposed in Section 1.3.5.2, as is shown in Figure 1.6.
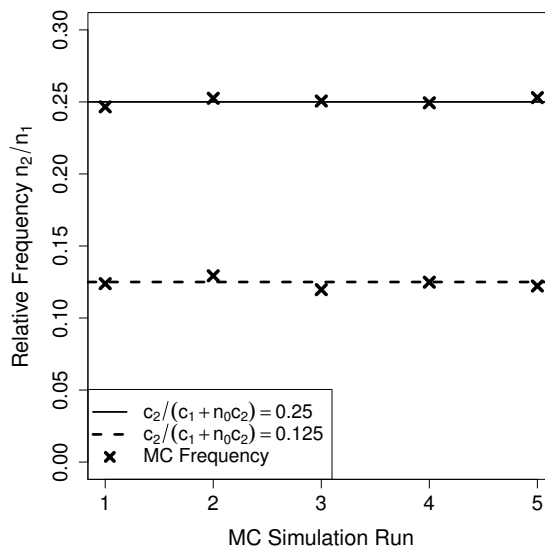
Figure 1.6: Comparison between the analytical solution (1.67) (lines) and corresponding statistics (crosses) obtained by the Monte Carlo (MC) method proposed in Section 1.3.5.2. Five independent runs are performed for two different parameters sets: $n_0 = 3$, $c_2/c_1 = 1$ (solid line) and $n_0 = 3$, $c_2/c_1 = 0.2$ (dashed line). The MC sample size is equal to $G = 10^4$.

1.5.3 Analytical Expression for Asymptotic Relative Frequencies of Constrained Events in CRP

Following the ideas described in Section 1.5.1, we want to derive the analytical expression for the asymptotic branching fraction in Controlled Radical Polymerization (CRP) of acrylic monomers. In particular, let n_p, n_d and n_r respectively be the asymptotic mean number of occurred propagations, deactivations and backbitings. Then the branching fraction can be calculated as a ratio between n_r and n_p using equations (1.54) and (1.55). As stated in the beginning of the chapter, propagation and deactivation are always possible, whereas backbiting needs at least $n_0 = 3$ previous propagations to occur. Hence, we have two subsets (the order is: propagation (p), deactivation (d), backbiting (r)):

$$(1, 1, 0), (1, 1, 1). \tag{1.68}$$

The following are the probabilities for each outcome in each subset:

$$
\begin{aligned}
\mathbb{P}_p(1,1,0) &= \mathbb{P}(T_p < T_d), \quad \mathbb{P}_p(1,1,1) = \mathbb{P}(T_p < T_d, T_r), \\
\mathbb{P}_d(1,1,0) &= \mathbb{P}(T_d < T_p), \quad \mathbb{P}_d(1,1,1) = \mathbb{P}(T_d < T_p, T_r), \\
\mathbb{P}_r(1,1,0) &= 0, \quad \mathbb{P}_r(1,1,1) = \mathbb{P}(T_r < T_p, T_d).
\end{aligned}
\tag{1.69}
$$

The total number of events that cannot be a backbiting, $n(1,1,0)$, is given by n_0 propagations for each occurred backbiting, and by the number of deactivations occurred when backbiting is not possible:

$$
n(1,1,0) = n_0 n_r + n_d(1,1,0) = n_0 n_r + \mathbb{P}(T_d < T_p)n(1,1,0).
\tag{1.70}
$$

Equation (1.70) can be rewritten as

$$
n(1,1,0) = \frac{n_0 n_r}{\mathbb{P}(T_p < T_d)}.
\tag{1.71}
$$

Apparently,

$$
n(1,1,1) = n_T - n(1,1,0).
\tag{1.72}
$$

Then, Equation (1.55) yields

$$
n_p = \mathbb{P}(T_p < T_d)n(1,1,0) + \mathbb{P}(T_p < T_d, T_r)[n_T - n(1,1,0)],
\tag{1.73}
$$

$$
n_d = \mathbb{P}(T_d < T_p)n(1,1,0) + \mathbb{P}(T_d < T_p, T_r)[n_T - n(1,1,0)],
\tag{1.74}
$$

$$
n_r = \mathbb{P}(T_r < T_p, T_d)[n_T - n(1,1,0)].
\tag{1.75}
$$

From Eqs. (1.73) and (1.75) we have:

$$
n_r = \frac{\mathbb{P}(T_p < T_d)\mathbb{P}(T_r < T_p, T_d)}{\mathbb{P}(T_p < T_d) + n_0\mathbb{P}(T_r < T_p, T_d)} n_T,
\tag{1.76}
$$

$$
n_p = \frac{\mathbb{P}(T_p < T_d)[\mathbb{P}(T_p < T_d, T_r) + n_0\mathbb{P}(T_r < T_p, T_d)]}{\mathbb{P}(T_p < T_d) + n_0\mathbb{P}(T_r < T_p, T_d)} n_T.
\tag{1.77}
$$

Equations (1.76) and (1.77) show that, as $n_T \to \infty$, the branching fraction n_r/n_p reaches the fixed asymptotic value

$$
\frac{n_r}{n_p} = \frac{\mathbb{P}(T_r < T_p, T_d)}{\mathbb{P}(T_p < T_d, T_r) + n_0\mathbb{P}(T_r < T_p, T_d)}.
\tag{1.78}
$$

In particular, the ratio (1.78) is a function of the probabilities involving the random variables T_p, T_d and T_r only. This implies two important consequences: (i) our solution holds for any choice of inter-event times PDF and (ii) it is possible to express the branching fraction as a function of the PDF parameters, once the probabilities of interest are computed. In the general case, the probabilities in (1.78) can be calculated as follows. Given $N \geq 2$ independent random variables $T_1, .., T_N$ with distributions $f_i(t)$, $i = 1, ..N$, the probability $\mathbb{P}(T_k < T_j, \forall j \neq k)$, with $k, j = 1, .., N$, can be computed as

$$
\mathbb{P}(T_k < T_j, \forall j \neq k) = \int_0^{+\infty} f_k(t) \prod_{j \neq k} \left[1 - \int_0^t f_j(\tau)\, d\tau \right] dt, \quad k, j = 1, .., N.
\tag{1.79}
$$

As summarised in Section 1.1, classical theories of chemical kinetics assume the memoryless exponential distributions $f_p(t)$, $f_d(t)$ and $f_r(t)$ for the value t of the required times T_p, T_d and T_r respectively, i.e.

$$
f_i(t) = c_i \exp(-c_i t), \quad t, c_i \in \mathbb{R}^+, \quad i = p, d, r,
\tag{1.80}
$$

where c_p, c_d and c_r are the corresponding occurrence rates. Given (1.80), we compute the probabilities in (1.78) following the formula (1.79):

$$\mathbb{P}(T_r < T_p, T_d) = \frac{c_r}{c_p + c_d + c_r}, \quad \mathbb{P}(T_p < T_d, T_r) = \frac{c_p}{c_p + c_d + c_r}. \tag{1.81}$$

Equation (1.78) gives

$$\frac{n_r}{n_p} = \frac{c_r}{c_p + n_0 c_r}, \tag{1.82}$$

showing that the resulting branching fraction n_r/n_p is independent from the additional process of chain deactivation. In other words, (1.82) suggests that the classical mathematical framework, assuming the memoryless exponential distributions, is not able to explain the reduction of the branching fraction, experimentally observed in the presence of the control agent. Our analytical approach is valid for any choice of inter-event PDF, allowing to extend the classical modelling to delayed PDF. To explain the experimentally observed reduction of the branching fraction, we will consider in Section 1.6 non-exponentially distributed random variables, allowing the presence of delays among the possible events.

1.5.4 Summary

In this section, we have derived the analytical expression for the relative asymptotic frequency of constrained events in general stochastic processes. The proposed analytical approach is based on the assumption that the asymptotic limit is reached. Thus, it describes the statistics of the asymptotic states of a stochastic process. Reaching the asymptotic limit via Monte Carlo (MC) simulations is costly, since also the transient dynamics need to be performed. In the considered application (CRP), the reactions continue until all the reactants are used up. For this reason, our method is appropriate for a study of CRP, where reactions may be seen as reaching their asymptotic state.

The analytical formula stands for any choice of inter-event PDF and well-posed constraints, being suitable for a wide range of applications. The result has been tested on an exactly solvable model and validated by comparison with the corresponding MC approach. Then, the general formula has been applied for the computation of the asymptotic branching fraction in Controlled Radical Polymerization (CRP) of acrylic monomers, assuming an arbitrary choice of PDFs. In addition, using the developed analytical approach we prove that memoryless models are not able to explain the experimentally observed reduction of branching fraction in CRP. We published in [3] the results presented in Section 1.5.

The next step will be to combine the mathematical framework, derived in Section 1.3, with the approaches, proposed in Section 1.4 and Section 1.5 for calculation of relative frequencies of constrained events, in order to develop a methodology for modelling CRP of acrylic monomers.

1.6 SSA for Modelling of Constrained Events in CRP

Our goal is to design a Stochastic Simulation Algorithm (SSA) based method for simulating the constrained events of Controlled Radical Polymerization (CRP). Such a method should be able to predict any quantity of interest in agreement with experimental evidences.

Section 1.6.1 discusses the inter-event PDFs to be used in SSA. The experimental trend of branching fractions motivates the need for delays in the PDF shape, as shown in Section 1.5. The required delays can be efficiently accounted for, as suggested in Section 1.3.5.4.

Section 1.6.2 designs the procedure for refining the parameters of the proposed delayed PDFs with the help of the available experimental data.

Section 1.6.3 employs the delayed PDFs, with optimal parameters, to build the SSA-based method simulating the CRP process in agreement with experimental evidences. The methodology is based on the MC framework suggested in Section 1.4.

Section 1.6.4 discusses the presented methodologies and provides the connections with the rest of the chapter.

1.6.1 Delayed Probability Density Functions

This section addresses the choice of the inter-event distributions to perform SSA simulating the CRP reaction in agreement with the experimental data.

The experimental branching fractions shown in Figure 1.7 present the example of the available data. The two sets of values, with corresponding uncertainty intervals, were obtained by performing the polymerization of n-Butyl Acrylate, under two different experimental conditions, known as *bulk* (80 °C) and *solution* (110 °C) polymerization. The trithiocarbonate RAFT agent, DTTC, was used as the control agent. Each polymerization was conducted at different control agent concentrations, thus giving a range of data points for analysing the effect of the deactivation event. Figure 1.7 shows that for the trithiocarbonate RAFT agent, DTTC, in both solution and bulk polymerizations the branching fraction decreases with increasing DTTC concentration. The results were supplied by the group of Prof. J. M. Asua in POLYMAT.
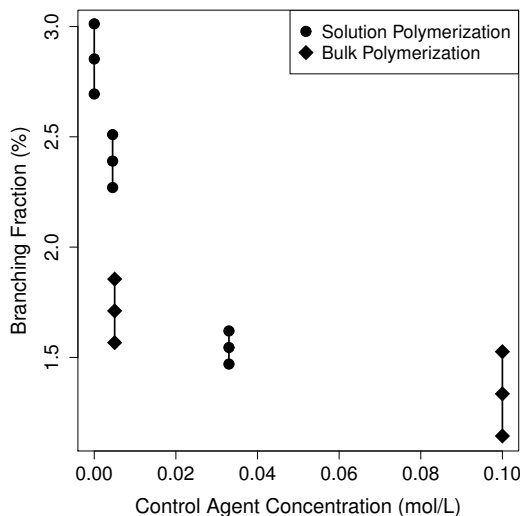
Figure 1.7: Experimental branching fractions and corresponding uncertainty intervals, provided by the research group of Prof. J. M. Asua in POLYMAT.

The inspection of Figure 1.7 confirms the strong reduction in branching fraction under CRP conditions, which cannot be predicted by simulating a (memoryless) Markovian process, as shown in Section 1.5. This motivates us to view a CRP process as non-Markovian and to assume delayed probability density functions.

In particular, we consider independent linear exponential distributions for the required times of the possible reactions, as proposed in Section 1.3.5.4. It means that the time required for a propagation is $T_p \sim \mathrm{Linexp}(b_p, \tau_p)$, for a backbiting is $T_r \sim \mathrm{Linexp}(b_r, \tau_r)$ and for a deactivation is $T_d \sim \mathrm{Linexp}(b_d, \tau_d)$. The linear exponential PDF is defined as:

$$T_i \sim \mathrm{Linexp}(b_i, \tau_i) \Leftrightarrow f_{LE}(t; b_i, \tau_i) = \begin{cases} \frac{2}{b_i^2 + 2b_i\tau_i}\, t, & \text{if } 0 \le t < b_i, \\ \frac{2b_i}{b_i^2 + 2b_i\tau_i} \exp\left[-\frac{(t - b_i)}{\tau_i}\right], & \text{if } t \ge b_i, \end{cases} \tag{1.83}$$

where $i = p, r, d$ and the indices p, r, d stand for propagation, backbiting and deactivation respectively. The parameters $b_i > 0$ quantify the amount of delay for the different reactions. In the absence of delay, i.e. $b_i \to 0$, the PDF (1.83) correctly recovers the memoryless exponential distribution.

1.6.2 Using Experimental Data for PDFs Parameters Quantification

The data, such as shown in Figure 1.7, allow for quantifying the parameters of the delayed PDFs. In particular, an optimisation scheme can be designed for a proper fitting of the simulated branching fractions into the experimentally measured data of Controlled Radical Polymerization.

Let us recall that the Monte Carlo (MC) framework of Section 1.4 and the analytical approach of Section 1.5 are able, in principle, to predict the data of Figure 1.7, provided the knowledge of inter-event PDFs. One can choose a particular functional shape for these PDFs, following the suggestions in Section 1.6.1. Assigning the constraint $n_0 = 3$ and assuming the PDF (1.83), either Algorithm 1.5 or Algorithm 1.6 can be readily used for a stochastic or analytical evaluation, respectively, of the final branching fraction of the created polymer chain for a given set of PDFs parameters values.

Algorithm 1.5: The MC method for computation of the final branching fraction ρ in CRP, corresponding to the parameters values $b_p, \tau_p, b_r, \tau_r, b_d, \tau_d \in \mathbb{R}^+$.

---

1 Define the random variables $T_i \sim \text{Linexp}(b_i, \tau_i)$ (1.83), for $i = p, d, r$;
2 Set the numbers $n_p = n_r = 0$ of occurred propagations (p) and backbitings (r);
3 Assign the number $n_0 = 3$ of required propagations to have a backbiting;
4 Initialise the propagations counter $k_p = 0$ and set the sample size $G \in \mathbb{N}$;
5 **for** $j = 1, .., G$ **do**
6   **if** $k_p < n_0$ **then**
7   Draw an independent realization t_i from T_i, for $i = p, d$;
8   **if** $t_p = \min\{t_p, t_d\}$ **then**
9   Propagation has occurred: $n_p \leftarrow n_p + 1$ and $k_p \leftarrow k_p + 1$;
10   **end**
11   **else**
12   Draw an independent realization t_i from T_i, for $i = p, d, r$;
13   **if** $t_p = \min\{t_p, t_d, t_r\}$ **then**
14   Propagation has occurred: $n_p \leftarrow n_p + 1$;
15   **end**
16   **if** $t_r = \min\{t_p, t_d, t_r\}$ **then**
17   Backbiting has occurred: $n_r \leftarrow n_r + 1$ and $k_p = 0$;
18   **end**
19   **end**
20 **end**
21 Return the value of the branching fraction $\rho \equiv n_r/n_p$;

Algorithm 1.6: The analytical approach for computation of the final branching fraction ρ in CRP, corresponding to the parameters values $b_p, \tau_p, b_r, \tau_r, b_d, \tau_d \in \mathbb{R}^+$.

---

1 Define the random variables $T_i \sim \text{Linexp}(b_i, \tau_i)$ (1.83), for $i = p, d, r$;
2 Assign the number $n_0 = 3$ of required propagations to have a backbiting;
3 Using the formula (1.79), compute the probabilities $\mathbb{P}(T_p < T_d, T_r)$ and $\mathbb{P}(T_r < T_p, T_d)$;
4 Apply (1.78) to calculate the ratio n_r/n_p;
5 Return the value of the branching fraction $\rho \equiv n_r/n_p$;

Algorithm 1.5 and Algorithm 1.6 rely on the knowledge of the parameters $b_p, \tau_p, b_r, \tau_r, b_d, \tau_d \in \mathbb{R}^+$ to compute the corresponding branching fraction ρ. In practice, appropriate PDFs parameters are difficult to identify, and the available experimental data may be taken into consideration to resolve this problem. Sometimes, the PDFs parameters can be obtained using the rate coefficients determined from experimental measurements. If the kinetic rate coefficient of a given reaction is independent of other processes, the PDF parameters and experimentally measured rate coefficient are explicitly related. This is the case of the propagation rate coefficient for linear polymer growth. However, when, as in the case of backbiting in CRP, the rate coefficient is determined in the presence of other competitive processes, then the relationship between the PDFs parameters and experimentally measured rate coefficients is not straightforward.

One possible way to estimate the unknown PDFs parameters is to employ an optimisation scheme, which uses available experimental data. The idea behind a fitting scheme is to build a cost function J

for measuring the disagreement between experimental and simulated branching fractions. The fitting scheme minimises the cost function J, in order to find such a set of PDFs parameters that gives the best agreement with the experimental data. The ability of the method to reproduce the experimental trend will serve as a proof of the reliability of our non-Markovian model for CRP, as will be shown in Section 1.7.

Algorithm 1.7 presents the scheme for fitting the simulated branching fractions ρ in CRP. The cost function J evaluates ρ by performing either the MC method described by Algorithm 1.5, or the analytical approach summarised in Algorithm 1.6. We have to stress that there are no particular restrictions on the choice of an optimisation algorithm. However, in practice one should go for the most efficient one available, since this would help to reduce the number of iterations required for finding the optimal parameters.

Algorithm 1.7: The scheme for fitting the simulated branching fractions ρ to the experimental data. The method returns the tuned parameters $\hat{b}_p, \hat{\tau}_p, \hat{b}_r, \hat{\tau}_r, \hat{b}_d, \hat{\tau}_d \in \mathbb{R}^+$ of the PDFs (1.83).

---

1 Define the cost function J measuring the disagreement between ρ and the experimental branching fractions, e.g. the data shown in Figure 1.7;

2 Set either the label $M = 1$ for the MC method, or $M = 2$ for the analytical approach;

3 Initialise the parameters $b_p, \tau_p, b_r, \tau_r, b_d, \tau_d \in \mathbb{R}^+$ of the PDFs (1.83);

4 **while** J is not minimised **do**

5   **if** $M = 1$ **then**

6   Run Algorithm 1.5 to calculate ρ;

7   **end**

8   **if** $M = 2$ **then**

9   Run Algorithm 1.6 to calculate ρ;

10   **end**

11   Compute J corresponding to ρ;

12   Update $b_p, \tau_p, b_r, \tau_r, b_d, \tau_d \in \mathbb{R}^+$ according to the chosen optimisation algorithm;

13 **end**

14 Return the optimal values $\hat{b}_p = b_p, \hat{\tau}_p = \tau_p, \hat{b}_r = b_r, \hat{\tau}_r = \tau_r, \hat{b}_d = b_d, \hat{\tau}_d = \tau_d$;

The fitting scheme presented in Algorithm 1.7 computes the branching fractions ρ by applying either the MC method (Algorithm 1.5), or the analytical approach (Algorithm 1.6). The analytical formula is obtained in the same terms as MC routine is defined, ensuring the equivalence of the two methodologies. However, the analytical approach is free of the statistical errors affecting MC-based simulations, and it can speed up the simulation by a factor of order of the sample size (at least $\approx 10^4$, as shown in Section 1.7).

In conclusion, the purpose of such a fitting scheme is twofold. On the one hand, we want to closely reproduce the observed experimental data and thus prove that the proposed model is a proper tool for studying CRP. On the other hand, the suggested scheme provides us with the refined parameters of the model that can be used for evaluation of other important properties of CRP, as discussed in Section 1.6.3.

1.6.3 SSA for Modelling of Constrained Events in CRP

This section designs the Stochastic Simulation Algorithm (SSA) for modelling the constrained events in Controlled Radical Polymerization (CRP). The method aims to prediction of any quantity of interest in agreement with experimental evidences. The routine can be divided in two consecutive stages.

First, the scheme presented in Section 1.6.2 allows tuning the parameters of PDFs (1.83) for better fitting of the simulated properties into the experimental branching fractions. Algorithm 1.7 can be used as an efficient tool for finding optimal values of the parameters in agreement with experimental data. The second stage of the simulation consists in using the tuned PDFs to perform a detailed MC simulation of CRP, in the line of Algorithm 1.3 formulated in Section 1.4.1.

Algorithm 1.8 presents the described method, summarising the routine to draw a single realisation of

the sequence of events and occurrence times building the polymer chain. The constraint of $n_0 = 3$ propagations to have a backbiting is taken into account as proposed in Algorithm 1.3. The inter-event PDFs are assumed linear exponential (1.83), as motivated in Section 1.6.1. The information provided by the experimental branching fractions is embedded in the optimal PDFs parameters, found by Algorithm 1.7. In order to save computational effort, we recommend to use the accurate and efficient analytical approach for optimising the PDFs parameters, i.e. $M = 2$ in Algorithm 1.7. In conclusion, the sequence of events and times, drawn according Algorithm 1.8, allows estimating any quantity of interest in agreement with experimental evidences.

1.6.4 Summary

This section has been devoted to the design of an SSA-based method for simulating the CRP process in agreement with available experimental evidences.

The decreasing trend of the experimental branching fraction, shown in Figure 1.7, imposes the introduction of delays in the inter-event PDFs of the SSA method, as proven in Section 1.5. The linear exponential PDF (1.83) accounts for the required delays, as motivated in Section 1.3.5.4.

The competitive nature of the processes building the CRP reaction makes the values of the delayed PDFs parameters difficult to identify. Algorithm 1.7 tunes the parameters of the PDFs (1.83) for the better matching of simulated and experimental branching fractions. As will be shown in Section 1.7, the resulting fitting validates our non-Markovian model for CRP of acrylic monomers.

Algorithm 1.8 summarises all these findings and describes the SSA-based method for simulating the CRP process in agreement with experimental evidences. The methodology relies on the MC framework discussed in Section 1.4, employing the linear exponential PDFs (1.83) with the optimal parameters values found by Algorithm 1.7.

The described in Algorithm 1.7 method, performed with Algorithm 1.5 ($M = 1$) and the Nelder-Mead optimisation scheme [35], has been successfully applied to the study of branching in Controlled Radical Polymerization of acrylic monomers. We published the results in [1].

The simulated branching fractions can be computed by either the MC method (Algorithm 1.5), or the analytical approach (Algorithm 1.6). The two methodologies are equivalent, since derived from the same rules. Section 1.7 will test the accuracy and the computational efficiency of the MC method and the analytical approach, for the evaluation of branching fractions in Controlled Radical Polymerization of acrylic monomers. As will be shown in Section 1.7, the analytical approach should be the method of choice because (i) it avoids the statistical errors affecting MC-based simulations and (ii) it speeds up the simulation by a factor of order of the sample size (at least $\approx 10^4$).

Algorithm 1.8: The Stochastic Simulation Algorithm (SSA) for modelling the constrained events in Controlled Radical Polymerization. SSA returns a single realisation of events and occurrence times building the polymer chain during the time interval $[t_0, t_{\max}]$.

1 Set the initial time t_0 and final time $t_{\max} > t_0$;

2 Define the occurrence time $t_k \in [t_0, t_{\max}]$ of the k-th event, with $k \in \mathbb{N}$;

3 Define $i_k = p, d, r$ to label the k-th event as propagation (p), deactivation (d) or backbiting (r);

4 Assign the number $n_0 = 3$ of required propagations to have a backbiting;

5 Initialise the propagations counter $k_p = 0$ and the index $k = 0$;

6 Run Algorithm 1.7 to find the optimal parameters $\hat{b}_p, \hat{\tau}_p, \hat{b}_r, \hat{\tau}_r, \hat{b}_d, \hat{\tau}_d \in \mathbb{R}^+$ of the PDFs (1.83);

7 Define the random variables $T_i \sim \text{Linexp}(\hat{b}_i, \hat{\tau}_i)$ (1.83), for $i = p, d, r$;

8 while $t_k < t_{\max}$ **do**

9   **if** $k_p < n_0$ **then**

10   Draw an independent realization τ_i from T_i, for $i = p, d$;

11   Compute the occurrence time $t_{k+1} = t_k + \min\{\tau_p, \tau_d\}$ of the $k + 1$-th event;

12   **if** $\tau_p = \min\{\tau_p, \tau_d\}$ **then**

13   Propagation has occurred: $i_{k+1} = p$ and $k_p \leftarrow k_p + 1$;

14   **end**

15   **if** $\tau_d = \min\{\tau_p, \tau_d\}$ **then**

16   Deactivation has occurred: $i_{k+1} = d$;

17   **end**

18   **else**

19   Draw an independent realization τ_i from T_i, for $i = p, d, r$;

20   Compute the occurrence time $t_{k+1} = t_k + \min\{\tau_p, \tau_d, \tau_r\}$ of the $k + 1$-th event;

21   **if** $\tau_p = \min\{\tau_p, \tau_d, \tau_r\}$ **then**

22   Propagation has occurred: $i_{k+1} = p$;

23   **end**

24   **if** $\tau_d = \min\{\tau_p, \tau_d, \tau_r\}$ **then**

25   Deactivation has occurred: $i_{k+1} = d$;

26   **end**

27   **if** $\tau_r = \min\{\tau_p, \tau_d, \tau_r\}$ **then**

28   Backbiting has occurred: $i_{k+1} = r$ and $k_p = 0$;

29   **end**

30   **end**

31   Update $k \leftarrow k + 1$;

32 end

33 Return the sequence $\{i_k\}_{k \in \mathbb{N}}$ of events occurred at times $\{t_k\}_{k \in \mathbb{N}}$;

1.7 Branching Fraction in Controlled Radical Polymerization: Numerical Experiments

This section tests the accuracy and computational efficiency of the Monte Carlo (MC) procedure, designed in Section 1.4, and the analytical approach, proposed in Section 1.5, for the evaluation of branching fractions in Controlled Radical Polymerization (CRP) of acrylic monomers.

As discussed in Section 1.6, Algorithm 1.5 and Algorithm 1.6 allow us computing the branching fractions by means of the MC framework of Section 1.4 and the analytical approach of Section 1.5 respectively. The metrics of the tests will be the performances of Algorithm 1.5 and Algorithm 1.6 in the fitting of experimental branching fractions shown in Figure 1.7. The fitting of the available data can be achieved by optimisation schemes similar to Algorithm 1.7. Different settings are tested, as summarised in Table 1.1.

Tests	Simulated ρ	PDFs	Experimental Branch. Fr.	Cost Fun. J	Optimisation Algorithm	Results
T1: Accuracy **T2**: Accuracy **T3**: Efficiency **T4**: Efficiency	Analytical Solution (Algorithm 1.6)	Linexp (1.83) for all events	**T1**: Solution **T2**: Bulk **T3**: Solution **T4**: Bulk	Mean Squared Error (MSE)	Nelder-Mead method [35]	**T1-T2**: Data Fitting (Fig. 1.8a) and Tuned Param. (Tab. 1.2) **T3-T4**: Comput. Times (Fig. 1.8b)
T5: Accuracy **T6**: Accuracy **T7**: Efficiency **T8**: Efficiency	Monte Carlo method (Algorithm 1.5, sample size $G = 10^4$)	Linexp (1.83) for all events	**T5**: Solution **T6**: Bulk **T7**: Solution **T8**: Bulk	Mean Squared Error (MSE)	Nelder-Mead method [35]	**T5-T6**: Data Fitting (Fig. 1.8a) and Tuned Param. (Tab. 1.2) **T7-T8**: Comput. Times (Fig. 1.8b)
T9: Accuracy **T10**: Accuracy **T11**: Efficiency **T12**: Efficiency	Analytical Solution (Algorithm 1.6)	Exponential for prop. and deact. Linexp (1.83) for backbiting	**T9**: Solution **T10**: Bulk **T11**: Solution **T12**: Bulk	Mean Squared Error (MSE)	Genetic Algorithm [36]	**T9-T10**: Data Fitting (Fig. 1.9a) and Tuned Param. (Tab. 1.3) **T11-T12**: Comput. Times (Fig. 1.9b)
T13: Accuracy **T14**: Accuracy **T15**: Efficiency **T16**: Efficiency	Monte Carlo method (Algorithm 1.5, sample size $G = 10^4$)	Exponential for prop. and deact. Linexp (1.83) for backbiting	**T13**: Solution **T14**: Bulk **T15**: Solution **T16**: Bulk	**T13-T14**: not employed **T15-T16**: Mean Squared Error (MSE)	**T13-T14**: not employed **T15-T16**: Genetic Algorithm [36]	**T13-T14**: Data Fitting (Fig. 1.9a) **T15-T16**: Comput. Times (Fig. 1.9b)

Table 1.1: The settings of the tests **T1**-**T16** to evaluate the performances of Algorithm 1.5 and Algorithm 1.6 in the simulation of the branching fractions ρ. Following Algorithm 1.7, the simulated values of ρ fit the experimental branching fractions, given as the middle points of the uncertainty intervals in Figure 1.7. The tests **T13**-**T14** use the tuned parameters, found by **T9**-**T10**, to verify the fitting achievable by the Monte Carlo method, as shown in Figure 1.9a. In particular, the tests **T13**-**T14** do not employ any optimisation algorithm minimising the cost function J. The numerical experiments have been performed with in-house packages written for this Thesis in the C++ language. The simulations have been run on a 2.70GHz processor with a 64-bit Linux operating system.

In Figure 1.8a, we assess the accuracy provided by Algorithm 1.5 and Algorithm 1.6 in the fitting of experimental branching fractions. The results of the tests **T1**-**T2** and **T5**-**T6** (Table 1.1) are compared. As it follows from Figure 1.8a, the sample size $G = 10^4$ in the Monte Carlo approach guarantees the same level of accuracy provided by the analytical method. Both, the Monte Carlo method and the analytical approach, use linear exponential PDFs (1.83) for all possible events. The achieved fitting validates our non-Markovian model for Controlled Radical Polymerization. Table 1.2 shows the optimised parameters for the linear exponential PDFs (1.83).

Although both methods can offer comparable accuracies, it is not the case for the computational cost. The optimisation routine performed with the analytical approach is up to 10^4 times faster than the one using the MC method of the same level of accuracy (MC sample size $G = 10^4$). The computational times are shown in Figure 1.8b comparing the results of tests **T3**-**T4** and **T7**-**T8** (Table 1.1).

It is clear that the degree of speed-up provided by the analytical approach over the MC method is determined by the MC sample size G. Indeed, the computational complexity of the analytical method is $O(1)$ whereas it is $O(G)$ in the case of Monte Carlo. This is confirmed by the numerical tests.

The proposed methodologies are general enough for evaluating the behaviour of different optimisation algorithms and inter-event PDFs. In Figure 1.9a, Figure 1.9b and Table 1.3, we present the results

obtained by Algorithm 1.7 in which both the optimisation routine and the inter-event PDFs differ from those applied in the previous tests, as specified for **T9**-**T16** in Table 1.1. In particular, a Genetic Algorithm [36] has been selected for optimisation. Exponential PDFs are assigned to propagation and deactivation, whereas linear exponential PDF (1.83) is chosen for backbiting. The rationale behind the choice of PDFs for propagation and deactivation is confirmed by our previous tests, described above, which result in very small optimal parameters b_p and b_d, shown in Table 1.2. This suggests that the optimal PDF choice for propagation and deactivation is very close to an exponential distribution. The results shown in Figure 1.9a justify this choice. Also, these results confirm that the proposed methodologies are valid for various choices of optimisation routines and inter-event PDFs. We published the presented results in [3].

(a) Comparison between **T1**-**T2** and **T5**-**T6**. Nelder-Mead Optimisation, Linexp PDFs.

(b) Comparison between **T3**-**T4** and **T7**-**T8**. Nelder-Mead Optimisation, Linexp PDFs.
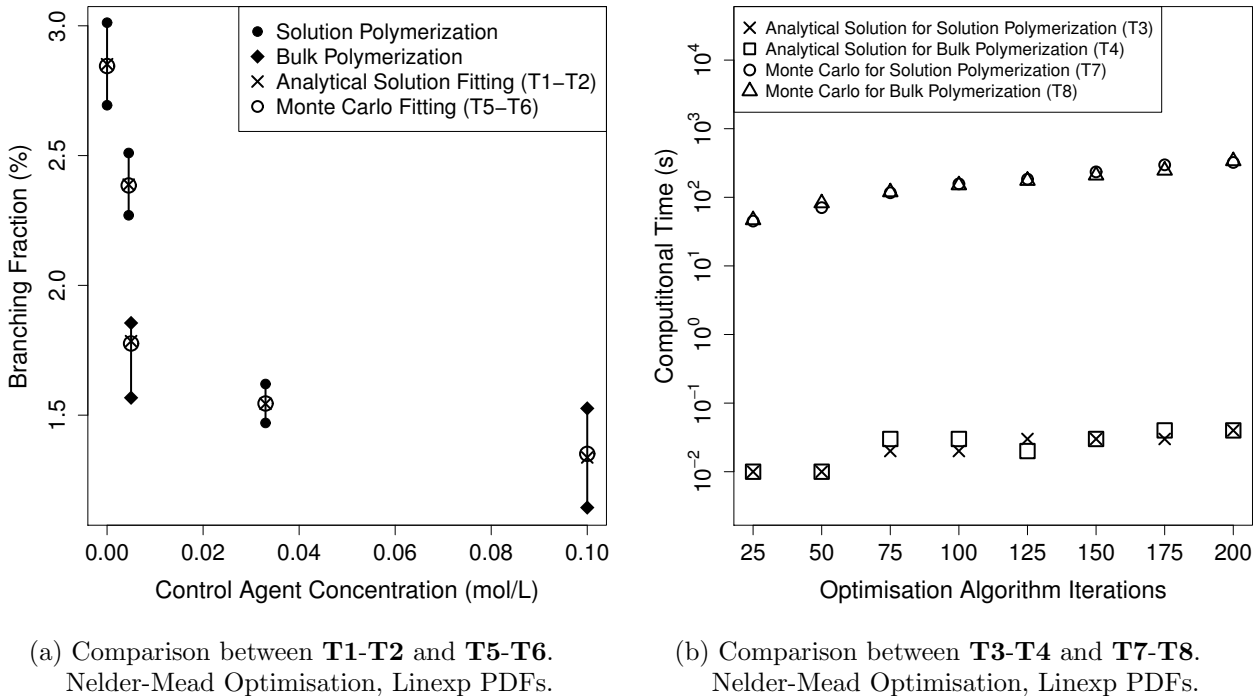
Figure 1.8: Comparison between the accuracy and efficiency of the Monte Carlo (MC) method and the Analytical Solution (AS) for matching the experimental branching fractions (Bulk and Solution Polymerization). The settings of the compared tests **T1**-**T8** are available in Table 1.1. The fitting achieved in Figure 1.8a corresponds to the parameters values given in Table 1.2. The computational times shown in Figure 1.8b are required by the optimisation algorithm performed with an increasing number of iterations. The AS speeds up the procedure by the factor of 10^4 compared with the MC method of the same level of accuracy.

Test	Polym.	Fitting	b_p	b_r	b_d	τ_p	τ_r	τ_d
T1	Solution	AS	1.74×10^{-1}	6.53	2.28×10^{-4}	9.1×10^{-1}	1.31	3.58×10^{-2}
T5	Solution	MC	1.74×10^{-1}	6.53	2.28×10^{-4}	9.1×10^{-1}	1.31	3.58×10^{-2}
T2	Bulk	AS	2.8×10^{-1}	1.58×10^{-1}	1.57×10^{-2}	8.53×10^{-1}	11.54	3.43×10^{-2}
T6	Bulk	MC	1.64×10^{-1}	1.40×10^{-1}	3.56×10^{-2}	9.16×10^{-1}	12.01	2.56×10^{-2}

Table 1.2: Optimised parameters obtained by the Analytical Solution fitting (AS) and the Monte Carlo fitting (MC) with the settings of tests **T1**-**T2** and **T5**-**T6** (Table 1.1). The computations have been performed using variables normalised over the propagation rate for a unitary concentration of monomers. The shown parameters correspond to unitary concentrations of monomers and control agent. Different concentrations are simulated by scaling such parameters, as proposed in the supporting information of [1].
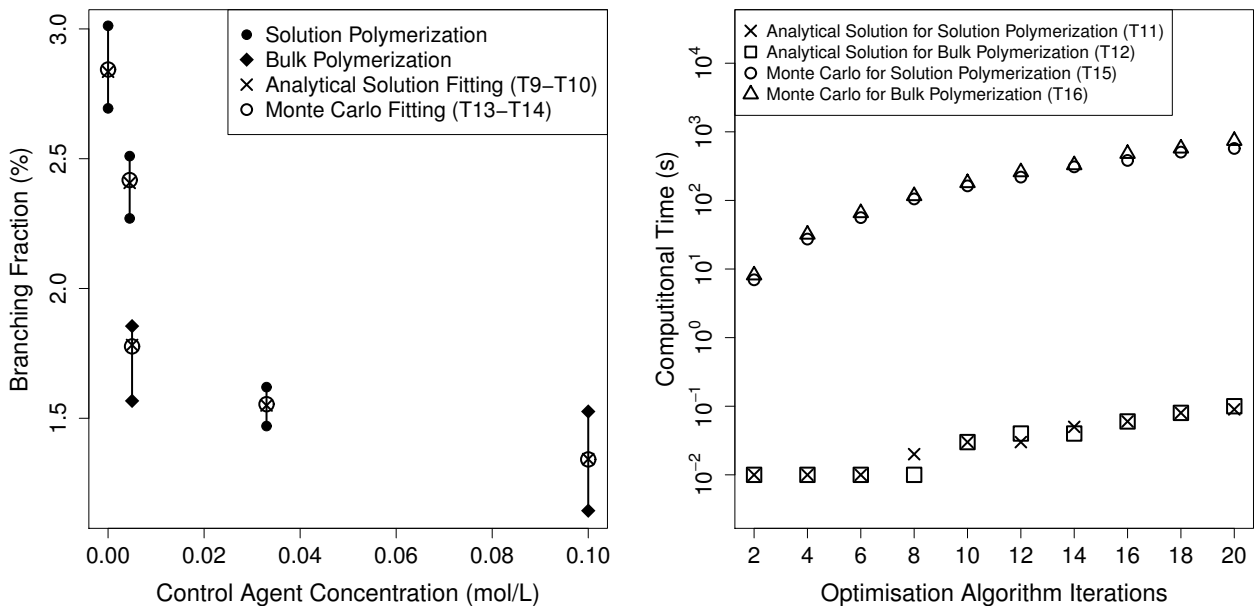
(a) Comparison between **T9-T10** and **T13-T14**. Genetic Optimisation, Exp and Linexp PDFs.

(b) Comparison between **T11-T12** and **T15-T16**. Genetic Optimisation, Exp and Linexp PDFs.

Figure 1.9: Comparison between the accuracy and efficiency of the Monte Carlo (MC) method and the Analytical Solution (AS) for matching the experimental branching fractions (Bulk and Solution Polymerization). The settings of the compared tests **T9-T16** are available in Table 1.1. The fitting achieved in Figure 1.9a corresponds to the parameters values given in Table 1.3. The computational times shown in Figure 1.9b are required by the optimisation algorithm performed with an increasing number of iterations. The AS speeds up the procedure by the factor of 10^4 compared with the MC method of the same level of accuracy.

Test	Polym.	Fitting	b_p	b_r	b_d	τ_p	τ_r	τ_d
T9	Solution	AS	-	5.94	-	1	5.97	4.78×10^{-2}
T10	Bulk	AS	-	3.82×10^{-1}	-	1	8.80	1.33

Table 1.3: Optimised parameters obtained by the Analytical Solution fitting (AS) with the settings of tests **T9-T10** (Table 1.1). The required times for backbiting (r) are distributed according to the Linexp PDF (1.83), while propagation (p) and deactivation (d) follow exponential distributions with expectations τ_p and τ_d respectively. The computations have been performed using variables normalised over the propagation rate for a unitary concentration of monomers. The shown parameters correspond to unitary concentrations of monomers and control agent. Different concentrations are simulated by scaling such parameters, as proposed in the supporting information of [1].

1.8 Conclusions & Discussion

Aiming to understand the reasons behind inconsistencies between the classical kinetics predictions and experimental evidences in Controlled Radical Polymerization (CRP), we develop the methodology which explains such inconsistencies and provides the accurate prediction of experimental observations. The key idea of this methodology is to assume non-Markovian kinetics and introduce delays among the competitive processes in CRP.

In Section 1.2, we propose (and review) the Stochastic Simulation Algorithm (SSA) as a possible framework for the modelling of the considered chemical reactions. SSA-based methods are ones of the most common approaches for studying stochastic processes. The non-Markovian kinetics and the delays can be accounted for in SSA either *explicitly* by introducing constraints, or *implicitly*, through a modification of inter-event time distributions. Thus, the SSA method is a good candidate for simulating the polymerization reactions with delays, being able to follow the kinetics of competitive processes and to introduce non-Markovian dynamics in the evolution of the system.

We show then in Section 1.3 that the introduction of delays significantly changes the statistics of the polymers chains growth. The equations and the corresponding properties derived for predicting the Markovian growth differ significantly from those describing a non-Markovian regime. The predicted time evolution of the mean lengths of the grown chain for different amounts of delay clearly demonstrate such differences. While in the Markovian case, the mean length is linear in time, the presence of delays may force the growth to show step-like variations at short times before settling into a linear behaviour later.

We also explain in Section 1.3 how to simulate the delayed growth, by formulating suitable implementations of the Stochastic Simulation Algorithm (SSA). A first methodology corresponds to the stochastic simulation of two Poisson processes. The delay is introduced by adding explicit constraints among the possible events. An equivalent approach simulates a single delayed process, with the delay built into the probability density function. We prove the equivalence between the two techniques. In addition, we propose an approximated methodology using linear exponential PDFs, and compare accuracy and efficiency of all three designed approaches. The approximated method enhances the simulation speed, especially for big sample sizes, still being able to reproduce the results of the other methods, guaranteeing a reasonable accuracy.

Since our objective is to explain the reduction in relative frequencies of propagations and backbitings experimentally observed in CRP, we concentrate on simulation of relative frequencies of constrained events. Following the SSA formulation of Section 1.3, we propose in Section 1.4 a Monte Carlo (MC) approach for the evaluation of relative frequencies of constrained events in stochastic processes. The technique can be applied to any system with well-posed constraints. The constraints among the possible events can be introduced either explicitly (Algorithm 1.3) or implicitly (Algorithm 1.4). Once the process properties are specified, it should be possible to show the equivalence between explicit and implicit approaches, by recovering the corresponding probability density functions. The implicit formulation can achieve better computational efficiency compared with the explicit method, especially for processes with a large number of events, provided computationally tractable PDFs.

Both proposed in Section 1.4 methodologies are Monte Carlo based, and thus inevitably computationally demanding. For this reason, we derive in Section 1.5 a significantly more effective analytical approach for computing the relative frequencies of constrained events in stochastic processes. The analytical formula is obtained in the same terms as the MC routine is defined, ensuring the equivalence of the two methodologies. The derivation is valid for any stochastic process with well-posed constraints among the possible events, making the method useful for various applications. The method is validated using the exactly solvable model introduced in Section 1.3 and then applied to the evaluation of branching fractions in CRP. With the derived approach we were also able to prove that memoryless models are not able to explain the experimentally observed reduction of the branching fraction, and thus only models with delays should be applied for study of CRP.

Section 1.6 presents an SSA-based method for simulating the CRP process in agreement with available experimental data. First, we discuss a choice of the delayed distributions to be used in the Monte Carlo method (Algorithm 1.5) and in the analytical approach (Algorithm 1.6) for the computation of the branching fraction in CRP. The linear exponential density (1.83) is chosen to account for the

required delays, as motivated in Section 1.3.5.4. The parameters of the given distributions are defined by Algorithm 1.7, maximising the fitting to available experimental data of the simulated branching fractions. Then, we formulate the SSA-based method for CRP modelling, which takes advantage of available experimental data. Algorithm 1.8 summarises the method, and uses the linear exponential densities (1.83), with the optimal parameters found by Algorithm 1.7. The algorithm can potentially provide a systematic study of all properties of the simulated system.

Finally, we investigate in Section 1.7 the performance and accuracy of the proposed algorithms, on the example of CRP of acrylic monomers. We demonstrate that the analytical approach (Algorithm 1.6) is free of statistical errors, and thus guarantees more accurate estimations, than those provided by a Monte Carlo simulation (Algorithm 1.5). In addition, the method is significantly (an order of the sample size $\geq 10^4$) faster than the Monte Carlo approach. As a result, we suggest the analytical approach as an efficient tool for finding, with Algorithm 1.7, the optimal set of parameters for inter-event distributions, to be further utilised in detailed Monte Carlo simulations (Algorithm 1.8). The performed tests show that the choice of optimisation algorithm is not important and the proposed methodologies work for several choices of the inter-event distributions.

In conclusion, we were able to explain the inconsistencies between the classical kinetics predictions and experimental evidences in CRP. Assuming non-Markovian kinetics and introducing delays among the competitive processes, we can provide the accurate prediction of such experimental observations. As shown in Section 1.7, the achieved fitting of experimental branching fractions validates our non-Markovian model for CRP of acrylic monomers.

The results derived in this Chapter have been published in:

1. N. Ballard, S. Rusconi, E. Akhmatskaya, D. Sokolovski, J. C. de la Cal, and J. M. Asua. Impact of Competitive Processes on Controlled Radical Polymerization. *Macromolecules*, 47(19):6580-6590, 2014.

2. D. Sokolovski, S. Rusconi, E. Akhmatskaya, and J. M. Asua. Non-markovian models of the growth of a polymer chain. *Proc. R. Soc. A*, 471(2180), 2015.

3. S. Rusconi, E. Akhmatskaya, D. Sokolovski, N. Ballard, and J. C. de la Cal. Relative frequencies of constrained events in stochastic processes: An analytical approach. *Phys. Rev. E*, 92:043306, 2015.

Chapter 2

Population Balance Approach for Predicting Polymer Particles Morphology

2.1 Motivation

2.1.1 Multi-Phase Polymer Particle Morphology

As a result of performance superiority of *multi-phase* particles over particles with *uniform* compositions, assembling the composite (multi-phase) polymer particles is of great practical interest in many important applications, such as, coatings, additives for constructing materials, cosmetics, diagnostic tests and drug delivery. Properties of a multi-phase polymer particle strongly depend on the particle *morphology*, and thus the control of particle morphology is a key factor for success in producing high quality polymer materials. The particle morphology is defined by the pattern formed by the phase-separated domains comprising the polymer particle [37]. Examples of particle morphologies are shown in Figure 2.1.

The synthesis of new morphologies is time and resources consuming, as it largely relies on heuristic knowledge. Thus, the predictive modelling of such processes is of great interest to practitioners. No general methodology is currently available for predicting the particles morphology in multiphase systems. Several modelling approaches describing the dynamic development of *a single particle* morphology in 2- and 3- phase composite systems have been suggested in the last few years [38, 39, 40, 41, 42, 43]. The most recent ones, [41, 42, 43], offer, for the first time, an accurate prediction of the morphology dynamics of a single particle in the composite waterborne systems, including the systems with in situ formation of graft copolymer [42]. In these studies, the proposed models utilise the stochastic dynamics (SD), and account for the effect of phase compatibility and internal viscosity of the particles. The deficit of these models, however, that they provide a detailed description of the morphology of a single particle, which is only a partial view of a real system. Better insight would be obtained by applying such methodologies to simulation of at least few particles but ideally of millions particles. However, a single particle simulations are computationally very demanding even with the use of High Performance Computers and just more realistic simulations of multiple particles do not look feasible with the suggested models.

In this Chapter we propose an alternative approach for modelling particles morphology, which calculates the *distribution* of morphologies for the whole *population* of polymer particles taking into account the relevant kinetic and thermodynamic effects.

2.1.2 Reaction Mechanisms of Particles Morphologies Development

From now on we focus on two-phase polymer systems, for which the formation of particles morphologies are better studied and understood than for any other multi-phase polymer [45].

The reaction mechanisms driving the development of two-phase polymer particles morphology has been proposed in [45] and can be described with help of the illustrative sketch presented in Figure 2.2
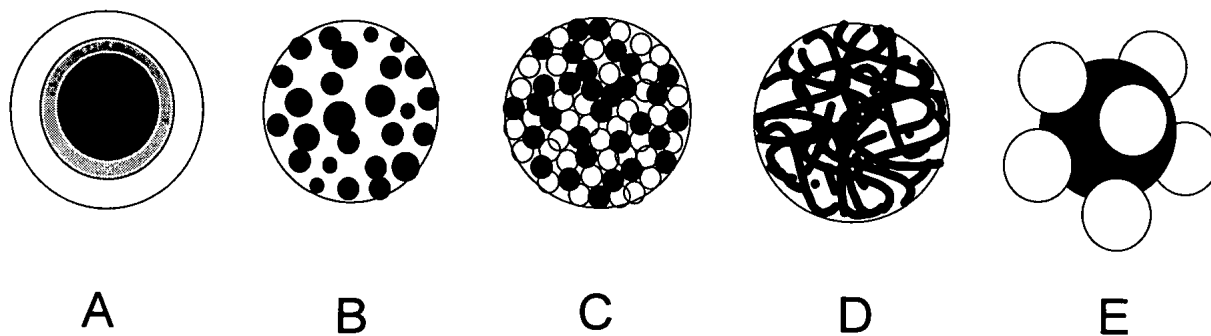
Figure 2.1: Examples of particle morphologies [44]: (A) core-shell with transition layer, (B) "raspberry" morphology, (C) "salt-and-pepper" morphology, (D) interpenetrating network, (E) lobed particle. The white and black areas indicate the phase-separated domains comprising the polymer particle.

as follows.

Let N_p be a number of particles placed in the polymerization reactor. At the beginning of the process, the particles are only made by the pre-formed Polymer 1, swollen with Monomer 2. The amount of Polymer 1 is equally distributed among the particulate matter and it does not change with time. The constant amount of Polymer 1 belongs to the so-called *matrix* phase during the full evolution of the process. Monomer 2 gradually polymerises into Polymer 2 chains, as the reaction is evolving (Figure 2.2 (a)). The Polymer 2 chains form agglomerates belonging to the matrix phase, until they reach the critical size $v_c > 0$ to change their phase and to nucleate into *clusters* (Figure 2.2 (b)). As a result, the matrix phase contains the total amount of Polymer 1, a part of the Monomer 2 and the Polymer 2 agglomerates with volumes smaller than v_c. On the other hand, the clusters phase holds the remaining amount of Monomer 2 and the Polymer 2 agglomerates of sizes exceeding v_c. The amount of Monomer 2 is uniformly distributed between the matrix and clusters phases. Given such compositions, the *unswollen* volume $\tilde{v}$ of any cluster is defined as the volume of Polymer 2 belonging to the considered cluster, without accounting for the amount of swelling Monomer 2. The clusters can increase their unswollen volume $\tilde{v}$ (Figure 2.2 (c)) because of (*i*) the polymerization of Monomer 2 with already clustered Polymer 2 chains and (*ii*) the diffusion of Polymer 2 chains from the matrix to the clusters phase. Two clusters can coagulate building an aggregated cluster with a size equal to the sum of volumes of the aggregating clusters (Figure 2.2 (d)). The clusters can be found in two positions: *non-equilibrium* and *equilibrium*. The equilibrium clusters have already reached the equilibrium position. The non-equilibrium clusters can migrate to the equilibrium position and become irreversibly equilibrium clusters (Figure 2.2 (e)). In summary, the clusters dynamics is driven by (*i*) the nucleation of non-equilibrium clusters from the matrix phase, (*ii*) the growth of the unswollen volume, (*iii*) the aggregation of clusters and (*iv*) the migration of clusters from non-equilibrium to equilibrium position. The different sizes and the distribution of the produced polymers clusters compose a particles morphology.

Our goal is to develop an efficient population-based method for predicting the Dynamic Development of Particles Morphology (DDPM) described above and provide computationally tractable algorithms for solving such a model. The speed of proposed predictive simulation techniques should be high enough for enabling on-the-fly recommendations for technological conditions in the synthesis of new multi-phase morphologies. To follow this strategy, we will derive a systematic modelling approach for the prediction of the kinetics of the expected size distribution of the polymer clusters, and thus the particles morphology. The large scale resolution of such approach should permit practical and efficient simulations of systems comprising many particles.

Four different numerical algorithms for solution of the proposed model will be then developed, implemented for particular choices of reaction rates and compared in accuracy and performance.

The chapter is organised as follows. Section 2.2 formulates the population-based model for predicting DDPM. The integration methods are presented in Section 2.3 and tested in Section 2.4. Conclusions and discussion are provided in Section 2.5. Potentially promising future developments are discussed
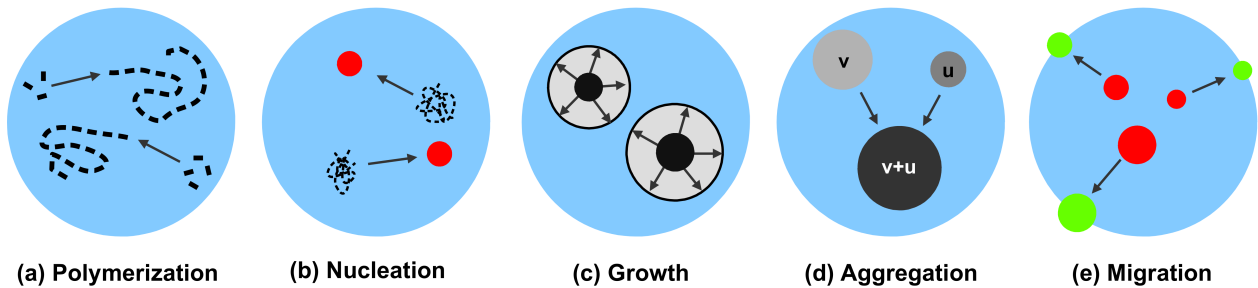
Figure 2.2: Reaction mechanisms driving the evolution of the polymer clusters composing the morphology of a single polymer particle [●]: (a) the *polymerization* of the Monomer 2 [▪] into the Polymer 2 chains [▪▪▪], (b) the *nucleation* of the Polymer 2 agglomerates [▪▪▪] into the non-equilibrium clusters [●], (c) the *growth* of the clusters volume [●], (d) the *aggregation* of the clusters with sizes v and u, (e) the *migration* of the non-equilibrium clusters [●] to the equilibrium position [●].

in Section 2.6.

2.2 Population Balance Equations Model for Development of Particles Morphology: Formulation

The aim of this section is to formulate a Population Balance Equations (PBE) [46] model for the size distribution of the polymer clusters, in order to describe the Dynamic Development of Particles Morphology (DDPM).

Section 2.2.1 derives a PBE model for the prediction of DDPM. Section 2.2.2 presents the novel procedure for scaling a PBE model to a dimensionless and computationally tractable model. Section 2.2.3 provides the analysis of the developed dimensionless PBE model.

2.2.1 PBE Model: Derivation

Aiming to derive a PBE model for predicting DDPM, we focus on the distributions $\tilde{m}(\tilde{v}, \tilde{t})$ [L^{-1}] and $\tilde{w}(\tilde{v}, \tilde{t})$ [L^{-1}] of the *unswollen volume* $\tilde{v}$ [L] at time $\tilde{t}$ [s] of non-equilibrium and equilibrium clusters respectively. The volume $\tilde{v}$ is measured in Litres [L] and the elapsed time $\tilde{t}$ in seconds [s]. For any fixed time $\tilde{t}$, the expected number of non-equilibrium and equilibrium clusters with unswollen volume $\tilde{v}$ in the interval $[\alpha, \beta]$ is provided by

$$\int_\alpha^\beta \tilde{m}(\tilde{v}, \tilde{t}) \, d\tilde{v} \quad \text{and} \quad \int_\alpha^\beta \tilde{w}(\tilde{v}, \tilde{t}) \, d\tilde{v} \tag{2.1}$$

respectively. The distributions $\tilde{m}(\tilde{v}, \tilde{t})$ and $\tilde{w}(\tilde{v}, \tilde{t})$ are not normalised to 1, but their zero-order moment corresponds to the expected total number of clusters, for any given time $\tilde{t}$. Our objective is to derive the evolution equations for the variables $\tilde{m}(\tilde{v}, \tilde{t})$ and $\tilde{w}(\tilde{v}, \tilde{t})$ and thus the PBE model for DDPM.

The following derivation stands for any set of particles involved in the dynamical mechanisms driving the evolution of the polymer clusters, as stated in Section 2.1.2 and illustrated in Figure 2.2. Such mechanisms include aggregation, growth, nucleation and migration. The non-equilibrium and equilibrium clusters can be viewed as distinct sets of particles belonging to separated phases. In fact, the migration of the non-equilibrium clusters to the equilibrium position can be interpreted as an irreversible transition of a phase. For the sake of generality, we will refer to the clusters as *particles*, the unswollen volume $\tilde{v}$ will be denoted as *size* (or simply volume) and we will keep the *phase transition* nomenclature for the migration reaction.

Since the derivation of PBE for equilibrium and non-equilibrium clusters follows the same route, we limit our discussion to study of non-equilibrium clusters and provide the final results for equilibrium clusters when necessary.

We consider a set of particles, whose size distribution $\tilde{m}(\tilde{v}, \tilde{t})$ [L^{-1}] is defined as (2.1). The particles dynamics and the time evolution of $\tilde{m}(\tilde{v}, \tilde{t})$ are driven by **aggregation**, **growth**, **nucleation** and dissipative **transition of phase**. First, we introduce the mathematical formulation of the rate functions for each of those processes, i.e. $\tilde{a}(\tilde{v}, \tilde{u}, \tilde{t})$ for aggregation, $\tilde{g}(\tilde{v}, \tilde{t})$ for growth, $\tilde{n}(\tilde{v}, \tilde{t})$ for nucleation and $\tilde{\mu}(\tilde{v}, \tilde{t})$ for phase transition. Then, the evolution equation for $\tilde{m}(\tilde{v}, \tilde{t})$ will be obtained by means of a balance equation accounting for all the introduced variables.

The aggregation rate $\tilde{a}(\tilde{v}, \tilde{u}, \tilde{t})$ [s^{-1}] expresses the expected frequency of coagulations between particles with volumes $\tilde{v}$ and $\tilde{u}$ at time $\tilde{t}$. The reasonable assumption is that it corresponds to a non-negative symmetric function:

$$\tilde{a}(\tilde{v}, \tilde{u}, \tilde{t}) = \tilde{a}(\tilde{u}, \tilde{v}, \tilde{t}) \geq 0, \quad \forall \tilde{v}, \tilde{u}, \tilde{t} \geq 0. \tag{2.2}$$

The assumption (2.2) means that two aggregating particles possess the same aggregation frequency, no matter the order in which they are considered. The symmetric shape of the rate $\tilde{a}$ prevents non-physical behaviours of the zero- and first-order moments of the density $\tilde{m}(\tilde{v}, \tilde{t})$, as explained in Section 2.2.3.2.

The growth rate $\tilde{g}(\tilde{v}, \tilde{t})$ [L s^{-1}] corresponds to the expected variation of volume $\tilde{v}$ per unit of time:

$$\frac{d\tilde{v}}{d\tilde{t}} = \tilde{g}(\tilde{v}, \tilde{t}), \quad [\text{L s}^{-1}]. \tag{2.3}$$

The nucleation rate $\tilde{n}(\tilde{v}, \tilde{t})$ [L^{-1} s^{-1}] describes the volume distribution of nucleating particles. The particles nucleation mechanism corresponds to the birth of new particles from the reaction solvent. Such new particles give rise to the further dynamical processes. Given any fixed time $\tilde{t} \geq 0$ and the non-negative function $\tilde{n}(\tilde{v}, \tilde{t})$, the expected number of particles, created per unit of time, with volume $\tilde{v} \in [\alpha, \beta]$, can be computed as:

$$\int_{\alpha}^{\beta} \tilde{n}(\tilde{v}, \tilde{t}) \, d\tilde{v}, \quad [\text{s}^{-1}]. \tag{2.4}$$

The phase transition rate $\tilde{\mu}(\tilde{v}, \tilde{t})$ [s^{-1}] provides the expected proportion of particles, with volume $\tilde{v}$ at time $\tilde{t}$, changing their phase per unit of time. Given any fixed time $\tilde{t} \geq 0$ and the non-negative function $\tilde{\mu}(\tilde{v}, \tilde{t})$, the expected number of particles, with volume $\tilde{v} \in [\alpha, \beta]$, moving to a different phase per unit of time, is given by:

$$\int_{\alpha}^{\beta} \tilde{\mu}(\tilde{v}, \tilde{t}) \, \tilde{m}(\tilde{v}, \tilde{t}) \, d\tilde{v}, \quad [\text{s}^{-1}]. \tag{2.5}$$

All the variables defined above will be used for derivation of (2.14).

Derivation of Balance Equation. We consider the expected number of particles with volume in the infinitesimal interval $[\tilde{v}, \tilde{v} + d\tilde{v}]$, $\forall \tilde{v} \in \mathbb{R}^+$ and $0 < d\tilde{v} \ll 1$. Its variation during the infinitesimal time interval $[\tilde{t}, \tilde{t} + d\tilde{t}]$, $\forall \tilde{t} \in \mathbb{R}^+$ and $0 < d\tilde{t} \ll 1$, is given by:

$$\int_{\tilde{v}}^{\tilde{v}+d\tilde{v}} \tilde{m}(\tilde{\nu}, \tilde{t} + d\tilde{t}) \, d\tilde{\nu} - \int_{\tilde{v}}^{\tilde{v}+d\tilde{v}} \tilde{m}(\tilde{\nu}, \tilde{t}) \, d\tilde{\nu}, \quad \forall \tilde{v}, \tilde{t} \in \mathbb{R}^+. \tag{2.6}$$

Following [46], we write down a balance equation for the considered number of particles by equating the expression (2.6) to the sum of the variations of the expected number of particles, associated with the processes of aggregation, growth, nucleation and phase transition. The PBE for $\tilde{m}(\tilde{v}, \tilde{t})$ is then obtained by dividing the derived balance equation by $d\tilde{t} \, d\tilde{v} > 0$ and by taking the limit for $d\tilde{t} \to 0$ and $d\tilde{v} \to 0$.

Below, we discuss the variation of the particles number associated with each process separately: particles formation and consumption by aggregation, particles volumetric growth, particles nucleation and particles transition of phase.

Particles Formation by Aggregation. Given any time $\tilde{s} \in \mathbb{R}^+$, the distribution of the particles with volume $\tilde{\nu} \in \mathbb{R}^+$, created per unit of time by the aggregation of two particles with volumes $\tilde{u} \in (0, \tilde{\nu})$ and $\tilde{\nu} - \tilde{u} \in (0, \tilde{\nu})$ can be computed as:

$$\frac{1}{2} \int_0^{\tilde{\nu}} \tilde{a}(\tilde{\nu} - \tilde{u}, \tilde{u}, \tilde{s}) \, \tilde{m}(\tilde{\nu} - \tilde{u}, \tilde{s}) \, \tilde{m}(\tilde{u}, \tilde{s}) \, d\tilde{u} \quad [\mathrm{L}^{-1} \, \mathrm{s}^{-1}], \quad \forall \tilde{\nu}, \tilde{s} \in \mathbb{R}^+. \tag{2.7}$$

Since the resulting particle volume $\tilde{\nu}$ is the sum of the aggregating particles volumes $\tilde{u}$ and $\tilde{\nu} - \tilde{u}$, its distribution (2.7) corresponds to the convolution of the distribution $\tilde{m}$ with itself, weighted by the kernel $\tilde{a}$ to account for the particles aggregation frequency. The pre-factor $1/2$ is needed to avoid double counting of pairs of aggregating particles. As a result, the variation of the expected number of particles, with volume in $[\tilde{v}, \tilde{v} + d\tilde{v}]$, during the time interval $[\tilde{t}, \tilde{t} + d\tilde{t}]$, provided by the formation of the aggregated particles, can be computed as:

$$\int_{\tilde{t}}^{\tilde{t}+d\tilde{t}} \left[\int_{\tilde{v}}^{\tilde{v}+d\tilde{v}} \left[\frac{1}{2} \int_0^{\tilde{\nu}} \tilde{a}(\tilde{\nu} - \tilde{u}, \tilde{u}, \tilde{s}) \, \tilde{m}(\tilde{\nu} - \tilde{u}, \tilde{s}) \, \tilde{m}(\tilde{u}, \tilde{s}) \, d\tilde{u} \right] d\tilde{\nu} \right] d\tilde{s}, \quad \forall \tilde{v}, \tilde{t} \in \mathbb{R}^+. \tag{2.8}$$

Particles Consumption by Aggregation. Given any time $\tilde{s} \in \mathbb{R}^+$, the distribution of the particles with volume $\tilde{\nu} \in \mathbb{R}^+$, aggregating per unit of time with any other possible particle can be expressed as:

$$\tilde{m}(\tilde{\nu}, \tilde{s}) \int_0^{+\infty} \tilde{a}(\tilde{\nu}, \tilde{u}, \tilde{s}) \, \tilde{m}(\tilde{u}, \tilde{s}) \, d\tilde{u} \quad [\mathrm{L}^{-1} \, \mathrm{s}^{-1}], \quad \forall \tilde{\nu}, \tilde{s} \in \mathbb{R}^+. \tag{2.9}$$

The product of the densities $\tilde{m}(\tilde{\nu}, \tilde{s})$ and $\tilde{m}(\tilde{u}, \tilde{s})$ provides the joint distribution of the pairs of particles with volumes $\tilde{\nu}$ and $\tilde{u}$. The kernel $\tilde{a}$ accounts for the particles aggregation frequency. The resulting term is integrated with respect to $\tilde{u} \in \mathbb{R}^+$, to allow any particle to aggregate. As a result, the quantity

$$-\int_{\tilde{t}}^{\tilde{t}+d\tilde{t}} \left[\int_{\tilde{v}}^{\tilde{v}+d\tilde{v}} \left[\tilde{m}(\tilde{\nu}, \tilde{s}) \int_0^{+\infty} \tilde{a}(\tilde{\nu}, \tilde{u}, \tilde{s}) \, \tilde{m}(\tilde{u}, \tilde{s}) \, d\tilde{u} \right] d\tilde{\nu} \right] d\tilde{s}, \quad \forall \tilde{v}, \tilde{t} \in \mathbb{R}^+, \tag{2.10}$$

provides the variation of the expected number of particles, with volume in $[\tilde{v}, \tilde{v} + d\tilde{v}]$, during the time interval $[\tilde{t}, \tilde{t} + d\tilde{t}]$, caused by the departure of the aggregating particles.

Particles Volumetric Growth. Given the growth velocity $\tilde{g}(\tilde{v}, \tilde{s})$ $[\mathrm{L} \, \mathrm{s}^{-1}]$ and the particles density $\tilde{m}(\tilde{v}, \tilde{s})$ $[\mathrm{L}^{-1}]$, the product $\tilde{g}(\tilde{v}, \tilde{s}) \, \tilde{m}(\tilde{v}, \tilde{s})$ $[\mathrm{s}^{-1}]$ corresponds to the particles growth flux: the expected number of particles, with volume $\tilde{v}$ at time $\tilde{s}$, flowing per unit of time, driven by the growth mechanism. As a result, the net variation of the expected number of particles, with volume in $[\tilde{v}, \tilde{v} + d\tilde{v}]$, during the time interval $[\tilde{t}, \tilde{t} + d\tilde{t}]$, can be computed as the difference of the particles fluxes, evaluated at the bounds of the interval $[\tilde{v}, \tilde{v} + d\tilde{v}]$ and integrated over the time interval $[\tilde{t}, \tilde{t} + d\tilde{t}]$:

$$\int_{\tilde{t}}^{\tilde{t}+d\tilde{t}} \tilde{g}(\tilde{v}, \tilde{s}) \, \tilde{m}(\tilde{v}, \tilde{s}) \, d\tilde{s} - \int_{\tilde{t}}^{\tilde{t}+d\tilde{t}} \tilde{g}(\tilde{v} + d\tilde{v}, \tilde{s}) \, \tilde{m}(\tilde{v} + d\tilde{v}, \tilde{s}) \, d\tilde{s}, \quad \forall \tilde{v}, \tilde{t} \in \mathbb{R}^+. \tag{2.11}$$

The sign of the particles flux $\tilde{g}(\tilde{v}, \tilde{s}) \, \tilde{m}(\tilde{v}, \tilde{s})$ must be in agreement with the sign of the growth velocity $\tilde{g}(\tilde{v}, \tilde{s})$, because it accounts for the arrival of new particles, in the case of $\tilde{g}(\tilde{v}, \tilde{s}) > 0$, and the departure of particles, in the case of $\tilde{g}(\tilde{v}, \tilde{s}) < 0$. On the other hand, the flux $\tilde{g}(\tilde{v} + d\tilde{v}, \tilde{s}) \, \tilde{m}(\tilde{v} + d\tilde{v}, \tilde{s})$ and the velocity $\tilde{g}(\tilde{v}+d\tilde{v}, \tilde{s})$ must have an opposite sign, because of the departure of particles, if $\tilde{g}(\tilde{v}+d\tilde{v}, \tilde{s}) > 0$, and the arrival of new particles, if $\tilde{g}(\tilde{v} + d\tilde{v}, \tilde{s}) < 0$.

Particles Nucleation. Using the definition (2.4), the variation of the expected number of particles, with volume in $[\tilde{v}, \tilde{v} + d\tilde{v}]$, during the time interval $[\tilde{t}, \tilde{t} + d\tilde{t}]$, caused by the nucleation process can be computed as:

$$\int_{\tilde{t}}^{\tilde{t}+d\tilde{t}} \left[\int_{\tilde{v}}^{\tilde{v}+d\tilde{v}} \tilde{n}(\tilde{\nu}, \tilde{s}) \, d\tilde{\nu} \right] d\tilde{s}, \quad \forall \tilde{v}, \tilde{t} \in \mathbb{R}^+. \tag{2.12}$$

Since the function $\tilde{n}$ is always non-negative, the contribution of (2.12) to the variation (2.6) is non-negative as well. In other words, the nucleation process is a source mechanism for the dynamics of the unknown distribution $\tilde{m}$.

Particles Phase Transition. With the help of (2.5), the variation of the expected number of particles, with volume in $[\tilde{v}, \tilde{v} + d\tilde{v}]$, during the time interval $[\tilde{t}, \tilde{t} + d\tilde{t}]$, caused by the phase transition mechanism can be obtained as:

$$-\int_{\tilde{t}}^{\tilde{t}+d\tilde{t}} \left[\int_{\tilde{v}}^{\tilde{v}+d\tilde{v}} \tilde{\mu}(\tilde{\nu}, \tilde{s}) \, \tilde{m}(\tilde{\nu}, \tilde{s}) \, d\tilde{\nu} \right] d\tilde{s}, \quad \forall \tilde{v}, \tilde{t} \in \mathbb{R}^+. \tag{2.13}$$

The quantity (2.13) cannot be positive because the phase transition process decreases the number of particles in the system, being a dissipative mechanism for dynamics of unknown distribution $\tilde{m}$.

The balance equation for the expected number of particles with volume in the infinitesimal interval $[\tilde{v}, \tilde{v} + d\tilde{v}]$, during the infinitesimal time interval $[\tilde{t}, \tilde{t} + d\tilde{t}]$, now can be obtained by equating (2.6) to the sum of the quantities (2.8), (2.10), (2.11), (2.12) and (2.13). Under regularity conditions, the Mean Value Theorem for definite integrals along with the definition of partial derivatives ensure that the limit for $d\tilde{t} \to 0$ and $d\tilde{v} \to 0$ of the derived balance equation, divided by $d\tilde{t} \, d\tilde{v} > 0$, is given by:

$$\frac{\partial \tilde{m}(\tilde{v}, \tilde{t})}{\partial \tilde{t}} = -\underbrace{\frac{\partial(\, \tilde{g}(\tilde{v}, \tilde{t}) \, \tilde{m}(\tilde{v}, \tilde{t})\,)}{\partial \tilde{v}}}_{\text{Transport}} + \underbrace{\tilde{n}(\tilde{v}, \tilde{t})}_{\text{Source}} - \underbrace{\tilde{\mu}(\tilde{v}, \tilde{t}) \, \tilde{m}(\tilde{v}, \tilde{t})}_{\text{Dissipation}} - \underbrace{\tilde{m}(\tilde{v}, \tilde{t}) \int_0^{+\infty} \tilde{a}(\tilde{v}, \tilde{u}, \tilde{t}) \, \tilde{m}(\tilde{u}, \tilde{t}) \, d\tilde{u}}_{\text{Integral Term}}$$

$$+ \underbrace{\frac{1}{2} \int_0^{\tilde{v}} \tilde{a}(\tilde{v} - \tilde{u}, \tilde{u}, \tilde{t}) \, \tilde{m}(\tilde{v} - \tilde{u}, \tilde{t}) \, \tilde{m}(\tilde{u}, \tilde{t}) \, d\tilde{u}}_{\text{Integral Term}}, \quad \forall \tilde{v}, \tilde{t} \in \mathbb{R}^+. \tag{2.14}$$

We have derived the PBE (2.14) for the size distribution $\tilde{m}(\tilde{v}, \tilde{t})$, whose evolution is driven by particles aggregation, growth, nucleation and phase transition. Equation (2.14) can be understood as a non-linear partial integro-differential equation with transport, source, dissipation and integral terms. The particles growth drives the transport, shifting the volume distribution $\tilde{m}(\tilde{v}, \tilde{t})$ from left to right. Nucleation provides the non-negative source term, with the creation of the new particles. The dissipative term accounts for the particles phase transition and the corresponding loss of particles. The integral terms correspond to the Smoluchowski coagulation equation [47].

The initial condition for (2.14) is provided by a non-negative distribution $\tilde{\omega}_0(\tilde{v})$:

$$\tilde{m}(\tilde{v}, 0) = \tilde{\omega}_0(\tilde{v}) \geq 0 \quad [\mathrm{L}^{-1}], \quad \forall \tilde{v} \in \mathbb{R}^+. \tag{2.15}$$

The boundary condition is specified by imposing the particles growth flux to be equal to zero, if evaluated at $\tilde{v} = 0$:

$$\tilde{g}(0, \tilde{t}) \, \tilde{m}(0, \tilde{t}) = 0 \quad [\mathrm{s}^{-1}], \quad \forall \tilde{t} \in \mathbb{R}^+. \tag{2.16}$$

Such a choice assures non-negative values of the particles size $\tilde{v}$.

Dynamic Development of Particles Morphology (DDPM). The PBE model (2.14)-(2.16) allows us to describe the volume distribution $\tilde{m}(\tilde{v}, \tilde{t})$ (2.1) of the *non-equilibrium clusters*, composing DDPM introduced in Section 2.1.2. Similarly, it can be shown that the volume distribution $\tilde{w}(\tilde{v}, \tilde{t})$ of the *equilibrium clusters* is the solution of the PBE:

$$\frac{\partial \tilde{w}(\tilde{v}, \tilde{t})}{\partial \tilde{t}} = -\underbrace{\frac{\partial(\tilde{g}(\tilde{v}, \tilde{t})\, \tilde{w}(\tilde{v}, \tilde{t}))}{\partial \tilde{v}}}_{\text{Transport}} + \underbrace{\tilde{\mu}(\tilde{v}, \tilde{t})\, \tilde{m}(\tilde{v}, \tilde{t})}_{\text{Source}} - \underbrace{\tilde{w}(\tilde{v}, \tilde{t}) \int_0^{+\infty} \tilde{a}(\tilde{v}, \tilde{u}, \tilde{t})\, \tilde{w}(\tilde{u}, \tilde{t})\, d\tilde{u}}_{\text{Integral Term}}$$

$$+ \underbrace{\frac{1}{2} \int_0^{\tilde{v}} \tilde{a}(\tilde{v} - \tilde{u}, \tilde{u}, \tilde{t})\, \tilde{w}(\tilde{v} - \tilde{u}, \tilde{t})\, \tilde{w}(\tilde{u}, \tilde{t})\, d\tilde{u}}_{\text{Integral Term}}, \quad \forall \tilde{v}, \tilde{t} \in \mathbb{R}^+. \tag{2.17}$$

Equations (2.14) and (2.17) possess a similar structure. We remark the difference in the source terms between (2.14) and (2.17), which is in agreement with the reaction mechanisms illustrated in Section 2.1.2. The source term in (2.14) is formed by the nucleation rate $\tilde{n}(\tilde{v}, \tilde{t})$ for non-equilibrium clusters, while in (2.17) it is given by the migration rate $\tilde{\mu}(\tilde{v}, \tilde{t})\, \tilde{m}(\tilde{v}, \tilde{t})$ of the non-equilibrium clusters. We note that the equilibrium clusters are not affected by transitions of phase and thus (2.17) does not account for the corresponding term.

Since no clusters are formed at the beginning of the polymerization, the initial conditions are zero everywhere, i.e. $\tilde{m}(\tilde{v}, 0) = \tilde{w}(\tilde{v}, 0) = 0$, $\forall \tilde{v} \in \mathbb{R}^+$. The boundary condition for (2.17) is analogous to (2.16), i.e. $\tilde{g}(0, \tilde{t})\, \tilde{w}(0, \tilde{t}) = 0$, $\forall \tilde{t} \in \mathbb{R}^+$.

The rate functions appearing in (2.14) and (2.17) strongly depend on the simulated system. In Appendix 2.A, we derive the chemical rates of the processes involved in the development of *latex* particles morphology.

Models Under Study. Aimed to search for the most efficient approach for solving the derived PBE, we propose three models which use less advanced chemical rates compared with the latex model presented in Appendix 2.A. Still, they can be viewed as coarse approximations of the DDPM process. In particular, the reaction mechanisms, discussed in Section 2.1.2 and Appendix 2.A, are mimicked in the simple models, as specified below.

(*i*) **Model I**. The reaction is simultaneously driven by aggregation, growth, nucleation and phase transition. The PBE model (2.14)-(2.16) is considered with the rate functions:

$$\tilde{a}(\tilde{v}, \tilde{u}, \tilde{t}) = \tilde{a}_0, \quad \tilde{g}(\tilde{v}, \tilde{t}) = \tilde{g}_0, \quad \tilde{n}(\tilde{v}, \tilde{t}) = \tilde{n}_0\, \tilde{\delta}(\tilde{v} - v_c), \quad \tilde{\mu}(\tilde{v}, \tilde{t}) = \tilde{\mu}_0, \tag{2.18}$$

where $\tilde{\delta}(\tilde{x})$ [L^{-1}] is the Dirac delta function. The positive constants $\tilde{a}_0$ [s^{-1}], $\tilde{g}_0$ [L s^{-1}] and $\tilde{\mu}_0$ [s^{-1}] express the particles uniform tendency to aggregate, to increase their size and to migrate to other phases respectively. On the other hand, the rate $\tilde{n}(\tilde{v}, \tilde{t})$ in (2.18) models the constant frequency $\tilde{n}_0 > 0$ [s^{-1}] of the particles nucleation at the critical size $v_c > 0$ [L].

Similar models have been studied previously [48, 49], but in contrast to Model I, none of these models simultaneously includes all the considered here dynamical processes. Still, the constant values of the rate functions and required additional hypothesis in Model I lead to a limited description of the reaction physics, as will be shown further.

(*ii*) **Model II**. We consider the reaction driven by aggregation, growth and phase transition. The nucleation process is neglected and the rate functions in (2.14)-(2.16) are chosen as:

$$\tilde{a}(\tilde{v}, \tilde{u}, \tilde{t}) = \tilde{a}_0, \quad \tilde{g}(\tilde{v}, \tilde{t}) = \tilde{g}_0\, \tilde{v}, \quad \tilde{n}(\tilde{v}, \tilde{t}) = 0, \quad \tilde{\mu}(\tilde{v}, \tilde{t}) = \tilde{\mu}_0. \tag{2.19}$$

The positive constants $\tilde{a}_0$ [s^{-1}] and $\tilde{\mu}_0$ [s^{-1}] express the particles uniform tendency to aggregate and to change their phases respectively. The rate $\tilde{g}(\tilde{v}, \tilde{t})$ is assumed directly proportional to $\tilde{v}$, with $\tilde{g}_0 > 0$ [L s^{-1}].

Model II corresponds to the study case 3 in [48] and the study case 5 in [49], with the addition of the phase transition process.

(*iii*) **Model III**. The processes of the particles aggregation, growth and phase transition are considered, whereas the nucleation mechanism is neglected. The uniform tendencies of the particles to aggregate, to increase their size and to change their phase are described by the corresponding rate functions in (2.14)-(2.16):

$$\tilde{a}(\tilde{v}, \tilde{u}, \tilde{t}) = \tilde{a}_0, \quad \tilde{g}(\tilde{v}, \tilde{t}) = \tilde{g}_0, \quad \tilde{n}(\tilde{v}, \tilde{t}) = 0, \quad \tilde{\mu}(\tilde{v}, \tilde{t}) = \tilde{\mu}_0, \tag{2.20}$$

where $\tilde{a}_0$ [s^{-1}], $\tilde{g}_0$ [L s^{-1}] and $\tilde{\mu}_0$ [s^{-1}] are positive constants characterising the system behaviour. Model III corresponds to the study case 1 in [48] and [49], with the addition of the growth and phase transition processes.

2.2.2 Dimensionless Model: Optimal Scaling

Experimental values of the parameters in a PBE model may lead to computationally intractable orders of magnitude of the involved variables, e.g. $\tilde{v} \propto \nu_0 \approx 10^{-21}$ L and $\tilde{m} \propto m_0 \approx 10^{+36}$ L^{-1}, as shown in Table 2.1. Here we propose the novel scaling procedure which allows us to address such a problem. Our aim is to derive from (2.14)-(2.17) the corresponding dimensionless model with computationally tractable orders of magnitude for parameters and involved variables.
Let us consider the equation

$$\tilde{f}\left(\tilde{x}_1, .., \tilde{x}_{N_x}; \tilde{p}_1, .., \tilde{p}_{N_p}\right) = 0, \tag{2.21}$$

where $\tilde{x}_1, .., \tilde{x}_{N_x}$ correspond to the unknown variables and the independent quantities, while $\tilde{p}_1, .., \tilde{p}_{N_p}$ are the parameters assuming experimental values. All variables and parameters in (2.21) are expressed in their physical units.
The PBE system (2.14)-(2.17) can be written in the form of (2.21), given $\tilde{x}_1 = \tilde{t}$, $\tilde{x}_2 = \tilde{v}$, $\tilde{x}_3 = \tilde{m}$, $\tilde{x}_4 = \tilde{w}$ and the appropriate choice of $\tilde{f}$. The auxiliary functions $\tilde{a}$, $\tilde{g}$, $\tilde{n}$ and $\tilde{\mu}$ can be expressed in terms of the variables $\tilde{x}_1, .., \tilde{x}_{N_x}$ and the physical parameters $\tilde{p}_1, .., \tilde{p}_{N_p}$.
The dimensionless counterparts of the variables $\tilde{x}_1, .., \tilde{x}_{N_x}$ are defined as:

$$x_1 \equiv \tilde{x}_1/\theta_1, \,..\,, x_{N_x} \equiv \tilde{x}_{N_x}/\theta_{N_x}, \tag{2.22}$$

where $\theta \equiv \{\theta_1, .., \theta_{N_x}\}$ are strictly positive characteristic constants with the same dimensions and orders of magnitude of the corresponding variables. The change of variables (2.22) allows rewriting (2.21) as the dimensionless equation

$$f\left(x_1, .., x_{N_x}; \lambda_1, .., \lambda_{N_d}\right) = 0, \tag{2.23}$$

where the dimensionless coefficients $\lambda \equiv \{\lambda_1, .., \lambda_{N_d}\}$ are functions of the characteristic constants θ and the physical parameters $\tilde{p} \equiv \{\tilde{p}_1, .., \tilde{p}_{N_p}\}$, i.e. $\lambda_i = \lambda_i(\theta; \tilde{p})$, $\forall i = 1, .., N_d$. Given the physical parameters $\tilde{p}$, the characteristic constants θ should be proposed by the user in order to specify the coefficients λ, i.e. $\lambda_i = \lambda_i(\theta)$, $\forall i = 1, .., N_d$. In other words, the characteristic constants θ correspond to the degrees of freedom in the scaling procedure.
One of the most common approaches for the definition of the characteristic constants θ consists in imposing as many λ as possible equal to 1, starting from the coefficients of the highest orders polynomial or derivative terms in (2.23), as explained in [50]. In the case $N_d \leq N_x$, it is possible to impose $\lambda_i(\theta) = 1$, $\forall i = 1, .., N_d$, and the constants θ are defined by solving a system of N_d equations with N_x unknowns. However, such a case rarely corresponds to realistic models, whose complexity leads to $N_d > N_x$. As a result, it is impossible to solve the system of equations $\lambda_i(\theta) = 1$, $\forall i = 1, .., N_d$. If $N_d > N_x$, the approach proposed in [50] ensures at most N_x coefficients λ equal to 1, while the remaining $N_d - N_x > 0$ are defined by plugging the computed θ, with no control on their orders of magnitude.
For this reason, we propose the alternative approach. More specifically, we suggest to look for the constants θ such that all the coefficients λ are of the order of $O(1)$. Given $N_d > N_x$, we define the constants θ as the *optimal scaling factors* $\theta_{opt} \in (0, +\infty)^{N_x}$, in the sense that they minimise the distance of the coefficients λ from 1, i.e.

$$\theta_{opt} \equiv \underset{\theta \in (0,+\infty)^{N_x}}{\operatorname{argmin}} C(\theta), \quad C(\theta) \equiv \sum_{i=1}^{N_d} H(\lambda_i(\theta)) \left[\log_{10}(\lambda_i(\theta)) - \Theta_i\right]^2, \qquad (2.24)$$

with $H(x) = 1$ if $x > 0$, and zero otherwise. The cost function $C(\theta)$ (2.24) measures the Euclidean distance between the vector $\{\log_{10}(\lambda_1), .., \log_{10}(\lambda_{N_d})\}$, holding the orders of magnitude of the coefficients λ, and the vector $\{\Theta_1, .., \Theta_{N_d}\}$, holding the desired orders of magnitude $\Theta_i = \log_{10}(1) = 0$, $\forall i = 1, .., N_d$. In the general case, it is possible to apply numerical optimisation methods to find θ_{opt}. For example, the Simulated Annealing Algorithm [51, 52] can be successfully applied for this purpose. The novel scaling procedure is summarised in Algorithm 2.1, while it is tested in Section 2.2.2.1 on the PBE system (2.14)-(2.17), with the rate functions derived in Appendix 2.A.

Algorithm 2.1: The procedure to scale the equation $\tilde{f}(\tilde{x}_1, .., \tilde{x}_{N_x}; \tilde{p}_1, .., \tilde{p}_{N_p}) = 0$ to dimensionless and computationally tractable variables, when the physical parameters $\tilde{p}_1, .., \tilde{p}_{N_p}$ are known experimental values.

1 Given $\tilde{f}(\tilde{x}; \tilde{p}) = 0$, where $\tilde{x} \equiv \{\tilde{x}_1, .., \tilde{x}_{N_x}\}$ correspond to unknown variables and independent quantities, expressed in physical units, and $\tilde{p} \equiv \{\tilde{p}_1, .., \tilde{p}_{N_p}\}$ are known physical parameters, introduce the strictly positive constants $\theta \equiv \{\theta_1, .., \theta_{N_x}\}$ with the same dimensions as $\tilde{x}_1, .., \tilde{x}_{N_x}$;

2 Define the dimensionless variables $x \equiv \{x_1 = \tilde{x}_1/\theta_1, .., x_{N_x} = \tilde{x}_{N_x}/\theta_{N_x}\}$;

3 Rewrite $\tilde{f}(\tilde{x}; \tilde{p}) = 0$ in the dimensionless form $f(x; \lambda) = 0$, with $\lambda(\theta) \equiv \{\lambda_1(\theta; \tilde{p}), .., \lambda_{N_d}(\theta; \tilde{p})\}$ being the dimensionless coefficients of the equation $f(x; \lambda) = 0$;

4 Define the cost function $C(\theta)$ (2.24), measuring the distance of $\lambda_i(\theta)$ from 1, $\forall i = 1, .., N_d$;

5 Compute $\theta_{opt} = \operatorname{argmin}_{\theta \in (0,+\infty)^{N_x}} C(\theta)$, using the appropriate minimisation algorithm;

6 Return the dimensionless and computationally tractable equation $f(x; \lambda(\theta_{opt})) = 0$;

2.2.2.1 Optimal Scaling: Application to DDPM for Latex

To test the derived scaling procedure, we consider the PBE system (2.14)-(2.17) with the rate functions $\tilde{n}(\tilde{v}, \tilde{t})$ (2.A.1), $\tilde{g}(\tilde{v}, \tilde{t})$ (2.A.2), $\tilde{\mu}(\tilde{v}, \tilde{t})$ (2.A.3), $\tilde{a}(\tilde{v}, \tilde{u}, \tilde{t})$ (2.A.4), describing the Dynamic Development of *latex* Particles Morphology discussed in Appendix 2.A. The values of the physical parameters given in Table 2.A.1 lead to computationally intractable orders of magnitude of the involved variables, e.g. $\tilde{v} \propto \nu_0 \approx 10^{-21}$ L, $\tilde{m} \propto m_0 \approx 10^{+36}$ L^{-1} and $\tilde{w} \propto w_0 \approx 10^{+35}$ L^{-1}, as shown in Table 2.1. The scaling procedure described in Algorithm 2.1 can address the problem by providing the feasible values for the dimensionless parameters λ and the corresponding variables. The derivation of the dimensionless counterpart of the PBE model (2.14)-(2.17) is presented in Appendix 2.B along with the resulting equations (2.B.6)-(2.B.18).

The Simulated Annealing Algorithm [51, 52] was used to perform the optimisation of the score function $C(\theta)$ (2.24), when the physical parameters assumed the experimental values provided in Table 2.A.1. Algorithm 2.1 has been implemented in MATLAB and used the function *simulannealbnd* [53] for Simulated Annealing. The numerical routine required less than 5 sec of computation of a 2.70GHz processor, running a 64-bit Linux operating system. Table 2.1 reports the numerical values θ_{opt} of the scaling factors $\theta \equiv \{t_0, \nu_0, m_0, w_0, V_0, \delta_0\}$ and the dimensionless parameters $\lambda(\theta_{opt})$, returned by the execution of Algorithm 2.1.

As shown in Table 2.1, the ratio between the maximum and the minimum parameter λ is $\approx 10^5$, i.e. $\lambda_d/\lambda_\mu^m \approx 10^5$. Such a difference looks computationally tractable, especially if compared with the original equation, where $m_0/\nu_0 \approx 10^{57}$ L^{-2}. Clearly, the proposed scaling procedure is able to reduce the computationally intractable orders of magnitude, caused by the experimental values of the physical parameters. From now on, we will consider the dimensionless and computationally tractable PBE model (2.25), assuming that the the optimal scaling (Algorithm 2.1) has been performed.

Factors θ		Value θ_{opt}	Factors θ		Value θ_{opt}
ν_0		9.110×10^{-21} L	t_0		9.907×10^2 s
m_0		1.671×10^{36} L^{-1}	w_0		1.512×10^{35} L^{-1}
V_0		7.687×10^{-2} L	δ_0		1.930×10^{16} L^{-1}
Param. λ	$\lambda(\theta)$	**Value $\lambda(\theta_{opt})$**	**Param. λ**	$\lambda(\theta)$	**Value $\lambda(\theta_{opt})$**
λ_a^m	$\frac{k_a\, m_0\, \nu_0^{2/3}\, t_0}{N_p}$	5.157	λ_a^w	$\frac{k_a\, w_0\, \nu_0^{2/3}\, t_0}{N_p}$	0.467
λ_d^m	$\frac{\sqrt[3]{36\pi}\, k_d\, \nu_0^{5/3}\, m_0\, t_0}{V_0}$	2.069	λ_d^w	$\frac{\sqrt[3]{36\pi}\, k_d\, \nu_0^{5/3}\, w_0\, t_0}{V_0}$	0.187
λ_μ^m	$k_\mu\, t_0$	0.010	λ_μ^w	$\frac{k_\mu\, m_0\, t_0}{w_0}$	0.110
λ_d	$\frac{\sqrt[3]{36\pi}\, k_d\, t_0}{\sqrt[3]{\nu_0}}$	1146.944	λ_p	$\frac{k_p\, R\, t_0\, \bar{V}_{pol2}}{V_{mon2}\, V_0}$	2.393
λ_f	$\frac{F_{mon2}\, \bar{V}_{mon2}\, t_0}{V_0}$	0	λ_n	$\frac{k_s\, \delta_0\, t_0}{v_c\, m_0}$	1.144
λ_c	v_c/ν_0	0.027	λ_{pol1}	V_{pol1}/V_0	3.252
λ_s	$k_s\, t_0/V_0$	0.322			
Other Param.	**Definition**	**Value**	**Other Param.**	**Definition**	**Value**
Φ_s	-	0.001	Ψ_r	$\bar{V}_{mon2}/\bar{V}_{pol2}$	1.05
Ψ_0	$M_0\, \bar{V}_{mon2}/V_{pol1}$	1			

Table 2.1: Factors $\theta \equiv \{t_0, \nu_0, m_0, w_0, V_0, \delta_0\}$ and dimensionless parameters $\lambda(\theta)$ derived in Appendix 2.B for scaling the PBE model (2.14)-(2.17), with the rates $\tilde{a}$, $\tilde{g}$, $\tilde{n}$ and $\tilde{\mu}$, driving the Dynamic Development of *latex* Particles Morphology (Appendix 2.A).

2.2.3 Dimensionless Model: Analysis

Consider the distribution $m(v, t)$ of the particles volume v at time t, whose evolution is driven by aggregation, growth, nucleation and phase transition. The density $m(v, t)$ corresponds to the solution of the *dimensionless* and computationally tractable counterpart of the PBE system (2.14)-(2.16):

$$
\begin{cases}
\begin{aligned}
\frac{\partial m(v,t)}{\partial t} &= -\underbrace{\frac{\partial(\, g(v,t)\, m(v,t)\,)}{\partial v}}_{\text{Transport}} + \underbrace{n(v,t)}_{\text{Source}} - \underbrace{\mu(v,t)\, m(v,t)}_{\text{Dissipation}} - \underbrace{m(v,t) \int_0^{+\infty} a(v,u,t)\, m(u,t)\, du}_{\text{Integral Term}} \\
&\quad + \underbrace{\frac{1}{2} \int_0^v a(v-u,u,t)\, m(v-u,t)\, m(u,t)\, du}_{\text{Integral Term}}, \quad \forall v, t \in \mathbb{R}^+,
\end{aligned} \\
m(v,0) = \omega_0(v) \geq 0, \quad \forall v \in \mathbb{R}^+, \qquad g(0,t)\, m(0,t) = 0, \quad \forall t \in \mathbb{R}^+.
\end{cases}
$$
$$(2.25)$$

The following section describes some properties of the solution $m(v, t)$ of (2.25). In Section 2.2.3.1, we show that the distribution $m(v, t)$ cannot assume negative values. The zero- and first-order moments are analysed in Section 2.2.3.2. The asymptotic behaviour for $v \to +\infty$ is discussed in Section 2.2.3.3.

2.2.3.1 Non-Negativity of $m(v, t)$

In agreement with the physical meaning of $m(v, t)$, it is possible to show that the distribution $m(v, t)$ is always non-negative:

$$m(v, t) \geq 0, \quad \forall v, t \in \mathbb{R}^+. \tag{2.26}$$

Let us define $t^* \geq 0$ as the minimal time at which there exists such a volume $v = v^* \in \mathbb{R}^+$ that $m(v^*, t^*) = 0$. Assuming the continuous evolution of $m(v, t)$ from the non-negative initial data of (2.25), we have

$$m(v, t^*) > 0, \quad \forall v \in \mathbb{R}^+ \setminus \{v^*\}, \quad m(v^*, t^*) = 0. \tag{2.27}$$

Equation (2.27) indicates v^* as a point of minimum for the function $m(v, t^*)$ of volume v. Under regularity assumptions, (2.27) implies $\partial m(v,t)/\partial v|_{\substack{v=v^* \\ t=t^*}} = 0$ and the transport term in (2.25) vanishes for $v = v^*$ and $t = t^*$.

Given the null transport term and the non-negative rates a and n, the time derivative of $m(v,t)$ is non-negative at $v = v^*$ and $t = t^*$:

$$\left.\frac{\partial m(v,t)}{\partial t}\right|_{\substack{v=v^* \\ t=t^*}} = n(v^*,t^*) + \frac{1}{2}\int_0^{v^*} a(v^*-u,u,t^*)\, m(v^*-u,t^*)\, m(u,t^*)\, du \geq 0. \tag{2.28}$$

As soon as $m(v,t)$ touches the zero level, its time derivative (2.28) becomes non-negative, repulsing m to positive values. In other words, (2.26) follows.

The statement (2.26) can be generalised to the cases (i) the growth rate g explicitly depends on the solution m, i.e. $g = g(m,v,t)$, and (ii) the extra term $\partial^2 m(v,t)/\partial v^2$ is considered in (2.25). The previous argument follows because the transport term is still null, for $v = v^*$ and $t = t^*$, and $\partial^2 m(v,t)/\partial v^2$ only adds a non-negative term in (2.28), with v^* being a point of minimum value.

2.2.3.2 Moments of $m(v,t)$

The zero-order moment $M(t)$ of the distribution $m(v,t)$ corresponds to the expected total number of particles in the system, whereas the first-order moment $V(t)$ provides the expected total volume of the particles. The moments are defined respectively as

$$M(t) \equiv \int_0^{+\infty} m(v,t)\, dv \quad \text{and} \quad V(t) \equiv \int_0^{+\infty} v\, m(v,t)\, dv, \quad \forall t \in \mathbb{R}^+. \tag{2.29}$$

The Zero-Order Moment. Integrating (2.25) with respect to v over $\mathbb{R}^+$, it is possible to get the evolution equation for the total number $M(t)$ of particles:

$$M'(t) = \int_0^{+\infty} n(v,t)\, dv - \int_0^{+\infty} \mu(v,t)\, m(v,t)\, dv - \frac{1}{2}\int_0^{+\infty} m(v,t)\left[\int_0^{+\infty} a(v,u,t)\, m(u,t)\, du\right] dv. \tag{2.30}$$

The Right-Hand Side (RHS) of (2.30) correctly models the dynamics of $M(t)$. The first term corresponds to the expected total number of particles, created per unit of time by the nucleation mechanism. The second term corresponds to the expected total loss of particles per unit of time due to the phase transition process. The last term is the expected total loss of particles per unit of time caused by the aggregation mechanism. In fact, the quantity

$$\int_0^{+\infty} m(v,t)\left[\int_0^{+\infty} a(v,u,t)\, m(u,t)\, du\right] dv \tag{2.31}$$

corresponds to the expected total number of aggregating particles. The pre-factor $1/2$ is placed because one particle is lost for each couple of aggregating particles. The last term in the RHS of (2.30) is obtained by taking advantage of the symmetric structure (2.2) of the rate function $a(v,u,t)$, validating the need for such a hypothesis to avoid non-physical behaviours of the zero-order moment $M(t)$.

The physics of the reaction suggests that the total number $M(t)$ of particles does not change if the particles grow or not. In other words, (2.30) must not account for the growth rate $g(v,t)$. For any fixed time $t \in \mathbb{R}^+$, the integration of the transport term in (2.25) provides

$$-\int_0^{+\infty} \frac{\partial(\,g(v,t)\,m(v,t)\,)}{\partial v}\, dv = -\lim_{v \to +\infty} g(v,t)\, m(v,t), \tag{2.32}$$

where the boundary condition $g(0,t)\, m(0,t) = 0$ has been imposed. For any fixed time $t \in \mathbb{R}^+$, we assume

$$\lim_{v \to +\infty} g(v,t)\, m(v,t) = 0 \tag{2.33}$$

to neglect any possible effect of the growth process on the particles number $M(t)$.

The First-Order Moment. The evolution equation for $V(t)$ is obtained by integrating (2.25), multiplied by v, with respect to v over $\mathbb{R}^+$:

$$V'(t) = \int_0^{+\infty} g(v,t)\, m(v,t)\, dv + \int_0^{+\infty} v\, n(v,t)\, dv - \int_0^{+\infty} v\, \mu(v,t)\, m(v,t)\, dv. \tag{2.34}$$

The first term in the RHS of (2.34) corresponds to the expected total volume variation per unit of time caused by the particles growth, in agreement with the dynamics of $V(t)$. The second and third terms in the RHS of (2.34) provide the expected total volume variation per unit of time, given by nucleation and phase transition respectively. Since the total volume of particles does not change if the particles aggregate or not, the dynamics of $V(t)$ must not be affected by the aggregation rate $a(v,u,t)$. The physical intuition is confirmed by assuming the symmetric shape (2.2) of the rate a. Given (2.2), it is possible to show that the integral terms in (2.25) cancel out, if multiplied by v and integrated with respect to v over $\mathbb{R}^+$. This validates the need for the symmetric structure (2.2) to avoid non-physical behaviours of the first-order moment $V(t)$.

We note that the first term in the RHS of (2.34) was obtained by integrating the transport term in (2.25) as follows

$$-\int_0^{+\infty} v\, \frac{\partial(\, g(v,t)\, m(v,t)\,)}{\partial v}\, dv = -\lim_{v \to +\infty} v\, g(v,t)\, m(v,t) + \int_0^{+\infty} g(v,t)\, m(v,t)\, dv. \tag{2.35}$$

Remembering that $v\, g(v,t)\, m(v,t)$ is the flux of volume given by particles with size v at time t, we assume

$$\lim_{v \to +\infty} v\, g(v,t)\, m(v,t) = 0, \tag{2.36}$$

for any fixed time $t \in \mathbb{R}^+$, to discard the flux of particles with infinite volume.

2.2.3.3   Asymptotic Behaviour of $m(v,t)$

The assumption (2.36) provides information on the asymptotic behaviour of the solution $m(v,t)$ of (2.25), for $v \to +\infty$ and fixed time $t \in \mathbb{R}^+$. As $v \to +\infty$, the distribution $m(v,t)$ should decrease to zero faster than $(v\, g(v,t))^{-1}$ to ensure (2.36), i.e.

$$m(v,t) = o((v\, g(v,t))^{-1}), \quad v \to +\infty, \tag{2.37}$$

for any fixed time $t \in \mathbb{R}^+$. For example, the growth rate $g(v,t)$ (2.B.8), such that $g(v,t) = O(v)$ as $v \to +\infty$, leads to $m(v,t) = o(v^{-2})$ for $v \to +\infty$ and fixed time $t \in \mathbb{R}^+$.

2.3   Population Balance Equations Model for Development of Particles Morphology: Solution

This section is devoted to the design of an accurate and efficient methodology for solving the Population Balance Equations (PBE) model which describes the Dynamic Development of Particles Morphology (DDPM). In the light of the scaling procedure of Section 2.2.2, from now on, we consider the dimensionless and computationally tractable PBE system (2.25).

Section 2.3.1 revises some available methods for the integration of a PBE system. Then, we concentrate on the most promising ideas for our purposes and consequently develop four approaches in the following sections. Advantages and limitations of the presented methodologies are also discussed.

Section 2.3.2 proposes a suitable implementation of the *Stochastic Simulation Algorithm* (SSA) for the integration of the PBE system (2.25). SSA provides a robust integration technique, potentially able to estimate any quantity of interest for the considered system. However, limitations and computational inefficiencies make the approach not competitive for solving (2.25).

Section 2.3.3 designs the *Generalised Method Of Characteristics* (GMOC). It presents a deterministic

discretization scheme for the integration of (2.25). GMOC ensures better accuracy and less computational effort than SSA can achieve, and thus is more preferable for our purposes.

Section 2.3.4 presents the *Laplace Transform Technique* (LTT) which inverts the analytical Laplace transformed solutions of (2.25), specifically obtained for the Models I-III of Section 2.2.1. The approach provides accurate and efficient solutions for the considered models, as demonstrated in Section 2.4. However, the required assumptions and comparatively simple choices of rate functions lead to a limited description of the physics of the process.

Section 2.3.5 proposes the *Laplace Induced Splitting Method* (LISM) to integrate the system (2.25) when realistic cases are addressed. The novel LISM is a splitting methodology, which takes advantage of Laplace induced analytical solutions of (2.25). It simultaneously accounts for all the considered dynamical processes, removing hypothesis and limitations of LTT. The requirements of accuracy and efficiency are also fulfilled by LISM, as will be shown in Section 2.4.

2.3.1 Revision of the Available Methods

An extensive revision of integration methods for PBE systems can be found in [54, 55, 56, 57]. Here we touch only those concepts which we use in our search for an optimal solver of (2.25). Solving the PBE (2.25) is far from being a trivial task, because of numerical and modelling complexities. For reactive particulate systems, the calculation of the rate functions may depend on bulk and particles concentrations, which change with time. As described in Appendix 2.A, the reactor and particles kinetics are coupled, leading to a challenging integration of the resulting system of equations, due to the increased problem size, but also due to a possible increase in the numerical stiffness.

The numerical difficulties include (i) potential inaccuracies in a computed solution $m(v, t)$ for highly aggregating processes, (ii) numerical instabilities for growth-dominated systems, (iii) increased stiffness for processes involving rapid particles nucleation, (iv) numerical implementation of singular nucleation rates in the presence of aggregation and growth mechanisms, (v) domain errors for high-order aggregation kernels. In addition, the inclusion of the particles growth mechanism in PBE gives rise to a notoriously difficult to solve numerical problem, imparting PBE with a hyperbolic nature. Moreover, numerical solutions require substantial computational resources since, in practical engineering processes, the particles size distribution may extend over several orders of magnitude and can be very sharp.

Several integration methods have been proposed in the past years, underlining the inherent difficulties in obtaining accurate and efficient numerical solutions. The majority of such numerical methods, however, is able to deal only with a limited range of variations of the rate functions.

The integration methods for PBE systems can be categorised as *Stochastic Algorithms*, *Discretization Methods* and *Analytical Techniques*.

Section 2.3.1.1 reviews the Monte Carlo (MC) approach for PBE systems, belonging to the family of *Stochastic Algorithms*. Such methods estimate the density $m(v, t)$ by computing statistics on properly drawn random samples. In general, they provide accurate results, at the cost of demanding computations.

Section 2.3.1.2 discusses available *Discretization Methods*. Such approaches solve PBE systems by discretization of the particles volume domain followed by integration of the resulting system of algebraic-differential equations. Usually, these methodologies provide a good compromise between precision and efficiency of the numerical solution of the one-dimensional problem (2.25). However, the stiffness of the equations to solve may lead to computational times exceeding the requirements of efficiency motivated at the beginning of the chapter.

Section 2.3.1.3 presents available *Analytical Techniques* for solving PBE systems, by means of variables manipulations and closed-form expressions. The Analytical Techniques allow for accurate and efficient solutions, but their applicability is often limited by the required assumptions.

2.3.1.1 Stochastic Algorithms

Spielman and Levenspiel [58] were the first to employ a Monte Carlo (MC) approach to study the effect of particle coalescence in a two-phase particulate reactive system. A general MC algorithm

for time varying particulate processes was developed in [59] and the precise mathematical connection between population balance and the MC approach was established in [60].

The leading idea of MC methods consists in drawing the events driving the dynamics of a sample of particles. The MC simulations can be time-driven [61], in the case the time step size $\Delta t > 0$ is explicitly specified and, subsequently, a number of events (e.g. particles growth, aggregation) are carried out during the assigned time interval. On the other hand, the MC simulations can be event-driven [62], if a single event is first selected and, subsequently, the time required for its occurrence is calculated based on a known event probability. Below, we describe a general process involving coagulation, growth and nucleation events in the context of the Stochastic Algorithms.

The *initial condition* $\omega_0(v)$ in (2.25) is imposed by assigning each particle in the sample to a selected volume v_i, such that the resulting size distribution closely follows $\omega_0(v)$.

The *particles coagulation* event fires if the following condition is met by any randomly selected pair of particles, with volumes v_i and v_j:

$$\frac{a(v_i, v_i, t)}{\max_{i,j} a(v_i, v_i, t)} \geq u \sim \mathcal{U}(0, 1), \tag{2.38}$$

where a is the coagulation kernel in (2.25) and u is an independent realisation from the uniform distribution $\mathcal{U}(0, 1)$ over the interval $[0, 1]$. If the criterion (2.38) is satisfied, the particles with volumes v_i and v_j are removed from the sample and the new particle with the volume $v_i + v_j$ is added.

The *particles growth* rate $g(v, t)$ in (2.25) updates the volume v_i during the time interval $[t, t + \Delta t]$, $\Delta t > 0$:

$$v_i \leftarrow v_i + \int_t^{t+\Delta t} g(v_i, s)\, ds. \tag{2.39}$$

The *particles nucleation* adds new particles to the sample, in agreement with the volume distribution specified by the rate $n(v, t)$ in (2.25).

The *density* $m(v, t)$ is recovered by computing statistics on the resulting samples of particles.

The number of sampled particles should be large enough to guarantee statistical accuracy, i.e. $10^4 - 10^6$ as suggested in [57]. Several approaches have been proposed to keep the particles number at desired levels. In the constant-number approach [63], the total number of particles is kept constant throughout the simulation by using either a random particle insertion when a successful particle aggregation event occurs or random particles removal process when new particles are generated due to particle nucleation. In another approach [62], the particles population is duplicated when the total number of particles in the sample population has been reduced to half of its initial value.

In general, the MC approaches are able to provide accurate estimations of the solution $m(v, t)$ of (2.25). This has been demonstrated, e.g. in [64], through comparison with experimental data [65]. However, the effectiveness of MC methods is limited by the size of the simulated systems.

Nevertheless, stochastic simulations offer several advantages when applied to the solution of the general PBE. First, they provide information about the history of each particle in the population and second, their implementation to higher dimensional problems can be easily realised, though often leading to high computational costs.

2.3.1.2 Discretization Methods

A numerical solution of the PBE (2.25) can be obtained by the discretization of the particle volume domain into a number of elements that results in a system of non-linear differential equations to be subsequently integrated. Several discretization methods have been developed for solving PBE systems. These include the fully discrete method [66], the finite difference methods [67], the discretized PBE [68], the high-order discretized PBE methods [69], the fixed and moving pivot discretized PBE methods [70, 71, 72], the Method of Characteristics (MOC) [73], the Orthogonal Collocation on Finite Elements (OCFE) [74] and the Galerkin method [75]. Based on the comparative studies presented in [76, 77, 78], the discretized PBE method [79], the pivot method [70], the Galerkin [75] and the OCFE [54] methods can be suggested as accurate and stable techniques for PBE systems.

The *discretized PBE method* [80] solves the evolution equation for the representative value $m_i(t)$ of

the density $m(v,t)$ in the volume interval (v_i, v_{i+1}). Finite difference schemes and quadrature rules approximate the partial derivatives and the integral terms in (2.25).

The *Method of Characteristics* [73] is based on the Lagrangian approach, describing the particles along their characteristics in the size-time plane. PBE systems are transformed into Ordinary Differential Equations by evaluation on the characteristic curves $v_i'(t) = g(v_i(t), t)$, $\forall i = 1, .., N$, with g the growth rate in (2.25).

The *pivot technique* [70, 71, 72] imposes the particles with size in (v_i, v_{i+1}) to assume the volume x_i, called the i-th pivot, with $v_i < x_i < v_{i+1}$. The distribution $m(v,t)$ is written as $m(v,t) = \sum_i M_i(t) \delta(v - x_i)$, where $\delta(x)$ is the Dirac delta and $M_i(t)$ is the expected number of particles with size x_i. The time derivative of $\int_{v_i}^{v_{i+1}} m(v,t) \, dv$ leads to an evolution equation for $M_i(t)$. The *moving pivot approach* [72] allows the pivot x_i to evolve with time, following the characteristic curve defined by MOC, i.e. $x_i'(t) = g(x_i(t), t)$.

A solution $m(v,t)$ of (2.25) can be approximated by the finite sum $m_k(v,t) \equiv \sum_{j=0}^{k} u_j(t) \phi_j(v)$, where $\phi_j(v)$ are basis functions and $u_j(t)$ are expansion coefficients. Once the basis functions are chosen, the expansion coefficients should be determined. The residual function $\mathcal{R}[m_k](v,t)$ of a trial solution $m_k(v,t)$ is defined as $\partial m_k(v,t)/\partial t - R[m_k](v,t)$, where $R[m_k]$ is the Right Hand Side of the PBE system, computed for m_k. In the *Galerkin* approach, the basis functions are recombined to satisfy the boundary conditions. Then, the expansion coefficients are found so that the residual $\mathcal{R}$ is orthogonal to as many of the recombined basis functions as possible. In the *Collocation* approach, the coefficients u_j are selected to satisfy the boundary conditions and to make the residual $\mathcal{R}$ vanish at as many grid points as possible.

The OCFE method is employed in [74] for solving time-dependent PBE systems. The Lagrange basis functions $\phi_j(v)$ are chosen in [54] and the Collocation procedure allows transforming PBE into a system of differential equations to be solved using the Petzold-Gear method [81].

The Galerkin formulation with piecewise linear basis functions is applied in [75] to solve PBE in the presence of aggregation and growth mechanisms. The Lagrange basis functions $\phi_j(v)$ are chosen in [56] and the Galerkin method transforms PBE in a system of differential equations, which can be solved using the Petzold-Gear method [81].

Discretization Methods usually require special attention to (i) a choice of the volume discretization rule, (ii) a selection of the finite difference scheme, (iii) a treatment of aggregation terms and (iv) an implementation of the nucleation mechanism.

The *discretization rule* of the volume domain is found to affect significantly the performance of the numerical solution. The geometric rule $v_{i+1} = 2v_i$ is proposed in [68]. However, the resulting volume grid is often inadequate for the accurate calculation of the density $m(v,t)$. Alternatively, the fractional geometric rule $v_{i+1} = 2^{1/q}v_i$ was suggested in [79], with q being an integer positive number. Aggregation dominated cases are treated in [54] using a logarithmic discretization of the volume domain. For growth dominated processes, the strategy of [54] consists in using a logarithmic volume discretization at small volumes and a constant discretization at larger volumes.

Finite difference schemes can approximate the partial derivatives accounting for convective flows, such as the growth mechanism. The first-order upwind scheme suffers from numerical diffusion unless a fine grid is used, as stated in [80]. To overcome the numerical diffusion problem, higher order approximation schemes can be used, as proposed in [69] and Section 2.3.3.1.

The *aggregation terms* require special treatment, when non-uniform grids are implemented. In the pivots approach, the particles can only assume the sizes $\{x_i\}_{i \in \mathbb{N}}$, while the aggregation process can produce volumes $v \neq x_i$, $\forall i \in \mathbb{N}$. As explained in [70], the aggregation terms can be modified to account for the produced particles with volume $v \neq x_i$, $\forall i \in \mathbb{N}$. The formation of aggregated particles with size $v \in (x_i, x_{i+1})$ is represented by assigning the fractions $p(v, x_i)$ and $q(v, x_{i+1})$ to the particles populations at x_i and x_{i+1} respectively. The unknowns $p(v, x_i)$ and $q(v, x_{i+1})$ are obtained by the conservation of the pre-chosen functions $f_k(v)$, i.e.

$$
\begin{aligned}
p(v, x_i) f_1(x_i) + q(v, x_{i+1}) f_1(x_{i+1}) &= f_1(v), \\
p(v, x_i) f_2(x_i) + q(v, x_{i+1}) f_2(x_{i+1}) &= f_2(v),
\end{aligned}
\tag{2.40}
$$

and thus the corresponding moments $F_k(t) = \int_0^{+\infty} f_k(v)\, m(v,t)\, dv$, with $k = 1, 2$.

The *particles nucleation* at the fixed size $v_0 > 0$ is not accurately represented by adaptive discretization grids, when v_0 falls outside the grid domain. In such a case, it is suggested in [72] to add new grid points where needed, while eliminating the grid points with the largest values. The particles density of the eliminated points has to be redistributed to preserve some quantities of interest.

It is observed in [55] that the choice of continuous basis functions for the OCFE and Galerkin methods cannot resolve impulsive nucleation terms, such as $n(v,t) \propto \delta(v - v_0)$, with $v_0 > 0$ and $\delta(x)$ the Dirac delta. This can be treated by assuming that the nucleation spreads over a specified size range, as proposed in [55] and used for the approximation of the nucleation rate in this dissertation (Section 2.4.1). The typical problems and benefits associated with discretization schemes are summarised below.

The *discretized PBE method* is found to be robust for dealing with numerical oscillations of the computed solutions, but it suffers from poor accuracy in the case of growth dominated systems [54]. The finite difference schemes, usually employed to simulate particles growth, are likely to introduce numerical instabilities caused by diffusion and dispersion errors [54].

The *Method of Characteristics* (MOC) avoids the numerical errors caused by the discretization of the growth term, because the partial derivatives are analytically accounted for in the resulting ODE system. However, the characteristics grid may lead to the inefficient integration of the PBE system (2.25), if the other dynamical mechanisms make the particles sizes behave differently from what prescribed by the transport rate $g(v,t)$ [72]. In addition, MOC can only work if the characteristic curves are not crossings each other, with the consequent formation of a shock [73]. The characteristics may also fail to cover some parts of the volume domain, if the given curves are diverging in the size-time plane [73].

The *pivot technique* shows accuracy and efficiency, when performed with geometrically distributed pivots [70, 71, 72]. The method is able to overcome the problems of diffusion and stability [72], affecting other discretization techniques [68, 82, 83]. The pivot methodology is also validated in [64], by comparison with experimental data available in [65]. The shown results suggest that the method is computationally efficient, but its accuracy is highly dependent on the discretization of the particles volume domain. The pivot technique was used in [45] to predict the Dynamic Development of *latex* Particles Morphology.

The *Orthogonal Collocation on Finite Elements* (OCFE) method is in general more accurate than the discretized PBE methods, providing an excellent agreement between numerical and analytical results, as shown in [54]. However, a numerical solution may be affected by strong oscillations. A common approach to the problem consists in adding an artificial term of diffusion, as suggested in [80].

The *Galerkin* method is found to be more robust than the OCFE method for the simulation of particulate systems [56]. However, the Galerkin method may suffer from tracking moving discontinuities that commonly arise for seeded particles processes and discontinuous initial distributions [56]. For dealing with moving discontinuities, additional nodal points can be placed and moved according to the particle growth rate, as proposed in [75]. The approach shows to improve the accuracy of the solution at the expense of a small increase in the computational time [75].

2.3.1.3   Analytical Techniques

Analytical Techniques offer *accurate* and *fast* solutions to the PBE (2.25), by solving analytically the dynamics of $m(v,t)$. Here we review three such techniques. The *Method of Moments* (MOM) derives closed-form evolution equations for chosen moments of the density $m(v,t)$. The *Laplace Transform Technique* provides an analytical formula for the Laplace transform of $m(v,t)$. The *Auxiliary Equation Method* deals with parametric solutions of (2.25).

The *Method Of Moments* (MOM) calculates some selected moments of the distribution $m(v,t)$:

$$m_k(t) \equiv \int_0^{+\infty} v^k\, m(v,t)\, dv, \tag{2.41}$$

with $k \in \mathbb{N}$ and $m(v,t)$ the solution of (2.25). Equation (2.25) is multiplied by v^k and then integrated with respect to $v \in \mathbb{R}^+$. With some particular choices of rate functions, the derived equation can be written in a closed form and integrated in time. However, it is not always the case and then

closure techniques such as (*i*) methods assuming the form of the unknown distribution [84] and (*ii*) interpolative closure methods [85] can be applied.

The MOM is proved to be fast and accurate in the calculation of the distribution moments [57]. However, its main challenge consists in the reconstruction of $m(v, t)$ from a finite set of moments. The problem can be addressed through approximation of the density $m(v, t)$ by a sum of known distributions, with coefficients expressed in terms of the calculated moments [57].

The *Laplace Transform Technique* [48, 86] analytically solves the dynamics of the Laplace transform

$$\hat{m}(\lambda, t) \equiv \int_0^{+\infty} e^{-\lambda v}\, m(v, t)\, dv \tag{2.42}$$

of the solution $m(v, t)$ of the PBE system (2.25). Closed-form expressions of the Laplace transform (2.42) are only available for particular choices of rate functions, limiting the applicability of the method. The studies presented in [48, 86] consider simple PBE systems, simultaneously accounting for few dynamical mechanisms governed by constant or linear rates. The original variables can be recovered by using numerical methods for the inversion of the Laplace transform functions (see Section 2.3.1.4 for details). Such approaches can be more computationally expensive than those using updating schemes in time, but they have the advantage of allowing evaluation at any time, without evolving from an initial condition.

The *Auxiliary Equation Method* [87, 88, 89] reduces PBE systems to ordinary integro-differential equations, using the independent variable ξ, where $\xi = \xi(v, t)$ is a function of the particles volume v and time t. The choice of $\xi = \xi(v, t)$ should be suitable to track the convective particles flux and to solve the problem in the new coordinate system. The solution of the resulting equations is defined in the form of the finite sum

$$m(\xi) = \sum_{i=0}^{N} a_i\, z^i(\xi), \tag{2.43}$$

where $a_0, .., a_N$ are constants to be further determined, N is an integer fixed by balancing principles and $z(\xi)$ is a solution of the auxiliary equation to be considered. The coefficients $a_0, .., a_N$ are determined by inserting (2.43) into the ordinary integro-differential equation arising from the PBE system. The function $z(\xi)$ can be defined as a solution of an auxiliary differential equation with a second-, or fourth-, order non-linear term. Using the described methodology, the parametric solution of the PBE system can be computed for various cases of study [88, 89]. However, the derived solutions depend on the non-trivial choices of the auxiliary quantities and the discussed technique only works for simple rate functions, as presented in [88, 89].

2.3.1.4   Numerical Methods for Inverse Laplace Transform

The numerical inverse Laplace transform is, in general, an ill-posed problem and no single method gives optimal results for all possible situations, leading to the diversity of viable numerical approaches in the literature [90]. This section reviews numerical methods for inversion of the Laplace transform function

$$\mathcal{L}\{f(v)\} \equiv \hat{f}(\lambda) = \int_0^{+\infty} f(v)\, e^{-\lambda v}\, dv. \tag{2.44}$$

Our interest in such methods arises from the need to invert the Laplace transform $\hat{m}(\lambda, t)$ of the solution $m(v, t)$ of (2.25), derived for Models I-III in Section 2.3.4. A closed-form expression for the inverse of $\hat{m}(\lambda, t)$ seems to be not available in the most of the cases, and thus numerical routines should be applied.

The inverse Laplace transform function $f(v)$ of $\hat{f}(\lambda)$ (2.44) is defined as the Bromwich contour integral [91]:

$$\mathcal{L}^{-1}\{\hat{f}(\lambda)\} = f(v) = \frac{1}{2\pi i} \int_{\sigma - i\infty}^{\sigma + i\infty} \hat{f}(\lambda)\, e^{\lambda v}\, d\lambda, \tag{2.45}$$

where $i \in \mathbb{C}$ is the imaginary unit and $\sigma \in \mathbb{R}$ must be greater than the real part of all the singularities of $\hat{f}(\lambda)$.

Given $\hat{f}(\lambda)$, (2.45) should be solved for the unknown $f(v)$. The numerical solution approaches can be broadly split into two categories: (i) methods based on quadrature rules and (ii) expansions using analytically invertible basis functions. Quadrature-based examples are the Fourier series [92] and the Talbot methods [93]. The Weeks method [94] expands $f(v)$ using Laguerre polynomials [95], whose Laplace transform is known and used to recover (2.44). The Schapery method [96] applies the same principle, using exponential basis functions. An extensive review is presented in [97], focusing on the numerical accuracy of the inversion methods for a set of test functions. The conclusion is that the methods based on Laguerre polynomials and Fourier series provide accurate results for the most of the tested cases. In another review [98], the authors investigate numerical inverse Laplace transform methods, focusing on their ability to calculate the inverted function values using the fewest Laplace function evaluations. The authors of [98] find Fourier series based inversion algorithms to provide the best performance, among the compared approaches.

Following the conclusions of [97, 98], we consider Fourier series methods suitable for our purposes. In particular, we will use in Section 2.4 the MATLAB routine *nilt* [99] for the numerical inversion of the Laplace transforms $\hat{m}(\lambda, t)$ derived in Section 2.3.4. The routine *nilt* implements the Fourier series method, expanding (2.45) into real and imaginary parts. Then, the trapezoid rule [100] and further manipulations lead to the corresponding Fourier series. The derived formula requires several evaluations of the Laplace transform functions. In order to accelerate the convergence of the sum to be computed, the routine *nilt* uses the ε-algorithm discussed in [101].

In the following sections, we develop three methods for solving (2.25). Each method represents one of the three classes of numerical approaches reviewed in this section, namely, stochastic, discretization and analytical. In addition, we propose a method which does not fit into any described class and is based on the idea which, to our knowledge, has never been explored in numerical methods for PBE. More specifically, we propose to combine a splitting integration scheme with Laplace induced analytical solutions derived for simplified PBEs, composing the PBE of interest.

2.3.2 Stochastic Simulation Algorithm

The aim of this section consists in formulating a suitable implementation of the Stochastic Simulation Algorithm (SSA) for integration of the PBE system (2.25). In particular, we consider the SSA formulation presented in Algorithm 1.1 of Section 1.2.1.

Given the volume grid $\mathbf{v} \equiv \{\varphi_k\}_{k=0}^N$, with $0 = \varphi_0 < \varphi_1 < .. < \varphi_N$, we define $X_k(t) \in \mathbb{N}$ as the number of particles with volume $v \in [\varphi_k, \varphi_{k+1})$ at time t, for all $k = 0, .., N-1$. The expected number $M_k(t) \in \mathbb{R}^+$ of particles with volume $v \in [\varphi_k, \varphi_{k+1})$ at time t is given by:

$$M_k(t) \equiv \langle X_k(t) \rangle \equiv \int_{\varphi_k}^{\varphi_{k+1}} m(v,t) \, dv, \quad \forall k = 0, .., N-1, \tag{2.46}$$

where $m(v,t)$ is the solution of (2.25). The volume grid $\mathbf{v}$ should be chosen such that the density $m(v,t)$ has no structure within each interval $[\varphi_k, \varphi_{k+1})$, for all $k = 0, .., N-1$. In other words, the distribution $m(v,t)$ is presumed to be uniform within the interval $[\varphi_k, \varphi_{k+1})$:

$$m(v,t) = m_k(t) = \frac{M_k(t)}{\varphi_{k+1} - \varphi_k}, \quad \forall v \in [\varphi_k, \varphi_{k+1}), \quad \forall k = 0, .., N-1. \tag{2.47}$$

Assuming (2.47), it is possible to select the value $v = \varphi_k$ as the representative volume of the particles with size in $[\varphi_k, \varphi_{k+1})$. For any time $t \in \mathbb{R}^+$, the system state

$$\mathbf{X}(t) \equiv \{X_k(t)\}_{k=0}^{N-1} \in \mathbb{N}^N \tag{2.48}$$

provides the numbers of particles with the volumes $\{\varphi_k\}_{k=0}^{N-1}$. Following the definitions (1.2)-(1.3) given in Section 1.2.1, we derive the propensity functions and state-change vectors driving the state (2.48) in agreement with the PBE system (2.25). We remark that the proposed derivation is based on

the intuitive meaning of the rate functions g, n, μ and a in (2.25).

Particles Growth. Given the state $\mathbf{X}(t) = \mathbf{x}$ (2.48), the propensity function $G_k(\mathbf{x})$ for the growth of any particle from the volume φ_k to the successive volume value can be computed as:

$$G_k(\mathbf{x}) \equiv g(\varphi_k, t) \frac{X_k(t)}{\Delta\varphi_k}, \quad \Delta\varphi_k \equiv \varphi_{k+1} - \varphi_k > 0, \quad \forall k = 0, .., N - 1, \tag{2.49}$$

where the growth speed $g(\varphi_k, t)$ of the particles with volume φ_k is multiplied by the density $X_k(t)/\Delta\varphi_k$ of the considered particles at time t. The resulting quantity corresponds to the particles growth flux, or the number of particles flowing per unit of time to the next volume value. In other words, it gives the desired propensity function $G_k(\mathbf{x})$. The system state $\mathbf{X}(t)$ (2.48) must be updated as

$$X_k(t) \leftarrow X_k(t) - 1, \quad X_{k+1}(t) \leftarrow X_{k+1}(t) + 1, \tag{2.50}$$

in correspondence with the growth of any particle with size φ_k to the next volume value.

Particles Nucleation. Given $\mathbf{X}(t) = \mathbf{x}$ (2.48), the propensity function $N_k(\mathbf{x})$ for the nucleation of the particles with volume in $[\varphi_k, \varphi_{k+1})$ is computed as

$$N_k(\mathbf{x}) \equiv \int_{\varphi_k}^{\varphi_{k+1}} n(v, t) \, dv, \quad \forall k = 0, .., N - 1, \tag{2.51}$$

where the function $n(v, t)$ provides the size distribution of the particles nucleating per unit of time, in agreement with the definition (2.4). The system state $\mathbf{X}(t)$ (2.48) must be updated as

$$X_k(t) \leftarrow X_k(t) + 1 \tag{2.52}$$

in correspondence with the nucleation of any particle with volume in $[\varphi_k, \varphi_{k+1})$.

Particles Phase Transition. For any time $t \in \mathbb{R}^+$, the function $\mu(v, t)$ in (2.25) provides the proportion of the particles with volume v changing their phase per unit of time. Consequently, the propensity function $\Pi_k(\mathbf{x})$ for the phase transition of the particles with volume φ_k is given by

$$\Pi_k(\mathbf{x}) \equiv \mu(\varphi_k, t) X_k(t), \quad \forall k = 0, .., N - 1, \tag{2.53}$$

where the system state $\mathbf{X}(t) = \mathbf{x}$ (2.48) provides the number $X_k(t)$ of the particles with volume φ_k at time t, updated as

$$X_k(t) \leftarrow X_k(t) - 1 \tag{2.54}$$

if the phase transition reaction occurs.

Particles Aggregation. The propensity function $A_{k,j}(\mathbf{x})$ for the aggregation of the particles with volumes φ_k and φ_j is computed as

$$A_{k,j}(\mathbf{x}) \equiv \begin{cases} a(\varphi_k, \varphi_j, t) X_k(t) X_j(t), & \forall k = 0, .., N - 1, \forall j = k + 1, .., N - 1, \\ a(\varphi_k, \varphi_k, t) (X_k(t) - 1) X_k(t) / 2, & \forall k = 0, .., N - 1, \text{ with } j = k, \end{cases} \tag{2.55}$$

where the system state $\mathbf{x} = \mathbf{X}(t)$ (2.48) provides the numbers $X_k(t)$ and $X_j(t)$ of particles with volumes φ_k and φ_j at time t respectively. For any time $t \in \mathbb{R}^+$, the function $a(v, u, t)$ in (2.25) gives the proportion of the particles with volumes v and u aggregating per unit of time. The propensity $A_{k,j}(\mathbf{x})$ (2.55) is obtained by multiplying the number of all the possible couples of particles by the proportion a. With the assumption of uniform volume grid, i.e.

$$\varphi_{k+1} - \varphi_k = h > 0, \quad \forall k = 0, .., N - 1, \tag{2.56}$$

the system state $\mathbf{X}(t)$ (2.48) can be updated as

$$X_k(t) \leftarrow X_k(t) - 1, \quad X_j(t) \leftarrow X_j(t) - 1, \quad X_{k+j}(t) \leftarrow X_{k+j}(t) + 1, \tag{2.57}$$

in correspondence with the aggregation of the particles with volumes φ_k and φ_j. The scheme (2.57) relies on (2.56) that ensures the volume of the resulting particle to be $\varphi_k + \varphi_j = (k + j)h = \varphi_{k+j}$.

The initial condition $\omega_0(v)$ of (2.25) is imposed by neglecting random fluctuations of the initial state, i.e. $\mathbf{X}(0) = \langle \mathbf{X}(0) \rangle \in \mathbb{N}^N$, and by taking the integer part of the computed integral:

$$X_k(0) = \langle X_k(0) \rangle = \int_{\varphi_k}^{\varphi_{k+1}} \omega_0(v)\,dv \approx \lfloor \omega_0(\varphi_k)\,h \rfloor \in \mathbb{N}, \quad \forall k = 0, .., N-1, \tag{2.58}$$

where h is given by (2.56) and $\lfloor x \rfloor \equiv \max_{i \in \mathbb{N}}\{i \leq x\}, \forall x \in \mathbb{R}^+$.

The approximation (2.58) may lead to inaccurate estimations of the initial state. As $h \to 0$, the product $\omega_0(\varphi_k)\,h$ can be arbitrarily small, and thus giving $X_k(0) = 0$, where the initial condition puts a non-negligible mass, i.e. for $\omega_0(\varphi_k) \gg 0$. The problem can be addressed by scaling the initial condition such that

$$\hat{\omega}_0(\hat{v})\,h \gg 1, \quad \hat{\omega}_0(v) \equiv \kappa\,\omega_0(v), \quad \forall v \in \mathbb{R}^+, \tag{2.59}$$

where $\kappa > 0$ is a tunable constant and $\hat{v} \in \mathbb{R}^+$ is a point of local maximum of $\omega_0(v)$. Condition (2.59) guarantees accurate estimations of the initial state, where the non-negligible mass is placed (the local maxima). The scaling (2.59) must be applied to the PBE system (2.25), and thus SSA will be implemented using the transformed variables:

$$\hat{m}(v,t) \equiv \kappa\,m(v,t), \quad \hat{g}(v,t) \equiv g(v,t), \quad \hat{n}(v,t) \equiv \kappa\,n(v,t),$$
$$\hat{\mu}(v,t) \equiv \mu(v,t), \quad \hat{a}(v,u,t) \equiv a(v,u,t)/\kappa, \quad \forall v,u,t \in \mathbb{R}^+. \tag{2.60}$$

The boundary condition in (2.25) is imposed by ensuring $g(0,t)\,X_0(t) = 0$, for all $t \in \mathbb{R}^+$.

The derived propensity functions and state-change vectors allow us to integrate (2.25) by implementing SSA formulated in Algorithm 1.1 of Section 1.2.1. The algorithm is used to draw a sample of $S > 0$ independent trajectories of $\mathbf{X}(t)$ (2.48), $t \in [0, T_{\max}]$. The solution $m(v,t)$ of (2.25) is recovered by (2.47), with $M_k(t)$ computed as the sample average of $X_k(t)$. Numerical experiments are presented in Section 2.4.

2.3.2.1   Benefits & Drawbacks

We have proposed the Stochastic Simulation Algorithm (SSA) for integration of the PBE system (2.25). The formulation of SSA is based on Algorithm 1.1, reviewed in Section 1.2.1. The main benefits of the presented SSA are summarised here:

1. Algorithm 1.1 guarantees unbiased estimations of the solution of the CME (1.4), as motivated in Section 1.2.1.

2. The definition (2.51) of the propensity function $N_k(\mathbf{x})$ allows us to analytically account for impulsive nucleation rates, such as $n(v,t) \propto \delta(v - v_0)$ with $v_0 > 0$ and $\delta(x)$ the Dirac delta.

3. The drawn sample of trajectories of $\mathbf{X}(t)$ can potentially provide the estimation of any quantity of interest by the computation of the corresponding statistics.

The drawbacks of the proposed approach are outlined below:

1. The derivation of the propensity functions is based on the intuitive meaning of the rates a, g, n and μ. As will be shown in Section 2.4, the tested choices of the rate functions allow the convergence of SSA to the solution of the PBE system (2.25). However, no rigorous proof is provided in the general case.

2. Despite the simplified choices of the rate functions in Models I-III of Section 2.2.1, the SSA method shows to be computationally demanding ($\approx 10^2$ sec to generate a single trajectory of $\mathbf{X}(t)$). See Section 2.4 for more details.

3. Following Algorithm 1.1, the time step size τ is automatically drawn from the distribution (1.7). The resulting step size can be particularly small, leading to the significant effort to produce a single trajectory of $\mathbf{X}(t)$.

4. The proposed implementation of the aggregation process requires the uniform grid (2.56), which may lead to the inefficient integration of the considered equations.

In conclusion, SSA provides a robust integration technique, potentially able to estimate any quantity of interest for the considered system. However, limitations and computational inefficiencies make the approach not competitive for solving (2.25). In order to overcome these issues, we explore the possibility to develop the discretization method for solving (2.25).

2.3.3 Generalised Method Of Characteristics

Our objective is to transform the PBE (2.25) to a corresponding system of Ordinary Differential Equations (ODE). We propose a discretization method which we called *Generalised Method Of Characteristics* (GMOC). As the name suggests, the Method Of Characteristics (MOC) [73] is a special case of GMOC, as will be shown below. The rest of this section is devoted to the derivation and implementation of GMOC. The numerical results for GMOC, in comparison with other proposed method, are shown in Section 2.4.

The solution $m(v,t)$ of (2.25) is evaluated along N curves, belonging to $P = \{(v,t) \in \mathbb{R}^2 : v, t \geq 0\}$, with the prescribed form $v = \varphi_k(t)$, $\forall k = 1, .., N$. Given $m_k(t) \equiv m(v,t)|_{v=\varphi_k(t)}$, the *chain rule* [102] provides the time derivative of $m_k(t)$. As a result, we get the ODE system arising from (2.25) by evaluating the solution $m(v,t)$ on the curves $v = \varphi_k(t)$, $\forall k = 1, .., N$, $\forall t \in \mathbb{R}^+$:

$$\frac{dm_k(t)}{dt} = \left[\frac{d\varphi_k(t)}{dt} - g(\varphi_k(t), t)\right] \left.\frac{\partial m(v,t)}{\partial v}\right|_{v=\varphi_k(t)} - \left[\rho(\varphi_k(t), t) + \mu(\varphi_k(t), t)\right] m_k(t) +$$
$$+ n(\varphi_k(t), t) + A^+(\varphi_k(t), t; m(\cdot, t)) - A^-(\varphi_k(t), t; m(\cdot, t)), \tag{2.61}$$

where $\rho(v,t) \equiv \partial g(v,t)/\partial v$ and

$$A^+(v, t; m(\cdot, t)) \equiv \frac{1}{2} \int_0^v a(v-u, u, t)\, m(v-u, t)\, m(u, t)\, du, \tag{2.62}$$

$$A^-(v, t; m(\cdot, t)) \equiv m(v, t) \int_0^{+\infty} a(v, u, t)\, m(u, t)\, du. \tag{2.63}$$

The particular choice of the curves $v = \varphi_k(t)$, for $k = 1, .., N$, as the solutions of the Cauchy problems

$$\varphi_k'(t) = g(\varphi_k(t), t), \quad \forall t \in \mathbb{R}^+, \quad \varphi_k(0) = \bar{\varphi}_k > 0, \quad \forall k = 1, .., N, \tag{2.64}$$

allows cancelling the partial derivatives with respect to v in (2.61). The curves $v = \varphi_k(t)$ in (2.64) correspond to the *characteristics* defined by MOC, showing that GMOC embeds MOC. Moreover, the Method of Lines (ML) [103] can be also recovered from GMOC by imposing:

$$\varphi_k(t) = \varphi_k(0), \quad \forall t \in \mathbb{R}^+, \quad \forall k = 1, .., N. \tag{2.65}$$

The novelty of GMOC consists in the freedom of a choice of the curves $v = \varphi_k(t)$. This can be beneficial for the case when the solution $m(v,t)$ has a complex shape potentially leading to numerical instabilities. The flexible choice of $v = \varphi_k(t)$ can address such a problem.

2.3.3.1 GMOC Implementation

The implementation of GMOC includes imposing the initial and boundary conditions of (2.25) in the ODE (2.61), as well as a numerical treatment of the partial derivatives with respect to v and the integral terms. Finally, the discretization scheme for simulating the time evolution in (2.61) is also required.

Initial and Boundary Conditions. The initial condition of (2.25) imposes:

$$m_k(0) = \omega_0(\varphi_k(0)), \quad \forall k = 1, .., N. \tag{2.66}$$

The curve $\varphi_0(t) = 0$, $\forall t \in \mathbb{R}^+$, is defined to prescribe the boundary condition of (2.25):

$$g(\varphi_0(t), t) \, m_0(t) = 0, \quad \forall t \in \mathbb{R}^+. \tag{2.67}$$

The information carried by $\varphi_0(t)$ and $m_0(t)$ is used to approximate the partial derivatives and the integral terms, as explained below. As a result, the boundary condition of (2.25) is imposed in the ODE system (2.61).

Partial Derivatives. Given $\{\varphi_k(t), m_k(t)\}_{k=0}^{N}$ for all $t \in \mathbb{R}^+$, finite difference schemes can approximate the partial derivatives $\partial m(v,t)/\partial v|_{v=\varphi_k(t)}$, $\forall k = 1, .., N$. As stated in [80], such schemes may suffer from numerical diffusion and a common solution consists in using high-order approximation schemes. Motivated by the statement, we select a fourth-order accurate scheme.

Given the hyperbolic Partial Differential Equation (2.25), it is possible to define the domain of dependence $D(v,t)$ as the subset of $P = \{(v,t) \in \mathbb{R}^2 : v, t \geq 0\}$, such that $m(v,t)$ only depends on the values of the solution inside $D(v,t)$. The negative integral term in (2.25) makes the domain $D(v,t)$ be the set $\mathbb{R}^+ \times [0,t]$. Both forward and backwards points have an influence on the solution at (v,t), motivating the choice of a central scheme for approximating the partial derivatives with respect to v. Assuming the condition

$$\varphi_k(t) - \varphi_{k-1}(t) = h(t) > 0, \quad \forall k = 1, .., N, \forall t \in \mathbb{R}^+, \tag{2.68}$$

we propose the following fourth-order accurate scheme [104]:

$$\left.\frac{\partial m(v,t)}{\partial v}\right|_{v=\varphi_k(t)} \approx \begin{cases} \frac{-m_{k+2}(t)+8m_{k+1}(t)-8m_{k-1}(t)+m_{k-2}(t)}{12h(t)}, & \forall k = 2, .., N-2, \\ \frac{25m_N(t)-48m_{N-1}(t)+36m_{N-2}(t)-16m_{N-3}(t)+3m_{N-4}(t)}{12h(t)}, & \text{if } k = N, \\ \frac{3m_N(t)+10m_{N-1}(t)-18m_{N-2}(t)+6m_{N-3}(t)-m_{N-4}(t)}{12h(t)}, & \text{if } k = N-1, \\ \frac{m_4(t)-6m_3(t)+18m_2(t)-10m_1(t)-3m_0(t)}{12h(t)}, & \text{if } k = 1. \end{cases} \tag{2.69}$$

The lack of either backwards or forward grid points does not allow the central scheme for $k = 1, N-1, N$, being replaced by asymmetric formulas.

Integral Terms. Known $\{\varphi_k(t), m_k(t)\}_{k=0}^{N}$ for all $t \in \mathbb{R}^+$, we approximate the integral terms A^- and A^+ in (2.61) by the quadrature rules

$$\int_0^{+\infty} l(u,t) \, m(u,t) \, du \approx \sum_{j=0}^{N} p_j(t) \, l(\varphi_j(t), t) \, m_j(t), \quad \forall t \in \mathbb{R}^+, \tag{2.70}$$

where the function $l(u,t)$ is defined as

$$l(u,t) \equiv \mathbb{1}_{(0,+\infty)}(u) \, a(\varphi_k(t), u, t), \quad \forall k = 1, .., N, \tag{2.71}$$

for A^- (2.63), while

$$l(u,t) \equiv \mathbb{1}_{(0,\varphi_k(t))}(u) \, a(\varphi_k(t) - u, u, t) \, m(\varphi_k(t) - u, t), \quad \forall k = 1, .., N, \tag{2.72}$$

for A^+ (2.62), with $\mathbb{1}_X(x) = 1$ if $x \in X$, zero otherwise. The weights $p_j(t)$, $j = 0, .., N$, in (2.70) specify the quadrature rule to be used. Assumed (2.68), the fourth-order accurate composite Simpson's rule

[105] is chosen in agreement with the accuracy of the numerical scheme (2.69). Taking advantage of (2.68), it is possible to evaluate $m(\varphi_k(t) - u, t)$ for all $u = \varphi_j(t)$, such that $\varphi_j(t) \in (0, \varphi_k(t))$:

$$m(\varphi_k(t) - \varphi_j(t), t) = m(\varphi_{k-j}(t), t) = m_{k-j}(t). \qquad (2.73)$$

In the case the hypothesis (2.68) does not hold, the evaluation of $m(\varphi_k(t) - \varphi_j(t), t)$ requires the interpolation of the data $\{\varphi_k(t), m_k(t)\}_{k=0}^{N}$.

Time Evolution. The state vector $y(t) \equiv [m_1(t), .., m_N(t)]$ corresponds to the solution of the Cauchy problem:

$$y' = F(y), \quad y(t_0) = y_0, \qquad (2.74)$$

where the function $F : [0, +\infty)^N \to \mathbb{R}^N$ is defined by the Right-Hand Side of (2.61), provided the approximation schemes (2.69) and (2.70). In agreement with the accuracy of the considered schemes, the fourth-order accurate Runge-Kutta method (RK4) [106] is chosen to integrate (2.74). For the sake of simplicity, the time step size $\tau > 0$ is assumed to be constant for all time t.

2.3.3.2 Benefits & Drawbacks

We have formulated the new discretization method for the integration of the PBE system (2.25), the Generalised Method Of Characteristics (GMOC). The main advantages of the presented GMOC are the following:

1. Under regularity assumptions, it is possible to rigorously prove the convergence of GMOC to the solution of (2.25). The same cannot be said for SSA, as outlined in Section 2.3.2.1.

2. The flexible choice of the curves $v = \varphi_k(t)$ can be beneficial for the case when the solution $m(v, t)$ of (2.25) has a complex shape potentially leading to numerical instabilities.

3. Given the simplified choices of the rate functions in Models I-III of Section 2.2.1, GMOC ensures a competitive speed of simulations. Section 2.4 will show that GMOC is faster than SSA in providing the same level of accuracy.

The limitations of GMOC are summarised here:

1. The point-wise evaluation of $n(\varphi_k(t), t)$ in (2.61) requires the approximation of impulsive nucleation rates, such as $n(v, t) \propto \delta(v - v_0)$ with $v_0 > 0$ and $\delta(x)$ the Dirac delta. See Section 2.4.1 for a possible approach. We remark that SSA analytically accounts for impulsive rates, as discussed in Section 2.3.2.1.

2. The finite difference scheme (2.69) and the evaluation (2.73) require the uniform grid (2.68), which may lead to the inefficient integration of the considered equations.

3. The appropriate choice of the curves $v = \varphi_k(t)$ is a non-trivial and problem-specific task. The numerical experiments shown in Section 2.4 will rely on the constant curves (2.65).

We have applied the proposed here GMOC along with the PBE model (2.25) to the Study Group Problem *Size Focussing of Nanoparticles*, at the European Study Group with Industry (ESGI 2016) [107].

2.3.4 Laplace Transform Technique

We present the Laplace Transform Technique (LTT) for solving the PBE system (2.25), in the cases of the Models I-III of Section 2.2.1. Given the scaling procedure of Section 2.2.2, we consider the dimensionless and computationally tractable counterparts of the rates defined by Models I-III.

The simple choices of the rate functions allow us to analytically derive the Laplace transform $\hat{m}(\lambda, t)$ of the unknown solution $m(v, t)$ of (2.25). Numerical routines can be applied to recover the density

$m(v, t)$ if a closed-form expression is not available, as discussed in Section 2.3.1.4.

The approach is similar to the proposed in [48, 86] and revised in Section 2.3.1.3. However, we extend the derivation of [48], as detailed in Section 2.2.1. In addition, Model II accounts for a size-dependent growth, forbidden in [86]. Numerical results are shown in Section 2.4.

2.3.4.1 Model I: Constant Aggregation, Growth, Nucleation and Phase Transition

In this section we consider the Model I, described in Section 2.2.1. The model simultaneously accounts for aggregation, growth, nucleation and phase transition. The processes are driven by the following dimensionless and computationally tractable rates:

$$a(v, u, t) = a_0 > 0, \quad g(v, t) = g_0 > 0, \quad n(v, t) = n_0\, \delta(v - v_0), \quad \mu(v, t) = \mu_0 > 0, \tag{2.75}$$

with $n_0, v_0 > 0$ and $\delta(x)$ the Dirac delta function. Given (2.75), the Laplace transform $\hat{m}(\lambda, t) \equiv \int_0^{+\infty} e^{-\lambda v}\, m(v, t)\, dv$ of the solution $m(v, t)$ of (2.25) satisfies

$$\frac{\partial \hat{m}(\lambda, t)}{\partial t} = n_0\, e^{-v_0 \lambda} - (g_0 \lambda + \mu_0 + a_0 M(t))\, \hat{m}(\lambda, t) + \frac{a_0}{2}\hat{m}^2(\lambda, t), \tag{2.76}$$

where $M(t)$ corresponds to the zero-order moment (2.29). The moment $M(t)$ can be computed as the solution of the following Riccati differential equation [108] with constant coefficients:

$$M'(t) = n_0 - \mu_0 M(t) - \frac{a_0}{2}M^2(t), \quad \forall t \in \mathbb{R}^+, \quad M(0) = M_0 \geq 0. \tag{2.77}$$

Given the unique positive equilibrium solution $\bar{M}$ of (2.77), i.e.

$$\bar{M} \equiv \sqrt{\frac{\mu_0^2}{a_0^2} + \frac{2n_0}{a_0}} - \frac{\mu_0}{a_0} > 0, \tag{2.78}$$

it is possible to get the general solution of (2.77) with the help of the auxiliary variable $z(t) \equiv e^{-(\mu_0 + a_0 \bar{M})t}/(M(t) - \bar{M})$:

$$M(t) = \bar{M} + \frac{2\, (M_0 - \bar{M})\, (\mu_0 + a_0 \bar{M})\, e^{-(\mu_0 + a_0 \bar{M})t}}{2\mu_0 \,+\, a_0\, (M_0 + \bar{M}) \,-\, a_0\, (M_0 - \bar{M})\, e^{-(\mu_0 + a_0 \bar{M})t}}, \quad \forall t \in \mathbb{R}^+. \tag{2.79}$$

Equation (2.76) can be interpreted as a family of non-autonomous Riccati differential equations [108], parametrized on $\lambda \in \mathbb{C}$:

$$y'(t) = a - b(t)\, y(t) + c\, y^2(t), \tag{2.80}$$

where

$$y(t) \equiv \hat{m}(\lambda, t), \quad a \equiv n_0\, e^{-v_0 \lambda}, \quad b(t) \equiv g_0 \lambda + \mu_0 + a_0 M(t), \quad c \equiv a_0/2. \tag{2.81}$$

For the sake of availability of the analytical solution of (2.80), we assume

$$M(t) = \bar{M} > 0, \quad \forall t \in \mathbb{R}^+. \tag{2.82}$$

Given (2.82), it follows $b(t) = \bar{b} \equiv g_0 \lambda + \mu_0 + a_0 \bar{M}$, $\forall t \in \mathbb{R}^+$, and (2.80) reads as a family of Riccati differential equations with time-independent coefficients, admitting two equilibrium solutions

$$\bar{m}_\pm(\lambda) = \left(\frac{g_0}{a_0}\lambda + \frac{\mu_0}{a_0} + \bar{M}\right) \pm \sqrt{\left(\frac{g_0}{a_0}\lambda + \frac{\mu_0}{a_0} + \bar{M}\right)^2 - \frac{2n_0}{a_0}e^{-v_0 \lambda}}. \tag{2.83}$$

Remembering that $\hat{m}(0, t) = M(t)$, $\forall t \in \mathbb{R}^+$, we must discard $\bar{m}_+(\lambda)$ because $\bar{m}_+(0) \neq \bar{M}$. Hence, it is possible to only accept $\bar{m}_-(\lambda)$ as the equilibrium solution $\bar{m}(\lambda)$ of (2.80):

$$\bar{m}(\lambda) \equiv \left(\frac{g_0}{a_0}\lambda + \frac{\mu_0}{a_0} + \bar{M} \right) - \sqrt{\left(\frac{g_0}{a_0}\lambda + \frac{\mu_0}{a_0} + \bar{M} \right)^2 - \frac{2n_0}{a_0}e^{-v_0\lambda}}. \tag{2.84}$$

Provided $\bar{m}(\lambda)$ (2.84), it is possible to get $y(t)$ as the general solution of (2.80), invoking the auxiliary variable $z(t) \equiv e^{(\bar{b}+2c\bar{m})t}/(y(t) - \bar{m})$. Then, the Laplace transform $\hat{m}(\lambda, t) = y(t)$ reads

$$\hat{m}(\lambda, t) = \frac{\left[\frac{a_0}{2}(\hat{\omega}_0(\lambda) + \bar{m}(\lambda)) - r(\lambda) \right] \bar{m}(\lambda)\, e^{(r(\lambda) - a_0\bar{m}(\lambda))t} + \left(\frac{a_0}{2}\bar{m}(\lambda) - r(\lambda) \right)(\hat{\omega}_0(\lambda) - \bar{m}(\lambda))}{\left[\frac{a_0}{2}(\hat{\omega}_0(\lambda) + \bar{m}(\lambda)) - r(\lambda) \right] e^{(r(\lambda) - a_0\bar{m}(\lambda))t} - \frac{a_0}{2}(\hat{\omega}_0(\lambda) - \bar{m}(\lambda))}, \tag{2.85}$$

where $r(\lambda) \equiv g_0\lambda + \mu_0 + a_0\bar{M}$ and $\hat{\omega}_0(\lambda)$ is the Laplace transform of the initial condition $\omega_0(v)$ in (2.25). Given the rate functions (2.75) and the assumption (2.82), we have derived the analytical expressions for (i) the Laplace transform $\bar{m}(\lambda)$ of the equilibrium solution $m^*(v)$ of (2.25) and (ii) the Laplace transform $\hat{m}(\lambda, t)$ of the time-dependent solution $m(v, t)$ of (2.25). The closed-form expressions for the inverse of the derived Laplace transforms seem to be not available. Aimed to recover the functions $m^*(v)$ and $m(v, t)$, it is possible to use numerical routines to compute values of the corresponding inverse Laplace transforms, as it was discussed in Section 2.3.1.4.

We remark that the equilibrium solution $m^*(v)$ will be used to select realistic orders of magnitude of initial condition and volume domain for the numerical experiments presented in Section 2.4.1.

2.3.4.2 Model II: Constant Aggregation, Linear Growth and Constant Phase Transition

We consider the Model II of Section 2.2.1, accounting for aggregation, growth and phase transition. The dimensionless and computationally tractable rates in (2.25) are defined as:

$$a(v, u, t) = a_0 > 0, \quad g(v, t) = g_0 v, \quad g_0 > 0, \quad n(v, t) = 0, \quad \mu(v, t) = \mu_0 > 0. \tag{2.86}$$

Given the nucleation rate $n(v, t) = 0$, $\forall v, t \in \mathbb{R}^+$, we must assume the initial condition $\omega_0(v)$ in (2.25) not to be zero everywhere. Otherwise, it follows $m(v, t) = 0$, $\forall v, t \in \mathbb{R}^+$.

Provided the rate functions (2.86), the Laplace transform $\hat{m}(\lambda, t) \equiv \int_0^{+\infty} e^{-\lambda v}\, m(v, t)\, dv$ of the solution $m(v, t)$ of (2.25) satisfies

$$\frac{\partial \hat{m}(\lambda, t)}{\partial t} - g_0\lambda\frac{\partial \hat{m}(\lambda, t)}{\partial \lambda} = -(\mu_0 + a_0 M(t))\,\hat{m}(\lambda, t) + \frac{a_0}{2}\,\hat{m}^2(\lambda, t), \tag{2.87}$$

where $M(t) \equiv \hat{m}(0, t)$ can be computed as the solution of the following Bernoulli differential equation [109]:

$$M'(t) = -\mu_0 M(t) - \frac{a_0}{2}M^2(t), \quad \forall t \in \mathbb{R}^+, \quad M(0) = M_0 \geq 0. \tag{2.88}$$

With the help of the auxiliary variable $z(t) \equiv e^{-\mu_0 t}/M(t)$, it is possible to find the general solution of (2.88):

$$M(t) = \frac{2\,\mu_0\,M_0\,e^{-\mu_0 t}}{2\mu_0 + a_0 M_0(1 - e^{-\mu_0 t})}, \quad \forall t \in \mathbb{R}^+. \tag{2.89}$$

We solve (2.87) using the Method of Characteristics [73]. Given $y(t) \equiv \hat{m}(\lambda, t)|_{\lambda=\varphi(t)}$, with

$$\varphi'(s) = -g_0\,\varphi(s), \quad \forall s \in [0, t], \quad \varphi(t) = \lambda, \tag{2.90}$$

we have $\varphi(s) = \lambda\,e^{g_0(t-s)}$, $\forall s \in [0, t]$, and the *chain rule* [102] provides the derivative of $y(s)$ with respect to s:

$$y'(s) = -(\mu_0 + a_0 M(s))\,y(s) + \frac{a_0}{2}\,y^2(s), \quad \forall s \in [0, t], \quad y(0) = \hat{m}(\varphi(0), 0) = \hat{\omega}_0(\lambda e^{g_0 t}), \tag{2.91}$$

where $\hat{\omega}_0(\lambda)$ corresponds to the Laplace transform of the initial condition $\omega_0(v)$ in (2.25).

With the help of the auxiliary variable $z(s) \equiv e^{-\mu_0 s - a_0 \int_0^s M(\sigma)d\sigma}/y(s)$, it is possible to find $y(s)$ as the

general solution of (2.91) for all $s \in [0,t]$. The Laplace transform $\hat{m}(\lambda, t)$ is recovered by evaluating the found $y(s)$ at the final time $s = t$:

$$\hat{m}(\lambda, t) = \frac{4\,\mu_0^2\,e^{-\mu_0 t}\,\hat{\omega}_0(\lambda e^{g_0 t})}{[2\mu_0 + a_0 M_0 (1 - e^{-\mu_0 t})]\,[2\mu_0 + a_0(1 - e^{-\mu_0 t})(M_0 - \hat{\omega}_0(\lambda e^{g_0 t}))]}, \tag{2.92}$$

where $\hat{\omega}_0(\lambda)$ is the Laplace transform of the initial condition $\omega_0(v)$ in (2.25).

In a general case, it is not possible to find the closed-form inverse $m(v,t)$ of the Laplace transform $\hat{m}(\lambda, t)$ (2.92), and thus numerical routines should be used. However, some particular choices of the initial condition $\omega_0(v)$ allow us to analytically solve the inversion problem and to get an expression for the solution $m(v,t)$ of (2.25). In particular, the initial condition

$$\omega_0(v) = \alpha\,e^{-\beta v}\,\sinh(\gamma v), \quad \alpha \geq 0,\ \beta > \gamma > 0, \tag{2.93}$$

leads to

$$m(v,t) = \hat{\alpha}(t)\,e^{-\hat{\beta}(t)\,v}\,\sinh\left(\hat{\gamma}(t)\,v\right), \quad \forall v, t \in \mathbb{R}^+, \tag{2.94}$$

where

$$\hat{\alpha}(t) \equiv \frac{4\,\alpha\,\gamma^{1/2}\,\mu_0^2\,e^{-(g_0 + \mu_0)t}}{(2\mu_0 + a_0 M_0 (1 - e^{-\mu_0 t}))^2}\left(\gamma + \frac{\alpha\,a_0\,(1 - e^{-\mu_0 t})}{2\mu_0 + a_0 M_0 (1 - e^{-\mu_0 t})}\right)^{-1/2} > 0, \quad \forall t \in \mathbb{R}^+, \tag{2.95}$$

$$\hat{\beta}(t) \equiv \beta\,e^{-g_0 t} > \hat{\gamma}(t) > 0, \quad \forall t \in \mathbb{R}^+, \tag{2.96}$$

$$\hat{\gamma}(t) \equiv \gamma^{1/2}\,e^{-g_0 t}\sqrt{\gamma + \frac{\alpha\,a_0\,(1 - e^{-\mu_0 t})}{2\mu_0 + a_0 M_0 (1 - e^{-\mu_0 t})}} > 0, \quad \forall t \in \mathbb{R}^+. \tag{2.97}$$

The flexibility in the choice of parameters α, β and γ in (2.93) allows us to control the shape of the initial condition. The values of α, β and γ can be selected to mimic the neglected nucleation process, as will be discussed in Section 2.4.2.

2.3.4.3   Model III: Constant Aggregation, Growth and Phase Transition

This section addresses the Model III of Section 2.2.1. We consider the particles aggregation, growth and phase transition, whereas the nucleation mechanism is neglected. The dimensionless and computationally tractable rates in (2.25) are defined as:

$$a(v, u, t) = a_0 > 0, \quad g(v,t) = g_0 > 0, \quad n(v,t) = 0, \quad \mu(v,t) = \mu_0 > 0, \tag{2.98}$$

where the null nucleation rate $n(v,t)$ implies the assumption of a non-null initial condition in (2.25), as discussed in Section 2.3.4.2.

Given (2.98), the Laplace transform $\hat{m}(\lambda, t) \equiv \int_0^{+\infty} e^{-\lambda v}\,m(v,t)\,dv$ of the solution $m(v,t)$ of (2.25) satisfies

$$\frac{\partial \hat{m}(\lambda, t)}{\partial t} = -\left(g_0\,\lambda + \mu_0 + a_0 M(t)\right)\hat{m}(\lambda, t) + \frac{a_0}{2}\hat{m}^2(\lambda, t), \quad \forall \lambda \in \mathbb{C}, \forall t \in \mathbb{R}^+, \tag{2.99}$$

where the zero-order moment $M(t) \equiv \hat{m}(0,t)$ can be computed as (2.89).

Equation (2.99) corresponds to a family of Bernoulli differential equations [109], parametrized on $\lambda \in \mathbb{C}$. With the help of the auxiliary variable $z(t) \equiv e^{-(g_0\lambda + \mu_0)t - a_0 \int_0^t M(s)\,ds} / \hat{m}(\lambda, t)$, it is possible to obtain the general solution of (2.99):

$$\hat{m}(\lambda, t) = \frac{4\,\mu_0^2\,e^{-\mu_0 t}\,e^{-(g_0 t)\lambda}}{(2\mu_0 + a_0 M_0(1 - e^{-\mu_0 t}))^2}\,\frac{(g_0\lambda - \mu_0)\,\hat{\omega}_0(\lambda)}{(g_0\lambda - \mu_0) + 2\,a_0\,\mu_0^2\,\hat{\omega}_0(\lambda)\,\hat{F}(\lambda, t)}, \quad \forall \lambda \in \mathbb{C}, \forall t \in \mathbb{R}^+, \tag{2.100}$$

where $\hat{\omega}_0(\lambda)$ corresponds to the Laplace transform of the initial condition $\omega_0(v)$ in (2.25). The function $\hat{F}(\lambda, t)$ is defined as

$$\hat{F}(\lambda, t) \equiv \left[\frac{x^{\frac{\mu_0 + g_0 \lambda}{\mu_0}} \, _2F_1 \left(1, 2; \frac{2\mu_0 - g_0 \lambda}{\mu_0}; \frac{2\mu_0 + a_0 M_0}{2\mu_0 + a_0 M_0 (1-x)} \right)}{(2\mu_0 + a_0 M_0 (1-x))^2} \right]_{x=1}^{x=e^{-\mu_0 t}}, \quad \forall \lambda \in \mathbb{C}, \, \forall t \in \mathbb{R}^+, \qquad (2.101)$$

with $_2F_1(a, b; c; z)$ the Gauss's Hypergeometric Function [110]. Equation (2.101) is obtained by using the symbolic tool *Integrate*, available in the Wolfram Language [111]. A closed-form expression for the inverse $m(v, t)$ of the Laplace transform (2.100) seems not to be available. Numerical routines should be used to recover the unknown solution $m(v, t)$ of (2.25), as it was discussed in Section 2.3.1.4.

2.3.4.4 Benefits & Drawbacks

We have presented the Laplace Transform Technique (LTT) for solving the PBE system (2.25), in the cases of the Models I-III of Section 2.2.1. The main benefits of LTT developed in this section are outlined here:

1. We have extended the derivation of LTT to a broader range of rate functions than has been previously available in the literature [48, 86].

2. The derived solutions analytically account for impulsive nucleation rates, such as $n(v, t) \propto \delta(v - v_0)$ with $v_0 > 0$ and $\delta(x)$ the Dirac delta. As discussed in Section 2.3.3.2, GMOC cannot analytically account for such impulsive rates.

3. The presented LTT allows the evaluation of the Laplace transformed solution of (2.25) at any time, without evolving from an initial condition, as required by GMOC.

4. LTT provides accurate and efficient solutions of the PBE (2.25), as will be shown in Section 2.4. The obtained results can be used as baselines for validation and evaluation of other numerical methods.

The principal drawbacks of LTT are discussed below:

1. The flexibility in the choice of the initial condition $\omega_0(v)$ for Model I is limited by the hypothesis (2.82), imposing the zero-order moment to its asymptotic value. In particular, (2.82) requires $\int_0^{+\infty} \omega_0(v) \, dv = \bar{M} > 0$, with $\bar{M}$ defined as (2.78). We remark that such an assumption is not needed by GMOC.

2. The analytical solution $m(v, t)$ (2.94) for Model II assumes the initial condition (2.93). In a general case, it is not possible to find the closed-form expression for $m(v, t)$. On the other hand, GMOC works for any choice of (suitable) initial condition.

3. The simplified choices of the rate functions and the required hypothesis lead to a limited description of the reaction physics.

4. LTT may result in complicated expressions for the derived Laplace transforms, such as (2.100). The numerical inversion of these functions is a challenging task, as will be discussed in Section 2.4.

The presented here LTT will be used in Section 2.4 as a baseline for validation, evaluation and comparison of the other methodologies derived in this Thesis.

2.3.5 Laplace Induced Splitting Method

Section 2.3.4 provides an efficient tool for solving (2.25) in the cases of Models I-III described in Section 2.2.1. However, this approach is only available under specific restrictive assumptions and for the limited choices of the rate functions. With the purpose to derive an efficient methodology for more realistic models, we design a novel splitting approach, which we call *Laplace Induced Splitting Method* (LISM).

The idea behind LISM is the following. First, one decomposes the PBE (2.25) into a sum of simpler sub-problems and solves them individually using the most efficient method available for simplified problems, i.e. LTT. Then, a splitting algorithm recovers the solution of the complete system (2.25) with the help of the derived solutions for the partial problems. In principle, the splitting of (2.25) into simpler sub-problems should support complex physical rate functions in (2.25), being only limited by the availability of efficient solutions for the considered sub-problems.

The idea of using splitting methodologies is not new, and it has been proposed previously for solving integro-differential equations, such as, e.g., Fokker-Planck equation [112, 113, 114]. However, to our knowledge, this is the first time when splitting schemes have been combined with Laplace induced analytical solutions for integrating PBE systems.

The section is structured as follows. Section 2.3.5.1 suggests the sub-problems the PBE (2.25) can be divided into, when the rates of Models I-III are considered. In addition, Section 2.3.5.1 presents the splitting methodology to recover the solution of the complete problem (2.25). As a splitting scheme, we choose the second-order accurate *Symmetrized Strang Splitting Method* (SSSM) [115], though other splitting algorithms can be considered within LISM. Then, Section 2.3.5.2, Section 2.3.5.3 and Section 2.3.5.4 provide the Laplace induced solutions for the defined sub-problems. Section 2.3.5.5 discusses a possible choice of volume grid to deal efficiently with the nucleation terms. Benefits and drawbacks of LISM are outlined in Section 2.3.5.6.

2.3.5.1 Splitting of PBE (2.25) for Models I-III

Let us decompose the PBE (2.25) into a sum of integral and differential operators:

$$\frac{\partial m(v,t)}{\partial t} = \mathcal{D}m(v,t) + \mathcal{I}m(v,t), \quad \forall v,t \in \mathbb{R}^+, \tag{2.102}$$

where the differential operator $\mathcal{D}$ and the integral operator $\mathcal{I}$ are defined as

$$\mathcal{D}m(v,t) \equiv -\frac{\partial(\,g(v,t)\,m(v,t)\,)}{\partial v} + n(v,t) - \mu(v,t)\,m(v,t), \quad \forall v,t \in \mathbb{R}^+, \tag{2.103}$$

$$\mathcal{I}m(v,t) \equiv \frac{1}{2}\int_0^v a(v-u,u,t)\,m(v-u,t)\,m(u,t)\,du$$
$$- m(v,t)\int_0^{+\infty} a(v,u,t)\,m(u,t)\,du, \quad \forall v,t \in \mathbb{R}^+. \tag{2.104}$$

In order to address the Models I-III, we consider the following sub-problems:

$$A: \begin{cases} \frac{\partial m(v,t)}{\partial t} &= \mathcal{D}m(v,t), \quad \forall v,t \in \mathbb{R}^+, \\ g(v,t) &= g_0\,v, \quad n(v,t) = n_0\,\delta(v-v_0), \quad \mu(v,t) = \mu_0, \quad \forall v,t \in \mathbb{R}^+, \end{cases} \tag{2.105}$$

$$B: \begin{cases} \frac{\partial m(v,t)}{\partial t} &= \mathcal{D}m(v,t), \quad \forall v,t \in \mathbb{R}^+, \\ g(v,t) &= g_0, \quad n(v,t) = n_0\,\delta(v-v_0), \quad \mu(v,t) = \mu_0, \quad \forall v,t \in \mathbb{R}^+, \end{cases} \tag{2.106}$$

$$C: \begin{cases} \frac{\partial m(v,t)}{\partial t} &= \mathcal{I}m(v,t), \quad \forall v,t \in \mathbb{R}^+, \\ a(v,u,t) &= a_0, \quad \forall v,u,t \in \mathbb{R}^+, \end{cases} \tag{2.107}$$

with $a_0, g_0, v_0, \mu_0 > 0$, $n_0 \geq 0$ and $\delta(x)$ the Dirac delta.

The solution of Model I can be recovered by combining the solutions of B (2.106) and C (2.107). The

Model II is given by the composition of A (2.105) and C (2.107), with $n_0 = 0$. The Model III is obtained from B (2.106) and C (2.107), with $n_0 = 0$.

In the following sections, we derive the solutions $m(v, t; \omega_0(\cdot))$ of the sub-problems A (2.105), B (2.106) and C (2.107), for any choice of the initial condition $m(v, 0) = \omega_0(v)$.

These solutions will be used for recovering, with the help of SSSM, the solution $m(v, t)$ of the complete problem (2.25).

In particular, let $y_i \equiv \{m_{k,i}\}_{k=0}^{N}$ be the values of the solution of (2.25) evaluated at time $t_i = i\tau$, with $i \in \mathbb{N}$ and a time step $\tau > 0$, along the volume grid $\mathbf{v} \equiv \{\varphi_k\}_{k=0}^{N}$, i.e. $m_{k,i} \equiv m(\varphi_k, t_i)$, $\forall i \in \mathbb{N}$, $\forall k = 0, .., N$.

The volume grid $\mathbf{v}$ is chosen such that $0 = \varphi_0 < \varphi_1 < .. < \varphi_N$. For the sake of simplicity, the time step $\tau > 0$ is constant.

Then, we define the operator $L_X : [0, +\infty)^{N+2} \to [0, +\infty)^{N+1}$ as the element-wise application of the solution $m_X(\cdot, \tau; \omega_0(\cdot))$ of a problem $X = A, B, C$ to a vector y_i:

$$L_X(y_i, \tau) \equiv m_X(\mathbf{v}, \tau; \omega_0(\mathbf{v})), \quad \omega_0(\mathbf{v}) \equiv y_i, \tag{2.108}$$

where the function $m_X(\cdot, \tau; \omega_0(\cdot))$ is computed for each element of the grid $\mathbf{v}$, i.e. $m_X(\mathbf{v}, \tau; \omega_0(\mathbf{v})) \equiv \{m_X(\varphi_k, \tau; \omega_0(\mathbf{v}))\}_{k=0}^{N}$ and $\omega_0(\mathbf{v}) \equiv \{\omega_0(\varphi_k)\}_{k=0}^{N}$ for a sub-problem $X = A, B, C$.

Given definition (2.108), the solution values y_i of Models I-III can be updated according to the SSSM scheme as:

$$y_{i+1/2} = L_X(y_i, \tau/2), \quad \tilde{y}_{i+1} = L_Y(y_{i+1/2}, \tau), \quad y_{i+1} = L_X(\tilde{y}_{i+1}, \tau/2), \tag{2.109}$$

with (i) $X = B$, $Y = C$ for Model I, (ii) $X = A$, $Y = C$, $n_0 = 0$ for Model II and (iii) $X = B$, $Y = C$, $n_0 = 0$ for Model III.

2.3.5.2 Solution of Sub-Problem A

Here, we derive the analytical solution of the sub-problem A (2.105), for any choice of the initial condition $m(v, 0) = \omega_0(v)$. The Laplace transform $\hat{m}(\lambda, t) \equiv \int_0^{+\infty} e^{-\lambda v} m(v, t) \, dv$ of the solution $m(v, t)$ of (2.105) satisfies:

$$\frac{\partial \hat{m}(\lambda, t)}{\partial t} - g_0 \lambda \frac{\partial \hat{m}(\lambda, t)}{\partial \lambda} = -\mu_0 \hat{m}(\lambda, t) + n_0 e^{-v_0 \lambda}, \quad \hat{m}(\lambda, 0) = \hat{\omega}_0(\lambda), \quad \forall \lambda \in \mathbb{C}, \forall t \in \mathbb{R}^+. \tag{2.110}$$

Following the Method of Characteristics [73], we define $y(t) \equiv \hat{m}(\lambda, t)|_{\lambda = \varphi(t)}$, where

$$\varphi'(s) = -g_0 \, \varphi(s), \quad \forall s \in [0, t], \quad \varphi(t) = \lambda. \tag{2.111}$$

It follows $\varphi(s) = \lambda \, e^{g_0(t-s)}$, $\forall s \in [0, t]$, and the *chain rule* [102] provides the derivative of $y(s)$ with respect to s:

$$y'(s) = -\mu_0 \, y(s) + n_0 \, e^{-\lambda \, v_0 \, e^{g_0(t-s)}}, \quad \forall s \in [0, t], \quad y(0) = \hat{\omega}_0(\lambda e^{g_0 t}). \tag{2.112}$$

With the help of auxiliary variable $z(s) \equiv y(s) \, e^{\mu_0 s}$, it is possible to obtain the general solution $y(s)$ of (2.112) for all $s \in [0, t]$. The Laplace transform $\hat{m}(\lambda, t) = y(t)$ is computed by evaluating the derived $y(s)$ at the final time $s = t$:

$$\hat{m}(\lambda, t) = \hat{\omega}_0(\lambda e^{g_0 t}) \, e^{-\mu_0 t} + \frac{n_0}{g_0} \left[E_{\frac{g_0 + \mu_0}{g_0}} (v_0 \lambda) - E_{\frac{g_0 + \mu_0}{g_0}} \left(v_0 e^{g_0 t} \lambda \right) e^{-\mu_0 t} \right], \tag{2.113}$$

where $E_a(z)$ corresponds to the Exponential Integral function [116], defined as

$$E_a(z) \equiv \int_1^{+\infty} e^{-zv} v^{-a} \, dv, \quad \forall a, z \in \mathbb{C}. \tag{2.114}$$

We rewrite (2.113) as

$$\hat{m}(\lambda, t) = \int_0^{+\infty} e^{-\lambda v} F(v, t)\, dv, \tag{2.115}$$

where

$$F(v, t) \equiv \omega_0(v e^{-g_0 t})\, e^{-(g_0 + \mu_0)\, t} + g_0^{-1}\, n_0\, v_0^{\mu_0/g_0}\, v^{-(g_0 + \mu_0)/g_0}\, \mathbb{1}_{[v_0, v_0\, e^{g_0 t})}(v), \tag{2.116}$$

and $\mathbb{1}_X(x) = 1$ if $x \in X$, zero otherwise. By definition of the Laplace transform, the solution $m(v, t)$ of (2.105) must be equal to the function $F(v, t)$ (2.116) up to a set of zero measure:

$$m(v, t) = \omega_0(v e^{-g_0 t})\, e^{-(g_0 + \mu_0)\, t} + g_0^{-1}\, n_0\, v_0^{\mu_0/g_0}\, v^{-(g_0 + \mu_0)/g_0}\, \mathbb{1}_{[v_0, v_0\, e^{g_0 t})}(v), \tag{2.117}$$

where $\omega_0(v)$ corresponds to any given initial condition of (2.105).

Operator L_A. The formula (2.117) allows us to update the defined in Section 2.3.5.1 vector $y_i \in [0, +\infty)^{N+1}$ according to the sub-problem A (2.105). As introduced before, we define the operator $L_A : [0, +\infty)^{N+2} \to [0, +\infty)^{N+1}$ as the element-wise application of $m(\cdot, \tau)$ (2.117), $\tau > 0$, to the vector y_i:

$$L_A(y_i, \tau) \equiv m(\mathbf{v}, \tau), \quad \omega_0(\mathbf{v}) \equiv y_i, \tag{2.118}$$

where the functions $m(\cdot, \tau)$ and $\omega_0(\cdot)$ in (2.117) are computed for each element of the grid $\mathbf{v}$, i.e. $m(\mathbf{v}, \tau) \equiv \{m(\varphi_k, \tau)\}_{k=0}^N$ and $\omega_0(\mathbf{v}) \equiv \{\omega_0(\varphi_k)\}_{k=0}^N$.
Formula (2.117) implies that the initial condition must be evaluated on the shifted grid

$$\mathbf{v}_{s1} \equiv \mathbf{v}\, e^{-g_0 \tau} \equiv \{\varphi_k\, e^{-g_0 \tau}\}_{k=0}^N. \tag{2.119}$$

A linear interpolation of the initial data y_i allows us to obtain the required values of the initial condition. Since $0 < e^{-g_0 \tau} < 1$, one gets $0 = \varphi_0 \leq \varphi_k\, e^{-g_0 \tau} < \varphi_N$, $\forall k = 0, .., N$. As a result, the proposed interpolation is computed without any data extrapolation.

2.3.5.3   Solution of Sub-Problem B

In this section we derive the analytical solution $m(v, t)$ of the sub-problem B (2.106), for any choice of the initial condition $m(v, 0) = \omega_0(v)$. The Laplace transform $\hat{m}(\lambda, t) \equiv \int_0^{+\infty} e^{-\lambda v} m(v, t)\, dv$ satisfies:

$$\frac{\partial \hat{m}(\lambda, t)}{\partial t} = -(g_0\, \lambda + \mu_0)\, \hat{m}(\lambda, t) + n_0\, e^{-v_0 \lambda}, \quad \hat{m}(\lambda, 0) = \hat{\omega}_0(\lambda), \quad \forall \lambda \in \mathbb{C}, \forall t \in \mathbb{R}^+. \tag{2.120}$$

The equilibrium solution of (2.120) is given by $\bar{m}(\lambda)$:

$$\bar{m}(\lambda) = \frac{n_0\, e^{-v_0 \lambda}}{g_0\, \lambda + \mu_0}. \tag{2.121}$$

The inverse function of $\bar{m}(\lambda)$ provides the equilibrium solution $m^*(v)$ of (2.106):

$$m^*(v) = g_0^{-1}\, n_0\, e^{-\frac{\mu_0}{g_0}(v - v_0)}\, \mathbb{1}_{[v_0, +\infty)}(v), \tag{2.122}$$

where $\mathbb{1}_X(x) = 1$ if $x \in X$, zero otherwise. Equation (2.120) corresponds to a family of linear Ordinary Differential Equations [117], parametrized on $\lambda \in \mathbb{C}$. With the help of the auxiliary variable $z(t) \equiv \hat{m}(\lambda, t)\, e^{(g_0 \lambda + \mu_0)t}$, we obtain the general solution $\hat{m}(\lambda, t)$:

$$\hat{m}(\lambda, t) = (\hat{\omega}_0(\lambda) - \bar{m}(\lambda))\, e^{-(g_0 \lambda + \mu_0)t} + \bar{m}(\lambda), \tag{2.123}$$

with $\bar{m}(\lambda)$ (2.121). The inverse function of $\hat{m}(\lambda, t)$ (2.123) provides the general solution $m(v, t)$ of B (2.106):

$$m(v, t) = e^{-\mu_0 t}\, \omega_0(v - g_0 t)\, \mathbb{1}_{[g_0 t, +\infty)}(v) + g_0^{-1}\, n_0\, e^{-\frac{\mu_0}{g_0}(v - v_0)}\, \mathbb{1}_{[v_0, v_0 + g_0 t)}(v), \tag{2.124}$$

where $\mathbb{1}_X(x) = 1$ if $x \in X$, zero otherwise. The solution (2.124) stands for any choice of the initial condition $m(v, 0) = \omega_0(v)$ of (2.106).

Operator L_B. The formula (2.124) allows us to update the solution vector $y_i \in [0, +\infty)^{N+1}$ according to the sub-problem B (2.106). As before, we define the operator $L_B : [0, +\infty)^{N+2} \to [0, +\infty)^{N+1}$ as the element-wise application of $m(\cdot, \tau)$ (2.124), $\tau > 0$, to the vector y_i:

$$L_B(y_i, \tau) \equiv m(\mathbf{v}, \tau), \quad \omega_0(\mathbf{v}) \equiv y_i, \tag{2.125}$$

where the functions $m(\cdot, \tau)$ and $\omega_0(\cdot)$ in (2.124) are computed for each element of the grid $\mathbf{v}$, i.e. $m(\mathbf{v}, \tau) \equiv \{m(\varphi_k, \tau)\}_{k=0}^N$ and $\omega_0(\mathbf{v}) \equiv \{\omega_0(\varphi_k)\}_{k=0}^N$.

Formula (2.124) implies that the initial condition must be evaluated on the shifted grid

$$\mathbf{v}_{s2} \equiv (\mathbf{v} - g_0\tau) \, \mathbb{1}_{[g_0\tau, +\infty)}(\mathbf{v}) \equiv \{(\varphi_k - g_0\tau) \, \mathbb{1}_{[g_0\tau, +\infty)}(\varphi_k)\}_{k=0}^N. \tag{2.126}$$

A linear interpolation of the initial data y_i allows us to get the required values of the initial condition. Since $g_0, \tau > 0$, one gets $0 = \varphi_0 \leq (\varphi_k - g_0\tau) \mathbb{1}_{[g_0\tau, +\infty)}(\varphi_k) < \varphi_N, \ \forall k = 0, .., N$. As a result, the proposed interpolation is computed without any data extrapolation.

2.3.5.4   Solution of Sub-Problem C

The Laplace transform $\hat{m}(\lambda, t) \equiv \int_0^{+\infty} e^{-\lambda v} m(v, t) \, dv$ of the solution $m(v, t)$ of C (2.107) satisfies the following differential equation:

$$\frac{\partial \hat{m}(\lambda, t)}{\partial t} = -a_0 M(t) \hat{m}(\lambda, t) + \frac{a_0}{2} \hat{m}^2(\lambda, t), \quad \hat{m}(\lambda, 0) = \hat{\omega}_0(\lambda), \quad \forall \lambda \in \mathbb{C}, \forall t \in \mathbb{R}^+, \tag{2.127}$$

where $M(t) \equiv \hat{m}(0, t)$. The moment $M(t)$ can be computed as the solution of the Bernoulli differential equation [109]:

$$M'(t) = -\frac{a_0}{2} M^2(t), \quad \forall t \in \mathbb{R}^+, \quad M(0) = M_0 \geq 0. \tag{2.128}$$

With the help of the auxiliary variable $z(t) \equiv 1/M(t)$, it is possible to obtain the general solution of (2.128):

$$M(t) = \frac{2 M_0}{2 + a_0 M_0 t}, \quad \forall t \in \mathbb{R}^+. \tag{2.129}$$

Equation (2.127) corresponds to a family of Bernoulli differential equations [109], parametrized on $\lambda \in \mathbb{C}$. The change of variable $z(t) \equiv e^{-a_0 \int_0^t M(s) \, ds} / \hat{m}(\lambda, t)$ allows solving (2.127):

$$\hat{m}(\lambda, t) = \frac{4 \hat{\omega}_0(\lambda)}{(2 + a_0 M_0 t) [2 + a_0 (M_0 - \hat{\omega}_0(\lambda)) t]}, \tag{2.130}$$

where $\hat{\omega}_0(\lambda)$ is the Laplace transform of the initial condition $m(v, 0) = \omega_0(v)$ of (2.107). Without specifying the initial condition $\omega_0(v)$, it is not possible to invert (2.130) in a closed form.

Assuming the dynamics during only a small time interval, (2.130) leads to the following second-order accurate approximation:

$$\hat{m}(\lambda, t) = (1 - a_0 M_0 t) \hat{\omega}_0(\lambda) + \frac{a_0}{2} t \hat{\omega}_0^2(\lambda) + O(t^2). \tag{2.131}$$

The inverse function of (2.131) gives an approximation of the solution of C (2.107), for any choice of the initial condition $\omega_0(v)$, with $M_0 \equiv \int_0^{+\infty} \omega_0(v) \, dv$:

$$m(v, t) = (1 - a_0 M_0 t) \omega_0(v) + \frac{a_0}{2} t \int_0^v \omega_0(v - u) \omega_0(u) \, du + O(t^2). \tag{2.132}$$

Re-arranging (2.132) as

$$\frac{m(v,t) - \omega_0(v)}{t} = -a_0 M_0 \,\omega_0(v) + \frac{a_0}{2} \int_0^v \omega_0(v-u)\,\omega_0(u)\,du + O(t), \tag{2.133}$$

we notice that (2.132) arises from the first-order accurate discretization in time of (2.107).

Operator L_C. The formula (2.132) updates the solution vector $y_i \in [0, +\infty)^{N+1}$ according to the sub-problem C (2.107), within a small interval of time. Thus, we define the operator $L_C : [0, +\infty)^{N+2} \to [0, +\infty)^{N+1}$ as the element-wise application of $m(\cdot, \tau)$ (2.132), $\tau > 0$, to the vector y_i:

$$L_C(y_i, \tau) \equiv m(\mathbf{v}, \tau), \quad \omega_0(\mathbf{v}) \equiv y_i, \tag{2.134}$$

where the functions $m(\cdot, \tau)$ and $\omega_0(\cdot)$ in (2.132) are computed for each element of the grid $\mathbf{v}$, i.e. $m(\mathbf{v}, \tau) \equiv \{m(\varphi_k, \tau)\}_{k=0}^N$ and $\omega_0(\mathbf{v}) \equiv \{\omega_0(\varphi_k)\}_{k=0}^N$.

The convolution term is approximated by using the Trapezoidal quadrature rule [100], evaluating the initial condition at $\varphi_k - \varphi_j$, $\forall k = 0, .., N$, $\forall j = 0, .., k$. The required values are computed by linear interpolation of y_i, without any data extrapolation, since $0 = \varphi_0 \le \varphi_k - \varphi_j \le \varphi_N$, $\forall k = 0, .., N$, $\forall j = 0, .., k$. The proposed interpolation can be avoided by choosing the uniform volume grid $\mathbf{v} \equiv \{\varphi_k = kh\}_{k=0}^N$, $h > 0$, as shown by (2.73). However, $\mathbf{v}$ should be kept without any particular structure, for the reason specified below.

2.3.5.5 Volume Grid for Nucleation

If the nucleation process is considered, i.e. $n_0 > 0$, the following remark should be made for the choice of the time step size τ and the volume grid $\mathbf{v}$. Given $\tau > 0$, the formulas (2.117) and (2.124), when incorporated in the scheme (2.109), imply that the grid $\mathbf{v}$ must contain some points in the intervals

$$I \equiv [v_0, v_0\, e^{g_0 \tau/2}) \quad \text{and} \quad J \equiv [v_0, v_0 + g_0 \tau/2) \tag{2.135}$$

respectively. Otherwise, the corresponding terms in (2.117) and (2.124) are discarded.

Taking $\tau \to 0$, the intervals (2.135) can be arbitrarily small, not holding any point of the grid $\mathbf{v}$, if the latter is not properly chosen. On the other hand, it is possible to fill in advance the intervals (2.135) with a reasonable amount of grid points. The resulting grid step size would be particularly small, especially if $\tau \to 0$. As a consequence, the uniform grid is not affordable and an uneven choice of points should be more efficient, providing the reason to keep $\mathbf{v}$ without any particular structure. As already stated, the drawback consists in the interpolation required for computing the convolution term.

Given $n_0 > 0$ and the volume domain $[0, v_{\max}]$, with $I, J \subset [0, v_{\max}]$, we propose the following uneven grid

$$\hat{\mathbf{v}} \equiv \mathbf{v}_1 \cup \mathbf{v}_2 \cup \mathbf{v}_3. \tag{2.136}$$

The grid $\mathbf{v}_1$ spreads over the interval $[0, v_0)$, placing $N_1 > 0$ uniformly distributed points with step size $h_1 > 0$. The grid $\mathbf{v}_2$ covers the intervals (2.135) with $N_2 > 0$ points equally spaced by $h_2 > 0$. The grid $\mathbf{v}_3$ ranges in the remaining part of the volume domain $[0, v_{\max}]$, with $N_3 > 0$ uniformly distributed points with step size $h_3 > 0$. The step sizes h_1 and h_3 can be chosen bigger than h_2. The proposed grid (2.136) covers the volume intervals (2.135) for any $\tau > 0$, without being affected by the small step size h_2.

2.3.5.6 Benefits & Drawbacks

We have presented the Laplace Induced Splitting Method (LISM) to integrate the PBE (2.25) in the cases of Models I-III. The main advantages of LISM are discussed here:

1. The presented LISM extends the LTT solutions of Models I-III, derived in Section 2.3.4. In particular, LISM simultaneously accounts for the processes of aggregation, growth, nucleation and phase transition. Also, it allows us to relax additional hypothesis, such as (2.82), and to consider any possible initial condition.

2. The novel LISM analytically accounts for impulsive nucleation rates, such as $n(v, t) \propto \delta(v - v_0)$ with $v_0 > 0$ and $\delta(x)$ the Dirac delta.

3. The analytical expressions (2.117) and (2.124) allow us to design the grid (2.136), carrying information on the solution of the PBE (2.25).

4. In the tested cases, LISM provides accurate and efficient solutions of the PBE (2.25). See Section 2.4 for more details.

5. The splitting of (2.25) into simpler sub-problems suggests a way for improving the accuracy of solutions of the PBE (2.25) in the case of the realistic shapes of the rate functions. See Section 2.6 for further discussion.

The principal limitations of the presented LISM method are summarised below:

1. The solutions of the sub-problems must be obtained for any choice of the initial condition $\omega_0(v)$. In fact, this is the requirement for using such formulas as the updating schemes of generic values of the solution of the complete problem.

2. The sub-problem C (2.107) can be solved analytically only for some particular shapes of $\omega_0(v)$, such as, e.g., (2.93). Otherwise, the numerical schemes should be applied, as discussed in Section 2.3.5.4.

3. The evaluation of (2.117), (2.124) and (2.132) requires the interpolation of the initial data, which potentially may affect the quality of the integration. An introduction of the control over such an error is advised.

Section 2.4 presents numerical experiments for testing LISM in comparison with the other approaches proposed in this Thesis.

2.4 Numerical Experiments

In this section we test the developed and presented in Section 2.3 methodologies for solving the PBE system (2.25). As motivated at the beginning of the chapter, special attention is paid to the efficiency of the methods in providing accurate results.

We use the solutions obtained with the Laplace Transform Technique (LTT) of Section 2.3.4 as baselines for the validation and comparative analysis of (a) the Laplace Induced Splitting Method (LISM) of Section 2.3.5, (b) the Generalised Method Of Characteristics (GMOC) of Section 2.3.3 and (c) the Stochastic Simulation Algorithm (SSA) of Section 2.3.2.

The accuracy of the solutions $m(v, t)$ provided by LISM, GMOC and SSA is quantified by the error function

$$\varepsilon(v, t) \equiv \frac{|m_{LTT}(v, t) - m(v, t)|}{\left[\int_0^{v_{\max}} m_{LTT}(v, t)^2 \, dv \right]^{1/2}}, \quad \forall v \in [0, v_{\max}], \, \forall t \in [0, T_{\max}], \tag{2.137}$$

where $m_{LTT}(v, t)$ is defined as the LTT solution, $[0, v_{\max}]$ and $[0, T_{\max}]$ are the integration domains of volume and time respectively.

The computational efficiency of the tested methodologies is measured by recording the computational times required to fulfil the following criterion:

$$\max_{\substack{v \in [0, v_{\max}] \\ t \in [0, T_{\max}]}} \varepsilon(v, t) \propto \varepsilon_{\max}, \tag{2.138}$$

with $\varepsilon_{\max} > 0$ a tunable order of magnitude and $\varepsilon(v, t)$ defined as (2.137).

In order to judge the performance of the different approaches for realistic settings, we employ the rate functions, modelling the Dynamic Development of *latex* Particles Morphology, discussed in Appendix 2.A. In particular, the parameters of Models I-III assume the orders of magnitude achieved by the dimensionless counterparts of the DDPM rates, summarised in Table 2.C.1 of Appendix 2.C.

Section 2.4.1 presents the proposed tests for the Model I introduced in Section 2.3.4.1. Section 2.4.2 analyses the performance of the new methods when applied to Model II from Section 2.3.4.2, whereas Section 2.4.3 uses the Model III of Section 2.3.4.3 as a benchmark for the evaluation of the derived numerical approaches.

2.4.1 Model I: Constant Aggregation, Growth, Nucleation and Phase Transition

This section investigates the accuracy (2.137) and the computational effort to meet (2.138) of the designed methodologies in the case of the Model I discussed in Section 2.3.4.1. The definition of Model I is completed by a choice of the rates parameters and the initial condition.

As discussed before, the parameters of Model I assume the orders of magnitude of the dimensionless rate functions summarised in Table 2.C.1 of Appendix 2.C and are chosen to be:

$$a(v, u, t) = a_0 = 10^2, \quad g(v, t) = g_0 = 10^3, \quad \mu(v, t) = \mu_0 = 10^{-2},$$
$$n(v, t) = n_0 \, \delta(v - v_0), \quad n_0 = 10^{-1}, \quad v_0 = 0.027, \tag{2.139}$$

with $\delta(x)$ the Dirac delta.

The initial condition $\omega_0(v)$ in (2.25) is set to

$$\omega_0(v) = \alpha \, v^\beta \, e^{-\gamma v}, \quad \forall v \in \mathbb{R}^+, \tag{2.140}$$

with $\beta = 10^{-1}$, $\gamma = 10^{-2}$ and α guaranteeing (2.82). As shown in Figure 2.3, the initial condition $\omega_0(v)$ (2.140) assumes the same orders of magnitude as of the equilibrium solution $m^*(v)$ of Model I for the rates (2.139). The equilibrium solution $m^*(v)$ is obtained using LTT, followed by inverting the Laplace transform $\bar{m}(\lambda)$ (2.84) with the MATLAB function *nilt*, revised in Section 2.3.1.4.
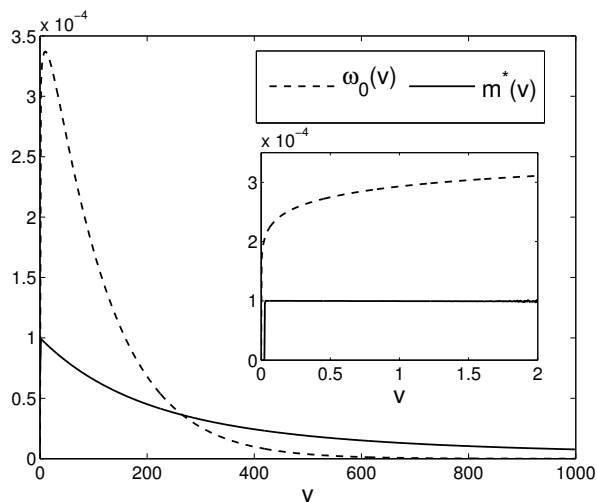
Figure 2.3: Initial condition $\omega_0(v)$ (2.140) (dashed) and equilibrium solution $m^*(v)$ (solid) of Model I for the rates (2.139). The equilibrium solution $m^*(v)$ is obtained using LTT, followed by inverting the Laplace transform $\bar{m}(\lambda)$ (2.84) with the MATLAB function *nilt*, revised in Section 2.3.1.4. The numerical routine requires 2×10^{-3} sec of computation of a 2.70GHz processor, running a 64-bit Linux operating system.

The defined in such a way model was then solved using three different numerical methods LISM, GMOC and SSA applied to the PBE system (2.25). We monitor the accuracy (2.137) and the computational effort required to fulfil (2.138) for

$$v_{\max} = 2, \quad T_{\max} = 10^{-3}, \quad \varepsilon_{\max} = 10^{-1}. \tag{2.141}$$

The integration of (2.25) by GMOC requires the point-wise evaluation (2.61) of the rate $n(v,t)$ (2.139). The numerical evaluation of the Dirac delta $\delta(v - v_0)$ in (2.139) is performed by assuming that the nucleation process spreads over a specified size range, as suggested in [55] and discussed in Section 2.3.1.2. In particular, we propose the following approximation:

$$\delta(v - v_0) \approx \mathcal{N}(v; v_0, \sigma_0), \quad \forall v \in \mathbb{R}^+, \quad v_0 \gg \sigma_0 > 0, \tag{2.142}$$

where $\mathcal{N}(v; \mu, \sigma)$ denotes the probability density function of a Gaussian with mean μ and standard deviation σ. In order to make the Gaussian very narrow, the standard deviation σ_0 should be chosen much smaller than v_0.

Table 2.2 summarises the settings for the integration methods meeting the criterion (2.138) with the choices of (2.141) and provides the required computational time in each case. The computed solutions $m(v,t)$ and the corresponding errors $\varepsilon(v,t)$ (2.137) are shown in Figure 2.4.

81

Method	Technical Details	Time Step τ	Volume Grid & Grid Step h	Software & Hardware	Error ε	CPU Time
LTT	Inversion of $\hat{m}(\lambda, t)$ (2.85) with *nilt* [99]	-	-	MATLAB **BCAM code** 64-bit Linux OS 2.70GHz proc.	-	6×10^{-3} sec
LISM	Updating Scheme (2.109) for Model I	Constant $\tau = 10^{-5}$	Uneven grid $\hat{\mathbf{v}}$ (2.136) $h_1 \approx 5.5 \times 10^{-4}$, $N_1 = 50$ $h_2 \approx 5 \times 10^{-5}$, $N_2 = 100$ $h_3 \approx 5 \times 10^{-4}$, $N_3 = 4000$	C++ **BCAM code** 64-bit Linux OS 2.40GHz proc.	Fig. 2.4a	10^3 sec
GMOC	Approximation (2.142) with $v_0 = 0.027$ and $\sigma_0 = 0.001$	Constant $\tau = 2.5 \times 10^{-8}$	Grid $\mathbf{v} = \{\varphi_k = kh\}_{k=0}^N$ $h = 2.5 \times 10^{-4}$, $N = 8000$	C++ **BCAM code** 64-bit Linux OS 2.40GHz proc.	Fig. 2.4b	7.5×10^3 sec
SSA	Scaling (2.60) with $\kappa = 10^7$ Sample Size $S = 10^3$	Sampled $\tau \in (0, 4) \times 10^{-8}$	Grid $\mathbf{v} = \{\varphi_k = kh\}_{k=0}^N$ $h = 8 \times 10^{-3}$, $N = 250$	C++ **BCAM code** 64-bit Linux OS 2.40GHz proc.	Fig. 2.4c	2.1×10^5 sec

Table 2.2: Settings and computational times for the integration methods meeting (2.138) at $v_{\max} = 2$, $T_{\max} = 10^{-3}$ and $\varepsilon_{\max} = 10^{-1}$, in the case of Model I with rates (2.139) and initial condition (2.140). All **BCAM codes** were developed within this Thesis.
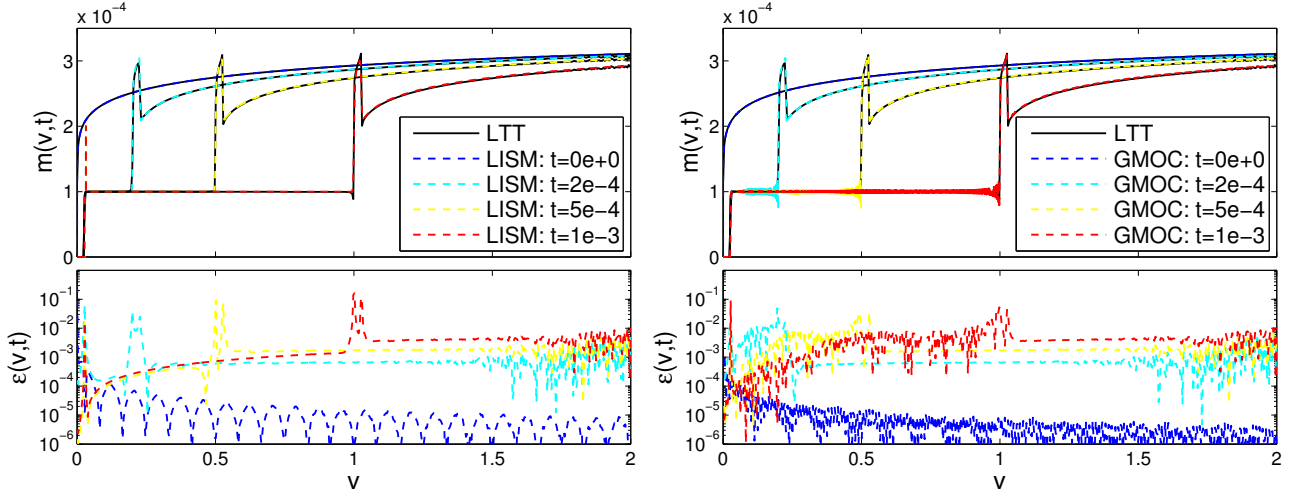
(a) LISM (dashed) vs. LTT (solid).

(b) GMOC (dashed) vs. LTT (solid).
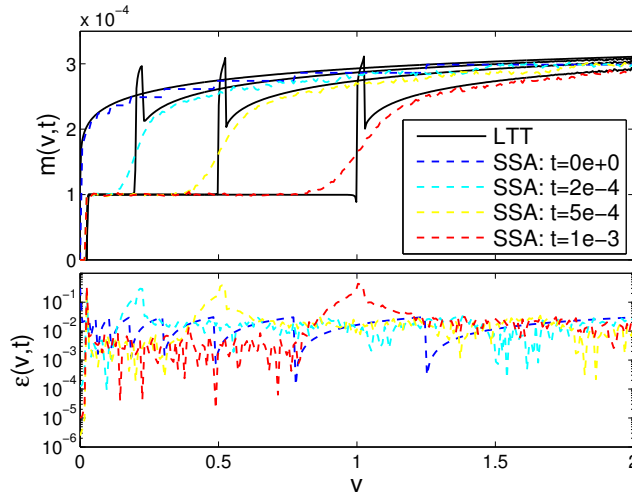
(c) SSA (dashed) vs. LTT (solid).

Figure 2.4: Comparison of (a) LISM, (b) GMOC and (c) SSA with LTT in computation of the solution $m(v,t)$ of (2.25), with rates (2.139) and initial condition (2.140). The error $\varepsilon(v,t)$ is defined as in (2.137). Table 2.2 reports simulation settings and computational times.

As shown in Table 2.2 and Figure 2.4, SSA turned to be computationally demanding and not able to provide the level of accuracy achieved by LISM and GMOC. In particular, SSA fails in detecting the peaks of the solution $m(v,t)$ and returns a bigger error $\varepsilon(v,t)$ than LISM and GMOC commit.

GMOC provides competitive speed and accuracy of simulation. However, small values of h and τ (Table 2.2) are required to deal with the steep distribution $\mathcal{N}(v; v_0, \sigma_0)$, plugged in the derivative of $m(v,t)$ through the approximation (2.142), with $v_0 = 0.027$ and $\sigma_0 = 0.001$. This negatively affects the overall simulation time.

LISM allows a bigger time step τ and a volume grid with a smaller number of points than required by GMOC. In addition, LISM eliminates the numerical oscillations affecting GMOC, as shown in Figures 2.4a and 2.4b. In conclusion, LISM is more accurate than GMOC, and ≈ 7.5 times faster in fulfilling the required accuracy.

The solutions shown in Figure 2.4 explore the small scales of volume and time, if compared to the equilibrium solution $m^*(v)$ in Figure 2.3. Thus, we now want to investigate the bigger volume and time values, i.e. $v \in [0, v_{\max}]$, $t \in [0, T_{\max}]$, with $v_{\max} = 10^3$ and $T_{\max} = 0.4$.

Both, SSA and GMOC, failed to provide the solutions of the required accuracy within the feasible computational time. The problem is that the desired accuracy and the simulated interval of time require from both methods to perform $\approx 2 \times 10^7$ time steps. In addition, GMOC needs a volume grid with 4×10^6 points equally spaced by $h = 2.5 \times 10^{-4}$. Such grids are too demanding and lead to computational times exceeding 10^6 seconds for both GMOC and SSA.

On the contrary, LISM allows us to explore the equilibrium solution scales with a feasible effort, as demonstrated in Table 2.3 and Figure 2.5.

Method	Technical Details	Time Step τ	Volume Grid & Grid Step h	Software & Hardware	Error ε	CPU Time
LTT	Inversion of $\hat{m}(\lambda, t)$ (2.85) with *nilt* [99]	-	-	MATLAB **BCAM code** 64-bit Linux OS 2.70GHz proc.	-	7×10^{-2} sec
LISM	Updating Scheme (2.109) for Model I	Constant $\tau = 8 \times 10^{-4}$	Uneven grid $\hat{\mathbf{v}}$ (2.136) $h_1 \approx 2.7 \times 10^{-4}$, $N_1 = 100$ $h_2 \approx 8 \times 10^{-4}$, $N_2 = 500$ $h_3 \approx 5 \times 10^{-1}$, $N_3 = 2000$	C++ **BCAM code** 64-bit Linux OS 2.40GHz proc.	Fig. 2.5	1.3×10^3 sec

Table 2.3: Settings and computational times for the integration methods meeting (2.138) at $v_{\max} = 10^3$, $T_{\max} = 0.4$ and $\varepsilon_{\max} = 10^{-2}$, in the case of Model I with rates (2.139) and initial condition (2.140). All **BCAM codes** were developed within this Thesis.
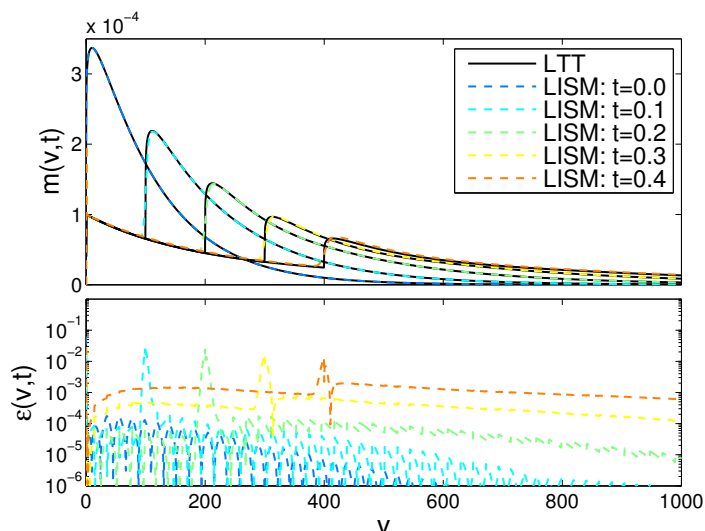
Figure 2.5: Comparison of LISM and LTT in computation of the solution $m(v,t)$ of (2.25), with rates (2.139), initial data (2.140) and $\varepsilon(v,t)$ (2.137). Table 2.3 reports settings and computational times.

2.4.2 Model II: Constant Aggregation, Linear Growth and Constant Phase Transition

In this section, we test the accuracy (2.137) and the computational effort to fulfil (2.138) of the proposed approaches in the case of the Model II discussed in Section 2.3.4.2. The definition of Model II is completed by a choice of the rates parameters and initial condition.

Aimed to evaluate the performance of the integration methods for realistic settings, the parameters of Models II assume the orders of magnitude achieved by the dimensionless counterparts of the DDPM rates, summarised in Table 2.C.1 of Appendix 2.C:

$$a(v, u, t) = a_0 = 10^2, \quad g(v, t) = g_0 \, v, \quad g_0 = 10^2, \quad n(v, t) = 0, \quad \mu(v, t) = \mu_0 = 10^{-2}. \tag{2.143}$$

As proved in Section 2.3.4.2, the initial condition

$$\omega_0(v) = \alpha \, e^{-\beta v} \, \sinh(\gamma v), \quad \alpha = 10^5, \quad \beta = 5, \quad \gamma = 1, \tag{2.144}$$

allows for the analytical solution (2.94) of the PBE (2.25) with rates (2.143). In order to mimic the nucleation process neglected by Model II, we select the values of α, β and γ in (2.144) to make the initial condition a narrow distribution on small values of volume v, as shown in Figure 2.6 for $t = 0$. Then, we employ the designed methodologies to integrate the PBE system (2.25) for the defined in such a way Model II.

We monitor the accuracy (2.137) and the computational effort required to fulfil (2.138) for

$$v_{\max} = 10^2, \quad T_{\max} = 10^{-5}, \quad \varepsilon_{\max} = 10^{-2}. \tag{2.145}$$

The proposed implementations of GMOC and SSA require the equally spaced grid $\mathbf{v} = \{\varphi_k = kh\}_{k=0}^{N}$ for the volume interval $[0, 100]$. On the contrary, LISM allows for a flexible choice of the integration grid. In particular, it can be unevenly spaced for better dealing with the narrow initial condition (2.144) on the volume domain $[0, 100]$. With such purpose, we define the volume grid

$$\hat{\mathbf{v}} \equiv \mathbf{v}_1 \cup \mathbf{v}_2 \cup \mathbf{v}_3. \tag{2.146}$$

The grid $\mathbf{v}_1$ spreads over $[0, 1)$, placing $N_1 > 0$ uniformly distributed points with step size $h_1 > 0$. The grid $\mathbf{v}_2$ covers the interval $[1, 3)$ with $N_2 > 0$ points equally spaced by $h_2 > 0$. The grid $\mathbf{v}_3$ ranges in $[3, 100]$ with $N_3 > 0$ uniformly distributed points with step size $h_3 > 0$.

Table 2.4 summarises the settings for the integration methods meeting the criterion (2.138) for (2.145) and provides the required computational time for each method. The computed solutions $m(v, t)$ and the corresponding errors $\varepsilon(v, t)$ (2.137) are shown in Figure 2.6.

As for Model I, SSA is computationally expensive. In addition, it is not able to provide the accuracy of LISM and GMOC, returning bigger values of the error $\varepsilon(v, t)$.

The GMOC method ensures accurate results with a competitive speed of simulation. However, the small time step τ and the demanding integration grid $\mathbf{v}$ (Table 2.4) are required to deal with the steep initial condition (2.144).

The LISM approach allows a bigger time step τ and a coarser volume grid than GMOC requires, as reported in Table 2.4. For this reason, LISM is ≈ 10 times faster than GMOC in fulfilling the criterion (2.138) for (2.145).

By inspecting Figures 2.6a and 2.6b, we remark that the error $\varepsilon(v, t)$ is growing faster for LISM than for GMOC, as the time is evolving. This effect is explained by the spreading of the solution $m(v, t)$ to the volume values $v \in [1, 100]$, for which LISM employs coarse grids, i.e. $h_3 > h_2 > h_1$ in Table 2.4.

Method	Technical Details	Time Step τ	Volume Grid & Grid Step h	Software & Hardware	Error ε	CPU Time
LTT	Analytical Solution (2.94)	-	-	-	-	-
LISM	Updating Scheme (2.109) for Model II	Constant $\tau = 2 \times 10^{-8}$	Uneven grid $\hat{\mathbf{v}}$ (2.146) $h_1 \approx 2.5 \times 10^{-2}$, $N_1 = 40$ $h_2 \approx 5 \times 10^{-2}$, $N_2 = 40$ $h_3 \approx 1.6 \times 10^{0}$, $N_3 = 60$	C++ **BCAM code** 64-bit Linux OS 2.40GHz proc.	Fig. 2.6a	6×10^{-1} sec
GMOC		Constant $\tau = 10^{-8}$	Grid $\mathbf{v} = \{\varphi_k = kh\}_{k=0}^{N}$ $h = 10^{-1}$, $N = 1000$	C++ **BCAM code** 64-bit Linux OS 2.40GHz proc.	Fig. 2.6b	5.3×10^{0} sec
SSA	Scaling (2.60) with $\kappa = 1$ Sample Size $S = 10^{2}$	Sampled $\tau \in (0, 1) \times 10^{-7}$	Grid $\mathbf{v} = \{\varphi_k = kh\}_{k=0}^{N}$ $h = 10^{-1}$, $N = 1000$	C++ **BCAM code** 64-bit Linux OS 2.40GHz proc.	Fig. 2.6c	9.6×10^{3} sec

Table 2.4: Settings and computational times for the integration methods meeting (2.138) at $v_{\max} = 10^2$, $T_{\max} = 10^{-5}$ and $\varepsilon_{\max} = 10^{-2}$, in the case of Model II with rates (2.143) and initial condition (2.144). All **BCAM codes** were developed within this Thesis.

(a) LISM (dashed) vs. LTT (solid).

(b) GMOC (dashed) vs. LTT (solid).

(c) SSA (dashed) vs. LTT (solid).

Figure 2.6: Comparison of (a) LISM, (b) GMOC and (c) SSA with LTT in computation of the solution $m(v,t)$ of (2.25), with rates (2.143) and initial condition (2.144). The error $\varepsilon(v,t)$ is defined as in (2.137). Table 2.4 reports simulation settings and computational times.

2.4.3 Model III: Constant Aggregation, Growth and Phase Transition

This section investigates the accuracy (2.137) and the computational effort to meet (2.138) of the designed methodologies, in the case of the Model III (Section 2.3.4.3) with initial condition

$$\omega_0(v) = \alpha \, e^{-\beta v} \sinh(\gamma v), \quad \alpha = \beta = 1, \quad \gamma = 1/4. \tag{2.147}$$

The rate parameters assume the orders of magnitude provided in Table 2.C.1 of Appendix 2.C:

$$a(v, u, t) = a_0 = 10^2, \quad g(v, t) = g_0 = 10^3, \quad n(v, t) = 0, \quad \mu(v, t) = \mu_0 = 10^{-2}. \tag{2.148}$$

We test the accuracy (2.137) of the integration methods and their efficiency in satisfying (2.138) for

$$v_{\max} = 20, \quad T_{\max} = 10^{-2}, \quad \varepsilon_{\max} = 10^{-2}. \tag{2.149}$$

For this model, LTT requires the evaluation of the Hypergeometric function $_2F_1$ in (2.101). A fast and reliable computation of $_2F_1$ is a challenging task [118]. We first investigated the applicability of the built-in MATLAB routine *hypergeom* [119], but we found that it returned undefined values (NaN) when employed for evaluating $_2F_1$ in (2.101), with parameters (2.147)-(2.149). Thus, we incorporated in our code the function *singlefraction2f1* [118], specifically designed for dealing with such a range of parameters values as in (2.147)-(2.149).

Table 2.5 summarises the settings for the integration methods meeting (2.138) at (2.149) and provides the required computational times. The computed solutions $m(v, t)$ and corresponding errors $\varepsilon(v, t)$ (2.137) are shown in Figure 2.7.

The numerical experiments with SSA demonstrated that, in order to achieve the required accuracy $\varepsilon_{\max} = 10^{-2}$, the computations significantly longer than 10^4 seconds may be needed. It was a serious argument for stopping the experiments and concluding that the SSA method in its current formulation and implementation is not an appropriate choice for solving (2.25) in the case of Model III.

GMOC was able to satisfy the condition (2.138) for (2.149). However, we remark the appearance of numerical oscillations for $v \in [0, 10]$ and $m \approx 0$ in Figure 2.7b. Such fluctuations are better visible when inspecting the error $\varepsilon(v, t)$ committed by GMOC for $v \in [0, 10]$ and $t = 10^{-2}$ (in red). Such error $\varepsilon(v, t)$ is several orders of magnitude bigger than the generated by LISM in these ranges of v and t, i.e. 10^{-3} against 10^{-15}. The small values of τ and h chosen for GMOC are motivated by the attempt to reduce the oscillations. Despite such numerical issues, the computational time required by GMOC is comparatively small.

The LISM approach allows us to eliminate the numerical fluctuations affecting GMOC, as shown in Figure 2.7. Moreover, LISM employs coarser grids of integration in volume and time than GMOC does. As a result, LISM enhances the simulation speed by a factor of two orders of magnitude, if compared to GMOC under conditions (2.138) and (2.149). LTT is comparatively expensive because of the demanding evaluation of the Hypergeometric function $_2F_1$.

To conclude, LTT ensures a high level of precision and speed, but its applicability is limited by the required assumptions, such as the simplified choices of initial condition and rate functions. The LTT approach may result in complicated expressions of Laplace transformed solutions, whose numerical inversion can slow down the speed of the methodology.

The numerical experiments show that SSA is a robust technique, potentially able to estimate any quantity of interest. However, its level of accuracy is lower than the achievable by LISM and GMOC. In addition, the computations are demanding and the simulation speed may not satisfy practitioners, facing real life applications.

GMOC provides competitive speed and accuracy of simulation. However, it may be affected by numerical oscillations, in the presence of moving fronts of the solution $m(v, t)$. Then, the GMOC efficiency is limited by the simultaneous presence of small nucleation sizes and large volume domains, demanding fine grid steps for the whole intervals of simulation.

LISM can eliminate the numerical oscillations affecting GMOC, through analytical solutions derived for the transport terms. In addition, LISM requires a smaller computational effort than GMOC does,

since bigger time steps and coarser volume grids are allowed.

In order to control the committed error, one should pay attention to the placement of volume grid points for the LISM approach. The analytical solutions derived for LISM allow us to design volume grids carrying information on the unknown $m(v,t)$.

Finally, LISM can efficiently deal with small nucleation sizes and large volume domains, through analytical solutions derived for impulsive rates of nucleation. LISM can remove additional hypothesis, applying to any initial condition with realistic shapes of the rate functions.

Method	Technical Details	Time Step τ	Volume Grid & Grid Step h	Software & Hardware	Error ε	CPU Time
LTT	Inversion of $\hat{m}(\lambda,t)$ (2.100) with *nilt* [99] Evaluate $_2F_1$ by *singlefraction2f1* [118]	-	-	MATLAB **BCAM code** 64-bit Linux OS 2.70GHz proc.	-	2.3×10^0 sec
LISM	Updating Scheme (2.109) for Model III	Constant $\tau = 2 \times 10^{-4}$	Grid $\mathbf{v} = \{\varphi_k = kh\}_{k=0}^N$ $h = 10^{-1}$, $N = 200$	C++ **BCAM code** 64-bit Linux OS 2.70GHz proc.	Fig. 2.7a	3×10^{-2} sec
GMOC		Constant $\tau = 10^{-5}$	Grid $\mathbf{v} = \{\varphi_k = kh\}_{k=0}^N$ $h = 2 \times 10^{-2}$, $N = 1000$	C++ **BCAM code** 64-bit Linux OS 2.70GHz proc.	Fig. 2.7b	5.2×10^0 sec
SSA	Scaling (2.60) with $\kappa = 10^4$ Sample Size $S = 1$	Sampled $\tau \in (0,4) \times 10^{-7}$	Grid $\mathbf{v} = \{\varphi_k = kh\}_{k=0}^N$ $h = 8 \times 10^{-2}$, $N = 250$	C++ **BCAM code** 64-bit Linux OS 2.70GHz proc.	$\max_{v,t} \varepsilon(v,t) \propto 10^{-1} > \varepsilon_{\max}$	9.8×10^1 sec

Table 2.5: Settings and computational times for the integration methods meeting (2.138) at $v_{\max} = 20$, $T_{\max} = 10^{-2}$ and $\varepsilon_{\max} = 10^{-2}$, in the case of Model III with rates (2.148) and initial condition (2.147). All **BCAM codes** were developed within this Thesis.

(a) LISM (dashed) vs. LTT (solid).

(b) GMOC (dashed) vs. LTT (solid).
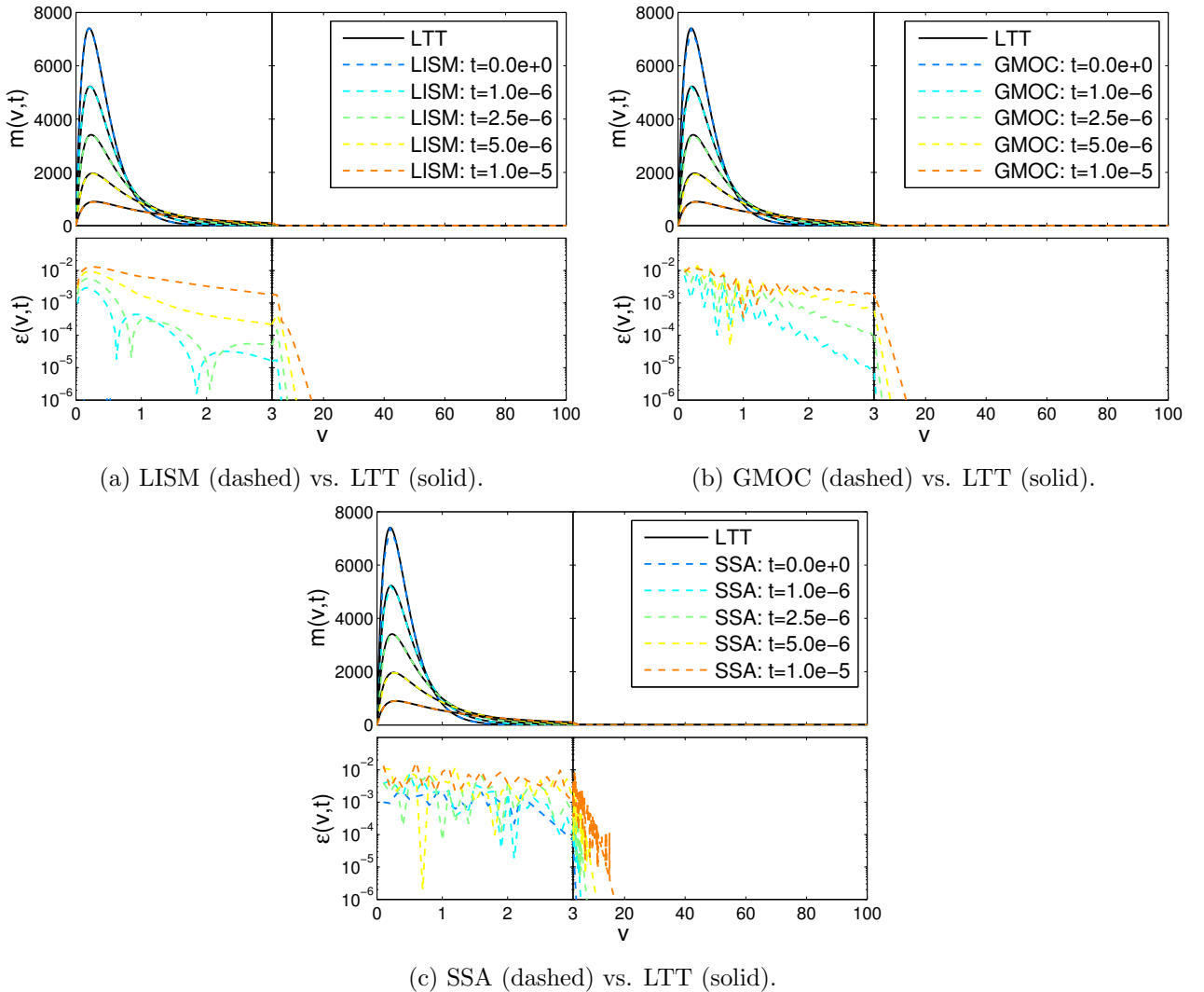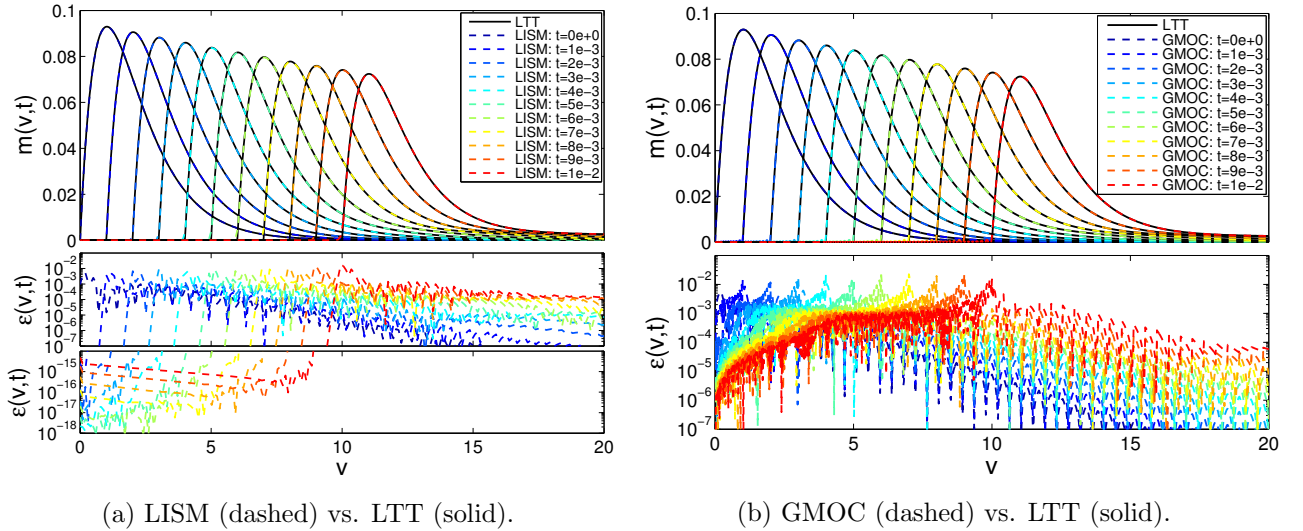
Figure 2.7: Comparison of (a) LISM and (b) GMOC with LTT in computation of the solution $m(v,t)$ of (2.25), with rates (2.148), initial condition (2.147) and error $\varepsilon(v,t)$ (2.137). Table 2.5 shows simulation settings and computational times.

2.5   Conclusions & Discussion

The objective of this chapter is to develop an accurate and efficient methodology for modelling the Dynamic Development of Particles Morphology (DDPM), introduced in Section 2.1.2. The first task consists in deriving a Population Balance Equations (PBE) based model for the distribution of the expected size of the polymer clusters, composing the particles morphology. Our second purpose is to develop an accurate and efficient methodology for the solution of the proposed model. The speed of the predictive simulations technique should be high enough for enabling on-the-fly recommendations for technological conditions in the synthesis of new multi-phase morphologies.

The introduced in Section 2.2.1 PBE model for the considered distributions accounts for the mechanisms driving the DDPM reaction: (i) aggregation of particles, (ii) volumetric growth, (iii) nucleation of particles and (iv) transition of phase. Under the assumptions of [45] summarised in Section 2.1.2, we derive in Appendix 2.A the chemical rates of the processes involved in the Dynamic Development of *latex* Particles Morphology. Aimed to search for the most efficient approach for solving the derived PBE, we also introduced the Models I-III of Section 2.2.1, which use less advanced chemical rates, but can be viewed as coarse approximations of the DDPM process.

Since the rates derived in Appendix 2.A lead to computationally intractable quantities, we propose in Section 2.2.2 a novel and automatic procedure for reducing the PBE model to dimensionless variables. In particular, Algorithm 2.1 summarises the steps needed for finding optimal scaling factors leading to a dimensionless PBE with computationally tractable parameters. The proposed optimisation scheme is not computationally demanding, provided the use of an efficient built-in optimisation routine. Moreover, it is performed once and does not interfere with the solver of a PBE. The validation of the scaling procedure is carried out using the Dynamic Development of *latex* Particles Morphology model, and results in decreasing a ratio between maximal and minimal parameters values from 10^{57} (original) to 10^5 (dimensionless).

In Section 2.2.3, we provide the analysis of the dimensionless PBE (2.25) describing the DDPM process. We show that the solution $m(v,t)$ of (2.25) must be non-negative. We also characterise the time evolution of the zero- and first-order moments of the distribution $m(v,t)$. Then, the asymptotic behaviour of $m(v,t)$ is discussed for $v \to +\infty$ and fixed time $t \in \mathbb{R}^+$.

Section 2.3 is devoted to the design of an accurate and efficient methodology for integrating the dimensionless PBE model describing the DDPM reaction. We develop three approaches belonging to the classes of methods revised in Section 2.3.1: the Stochastic Simulation Algorithm (SSA), the Generalised Method of Characteristics (GMOC) and the Laplace Transform Technique (LTT). In addition, we propose the Laplace Induced Splitting Method (LISM) which does not fit into any described class and is based on the idea which, to our knowledge, has never been explored in numerical methods for PBE. More specifically, we combine a splitting integration scheme with Laplace induced analytical solutions derived for simplified PBEs, composing the PBE for DDPM.

In order to judge the performance of the derived approaches for realistic settings, we employ the rate functions, modelling the morphology of *latex* particles, discussed in Appendix 2.A. In the tests of Section 2.4, the parameters of Models I-III assume the orders of magnitude achieved by the dimensionless counterparts of the DDPM rates, summarised in Table 2.C.1 of Appendix 2.C.

Although LTT provides high levels of precision and speed, its applicability is limited by the required assumptions and it should not be able to deal with more complicated models than the discussed in Section 2.3.4. However, it played an important role in the validation and comparison procedure applied to other three developed methods, i.e. SSA, GMOC and LISM. Moreover, it is a vital part of the LISM approach.

The experiments of Section 2.4 show that SSA is a robust integration technique, but limitations and computational inefficiencies make the approach not competitive for solving (2.25).

The numerical results of Section 2.4 allow us to illustrate the main features of GMOC and LISM, and compare their performance. In particular, the following conclusions are made:

- LISM eliminates the numerical oscillations affecting GMOC, because the transport terms of PBE and the moving fronts of the solution $m(v,t)$ are analytically accounted for.

- LISM can simultaneously deal with small nucleation sizes and large volume domains, since it

analytically accounts for impulsive rates of nucleation. On the contrary, GMOC is limited by the requirements of uniform grid and small step sizes.

- In the performed experiments, LISM outperforms GMOC in computational speed by up to a factor of two orders of magnitude, still guaranteeing the same accuracy.

In summary, we derived and analysed a computationally tractable PBE-based model for predicting the DDPM reaction, and proposed and implemented four different numerical approaches for solving such a model. The comparative analysis and numerical experiments confirm that the conceptually new LISM is the most promising approach for solving accurately and efficiently the PBE for DDPM. Due to its robustness and flexibility, it can potentially deal with realistic models, as will be discussed in Section 2.6.

The methodologies and results derived in this Chapter have been presented in four invited talks delivered in International Conferences, as reported in Contributions & Developed Software. The proposed GMOC and the PBE model (2.25) have been included in the final report [107] at ESGI 2016.

2.6 Future Developments

We discuss some potentially promising directions to take in the future. Based on the shown performance, we plan to use LISM for the integration of the complex DDPM model summarised in Appendix 2.B. In particular, the solution of the PBE system (2.B.6) can be approximated by LISM, using the rate functions with the same volume dependencies as in (2.B.7)-(2.B.10):

$$a_{m,w}(v,u,t) = a_0^{m,w} \left[v^{-1/3} + u^{-1/3} \right], \quad g(v,t) = g_1\, v\, +\, g_2\, v^{2/3},$$
$$n(v,t) = n_0\, \delta(v - v_0), \quad \mu_{m,w}(v,t) = \mu_0^{m,w}, \tag{2.150}$$

where $\delta(x)$ is the Dirac delta. The values of the constants $a_0^{m,w}, v_0, \mu_0^{m,w} > 0$ and $g_{1,2}, n_0 \geq 0$ should be updated at each time step to fit to the evolution of the rates shown in Appendix 2.C. However, the given parameters are assumed to be constant during each time step and the corresponding solutions can be used to update the computed distributions $m(v,t)$ and $w(v,t)$.

To take advantage of analytical solutions of simplified PBEs composing the system (2.B.6) with rates (2.150), we can split (2.B.6) in three sub-problems:

$$\begin{cases} \frac{\partial m(v,t)}{\partial t} & = -\frac{\partial(\,g(v,t)\,m(v,t)\,)}{\partial v} + n(v,t) - \mu_m(v,t)\,m(v,t), \quad \forall v,t \in \mathbb{R}^+, \\ \frac{\partial w(v,t)}{\partial t} & = -\frac{\partial(\,g(v,t)\,w(v,t)\,)}{\partial v} + \mu_w(v,t)\,m(v,t), \quad \forall v,t \in \mathbb{R}^+, \\ g(v,t) & = g_1\,v, \quad n(v,t) = n_0\,\delta(v-v_0), \quad \mu_{m,w}(v,t) = \mu_0^{m,w}, \quad \forall v,t \in \mathbb{R}^+, \end{cases} \tag{2.151}$$

$$\begin{cases} \frac{\partial m(v,t)}{\partial t} & = -\frac{\partial(\,g(v,t)\,m(v,t)\,)}{\partial v}, \quad \forall v,t \in \mathbb{R}^+, \\ \frac{\partial w(v,t)}{\partial t} & = -\frac{\partial(\,g(v,t)\,w(v,t)\,)}{\partial v}, \quad \forall v,t \in \mathbb{R}^+, \\ g(v,t) & = g_2\,v^{2/3}, \quad \forall v,t \in \mathbb{R}^+, \end{cases} \tag{2.152}$$

$$\begin{cases} \frac{\partial m(v,t)}{\partial t} & = -\,m(v,t) \int_0^{+\infty} a_m(v,u,t)\,m(u,t)\,du \\ & \quad + \frac{1}{2} \int_0^v a_m(v-u,u,t)\,m(v-u,t)\,m(u,t)\,du, \quad \forall v,t \in \mathbb{R}^+, \\ \frac{\partial w(v,t)}{\partial t} & = -\,w(v,t) \int_0^{+\infty} a_w(v,u,t)\,w(u,t)\,du \\ & \quad + \frac{1}{2} \int_0^v a_w(v-u,u,t)\,w(v-u,t)\,w(u,t)\,du, \quad \forall v,t \in \mathbb{R}^+, \\ a_{m,w}(v,u,t) & = a_0^{m,w} \left[v^{-1/3} + u^{-1/3} \right], \quad \forall v,u,t \in \mathbb{R}^+. \end{cases} \tag{2.153}$$

The first equation in the sub-problem (2.151) can be analytically solved for any choice of the initial condition $m(v,0) = \omega_0(v)$, as already proved in Section 2.3.5.2. The second equation in (2.151) and the sub-problem (2.152) are analytically solvable by the Method of Characteristics, for any choice of the initial conditions $m(v,0) = \omega_0(v)$ and $w(v,0) = \psi_0(v)$. Finally, the sub-problem (2.153) can be

solved using numerical schemes, as suggested in Section 2.3.5.4.

The solution of the complete PBE system (2.B.6), with rates (2.150), can be recovered by a splitting integration scheme that combines the solutions of the sub-problems (2.151), (2.152) and (2.153), as proposed in Section 2.3.5.1.

The solution of (2.B.6), obtained with GMOC of Section 2.3.3, can be used as a baseline for comparison.

As detailed in Section 2.3.5, we have selected the Symmetrized Strang Splitting Method (SSSM) to recover the solutions of Models I-III with the use of the Laplace induced solutions of the sub-problems (2.105), (2.106) and (2.107). However, this is not the only possible choice and similar splitting schemes [120, 121, 122] can be applied within LISM.

The selection of the most appropriate splitting methodology for LISM will be yet another area of research in future work. Convergence, order of accuracy, non-negativity and conservativeness of the different schemes should be investigated.

The realistic settings of Model I-III employed in Section 2.4 give us the appropriate benchmark to judge the efficiency of different splitting approaches. The similar analysis can also be performed on the discussed above splitting of the system (2.B.6).

Another possible direction for the future work is the further improvement of the scaling procedure introduced in Section 2.2.2. As discussed in Section 2.2.2, the application of the scaling procedure to the DDPM model summarised in Appendix 2.A resulted in computationally tractable parameters, with the ratio r_p between the maximum and minimum parameters values being $\approx 10^5$. Such a difference looks computationally tractable, especially if compared with the original equation, where $r_p \approx 10^{57}$ L^{-2}.

In order to reduce further the ratio r_p, the following modification of the scaling procedure can be explored. The cost function $C(\theta)$ (2.24), which takes into account all the characteristic constants and physical parameters through the Euclidean distance, can be replaced by the more stringent maximum norm

$$C_{\max}(\theta) \equiv \max_{i=1,..,N_d} H(\lambda_i(\theta)) \,|\log_{10}(\lambda_i(\theta)) - \Theta_i|, \qquad (2.154)$$

with $H(x) = 1$ if $x > 0$, and zero otherwise. The functional (2.154) is less regular than (2.24), but the Simulated Annealing Algorithm [51, 52] can successfully deal with non-smooth cost functions.

A more efficient approach for computation of the rate functions (2.B.7)-(2.B.10) than proposed in this Thesis can be yet another task for the future research.

As discussed in Appendix 2.C, the computation of the rate functions (2.B.7)-(2.B.10) depends on the knowledge of the solution of the PBE system (2.B.6).

One possible approach to decouple the considered quantities is proposed in Appendix 2.C and validated in Figure 2.C.3. However, it is based on the crude approximation (2.C.6), without any justification other than the decoupling itself. In addition, Figure 2.C.3 only stands for a small interval of time, as outlined in Appendix 2.C.

Clearly, finer approximations providing independent calculation of the rate functions are required. The *Method of Moments* revised in Section 2.3.1.3 suggests a promising line of research, assisting in deriving closed-form evolution equations for the first-order and two-thirds-order moments of the distributions $m(v,t)$ and $w(v,t)$.

Finally, the experimental values of the parameters in Table 2.A.1 are taken as known constants. However, they are far from being exact and they can introduce significant errors in the model. Once all the modelling issues are resolved and the suitable integration method is designed, the resulting solution can be used as a core for optimisation schemes refining the values of the considered parameters. The criterion of optimality can be given by the fitting of the computed solution to accessible experimental data. The speed and precision of the integration method will be crucial for avoiding a heavy resolution core and for making the optimisation routine a viable approach.

Appendix

2.A PBE Model for Latex Particles: Rate Functions Definition

We introduce the rate functions for modelling the Dynamic Development of *latex* Particles Morphology. The rates $\tilde{n}(\tilde{v},\tilde{t})$, $\tilde{g}(\tilde{v},\tilde{t})$, $\tilde{\mu}(\tilde{v},\tilde{t})$ and $\tilde{a}(\tilde{v},\tilde{u},\tilde{t})$ in the PBE system (2.14)-(2.17) are proposed taking into account the assumptions of [45], summarised in Section 2.1.2. Table 2.A.1 provides the nomenclature of all physical quantities involved in the computation of the rates, with the corresponding definitions, and the experimental values of the parameters.

The **nucleation rate** $\tilde{n}(\tilde{v},\tilde{t})$ [L^{-1} s^{-1}] accounts for the expected number of non-equilibrium clusters, created per second by the phase separation of the Polymer 2 agglomerates from the matrix to the clusters domain. The Polymer 2 agglomerates belong to the matrix phase until the critical volume v_c [L] is reached. Then, the agglomerates change their phase, becoming non-equilibrium clusters. The rate $\tilde{n}(\tilde{v},\tilde{t})$ can be computed as:

$$\tilde{n}(\tilde{v},\tilde{t}) = k_s \, v_c^{-1} \, \tilde{\Phi}(\tilde{t}) \, \tilde{\delta}(\tilde{v} - v_c) \quad [\text{L}^{-1} \text{ s}^{-1}], \tag{2.A.1}$$

where $\tilde{\delta}(\tilde{x})$ [L^{-1}] is the Dirac delta function.

The **growth rate** $\tilde{g}(\tilde{v},\tilde{t})$ [L s^{-1}] corresponds to the expected unswollen volume increase per second of clusters with unswollen volume $\tilde{v}$ at time $\tilde{t}$. The growth is driven by the diffusion of the Polymer 2 chains from the matrix to the clusters, assumed to be spherically shaped. In addition, the clusters increase their unswollen volume $\tilde{v}$ because Monomer 2 polymerises with already clustered Polymer 2 chains. The expression

$$\tilde{g}(\tilde{v},\tilde{t}) = \sqrt[3]{36\pi} \, k_d \, \tilde{\Phi}(\tilde{t}) \, (\tilde{\Psi}(\tilde{t}) + 1)^{2/3} \, \tilde{v}^{2/3} + \frac{k_p R \bar{V}_{pol2}}{\bar{V}_{mon2}} \, \frac{\tilde{\Psi}(\tilde{t})}{\tilde{V}_p(\tilde{t})} \, \tilde{v} \quad [\text{L s}^{-1}] \tag{2.A.2}$$

provides the volumetric growth rate $\tilde{g}(\tilde{v},\tilde{t})$.

The **migration rate** $\tilde{\mu}(\tilde{v},\tilde{t})$ [s^{-1}] is the expected proportion of non-equilibrium clusters moving per second to the equilibrium position. We have

$$\tilde{\mu}(\tilde{v},\tilde{t}) = k_\mu \quad [\text{s}^{-1}], \tag{2.A.3}$$

since $\tilde{\mu}(\tilde{v},\tilde{t})$ is assumed to be volume and time independent.

The **aggregation rate** $\tilde{a}(\tilde{v},\tilde{u},\tilde{t})$ [s^{-1}] corresponds to the expected frequency of coagulations between clusters with unswollen volumes $\tilde{v}$ and $\tilde{u}$ at time $\tilde{t}$. Assuming spherically shaped clusters, the rate $\tilde{a}$ accounts for the clusters diffusivity in the matrix phase. The Stokes-Einstein equation [123] specifies the diffusivity to be inversely proportional to the clusters actual radius and the matrix viscosity, empirically estimated by the Van Krevelen-Hoftyzer method [124]. As a result, the rate $\tilde{a}(\tilde{v},\tilde{u},\tilde{t})$ is given by:

$$\tilde{a}(\tilde{v},\tilde{u},\tilde{t}) = k_a \, N_p^{-1} \, (\tilde{\Psi}(\tilde{t}) + 1)^{14/3} \left[\tilde{v}^{-1/3} + \tilde{u}^{-1/3} \right] \quad [\text{s}^{-1}]. \tag{2.A.4}$$

The factor N_p^{-1} in (2.A.4) accounts for the partitioning of the clusters into N_p non-communicating particles.

Below we explain how the non-constant physical quantities, listed in Table 2.A.1, can be computed in order to generate (2.A.1)-(2.A.4).

Expected Total Volume $\tilde{V}_{pol2}^{mat}(\tilde{t})$ [L] of Polymer 2 in Matrix. Time evolution driven by (i) polymerization of Monomer 2, (ii) nucleation of non-equilibrium clusters and (iii) diffusion of Polymer 2 chains from matrix to clusters:

$$
\begin{cases}
\frac{d\tilde{V}_{pol2}^{mat}(\tilde{t})}{d\tilde{t}} &= \frac{k_p R \bar{V}_{pol2}}{\bar{V}_{mon2}} \frac{\tilde{\Psi}(\tilde{t})}{\tilde{V}_p(\tilde{t})} \left[\tilde{V}_{pol2}^{mat}(\tilde{t}) + V_{pol1} \right] - k_s \tilde{\Phi}(\tilde{t}) - k_d \tilde{\Phi}(\tilde{t}) \left[\tilde{\Sigma}_m(\tilde{t}) + \tilde{\Sigma}_w(\tilde{t}) \right] \quad [\text{L s}^{-1}], \\
\tilde{V}_{pol2}^{mat}(0) &= 0 \quad [\text{L}],
\end{cases}
$$
(2.A.5)

where $\tilde{V}_{pol2}^{mat}(0) = 0$ [L] because there is no Polymer 2 at $\tilde{t} = 0$ [s].

Expected Total Volume $\tilde{V}_{pol2}^{cm}(\tilde{t})$ [L] of Polymer 2 in Non-Equilibrium Clusters. Time evolution driven by (i) polymerization of Monomer 2, (ii) nucleation of non-equilibrium clusters, (iii) diffusion of Polymer 2 chains from matrix to clusters and (iv) migration of non-equilibrium clusters to equilibrium stage:

$$
\begin{cases}
\frac{d\tilde{V}_{pol2}^{cm}(\tilde{t})}{d\tilde{t}} &= \frac{k_p R \bar{V}_{pol2}}{\bar{V}_{mon2}} \frac{\tilde{\Psi}(\tilde{t})}{\tilde{V}_p(\tilde{t})} \tilde{V}_{pol2}^{cm}(\tilde{t}) + k_s \tilde{\Phi}(\tilde{t}) + k_d \tilde{\Phi}(\tilde{t}) \tilde{\Sigma}_m(\tilde{t}) - k_\mu \tilde{V}_{pol2}^{cm}(\tilde{t}) \quad [\text{L s}^{-1}], \\
\tilde{V}_{pol2}^{cm}(0) &= 0 \quad [\text{L}],
\end{cases}
$$
(2.A.6)

where $\tilde{V}_{pol2}^{cm}(0) = 0$ [L] because there is no Polymer 2 at $\tilde{t} = 0$ [s].

Expected Total Volume $\tilde{V}_{pol2}^{cw}(\tilde{t})$ [L] of Polymer 2 in Equilibrium Clusters. Time evolution driven by (i) polymerization of Monomer 2, (ii) diffusion of Polymer 2 chains from matrix to clusters and (iii) migration of non-equilibrium clusters to equilibrium stage:

$$
\begin{cases}
\frac{d\tilde{V}_{pol2}^{cw}(\tilde{t})}{d\tilde{t}} &= \frac{k_p R \bar{V}_{pol2}}{\bar{V}_{mon2}} \frac{\tilde{\Psi}(\tilde{t})}{\tilde{V}_p(\tilde{t})} \tilde{V}_{pol2}^{cw}(\tilde{t}) + k_d \tilde{\Phi}(\tilde{t}) \tilde{\Sigma}_w(\tilde{t}) + k_\mu \tilde{V}_{pol2}^{cm}(\tilde{t}) \quad [\text{L s}^{-1}], \\
\tilde{V}_{pol2}^{cw}(0) &= 0 \quad [\text{L}],
\end{cases}
$$
(2.A.7)

where $\tilde{V}_{pol2}^{cw}(0) = 0$ [L] because there is no Polymer 2 at $\tilde{t} = 0$ [s].

Expected Odds Monomers-Polymers $\tilde{\Psi}(\tilde{t})$. Defined as the ratio between the volume fractions of Monomer 2 and polymers, simultaneously accounting for Polymer 1 and Polymer 2. The assumption of uniform concentration of Monomer 2 implies $\tilde{\Psi}(\tilde{t})$ to be equal in all the phases. The time derivative is given by a polymerization term and a feeding term. The initial value can be computed as the ratio between the initial volume of Monomer 2 and the initial volume of Polymer 1:

$$
\begin{cases}
\frac{d\tilde{\Psi}(\tilde{t})}{d\tilde{t}} &= -\frac{k_p R \bar{V}_{pol2}}{\bar{V}_{mon2}} \frac{\tilde{\Psi}(\tilde{t})}{\tilde{\Psi}(\tilde{t})+1} \frac{\tilde{\Psi}(\tilde{t}) + \bar{V}_{mon2}/\bar{V}_{pol2}}{\tilde{V}_{pol2}(\tilde{t}) + V_{pol1}} + \frac{F_{mon2} \bar{V}_{mon2}}{\tilde{V}_{pol2}(\tilde{t}) + V_{pol1}} \quad [\text{s}^{-1}], \\
\tilde{\Psi}(0) &= \frac{M_0 \bar{V}_{mon2}}{V_{pol1}}.
\end{cases}
$$
(2.A.8)

Expected Total Volume $\tilde{V}_{pol2}(\tilde{t})$ [L] of Polymer 2. Time evolution driven by the polymerization of Monomer 2:

$$
\begin{cases}
\frac{d\tilde{V}_{pol2}(\tilde{t})}{d\tilde{t}} &= \frac{k_p R \bar{V}_{pol2}}{\bar{V}_{mon2}} \frac{\tilde{\Psi}(\tilde{t})}{\tilde{\Psi}(\tilde{t})+1} \quad [\text{L s}^{-1}], \\
\tilde{V}_{pol2}(0) &= 0 \quad [\text{L}],
\end{cases}
$$
(2.A.9)

where $\tilde{V}_{pol2}(0) = 0$ [L] because there is no Polymer 2 at $\tilde{t} = 0$ [s].

The following definitions complete the presented model:

$$
\tilde{\Phi}(\tilde{t}) \equiv \left[\frac{\tilde{V}_{pol2}^{mat}(\tilde{t})}{(\tilde{\Psi}(\tilde{t}) + 1)(\tilde{V}_{pol2}^{mat}(\tilde{t}) + V_{pol1})} - \Phi_s \right]^+, \quad \text{with} \quad x^+ \equiv \max\{x, 0\}, \tag{2.A.10}
$$

$$
\tilde{V}_p(\tilde{t}) \equiv \left(\tilde{\Psi}(\tilde{t}) + 1 \right) \left[\tilde{V}_{pol2}^{mat}(\tilde{t}) + \tilde{V}_{pol2}^{cm}(\tilde{t}) + \tilde{V}_{pol2}^{cw}(\tilde{t}) + V_{pol1} \right] \quad [\text{L}], \tag{2.A.11}
$$

$$\tilde{\Sigma}_{m,w}(\tilde{t}) \equiv \sqrt[3]{36\pi}\,(\tilde{\Psi}(\tilde{t}) + 1)^{2/3} \int_0^{+\infty} \tilde{v}^{2/3}\,\tilde{m},\tilde{w}(\tilde{v}, \tilde{t})\,d\tilde{v} \quad [\text{dm}^2], \tag{2.A.12}$$

where $\tilde{m}$ and $\tilde{w}$ are the solutions of (2.14)-(2.17).

Nomenclature	Definition	Value
$\tilde{v}$ [L]	unswollen volume of Polymer 2 in a given cluster	-
$\tilde{t}$ [s]	elapsed time	-
$\tilde{n}(\tilde{v},\tilde{t})$ [L^{-1} s^{-1}]	expected distribution of nucleation frequency of non-equilibrium clusters with unswollen volume $\tilde{v}$ at time $\tilde{t}$	-
$\tilde{g}(\tilde{v},\tilde{t})$ [L s^{-1}]	expected unswollen volume growth speed of clusters with unswollen volume $\tilde{v}$ at time $\tilde{t}$	-
$\tilde{\mu}(\tilde{v},\tilde{t})$ [s^{-1}]	expected frequency of non-equilibrium clusters with unswollen volume $\tilde{v}$, migrating to equilibrium stage at time $\tilde{t}$	-
$\tilde{a}(\tilde{v},\tilde{u},\tilde{t})$ [s^{-1}]	expected frequency of aggregations between clusters with unswollen volumes $\tilde{v}$ and $\tilde{u}$ at time $\tilde{t}$	-
$\tilde{V}_{pol2}^{mat}(\tilde{t})$ [L]	expected total volume of Polymer 2 in the matrix at time $\tilde{t}$	-
$\tilde{V}_{pol2}^{c_m}(\tilde{t})$ [L]	expected total volume of Polymer 2 in non-equilibrium clusters at time $\tilde{t}$	-
$\tilde{V}_{pol2}^{c_w}(\tilde{t})$ [L]	expected total volume of Polymer 2 in equilibrium clusters at time $\tilde{t}$	-
$\tilde{\Psi}(\tilde{t})$	expected odds monomers-polymers at time $\tilde{t}$	-
$\tilde{V}_{pol2}(\tilde{t})$ [L]	expected total volume of Polymer 2 at time $\tilde{t}$	-
$\tilde{\Phi}(\tilde{t})$	expected Polymer 2 volume fraction excess in matrix at time $\tilde{t}$	-
$\tilde{V}_p(\tilde{t})$ [L]	expected total volume of particles at time $\tilde{t}$	-
$\tilde{\Sigma}_m(\tilde{t})$ [dm^2]	expected total surface of non-equilibrium clusters at time $\tilde{t}$	-
$\tilde{\Sigma}_w(\tilde{t})$ [dm^2]	expected total surface of equilibrium clusters at time $\tilde{t}$	-
$\tilde{m}(\tilde{v},\tilde{t})$ [L^{-1}]	expected distribution of non-equilibrium clusters with unswollen volume $\tilde{v}$ at time $\tilde{t}$	-
$\tilde{w}(\tilde{v},\tilde{t})$ [L^{-1}]	expected distribution of equilibrium clusters with unswollen volume $\tilde{v}$ at time $\tilde{t}$	-
k_a [L$^{1/3}$ s^{-1}]	aggregation rate of clusters	2×10^{-8} L$^{1/3}$ s^{-1}
k_d [L$^{1/3}$ s^{-1}]	diffusion rate of Polymer 2 volume	5×10^{-8} L$^{1/3}$ s^{-1}
k_p [L mol^{-1} s^{-1}]	polymerization rate of Monomer 2	850 L mol^{-1} s^{-1}
k_s [L s^{-1}]	phase separation rate of Polymer 2 volume	2.5×10^{-5} L s^{-1}
k_μ [s^{-1}]	migration frequency of non-equilibrium clusters	10^{-5} s^{-1}
F_{mon2} [mol s^{-1}]	feeding rate of Monomer 2 amount	0 mol s^{-1}
M_0 [mol]	initial amount of Monomer 2	2.5 mol
$\bar{V}_{mon2}$ [L mol^{-1}]	molar volume of Monomer 2	0.1 L mol^{-1}
V_{pol1} [L]	total volume of Polymer 1	0.25 L
v_c [L]	critical Polymer 2 volume for phase separation	2.5×10^{-22} L
$\bar{V}_{pol2}$ [L mol^{-1}]	molar volume of Polymer 2	0.095 L mol^{-1}
Φ_s	saturation volume fraction of Polymer 2 in the matrix	10^{-3}
N_p	total number of particles in the reactor	2.8×10^{17}
R [mol]	expected total amount of radicals in the particles	2.3×10^{-7} mol

Table 2.A.1: Nomenclature of the physical quantities involved in the computation of the rates (2.A.1)-(2.A.4), with the corresponding definitions, and the experimental values of the parameters. The symbols s, L, mol and dm stand for second, Litre, mole and decimetre respectively. The data were provided by the research group POLYMAT, led by Prof. J. M. Asua.

2.B Dimensionless PBE Model for Latex Particles

We derive the dimensionless PBE model for the Dynamic Development of *latex* Particles Morphology, using the rate functions defined in Appendix 2.A.

The scaled counterparts of the variables in the PBE system (2.14)-(2.17) are defined as:

$$t \equiv \tilde{t}/t_0, \quad v \equiv \tilde{v}/\nu_0, \quad m(v,t) \equiv \tilde{m}(\tilde{v},\tilde{t})/m_0, \quad w(v,t) \equiv \tilde{w}(\tilde{v},\tilde{t})/w_0, \tag{2.B.1}$$

where t_0 [s], ν_0 [L], m_0 [L^{-1}] and w_0 [L^{-1}] belong to the set of the strictly positive characteristic constants θ defined by Algorithm 2.1. The variables $\tilde{\Psi}(\tilde{t})$ (2.A.8) and $\tilde{\Phi}(\tilde{t})$ (2.A.10) are dimensionless and computationally tractable since they are given by the ratios between quantities of the same dimensions and orders of magnitude. Then

$$\Psi(t) \equiv \tilde{\Psi}(\tilde{t}), \quad \Phi(t) \equiv \tilde{\Phi}(\tilde{t}), \tag{2.B.2}$$

where $\Psi(t)$ and $\Phi(t)$ are the dimensionless counterparts of $\tilde{\Psi}(\tilde{t})$ and $\tilde{\Phi}(\tilde{t})$. For the sake of simplicity, the quantities $\tilde{V}_{pol2}^{mat}(\tilde{t})$ (2.A.5), $\tilde{V}_{pol2}^{c_m}(\tilde{t})$ (2.A.6), $\tilde{V}_{pol2}^{c_w}(\tilde{t})$ (2.A.7), $\tilde{V}_{pol2}(\tilde{t})$ (2.A.9), $\tilde{V}_p(\tilde{t})$ (2.A.11) and V_{pol1} are scaled by the same factor V_0 [L]:

$$V_{pol2}^{mat}(t) \equiv \frac{\tilde{V}_{pol2}^{mat}(\tilde{t})}{V_0}, \quad V_{pol2}^{c_{m,w}}(t) \equiv \frac{\tilde{V}_{pol2}^{c_{m,w}}(\tilde{t})}{V_0}, \quad V_{pol2}(t) \equiv \frac{\tilde{V}_{pol2}(\tilde{t})}{V_0}, \quad V_p(t) \equiv \frac{\tilde{V}_p(\tilde{t})}{V_0}, \quad \lambda_{pol1} \equiv \frac{V_{pol1}}{V_0}. \tag{2.B.3}$$

The definitions (2.A.12) of the variables $\tilde{\Sigma}_m(\tilde{t})$ and $\tilde{\Sigma}_w(\tilde{t})$ suggest the proper scaling factors:

$$\Sigma_m(t) \equiv \frac{\tilde{\Sigma}_m(\tilde{t})}{\sqrt[3]{36\pi}\,\nu_0^{5/3}\,m_0}, \quad \Sigma_w(t) \equiv \frac{\tilde{\Sigma}_w(\tilde{t})}{\sqrt[3]{36\pi}\,\nu_0^{5/3}\,w_0}. \tag{2.B.4}$$

The Dirac delta function $\tilde{\delta}(\tilde{v}-v_c)$ [L^{-1}] is scaled by the factor δ_0 [L^{-1}]:

$$\delta(v-\lambda_c) \equiv \tilde{\delta}(\tilde{v}-v_c)/\delta_0, \quad \text{with} \quad \lambda_c \equiv v_c/\nu_0. \tag{2.B.5}$$

Given the characteristic constants $\theta \equiv \{t_0, \nu_0, m_0, w_0, V_0, \delta_0\}$ and the corresponding scaled quantities, it is possible to rewrite the PBE system (2.14)-(2.17) and the rate functions of Appendix 2.A in terms of the defined dimensionless variables. The equations (2.B.6)-(2.B.18) summarise the arising dimensionless model, where the parameters values are specified in Table 2.1.

$$\begin{cases} \frac{\partial m(v,t)}{\partial t} & = -\frac{\partial(\,g(v,t)\,m(v,t)\,)}{\partial v} + n(v,t) - \mu_m(v,t)\,m(v,t) - m(v,t)\int_0^{+\infty} a_m(v,u,t)\,m(u,t)\,du \\ & \quad + \frac{1}{2}\int_0^v a_m(v-u,u,t)\,m(v-u,t)\,m(u,t)\,du, \qquad \forall v,t \in \mathbb{R}^+, \\[2mm] \frac{\partial w(v,t)}{\partial t} & = -\frac{\partial(\,g(v,t)\,w(v,t)\,)}{\partial v} + \mu_w(v,t)\,m(v,t) - w(v,t)\int_0^{+\infty} a_w(v,u,t)\,w(u,t)\,du \\ & \quad + \frac{1}{2}\int_0^v a_w(v-u,u,t)\,w(v-u,t)\,w(u,t)\,du, \qquad \forall v,t \in \mathbb{R}^+, \\[2mm] m(v,0) & = w(v,0) = 0, \quad \forall v \in \mathbb{R}^+, \qquad m(0,t) = w(0,t) = 0, \quad \forall t \in \mathbb{R}^+, \end{cases} \tag{2.B.6}$$

$$a_{m,w}(v,u,t) \equiv \lambda_a^{m,w}\,(\Psi(t)+1)^{14/3}\left[v^{-1/3} + u^{-1/3}\right], \tag{2.B.7}$$

$$g(v,t) \equiv \lambda_d\,\Phi(t)\,(\Psi(t)+1)^{2/3}\,v^{2/3} + \lambda_p\,\Psi(t)\,V_p(t)^{-1}\,v, \tag{2.B.8}$$

$$n(v,t) \equiv \lambda_n\,\Phi(t)\,\delta(v-\lambda_c), \quad \text{with } \delta(x) \text{ the Dirac delta}, \tag{2.B.9}$$

$$\mu_{m,w}(v,t) \equiv \lambda_\mu^{m,w}, \tag{2.B.10}$$

$$\begin{cases} \dfrac{dV_{pol2}^{mat}(t)}{dt} &= \lambda_p\,\Psi(t)\,V_p(t)^{-1}\left[V_{pol2}^{mat}(t)+\lambda_{pol1}\right]-\Phi(t)\left[\lambda_s+\lambda_d^m\,\Sigma_m(t)+\lambda_d^w\,\Sigma_w(t)\right], \\ V_{pol2}^{mat}(0) &= 0, \end{cases} \quad (2.\text{B}.11)$$

$$\begin{cases} \dfrac{dV_{pol2}^{c_m}(t)}{dt} &= \lambda_p\,\Psi(t)\,V_p(t)^{-1}\,V_{pol2}^{c_m}(t)+\Phi(t)\left[\lambda_s+\lambda_d^m\,\Sigma_m(t)\right]-\lambda_\mu^m\,V_{pol2}^{c_m}(t), \\ V_{pol2}^{c_m}(0) &= 0, \end{cases} \quad (2.\text{B}.12)$$

$$\begin{cases} \dfrac{dV_{pol2}^{c_w}(t)}{dt} &= \lambda_p\,\Psi(t)\,V_p(t)^{-1}\,V_{pol2}^{c_w}(t)+\lambda_d^w\,\Phi(t)\,\Sigma_w(t)+\lambda_\mu^m\,V_{pol2}^{c_m}(t), \\ V_{pol2}^{c_w}(0) &= 0, \end{cases} \quad (2.\text{B}.13)$$

$$\begin{cases} \dfrac{d\Psi(t)}{dt} &= -\lambda_p\,\dfrac{\Psi(t)}{\Psi(t)+1}\,\dfrac{\Psi(t)+\Psi_r}{V_{pol2}(t)+\lambda_{pol1}}+\dfrac{\lambda_f}{V_{pol2}(t)+\lambda_{pol1}}, \\ \Psi(0) &= \Psi_0, \end{cases} \quad (2.\text{B}.14)$$

$$\begin{cases} \dfrac{dV_{pol2}(t)}{dt} &= \lambda_p\,\dfrac{\Psi(t)}{\Psi(t)+1}, \\ V_{pol2}(0) &= 0, \end{cases} \quad (2.\text{B}.15)$$

$$\Phi(t) \equiv \left[\frac{V_{pol2}^{mat}(t)}{(\Psi(t)+1)(V_{pol2}^{mat}(t)+\lambda_{pol1})}-\Phi_s\right]^+, \quad \text{with} \quad x^+ \equiv \max\{x,0\}, \quad (2.\text{B}.16)$$

$$V_p(t) \equiv (\Psi(t)+1)\left[V_{pol2}^{mat}(t)+V_{pol2}^{c_m}(t)+V_{pol2}^{c_w}(t)+\lambda_{pol1}\right], \quad (2.\text{B}.17)$$

$$\Sigma_{m,w}(t) \equiv (\Psi(t)+1)^{2/3}\int_0^{+\infty} v^{2/3}\,m,w(v,t)\,dv. \quad (2.\text{B}.18)$$

2.C PBE Model for Latex Particles: Rate Functions Analysis

We provide the analysis of the dimensionless rate functions (2.B.7)-(2.B.10), when the parameters assume the values specified in Table 2.1. The evolution and the orders of magnitude of the arising rates are monitored and then summarised in Table 2.C.1.

The phase transition rates $\mu_{m,w}(v,t)$ (2.B.10) are constants whose orders of magnitude are available in Table 2.1:

$$\mu_m(v,t) = \lambda_\mu^m \propto \mu_0 = 10^{-2} \quad \text{and} \quad \mu_w(v,t) = \lambda_\mu^w \propto \hat{\mu}_0 = 10^{-1}. \quad (2.\text{C}.1)$$

The aggregation rates $a_{m,w}(v,u,t)$ (2.B.7) can be factorised into the time-dependent factors $f_{m,w}(t)$ multiplied by the volume-dependent factor $f_a(v,u)$:

$$a_{m,w}(v,u,t) = f_{m,w}(t)\,f_a(v,u), \quad f_{m,w}(t) \equiv \lambda_a^{m,w}(\Psi(t)+1)^{14/3}, \quad f_a(v,u) \equiv v^{-1/3}+u^{-1/3}. \quad (2.\text{C}.2)$$

Figure 2.C.1a shows the factor $f_a(v,u)$, whose order of magnitude can be estimated by the average value $\bar{a}$ over the volume domain $[0,v_{\max}]^2$, with $v_{\max}=10$:

$$\bar{a} \equiv \frac{1}{v_{\max}^2}\int_0^{v_{\max}}\int_0^{v_{\max}} f_a(v,u)\,dv\,du = 3\,v_{\max}^{-1/3} \approx 10^0. \quad (2.\text{C}.3)$$

The factors $f_{m,w}(t)$ in Eq. (2.C.2) depend on the solution of (2.B.14)-(2.B.15), obtained by the MATLAB solver *ode45* [125]. Figure 2.C.1b shows the time evolution of $f_{m,w}(t)$. After a monotonic decay, the time-dependent factors $f_{m,w}(t)$ stabilise on positive constant values. Given $\bar{a} \propto 10^0$, the shown trends allow us to estimate the orders of magnitude of the aggregation rates $a_{m,w}(v,u,t)$ (2.B.7):

$$a_m(v,u,t) \propto a_0 = 10^2 \quad \text{and} \quad a_w(v,u,t) \propto \hat{a}_0 = 10^1. \quad (2.\text{C}.4)$$

(a) Volume-dependent Factor $f_a(v,u)$.

(b) Time-dependent Factors $f_{m,w}(t)$.
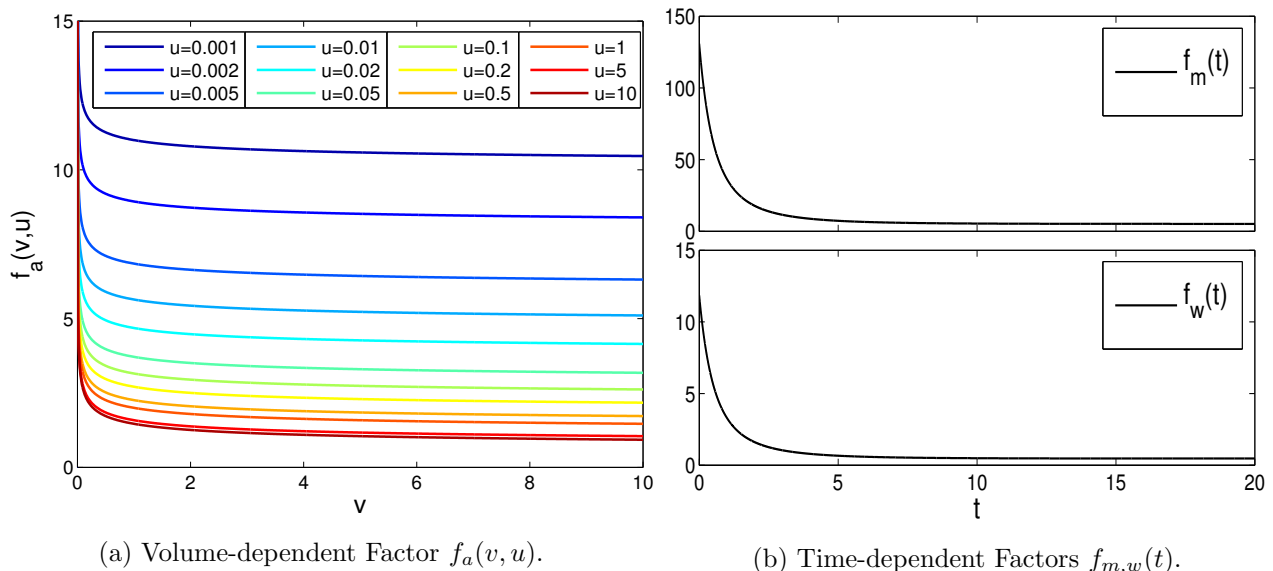
Figure 2.C.1: Factors building the aggregation rates $a_{m,w}(v,u,t) = f_{m,w}(t) f_a(v,u)$ in Eq. (2.C.2). Figure 2.C.1a shows the volume-dependent factor $f_a(v,u)$, whose order of magnitude can be estimated by the average value $\bar{a} \propto 10^0$ (2.C.3). After a monotonic decrease, the time-dependent factors $f_{m,w}(t)$ (Figure 2.C.1b) stabilise on positive constant values. Given $\bar{a} \propto 10^0$, the order of magnitude of the aggregation rate $a_m(v,u,t)$ is $a_0 = 10^2$, while $a_w(v,u,t) \propto \hat{a}_0 = 10^1$.

The nucleation rate $n(v,t)$ (2.B.9) can be factorised into the nucleation frequency $\eta(t)$ multiplied by the Dirac delta $\delta(v - \lambda_c)$:

$$n(v,t) = \eta(t)\,\delta(v - \lambda_c), \quad \eta(t) \equiv \lambda_n\,\Phi(t). \tag{2.C.5}$$

The computation of the growth rate $g(v,t)$ (2.B.8) and the nucleation frequency $\eta(t)$ (2.C.5) depends on the solution of (2.B.6) through the quantities $\Sigma_{m,w}(t)$ (2.B.18). The numerical solution of (2.B.6) can be obtained by GMOC presented in Section 2.3.3. However, the computations are time-consuming, allowing for an exploration of small domains of volume and time.
The complete evolution of the rates $g(v,t)$ and $\eta(t)$ can be analysed by decoupling their computation from the solution of (2.B.6) (Uncoupled Computation). Since it is possible to show that $V_{pol2}^{c_{m,w}}(t) \propto \int_0^{+\infty} v\, m,w(v,t)\,dv$, the 2/3-th order moments of the densities $m(v,t)$ and $w(v,t)$ can be approximated by the first-order moments $V_{pol2}^{c_m}(t)$ (2.B.12) and $V_{pol2}^{c_w}(t)$ (2.B.13) respectively:

$$\Sigma_{m,w}(t) \equiv (\Psi(t)+1)^{2/3} \int_0^{+\infty} v^{2/3}\, m,w(v,t)\,dv \approx Z_{m,w}(t) \equiv z_{m,w}\,(\Psi(t)+1)^{2/3}\,V_{pol2}^{c_{m,w}}(t), \tag{2.C.6}$$

where $z_{m,w}$ are positive constants tuned to fit $\Sigma_{m,w}(t)$ (2.B.18). By replacing the variables $\Sigma_{m,w}(t)$ with the fitted quantities $Z_{m,w}(t)$, the ODE system (2.B.11)-(2.B.15) becomes independent from the solution of (2.B.6), allowing the Uncoupled Computation of the rates $g(v,t)$ and $\eta(t)$.
The numerical solution of (2.B.11)-(2.B.15), with $Z_{m,w}(t)$ in place of $\Sigma_{m,w}(t)$, can be efficiently obtained by the MATLAB solver *ode45* [125]. Such integration is repeated for different choices of $z_{m,w}$ (2.C.6), targeting the fitting of $Z_{m,w}(t)$ (2.C.6) to $\Sigma_{m,w}(t)$ (2.B.18). The quantities $\Sigma_{m,w}(t)$ (2.B.18) are obtained by solving (2.B.6) with GMOC applied to small intervals of volume v and time t:

$$v \in [0, V_{\max}], \quad t \in [0, T_{\max}], \quad V_{\max} = 0.4, \quad T_{\max} = 0.2. \tag{2.C.7}$$

The resulting fitting and the chosen constants $z_{m,w}$ (2.C.6) are shown in Figure 2.C.2.
The approximation $\Sigma_{m,w}(t) \approx Z_{m,w}(t)$ (2.C.6) allows us to compute the rates $g(v,t)$ (2.B.8) and $\eta(t)$ (2.C.5), without knowing the solution of (2.B.6) (Uncoupled Computation). For $t \in [0, T_{\max}]$ (2.C.7), it is also possible to compute $g(v,t)$ (2.B.8) and $\eta(t)$ (2.C.5) by using the values of $\Sigma_{m,w}(t)$

(2.B.18) provided by the numerical solution of (2.B.6) (Coupled Computation). Figure 2.C.3 shows the comparison between the Coupled and the Uncoupled Computation of the rates $g(v,t)$ and $\eta(t)$. The achieved match validates the uncoupled approach to calculate $g(v,t)$ and $\eta(t)$ for

$$v \in [0, v_{\max}], \quad t \in [0, T_{\max}], \quad v_{\max} = 10, \quad T_{\max} = 0.2. \tag{2.C.8}$$

Comparing (2.C.7) to (2.C.8), we notice that the presented validation stands for a volume domain with reasonable size, i.e. $v_{\max} = 10 \gg V_{\max} = 0.4$. However, the explored time interval (2.C.8) does not allow us to validate the uncoupled approach during the complete evolution of the involved quantities, as will be shown in Figure 2.C.4.

(a) Fitted $Z_m(t)$ (2.C.6) to $\Sigma_m(t)$ (2.B.18).

(b) Fitted $Z_w(t)$ (2.C.6) to $\Sigma_w(t)$ (2.B.18).
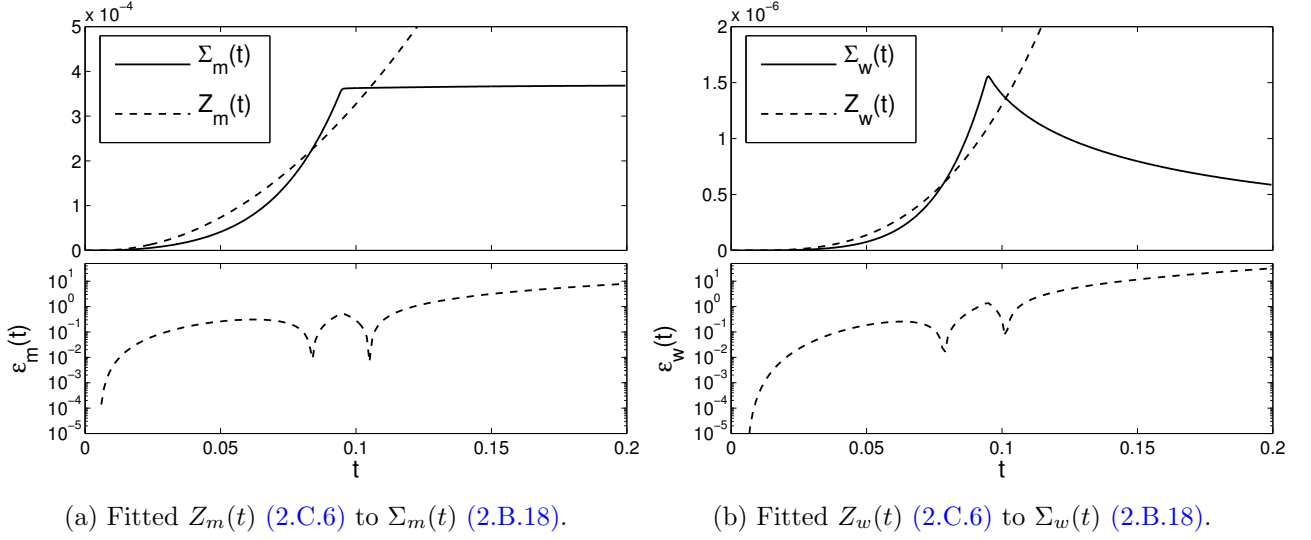
Figure 2.C.2: Variables $Z_{m,w}(t)$ (2.C.6) fitted to $\Sigma_{m,w}(t)$ (2.B.18), with $\Sigma_{m,w}(t)$ obtained by the numerical solution of (2.B.6). The values of $Z_{m,w}(t)$ are computed by solving (2.B.11)-(2.B.15), with $\Sigma_{m,w}(t)$ replaced by $Z_{m,w}(t)$ (2.C.6), $z_m = 0.8$ and $z_w = 10$. The variables $\Sigma_{m,w}(t)$ assume unreliable values for $t \geq 0.1$ because the support of the solution of (2.B.6) exceeds the integration domain (2.C.7). Given $T_{\max} = 0.2$, the errors $\varepsilon_{m,w}(t)$ are computed as $|\Sigma_{m,w}(t) - Z_{m,w}(t)|/(\int_0^{T_{\max}} \Sigma_{m,w}(t)^2 \, dt)^{1/2}$.

(a) Coupled vs. Uncoupled Computation: $g(v,t)$.

(b) Coupled vs. Uncoupled Computation: $\eta(t)$.
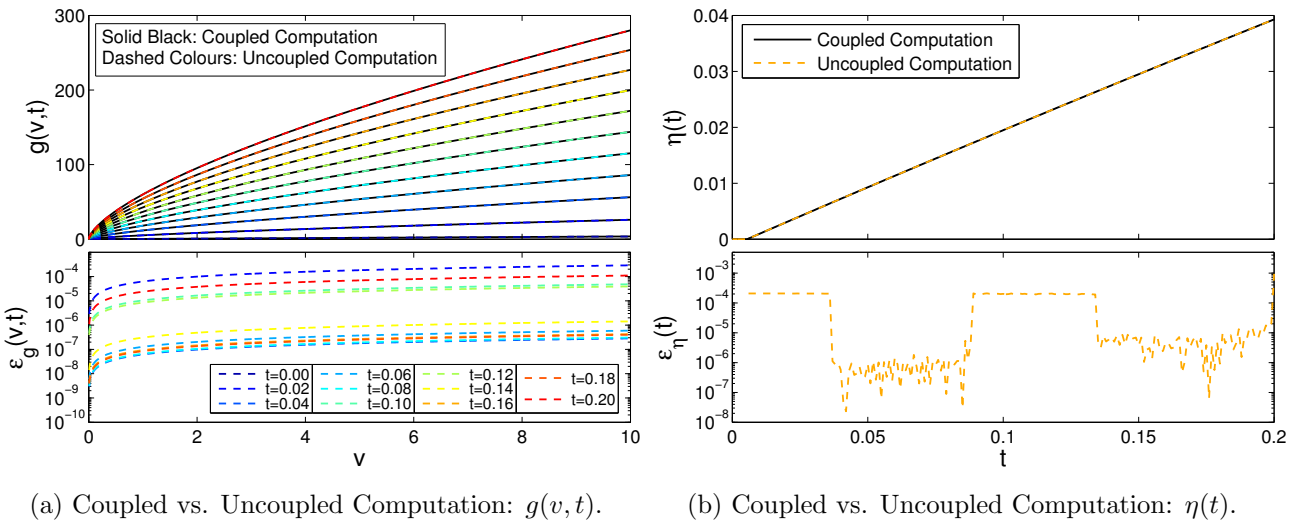
Figure 2.C.3: Comparison between the Coupled and the Uncoupled Computation of (a) $g(v,t)$ (2.B.8) and (b) $\eta(t)$ (2.C.5), obtained for $z_m = 0.8$ and $z_w = 10$ in (2.C.6). The error $\varepsilon_g(v,t)$ is defined as $|g_u(v,t) - g_c(v,t)|/(\int_0^{v_{\max}} g_c(v,t)^2 \, dv)^{1/2}$, while $\varepsilon_\eta(t) \equiv |\eta_u(t) - \eta_c(t)|/(\int_0^{T_{\max}} \eta_c(t)^2 \, dt)^{1/2}$, where $v_{\max} = 10$ and $T_{\max} = 0.2$. The subscripts c and u stand for Coupled and Uncoupled Computation of $g(v,t)$ and $\eta(t)$ respectively.

The Uncoupled Computation can provide the complete evolution of the rates $g(v, t)$ (2.B.8) and $\eta(t)$ (2.C.5), as shown in Figure 2.C.4.

The presented data allow us to estimate the orders of magnitude of the constant and the linear functions approximating the rate $g(v, t)$:

$$g(v, t) \propto g_0 = 10^3 \quad \text{and} \quad g(v, t) \propto g_0 v, \quad \text{with} \quad g_0 = 10^2. \tag{2.C.9}$$

It is also possible to estimate the order of magnitude of the nucleation rate $n(v, t)$ (2.B.9):

$$n(v, t) = \eta(t) \, \delta(v - \lambda_c) \quad \propto \quad n_0 \, \delta(v - v_0), \quad n_0 = 10^{-1}, \, v_0 = \lambda_c = 0.027, \tag{2.C.10}$$

with $\delta(x)$ the Dirac delta and λ_c taken from Table 2.1. Table 2.C.1 summarises the approximating functions and the corresponding orders of magnitude of all the considered rates.
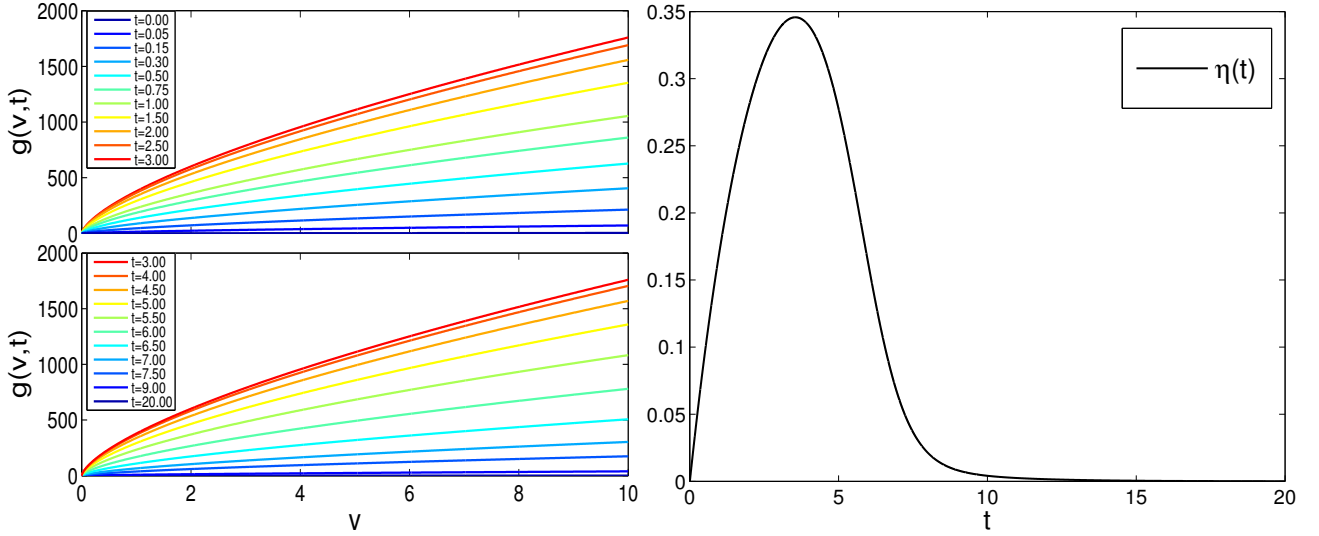
(a) Full Dynamics of $g(v, t)$ (2.B.8).   (b) Full Dynamics of $\eta(t)$ (2.C.5).

Figure 2.C.4: Complete evolution of (a) the growth rate $g(v, t)$ (2.B.8) and (b) the nucleation frequency $\eta(t)$ (2.C.5), provided by the Uncoupled Computation and validated for $v \in [0, v_{\max}]$ and $t \in [0, T_{\max}]$, where $v_{\max} = 10$ and $T_{\max} = 0.2$. The rate $g(v, t)$ can be approximated by the constant $g_0 = 10^3$, or by the linear function $g_0 v$, with $g_0 = 10^2$. The nucleation frequency $\eta(t)$ is of the order of $n_0 = 10^{-1}$.

Rate	Approximation	Order of Magnitude
$a_m(v, u, t)$	a_0	$a_0 = 10^2$
$a_w(v, u, t)$	$\hat{a}_0$	$\hat{a}_0 = 10^1$
$g(v, t)$	g_0	$g_0 = 10^3$
	$g_0 v$	$g_0 = 10^2$
$n(v, t)$	$n_0 \, \delta(v - v_0)$	$n_0 = 10^{-1}$
		$v_0 = 0.027$
$\mu_m(v, t)$	μ_0	$\mu_0 = 10^{-2}$
$\mu_w(v, t)$	$\hat{\mu}_0$	$\hat{\mu}_0 = 10^{-1}$

Table 2.C.1: Approximating functions and corresponding orders of magnitude for the rates (2.B.7)-(2.B.10), when the parameters assume the values specified in Table 2.1. The arising rates have been monitored for $v, u \in [0, v_{\max}]$ and $t \in [0, T_M]$, with $v_{\max} = 10$ and $T_M = 20$. The values of $g(v, t)$ and $n(v, t)$ have been estimated through the Uncoupled Computation, validated for $v \in [0, v_{\max}]$ and $t \in [0, T_{\max}]$, where $T_{\max} = 0.2$.

Chapter 3

Stochastic Simulation of Continuous Quantum Measurements

3.1 Motivation

3.1.1 Continuous Quantum Measurements

This Chapter is dedicated to continuous quantum measurements and stochastic simulation of such measurements on a computer. We start with some introductory notes. In a classical world we can monitor the progress of a billiard ball as it rolls along the surface of the table, falls off its edge, and continues on the floor. Our observation can be sufficiently discreet so as not to alter the ball's motion, and the moment finally drops off. In the quantum world, with objects of the size of atoms, the situation is by far more complex. Consider a two-level atom, initially in its excited upper state, dropping down to its lower state after emitting a photon. When precisely did the transition occur? To know it, we need to subject the atom to continuous monitoring. In the simplest case, the monitoring can consist of a series of measurements, in each of which a detector would tell us whether the atom is still in the upper, or already in the lower state. It is reasonable to neglect the duration of each measurement (von Neumann's impulsive limit [126]), and assume that a measurement occurs every τ seconds. The sequence of the meter's readings, say $f_k = upper$ or $lower$, will then constitute a measurement *readout.*

The main difference from the classical case is that the measurements will have to perturb the atom's evolution, or no information about the measured system would, in general, be gathered. The best known example is the Zeno effect [127]. If the measurements are too dense, $\tau \to 0$, the atom will always be found in upper state, will not decay at all. If, on the other hand the measurements are to be made "weak", so as to not perturb the atom's evolution, we will never know which state it is in. Thus, there is a need to find an optimal regime where the information about a phenomenon can be obtained without "killing" the phenomenon we set out to study.

The theory and practice of such (quasi-) continuous measurements is an important and popular subject (see, for example, [128]), recently helped by the advances of modern technology. An easily accessible yet extensive introduction to continuous measurements of two-state systems can be found in [129]. A straightforward introduction to measurements of more general observable was given in [130]. A mathematical formalism, presented in [131], allows one to treat imprecise measurements distributed in time. Possible applications of continuous measurements include quantum state estimation [132], the preparation of entangled states [133], and the feedback control in quantum systems [134]. The measurements formalism was also used in studying the dynamics of electronic charge [135], in the analysis of neural networks [136] and in the study of large deviations from typical behaviours [137]. Other applications of continuous measurements can be found in quantum optics [138], experiments with ions in traps [139] and electromagnetic fields [140].

3.1.2 Mensky's Measurements & Question Marks Over Them

The scope of our discussion is, however, much narrower, and concerns only one aspect of the theory. In the nineties of the last century, Mensky [141] reconsidered the need for a compromise between the accuracy and the perturbation incurred. His proposal consisted in using a sequence of weakly perturbing meters, with a large uncertainty Δf in their pointer position. In the limit $\Delta f \to \infty$, such a meter decouples from the measured system, and yields no useful information about it. However, if many such meters are used ever more densely, $\tau \to 0$, their combined effect, which depends on $\Delta f \tau^{1/2}$, may not be negligible. In the limit $\tau \to 0$, the readout f_k can then be replaced by a function $f(t)$, and the measurement becomes truly continuous. The approach relied on the Feynman path integral formulation of quantum mechanics, which is of no particular interest to us here.

As an application of the theory, Audretsch and Mensky (later referred to as AM) considered in [142] a two-level system in a superposition of the eigenstates of a variable $\hat{A}$, subjected it to a "fuzzy" continuous monitoring discussed above. They suggested that, after a sufficiently long time, two things should happen:

(i) the system's pure state will be turned into a density matrix, diagonal in the chosen representation (decoherence);

(ii) every readout $f(t)$ will eventually align with one of the eigenvalues of $\hat{A}$, indicating the eigenstate into which the system is driven as a result of being monitored.

Certain importance was later ascribed by Mensky [143] to the fact that the obtained information (the readout $f(t)$), may be seen to determine the final state of the observed system.

It is the statement (ii) which needs to be subjected to scrutiny. Why should a readout become a constant curve (with possible deviations for short periods of time (AM)) if we wait long enough? This certainly will not be the case for a system prepared in an eigenstate of $\hat{A}$, in which it will then remain at all times. The readings of different meters will be independent of each other, and will simply reflect the large initial uncertainty of the position of each pointer. In other words, a typical readout will have to remain extremely "hairy" at all times, and not tend to the constant eigenvalue curve.

One may, therefore, ask whether AM are correct in their predictions about the decoherence (i)? And if they are right about the decoherence, but wrong about the long-time behaviour of readouts, how can we know into which of the two eigenstates the system ends up driven into? In other words, how the information about the final state of the system can be extracted from a wildly fluctuating readout, showing no sign of settling into one of the constant curves?

These are the questions we will be answering in what follows. To do so we will require a reliable, if simple, computational algorithm, capable of modelling the behaviour of a quantum system under a continuous observation in the Mensky's regime.

3.1.3 Brief Summary of Our Results

Below we will show that while AM are correct in their analysis of the decoherence process, they fail to correctly describe the properties of the observed readouts. The fallacy is in neglecting the density of states available to the readouts f_1, f_2, ..., f_K in a K-dimensional space. While a constant readout does have the largest statistical weight, it is vastly outnumbered by highly irregular ones, which will be observed in almost every run of the experiment. This is even more true in the Mensky limit $K \to \infty$, $\Delta f \to \infty$, where the chance of obtaining an almost constant (or, indeed, a smooth) readout curve is virtually null.

The same argument applies to a system prepared in a superposition of the eigenstates of the measured operator. Numerical simulation of a "free" two-level system (i.e., of a system, whose own Hamiltonian is identically zero) reveals decoherence on the time scale, predicted by AM. At the same time, the measurement readouts remain highly irregular throughout the monitoring, and offer no obvious clue as to the final destination of the measured system. We will show that this information can be extracted from a particular readout, although the manner in which it can be done depends on the properties of the meter(s) employed. We will consider two particular cases, one in which the meter's initial state

has a sharp cut-off and vanishes outside an interval of a width Δf. In the other example, similar to the case studied by AM, this state is chosen to be a Gaussian of a width of Δf.

In the first case reduction of the initial state is sudden, and occurs at the moment a fluctuation sends the corresponding meter reading outside the specified range for the first time. Thus, to determine the result of decoherence, one needs to inspect the readout, find the first value outside the range, and use its sign to decide in which of the two eigenstates the system will henceforth reside. In the second case, the reduction is gradual, and can be seen as driven by a Gaussian walk with a drift, in which the sum of all readings (rescaled and shifted) represents the final position of the walker. The walks, ending far to the left or to the right, indicate whether the system has been directed towards the first or the second eigenstate of the measured operator $\hat{A}$.

A similar analysis applies also in the case the system is "driven", and would perform Rabi oscillations if left on its own. We will model such systems, in different measurement regimes, using the same stochastic algorithm. Increasing the accuracy of Mensky's meters (e.g., choosing a smaller value of $\Delta f \tau^{1/2}$ in the Gaussian case) will at first de-phase Rabi oscillations of the system. In the high accuracy limit, the decoherence of the initial superposition will eventually be completed at times much shorter than the Rabi period, much like in the case of a "free" system. After that Zeno effect will "freeze" the system in one of the eigenstates for the foreseeable future. In the near-Zeno regime the system resides in an eigenstate for a considerable period of time, before making a rapid transition into the other state available. The probability of remaining in a given state will, therefore, show the typical "telegraph noise" behaviour, with additional "spikes" corresponding to aborted transitions [144, 145, 146]. While the "sudden reduction" model allows for an analytical description of these features, the Gaussian case requires a numerical treatment.

In summary, we revisited the analysis of the "fuzzy continuous measurements" proposed by AM, exposed some of its deficiencies, and made amendments where necessary. Our results are published in [4].

The chapter is organised as follows. Basic principles of elementary quantum mechanics are reviewed in Appendix 3.A. Classical meters, individual and successive von Neumann quantum measurements are reviewed in Appendix 3.B. A stochastic algorithm for modelling successive quantum measurements of finite-dimensional quantum systems is proposed and tested in Section 3.2. In Section 3.3 we consider fuzzy continuous measurements performed on a two-level system, as presented by AM. In Section 3.4 we re-examine the fuzzy measurements of two-level systems. Section 3.5 contains our detailed conclusions.

3.2 Monte Carlo Method for Quantum Measurements

This section proposes a stochastic model and corresponding Monte Carlo (MC) method to simulate the quantum measurements described in Appendix 3.B. The probabilistic model and the MC method are formulated in Section 3.2.1. The simulation method is validated in Section 3.2.2 by comparison with available analytical solutions. The proposed MC method is used to verify the non-Markovian behaviour of the quantum meters, as shown in Section 3.2.3.

3.2.1 Monte Carlo Method Formulation

Based on the formalism discussed in Appendix 3.B.3, we propose a stochastic model and corresponding Monte Carlo (MC) method to simulate the continuous quantum measurements and to provide estimations of quantities of interest.

Defining $|\psi(t_k)\rangle$ as the state of the quantum system *just before* the meter firing at time $t_k = k\tau$, $\tau = T/K > 0$, $k = 1, .., K$, we can rewrite (3.B.15) as

$$|\psi(t_{k+1})\rangle = \exp(-i\hat{H}\tau)\, G(f_k - \hat{A})\, |\psi(t_k)\rangle, \quad \forall k = 1, .., K-1, \tag{3.1}$$

where $|\psi(t_1)\rangle = \exp(-i\hat{H}\tau)|\psi_0\rangle$ and $|\psi_0\rangle$ is the initial state of the quantum system. By plugging the identity operator $\sum_n |a_n\rangle\langle a_n|$, (3.1) is rewritten in matrix form:

$$|\psi(t_{k+1})\rangle = \sum_{n_1,n_2,n_3} |a_{n_3}\rangle\langle a_{n_3}|\exp(-i\hat{H}\tau)|a_{n_2}\rangle\langle a_{n_2}|G(f_k - \hat{A})|a_{n_1}\rangle\langle a_{n_1}|\psi(t_k)\rangle =$$

$$= \sum_{n_3} |a_{n_3}\rangle \sum_{n_2}\langle a_{n_3}|\exp(-i\hat{H}\tau)|a_{n_2}\rangle \sum_{n_1}\langle a_{n_2}|G(f_k - \hat{A})|a_{n_1}\rangle\langle a_{n_1}|\psi(t_k)\rangle =$$

$$= \sum_{n_3} |a_{n_3}\rangle \sum_{n_2} \hat{U}_{n_3,n_2}(\tau) \sum_{n_1} \hat{G}_{n_2,n_1}(f_k)\, c_{n_1}(t_k), \tag{3.2}$$

where $c_{n_1}(t_k) \equiv \langle a_{n_1}|\psi(t_k)\rangle$ is the n_1-th component of the vector $|\psi(t_k)\rangle$ in the basis of the eigenvectors $|a_n\rangle$. $\hat{G}_{n_2,n_1}(f_k)$ is the element of row n_2 and column n_1 of the matrix $\hat{G}(f_k) = G(f_k - \hat{A})$ in the basis of the eigenvectors $|a_n\rangle$. $\hat{U}_{n_3,n_2}(\tau)$ is the element of row n_3 and column n_2 of the matrix $\hat{U}(\tau) = \exp(-i\hat{H}\tau)$ in the basis of the eigenvectors $|a_n\rangle$. Equation (3.2) corresponds to the explicit expression of the matrix product in the basis of the eigenvectors $|a_n\rangle$:

$$|\psi(t_{k+1})\rangle = \hat{U}(\tau)\,\hat{G}(f_k)\,|\psi(t_k)\rangle, \quad \forall k = 1,..,K-1, \tag{3.3}$$

where $|\psi(t_k)\rangle = \sum_n c_n(t_k)|a_n\rangle$ and $c_n(t_k) = \langle a_n|\psi(t_k)\rangle \in \mathbb{C}$. In the chosen basis, the matrix $\hat{G}(f_k)$ is diagonal ($\delta_{i,j}$ is the Kronecker delta):

$$\hat{G}_{i,j}(f_k) \equiv \langle a_i|G(f_k - \hat{A})|a_j\rangle = \langle a_i| \sum_n |a_n\rangle G(f_k - a_n)\langle a_n|a_j\rangle = G(f_k - a_i)\,\delta_{i,j}. \tag{3.4}$$

The stochastic model is formulated in the basis of the eigenvectors $|a_n\rangle$ and the evolution of the state vector $|\psi(t_k)\rangle$ is given by the matrices multiplication (3.3).

The definition of the meter reading f_k provides the stochastic nature of the model. *Just after* the meter impulsive firing at time t_k, with the pointer value f_k, the quantum state $|\psi(t_k)\rangle = \sum_n c_n(t_k)|a_n\rangle$ becomes $|\varphi(f_k)\rangle$:

$$|\varphi(f_k)\rangle \equiv \hat{G}(f_k)\,|\psi(t_k)\rangle = \sum_n G(f_k - a_n)\, c_n(t_k)\,|a_n\rangle, \tag{3.5}$$

in agreement with the diagonal form of the matrix $\hat{G}(f_k)$. Following the Born postulate (*ii*) from Appendix 3.A.3, the probability density of the meter readout f_k is given by $p(f_k)$:

$$p(f_k) \equiv \langle\varphi(f_k)|\varphi(f_k)\rangle = \sum_n |c_n(t_k)|^2 G^2(f_k - a_n). \tag{3.6}$$

In other words, the meter reading f_k can be understood as an independent realisation of the random variable distributed according to the mixture (3.6) of the measures $G^2(f_k - a_n)$ with corresponding weights $|c_n(t_k)|^2$. In summary, the stochastic model can be written for all $k = 1,..,K$ as:

$$\begin{cases} |\psi(t_k)\rangle & = \sum_n c_n(t_k)\,|a_n\rangle, \\ f_k & \overset{\text{ind.}}{\sim} p(f_k) = \sum_n |c_n(t_k)|^2\, G^2(f_k - a_n), \\ |\varphi(f_k)\rangle & = p(f_k)^{-1/2} \sum_n G(f_k - a_n)\, c_n(t_k)\,|a_n\rangle, \\ |\psi(t_{k+1})\rangle & = \exp(-i\hat{H}\tau)\,|\varphi(f_k)\rangle, \end{cases} \tag{3.7}$$

where $|\psi(t_1)\rangle = \exp(-i\hat{H}\tau)|\psi_0\rangle$ and $|\psi_0\rangle$ is the initial state of the quantum system living in the Hilbert space H. The factor $p(f_k)^{-1/2}$ ensures the normalisation of the state $|\varphi(f_k)\rangle$, i.e. $\langle\varphi(f_k)|\varphi(f_k)\rangle = 1$. Given the Hamiltonian $\hat{H} : H \to H$ and the time step $\tau > 0$, the operator $\exp(-i\hat{H}\tau)$ provides the evolution of the system state $|\psi(t)\rangle \in H$ driven by the Schrödinger Equation (SE), with $\hbar = 1$:

$$i\partial_t|\psi(t)\rangle = \hat{H}|\psi(t)\rangle. \tag{3.8}$$

In the stochastic model (3.7), the operator $\exp(-i\hat{H}\tau)$ must be thought as a matrix in the basis of the eigenvectors $|a_n\rangle$.

The stochastic model (3.7) can be solved using the Monte Carlo (MC) method proposed in Algorithm 3.1 for simulating quantum measurements. Algorithm 3.1 obtains a single realisation of the system dynamics by iterating over the index k the procedure (3.7).

Sampling of the random process is obtained by the independent repetition of the procedure described in Algorithm 3.1 for $S \geq 1$ times. The quantities of interest can be approximated by averaging computed statistics on the drawn MC sample with the size S.

For example, the density matrix $\rho(t_k)$ discussed in Appendix 3.A.5,

$$\rho(t_k) \equiv \int p(f_k) \, |\varphi(f_k)\rangle \, \langle\varphi(f_k)| \, df_k, \quad \forall k = 1, .., K, \tag{3.9}$$

with $|\varphi(f_k)\rangle$ defined in (3.7) and $p(f_k)$ in (3.6), can be estimated as

$$\rho(t_k) \approx \tilde{\rho}_k \equiv \frac{1}{S} \sum_{j=1}^{S} |\varphi_k^j\rangle\langle\varphi_k^j|, \quad \forall k = 1, .., K, \tag{3.10}$$

where $\{|\varphi_k^j\rangle\}_{j=1}^{S}$ is the MC sample drawn by Algorithm 3.1 and $\tilde{\rho}_k$ is the classical MC estimator [147] of $\rho(t_k)$.

Analogously, we approximate the expected meter reading $F(t_k)$ using the MC estimator $\tilde{F}_k$:

$$F(t_k) \equiv \int f_k \, p(f_k) \, df_k \approx \tilde{F}_k \equiv \frac{1}{S} \sum_{j=1}^{S} f_k^j, \quad \forall k = 1, .., K, \tag{3.11}$$

with $\{f_k^j\}_{j=1}^{S}$ being the MC sample of the meter readings f_k, drawn by Algorithm 3.1.

Algorithm 3.1: The Monte Carlo (MC) method to draw one realisation of the dynamics of the $N \geq 1$ levels quantum system, during the time interval $[0, T]$. The evolution is driven by the Hamiltonian $\hat{H}$ and the operator $\hat{A}$ represents the measured quantity, $[\hat{A}, \hat{H}] \neq 0$, $\hat{A}|a_n\rangle = a_n|a_n\rangle$.

---

1 Assign the measured operator $\hat{A} = \sum_{n=1}^{N} |a_n\rangle a_n \langle a_n|$;

2 Assign the number $K \geq 1$ of measurements and the time step size $\tau = T/K > 0$;

3 Assign the evolution operator $\hat{U} = \exp(-i\hat{H}\tau)$;

4 Assign the measure $G(f)$, $\int G^2(f) \, df = 1$, with $\int f \, G^2(f) \, df = 0$;

5 Assign the initial state of the system $|\varphi_0\rangle = \sum_{n=1}^{N} c_0^n \, |a_n\rangle$, with $\sum_{n=1}^{N} |c_0^n|^2 = 1$;

6 **for** $k = 1, .., K$ **do**

7 $\quad$ Assign time $t_k = k\tau$;

8 $\quad$ Evolve the state of the system: $|\psi_k\rangle = \hat{U}|\varphi_{k-1}\rangle = \sum_{n=1}^{N} c_k^n \, |a_n\rangle$;

9 $\quad$ Compute the probabilities $\underline{p}_k = \{|c_k^1|^2, .., |c_k^N|^2\}$;

10 $\quad$ Select the state index $i_k \in \{1, .., N\}$ with the probabilities $\underline{p}_k$;

11 $\quad$ Draw the observed value $f_k \sim G^2(f - a_{i_k})$, with $f \in \mathbb{R}$;

12 $\quad$ Compute the normalisation factor $M_{f_k} = \sum_{n=1}^{N} G^2(f_k - a_n) \, |c_k^n|^2$;

13 $\quad$ Use f_k to construct $|\varphi_k\rangle$: $|\varphi_k\rangle = M_{f_k}^{-1/2} \sum_{n=1}^{N} G(f_k - a_n) \, c_k^n \, |a_n\rangle$;

14 **end**

3.2.2 Monte Carlo Method Validation

The MC method of Section 3.2.1 is validated by comparison with available analytical solutions. In particular, we compute the expected meter reading $F(\tau)$ defined in (3.11), for any time step size $\tau = t_1 > 0$ and any square-integrable measure G, with $\int f \, G^2(f) \, df = 0$. The MC estimator $\tilde{F}_1$ defined in (3.11) is validated by comparison with the derived below solution $F(\tau)$. The width $\Delta f > 0$ of the chosen *Gaussian* measure

$$G(f) \equiv C^{-1/2} \exp(-f^2/2\Delta f^2), \quad C \equiv (\pi \Delta f^2)^{1/2}, \tag{3.12}$$

quantifies the accuracy of the measurements. Since the MC estimator $\tilde{F}_1$ and the derived analytical solution $F(\tau)$ stand for any $\Delta f > 0$ in (3.12), we perform the validation for different levels of accuracy and corresponding values of Δf, as shown in Figure 3.1a.

Then, we test the convergence rate of the MC estimator $\tilde{\rho}_k$ defined in (3.10). Such rate is quantified by the speed at which the error function

$$\varepsilon(S) \equiv \max_{k,m,n} |\langle a_m | \tilde{\rho}_k(S) - \rho(t_k) | a_n \rangle| \tag{3.13}$$

converges to zero as the sample size S increases. The density matrix $\rho(t_k)$ in (3.13) is given by the analytical solution (3.26) derived in Section 3.2.3, under the condition (3.20). The *rectangular* measure

$$G(f) = \begin{cases} 1/\sqrt{\Delta f}, & \text{for } |f| \leq \Delta f/2, \\ 0, & \text{otherwise,} \end{cases} \tag{3.14}$$

and the value of $\Delta f > 0$ are chosen to ensure the assumption (3.20). Figure 3.1b shows that the convergence rate of the estimator $\tilde{\rho}_k$ (3.10) is of order $O(S^{-1/2})$, in agreement with the Central Limit Theorem [147].

As stated above, we derive the analytical formula to compute the expected meter reading $F(\tau)$ in (3.11), for any $\tau = t_1 > 0$ and any square-integrable measure G, with $\int f \, G^2(f) \, df = 0$. Given the initial condition $|\psi_0\rangle = \sum_n c_n(0) |a_n\rangle$, with $\sum_n |c_n(0)|^2 = 1$, (3.7) leads to

$$|\psi(\tau)\rangle = \hat{U}(\tau) |\psi_0\rangle = \sum_n c_n(\tau) |a_n\rangle, \quad c_n(\tau) \equiv \sum_m \hat{U}_{n,m}(\tau) \, c_m(0), \tag{3.15}$$

where $\hat{U}_{n,m}(\tau)$ is the element of row n and column m of the evolution matrix $\hat{U}(\tau) = \exp(-i\hat{H}\tau)$ in the basis of the eigenvectors $|a_n\rangle$, i.e. $\hat{U}_{n,m}(\tau) \equiv \langle a_n | \exp(-i\hat{H}\tau) | a_m \rangle$. Following (3.7), the meter readout f_1 is drawn from the distribution

$$f_1 \sim \sum_n |c_n(\tau)|^2 \, G^2(f_1 - a_n), \tag{3.16}$$

whose expectation is

$$F(\tau) = \sum_n |c_n(\tau)|^2 \, a_n, \quad c_n(\tau) = \sum_m \hat{U}_{n,m}(\tau) \, c_m(0). \tag{3.17}$$

Figure 3.1a shows the comparison between the MC estimator $\tilde{F}_1$ in (3.11) and the analytical solution $F(\tau)$ (3.17) for different values of the width $\Delta f > 0$ of the measure $G(f)$ (3.12). The performed measurements monitor the observable $\hat{A}$ of a two-level system:

$$\hat{A}|a_n\rangle = a_n|a_n\rangle, \quad n = 1, 2. \tag{3.18}$$

The system is driven by the evolution matrix $\hat{U}(\tau)$, with

$$\hat{U}_{1,1}(\tau) = \hat{U}_{2,2}(\tau) = \cos\tau, \quad \hat{U}_{1,2}(\tau) = \hat{U}_{2,1}(\tau) = -i\sin\tau, \tag{3.19}$$

starting from the initial state $|\psi_0\rangle = |a_1\rangle$. As shown in Figure 3.1a, the sample size $S = 10^7$ ensures the good accuracy of $\tilde{F}_1$, for the tested values of Δf.

Figure 3.1b shows the convergence rate $O(S^{-1/2})$ of the MC estimator $\tilde{\rho}_k$ in (3.10) for different numbers $K \geq 1$ of performed measurements. The measure $G(f)$ (3.14) inspects the observable $\hat{A}$ (3.18), with $a_2 = -a_1 = 1$ and $\Delta f = 1$ fulfilling (3.20). The initial state $|\psi_0\rangle = |a_1\rangle$ is evolved by the matrix $\hat{U}(\tau)$ (3.19), with $\tau = 1$. The shown error $\varepsilon(S)$ is defined in (3.13).
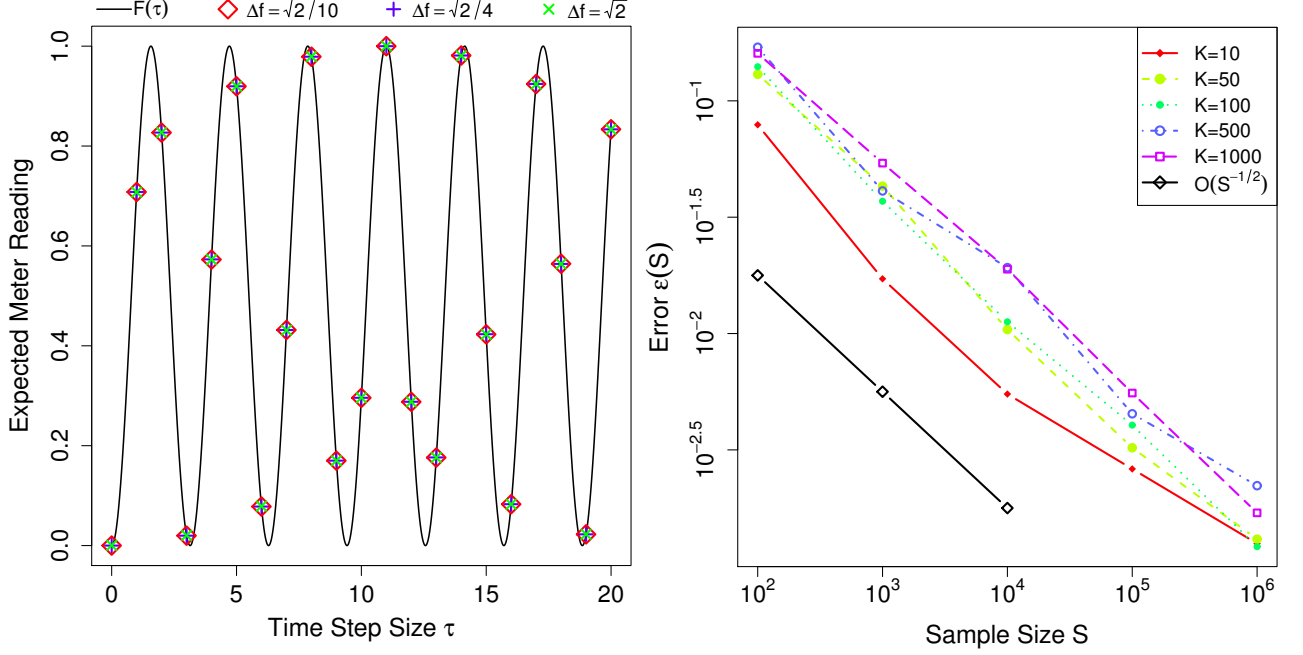
(a) Comparison between $\tilde{F}_1$ (3.11) and $F(\tau)$ (3.17).

(b) Convergence Rate of $\tilde{\rho}_k$ (3.10).

Figure 3.1: Figure (a) shows the comparison between the MC estimator $\tilde{F}_1$ (3.11) (diamonds and crosses) and the analytical solution $F(\tau)$ (3.17) (solid line), when the measure $G(f)$ (3.12) monitors the observable $\hat{A}$ (3.18), with $a_1 = 0$ and $a_2 = 1$. The system is driven by $\hat{U}(\tau)$ (3.19), starting from $|\psi_0\rangle = |a_1\rangle$. The sample size $S = 10^7$ ensures the good accuracy of $\tilde{F}_1$ (3.11), for the tested values of $\Delta f > 0$ in (3.12). Figure (b) shows the convergence rate $O(S^{-1/2})$ of the MC estimator $\tilde{\rho}_k$ (3.10) for different numbers $K \geq 1$ of performed measurements. The measure $G(f)$ (3.14) inspects the observable $\hat{A}$ (3.18), with $a_2 = -a_1 = 1$ and $\Delta f = 1$ fulfilling (3.20). The initial state $|\psi_0\rangle = |a_1\rangle$ is evolved by $\hat{U}(\tau)$ (3.19), with $\tau = 1$. The shown error $\varepsilon(S)$ is defined in (3.13).

3.2.3 Non-Markovian Behaviour of Meter Reading

The meter reading f_k in (3.7) follows, in general, a non-Markovian behaviour. In fact, the weights $|c_n(t_k)|^2$ of the distribution $p(f_k)$ are determined by the complete history of the process. However, particular choices of the measure G can destroy the dependency on the history, leading to the Markovian behaviour shown below. The MC method designed in Section 3.2.1 is used to verify the different regimes of the meter reading f_k, as shown in Figure 3.2.

The meter reading f_k in (3.7) follows a Markovian behaviour, in the case the function $G = G(f)$ is narrow enough. In particular, the meter readouts $\{f_1, .., f_K\}$ form a Markov chain over the eigenvalues a_n of the measured operator $\hat{A}$, $\hat{A}|a_n\rangle = a_n|a_n\rangle$, with $\hat{P}(\tau)$ being the transition probability matrix for a time step of length $\tau > 0$.

If G is narrow enough, with $\int f\, G^2(f)\, df = 0$, the mixture $p(f_k)$ in (3.7) draws the meter readout f_k close to the expectation of each component, i.e. $f_k \approx a_n$. The proximity of f_k to a_n is determined by the width of the measure G. We assume $G(f)$ narrow enough to give

$$G(f - a_n)\, G(f - a_m) \approx 0, \quad \forall f \in \mathbb{R}, \forall n \neq m. \tag{3.20}$$

Condition (3.20) means that the sets $S_n \equiv \{f \in \mathbb{R},\, G(f - a_n) \gg 0\}$ and $S_m \equiv \{f \in \mathbb{R},\, G(f - a_m) \gg 0\}$ are *non-overlapping* for all $n \neq m$. Any drawn value of f_k can be associated to a unique a_n, falling in the corresponding set S_n. In this sense, we say that $f_k \approx a_n$ and the Markov chain moves across the eigenvalues a_n.

Then, the mixture $p(f_k)$ in (3.7) draws the meter readout $f_k \approx a_n$ with probability (w.p.) proportional to the corresponding weight:

$$f_k \approx a_n, \quad \text{w.p.} \quad |c_n(t_k)|^2, \quad c_n(t_k) = \langle a_n | \psi(t_k) \rangle, \quad \forall k = 1, .., K. \tag{3.21}$$

Provided $f_k \approx a_m$, the state $|\varphi(f_k)\rangle$ in (3.7) reduces to the eigenstate $|a_m\rangle$ because (3.20) implies

$$G(f_k - a_m) \gg 0, \quad \text{and} \quad G(f_k - a_n) \approx 0, \quad \forall n \neq m. \tag{3.22}$$

Thus, (3.7) leads to

$$|\psi(t_{k+1})\rangle = \exp(-i\hat{H}\tau)|a_m\rangle. \tag{3.23}$$

Given $f_k \approx a_m$, (3.21) provides the distribution of the readout f_{k+1}:

$$f_{k+1} \approx a_n, \quad \text{w.p.} \quad \hat{P}_{n,m}(\tau), \quad \hat{P}_{n,m}(\tau) \equiv |\langle a_n | \exp(-i\hat{H}\tau)|a_m\rangle|^2, \tag{3.24}$$

where $\hat{P}_{n,m}(\tau)$ corresponds to the probability for the transition from state $f_k \approx a_m$ to state $f_{k+1} \approx a_n$ within a time step of length τ. In other words, $\hat{P}_{n,m}(\tau)$ is the element of row n and column m of the transition matrix $\hat{P}(\tau)$ in the basis of the eigenvectors $|a_n\rangle$, i.e. $\hat{P}_{n,m}(\tau) = \langle a_n | \hat{P}(\tau)|a_m\rangle$.

In summary, the meter reading f_k can be understood as a realisation of the Markov chain visiting the eigenvalues a_n, whose distribution can be computed as

$$\pi_k = \hat{P}(\tau)^{k-1}\pi_1, \quad \forall k = 1, .., K, \tag{3.25}$$

with π_1 the distribution at time $t_1 = \tau$, i.e. $\pi_1(a_n) = |\langle a_n | \exp(-i\hat{H}\tau)|\psi_0\rangle|^2$, and $|\psi_0\rangle$ the initial state of the quantum system.

Assuming (3.20), the analytical solution for the density matrix $\rho(t_k)$ (3.9) is also available. The state $|\varphi(f_k)\rangle$ is found to be the eigenvector $|a_n\rangle$ with probability $\pi_k(a_n)$, i.e. if $f_k \approx a_n$. As explained in Appendix 3.A.5, the quantum system is found in the mixed state

$$\rho(t_k) = \sum_n \pi_k(a_n)|a_n\rangle\langle a_n|, \quad \forall k = 1, .., K, \tag{3.26}$$

where $\pi_k(a_n)$ is given by (3.25).

We now use the MC method formulated in Section 3.2.1 to verify the different regimes of the meter reading f_k. In particular, the width of the measure $G(f - a_n)$ can determine the Markovian behaviour of the meter reading f_k, by ensuring the condition (3.20). On the other hand, the measure $G(f - a_n)$ can be broad enough to reject the hypothesis (3.20), leading to the non-Markovian behaviour of the meter reading f_k.

With the aim to verify the discussed regimes, we propose the following experiment. Chosen the broadness of the measure G, Algorithm 3.1 draws two independent realisations $\{f_1, .., f_k\}$ and $\{g_1, .., g_h\}$ of the meter readings, such that the readouts f_k and g_h are found close enough, i.e. $|f_k - g_h| < \varepsilon$, with $0 < \varepsilon \ll 1$. The corresponding states of the system are stored. The computation of the next time steps is performed for $S \geq 1$ independent times, providing samples of the readouts f_{k+1} and g_{h+1}. Given $f_k \approx g_h$, the samples can approximate the distributions of the next meter readings f_{k+1} and g_{h+1}.

In the Markovian regime, the distributions of f_{k+1} and g_{h+1} must depend only on the previous readouts f_k and g_h respectively. Since $f_k \approx g_h$, the distributions of f_{k+1} and g_{h+1} must be similar, as shown in Figure 3.2a verifying the Markovian nature of the meter. In the non-Markovian regime, the distributions of f_{k+1} and g_{h+1} depend on the full histories $\{f_1, .., f_k\}$ and $\{g_1, .., g_h\}$ respectively. Since $\{f_1, .., f_k\} \neq \{g_1, .., g_h\}$, the distributions of f_{k+1} and g_{h+1} can be significantly different, as demonstrated in Figure 3.2b, thus confirming the non-Markovian behaviour of the meter.

(a) Markovian Regime.

(b) Non-Markovian Regime.
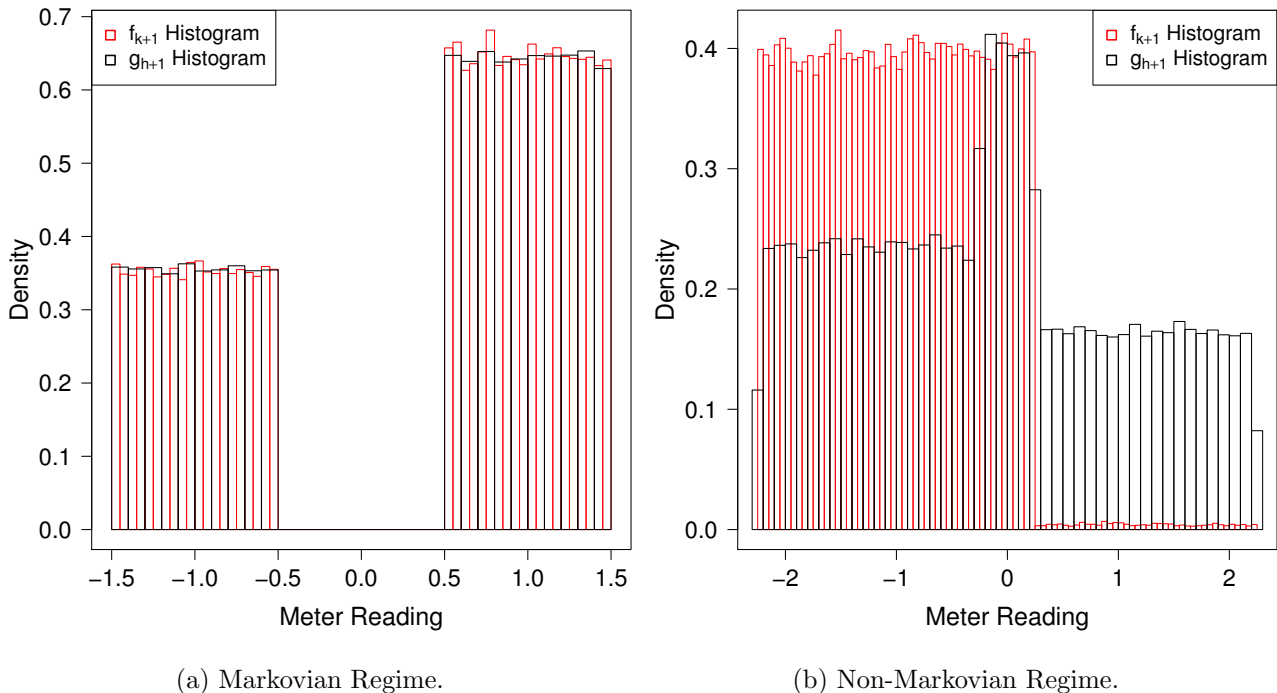
Figure 3.2: Given the measurements histories $\{f_1, .., f_k\} \neq \{g_1, .., g_h\}$, with $|f_k - g_h| < \varepsilon = 10^{-3}$, the shown histograms approximate the densities of the meter readings f_{k+1} and g_{h+1} by samples with size $S = 10^5$. The rectangular measure G (3.14) monitors the observable $\hat{A}$, $\hat{A}|a_n\rangle = a_n|a_n\rangle$, of a two-level system, with $a_2 = -a_1 = 1$. The dynamics is driven by the matrix $\hat{U}(\tau)$, with $\hat{U}_{1,1}(\tau) = \hat{U}_{2,2}^*(\tau) = \cos\tau - i\sqrt{1/2}\sin\tau$, $\hat{U}_{1,2}(\tau) = \hat{U}_{2,1}(\tau) = -i\sqrt{1/2}\sin\tau$ and $\tau = 1$, starting from the initial state $|\psi_0\rangle = |a_1\rangle$. Since $f_k \approx g_h$, the Markovian regime imposes the similar distribution for the next meter readings f_{k+1} and g_{h+1}, as shown in Figure 3.2a for $\Delta f = 1$. Depending on the full histories $\{f_1, .., f_k\} \neq \{g_1, .., g_h\}$, the densities of f_{k+1} and g_{h+1} can be significantly different in the non-Markovian case, as shown in Figure 3.2b for $\Delta f = 2.5$.

3.3 Continuous Fuzzy Measurement on Two-Level Systems

As discussed in Appendix 3.B.2 and Appendix 3.B.3, the width $\Delta f > 0$ of the meter measure $G(f)$ characterises the regime of the performed measurements. Two limiting cases can be distinguished. A broad measure G, i.e. $\Delta f \to +\infty$, gives rise to inaccurate measurements, allowing the system natural evolution. The paths travelled by the system, within the large width Δf, cannot be distinguished, since the corresponding routes are allowed to interfere. On the other hand, a narrow measure G, i.e. $\Delta f \to 0$, produces accurate measurements, obtained at the price of a strong influence of the meters on the free evolution of the system. The travelled paths can be distinguished, because the interference among the corresponding routes is destroyed.

As introduced in Section 3.1.2, Mensky [141] reconsidered the need for a compromise between the accuracy and the perturbation incurred. A sequence of weakly perturbing meters, with large Δf, allows the free dynamics, yielding no useful information about the measured system. However, if many such meters are used ever more densely, their combined effect may not be negligible, providing some useful information. In particular, Audretsch and Mensky [142] suggested that such a dense sequence of weakly perturbing meters would allow one to read off the system state directly from the registered readouts. They also predicted a rapid decoherence of a pure initial state if the measured quantity $\hat{A}$ commutes with the Hamiltonian $\hat{H}$ of the system, and formulated the conditions for the Zeno effect in case the two do not commute.

We explain in Section 3.3.1 what stated by Audretsch and Mensky, outlining the main conclusions of [142]. Section 3.3.2 proves one statement to be incorrect, providing a counterexample. The other conclusions are reconsidered in Section 3.4.

3.3.1 Mensky Regime & Conclusions

Audretsch and Mensky considered in [142] a regime of measurements becoming more inaccurate as they are more frequently performed (Mensky regime). The Gaussian measure $G(f)$ (3.12) is chosen to monitor the observable $\hat{A} : H \to H$, $\hat{A}|a_n\rangle = a_n|a_n\rangle$, of a two-level system in the Hilbert space H, with Hamiltonian $\hat{H}$ and initial state

$$|\psi_0\rangle = \alpha_0|a_1\rangle + \beta_0|a_2\rangle, \quad \langle\psi_0|\psi_0\rangle = 1. \tag{3.27}$$

The amplitude $\langle a_n|\psi(T;\underline{f})\rangle$ (3.B.18) reads

$$\langle a_n|\psi(T;\underline{f})\rangle = C^{-K/2} \sum_{m_1,..,m_{K-1}} F_n(m_1,..,m_{K-1}) \exp\left[-\frac{\frac{\tau}{T}\sum_{k=1}^{K}(f_k - a_{m_k})^2}{\Delta a_T^2}\right], \quad n = 1,2, \tag{3.28}$$

with $\Delta a_T^2 \equiv 2\tau\Delta f^2/T > 0$. The Mensky regime is reached for

$$\tau \to 0, \quad \Delta f \to +\infty, \quad 2\tau\Delta f^2 = \kappa^{-1}, \tag{3.29}$$

where $\kappa > 0$ is a tunable constant. As proposed in [131], the limit (3.29) leads to the continuous formulation of the amplitude (3.28):

$$\langle a_n|\psi(T;\underline{f})\rangle = \sum_{\forall a(t)} F_n[a(t)] \exp\left[-\frac{\frac{1}{T}\int_0^T[f(t) - a(t)]^2\,dt}{\Delta a_T^2}\right], \quad n = 1,2, \tag{3.30}$$

where the path $a(t)$ is a function taking only the values a_1 or a_2 at any time $0 \leq t \leq T$. The factor

$$F_n[a(t)] \equiv \lim_{K \to +\infty}\langle a_n|\exp(-i\hat{H}\tau)|a_{m_{K-1}}\rangle .. \langle a_{m_1}|\exp(-i\hat{H}\tau)|\psi_0\rangle, \quad n = 1,2, \tag{3.31}$$

is the probability amplitude to reach $|a_n\rangle$ from $|\psi_0\rangle$ via $a(t)$ with no meters present. Finally,

$$\Delta a_T = 1/\sqrt{\kappa T} \tag{3.32}$$

and the factor divided by Δa_T^2 is the time averaged square of the deviation of the path $a(t)$ from the observed readout $f(t)$.

The role of the meters is to modify the amplitudes of the system's Feynman paths, suppressing them for the paths deviating from a readout $f(t)$, and leaving them untouched for $a(t)$ close to $f(t)$. Given (3.30), it is tempting to assume, as was done in [142], that for $\Delta a_T \ll |a_1 - a_2|$, $f(t)$ and $a(t)$ must be point-wise close, with $a(t)$ rarely differing from $f(t)$ by more than Δa_T. By the same token, one may expect the observed readouts to be not too different from one of the Feynman paths $a(t)$, i.e. to alternate between the values a_1 and a_2.

Based on the above, the authors of [142] predicted the following conclusions for $\hat{A}$ and $\hat{H}$ commuting:

(i) for a small $\Delta a_T \ll |a_1 - a_2|$, e.g. in the case of $T \to \infty$, one would observe only the readouts lying in very narrow bands close to the constant curves $f(t) \equiv a_i$, such that for most of the monitoring one has $|f(t) - a_i| \lesssim \Delta a_T \ll |a_1 - a_2|$.

(ii) The initial superposition (3.27) would undergo complete decoherence if the duration of the monitoring exceeds $1/\kappa|a_1 - a_2|^2$, i.e. a pure state $|\psi_0\rangle$ will be turned into a mixture $\rho(T) = |a_1\rangle|\alpha_0|^2\langle a_1| + |a_2\rangle|\beta_0|^2\langle a_2|$ for $T \gtrsim 1/\kappa|a_1 - a_2|^2$.

We show in Section 3.3.2 that the assumption (i) is incorrect, and we explain in Section 3.4.1 how (ii) is possible without (i). In [142] the authors considered also monitoring of a system, capable of making transitions between the states $|a_1\rangle$ and $|a_2\rangle$, described by the Hamiltonian $\hat{H}$:

$$\langle a_n|\hat{H}|a_n\rangle = 0, \quad \langle a_1|\hat{H}|a_2\rangle = \langle a_2|\hat{H}|a_1\rangle \equiv \omega. \tag{3.33}$$

In the absence of the meters, such a system performs Rabi oscillations with a period $T_R = 2\pi/\omega$. Following [142], we choose to measure an operator $\hat{A}$, $\langle a_i|\hat{A}|a_j\rangle = a_i\delta_{ij}$. In the Zeno regime, i.e. for $1/\kappa|a_1 - a_2|^2 \ll T_R \ll T$, the authors of [142] made the following suggestions:

(I) Only those measurement outputs $f(t)$ that are close to one of the constant curves $f(t) = a_1$ and $f(t) = a_2$ have high probability.

(II) The probability of the output to be close to a_1 or a_2 is given by the initial values of the decomposition coefficients $|\alpha_0|^2$ or $|\beta_0|^2$ correspondingly.

(III) In the case of the output being close to a_1 or a_2, the final state is correspondingly the eigenstate $|a_1\rangle$ or $|a_2\rangle$.

The statements (I)-(III) are reconsidered in Section 3.4.2.

3.3.2 The Single Path Case

This section shows that the conclusion (i) of Section 3.3.1 is incorrect. Being κ a given constant, the factor Δa_T^2 (3.32) is decreasing to zero, as $T \to +\infty$. Motivated by the form of (3.30), the statement (i) ensures the point-wise convergence of the meter reading $f(t)$ to the path $a(t)$. This disagrees with the highly inaccurate nature of the performed measurements, i.e. $\Delta f \to +\infty$ in (3.29). In fact, the meter readouts $f(t)$, with mean squared deviation from $a(t)$ greater than Δa_T^2, are by far more numerous than the ones with squared deviation less than Δa_T^2. As a consequence, the former kind of readouts is way more likely than the latter, solving the apparent paradox. In other words, the distance $|f(t) - a(t)|^2$ is allowed to exceed the small value of Δa_T^2, rejecting the conclusion (i).

To quantify the discussed criticism to the conclusion (i), we assume that $|\psi_0\rangle = |a_1\rangle$ and $\hat{H} \equiv 0$. Then, we subject the system permanently residing in the state $|a_1\rangle$ to monitoring by a set of identical Gaussian meters, as discussed above. If the statement (i) of Section 3.3.1 is correct, we should observe only the readouts clinging to the constant curve $f(t) = a_1$, by choosing a T sufficiently large. This appears to be unlikely, since now we have $K \gg 1$ independent measurements of a normally distributed variable f. The meter firing at a time t_k has no knowledge of what has happened in the past, at t_i, $1 \leq i < k$. Thus, there is no reason to expect its output to fit into a narrow band around a_1. Rather, the mean value of $|f(t) - a_1|^2$ should be determined only by $\Delta f = 1/\sqrt{2\kappa\tau}$, which is very large if τ is small. Returning to (3.28), we have that the distribution $W(\underline{f})$ of the meter readings $\underline{f} \equiv \{f_1, .., f_K\}$ is given by:

$$W(\underline{f}) \equiv \langle\psi(T;\underline{f})|\psi(T;\underline{f})\rangle = C^{-K} \exp\left[-\frac{\frac{1}{K}\sum_{k=1}^{K}(f_k - a_1)^2}{\Delta a_T^2/2}\right]. \tag{3.34}$$

Now the statement (i) is equivalent to the assertion that the most probable readouts are those for which $\Theta(\underline{f}) \equiv \sum_{k=1}^{K}(f_k - a_1)^2/K \lesssim \Delta a_T^2$, but this is incorrect. To determine the most probable value of Θ we also need to take into account the density of states available for $\underline{f}$. An output $\underline{f}$ is represented by a point in a K-dimensional space, and $R^2 \equiv \sum_{k=1}^{K}(f_k - a_1)^2$ is just the square of its distance from a_1. Other readouts sharing the same value of the R^2 lie on an K-dimensional sphere centred at a_1, and the probability to find a value of R between r and $r + dr$ is, therefore, given by $C^{-K}\,dV_K(r)/dr\,\exp(-2r^2/\Delta a_T^2 K)\,dr$, where V_K is the volume a K-dimensional ball. The derivative is just the surface area of a $K-1$-dimensional sphere, and is well known to be $dV_K(r)/dr = 2\pi^{K/2}r^{K-1}/\Gamma(K/2)$, where $\Gamma(z) = \int_0^\infty y^{z-1}\exp(-y)dy$ is the Gamma function [148]. Thus, for the probability $dP(x)$ to have the value of Θ between x and $x + dx$, we find

$$\frac{dP}{dx} = \frac{(\Delta a_T^2/2)^{-1}}{\Gamma(K/2)}\left(\frac{x}{\Delta a_T^2/2}\right)^{K/2-1}\exp\left(-\frac{x}{\Delta a_T^2/2}\right). \tag{3.35}$$

The r.h.s. of (3.35) peaks at $x_0 = (\Delta a_T^2/2)(K/2 - 1) \approx \Delta f^2/2$, which means that we are most likely to see the readouts wildly fluctuating around a_1 on the scale of $\pm\Delta f$, rather than those lying in a narrow band of a width $\approx \Delta a_T$, as shown by Figure 3.3.

The behaviour of the meter readings f_k is also confirmed by the stochastic formulation (3.7) of the two-level system permanently residing in the state $|a_1\rangle$, i.e. $|\psi_0\rangle = |a_1\rangle$ and $\hat{H} \equiv 0$. Being $G(f)$ (3.12), the meter readouts $f_1, .., f_K$ correspond to independent realisations of the random variables

$$f_1, .., f_K \overset{\text{ind.}}{\sim} \mathcal{N}(f|a_1, \Delta f/\sqrt{2}), \tag{3.36}$$

where $\mathcal{N}(x|\mu, \sigma)$ denotes a normal distribution [149] with mean μ and standard deviation $\sigma > 0$:

$$\mathcal{N}(x|\mu, \sigma) \equiv (2\pi\sigma^2)^{-1/2} \exp[-(x - \mu)^2/2\sigma^2]. \tag{3.37}$$

It follows that the meter readings f_k deviate from their mean a_1 on the scale of the standard deviation $\approx \Delta f$, rather than converge in a narrow band of width $\approx \Delta a_T$, as guaranteed by the conclusion (i). The analytical finding (3.35) is obtained from (3.36) by applying the *change of variable* formula for probability density functions and by using the definition of Chi-squared distribution, as shown in [150]. In conclusion, while it is true that the contribution of the constant readout $f(t) = a_1$ is far greater than the one from a readout for which $\int_0^T [f(t) - a_1]^2 \, dt/T \gg \Delta a_T^2$, the contribution itself vanishes as the number K of meters increases. At the same time, the readouts with smaller individual probabilities are by far more numerous, and therefore more likely. The same argument applies in the two paths case, where $|\psi_0\rangle$ is chosen to be a superposition (3.27). Also in this case, by choosing $\Delta a_T \ll |a_1 - a_2|$, one would not obtain readouts clinging to the constant curves $f(t) = a_i$. Rather, the spread of the readings would greatly exceed the separation between the eigenvalues a_1 and a_2, making it impossible to decide immediately which of the two states the system is in. This poses a further question. If the readouts were an eigenvalue curve $f(t) = a_1$ or $f(t) = a_2$, it would be easy to conclude that, as a result of the decoherence, the system has indeed settled into one of the eigenstates of $\hat{A}$. But since this is not the case, how sure can we be that decoherence has taken place? In other words, is statement (ii) of Section 3.3.1 correct, and if it is, what is the precise mechanism of the decoherence? We answer these questions in Section 3.4.1.
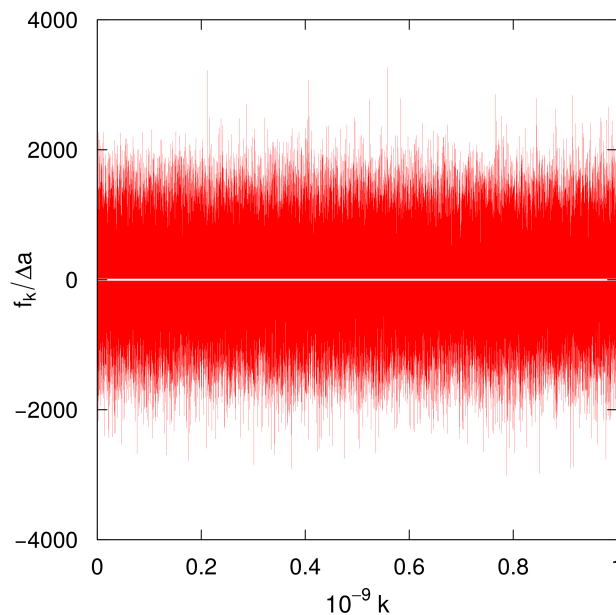

Figure 3.3: A randomly chosen readout $f_k/\Delta a$, $\Delta a \equiv a_2 - a_1 = 2$, for $K = 10^9$ Gaussian meters defined by (3.12) (only 10^5 values are shown), for the system in the first state $|a_1\rangle$, $\beta_0 = 0$, $\hat{H} = 0$, and $\Delta a_T = 0.03$. Also shown by a horizontal white line is $a_1/\Delta a = -1/2$.

3.4 Reexamination of Continuous Fuzzy Measurement on Two-Level Systems

The purpose of this section is to reexamine the propositions given in [142] and summarised in Section 3.3.1. We have shown in Section 3.3.2 that the Gaussian restriction imposed on Feynman paths cannot guarantee their closeness to readouts which, in the continuous limit, tend to become infinite, rather than lie close to one of the eigenvalues of $\hat{A}$. In other words, the statement (i) of Section 3.3.1 is incorrect. With this, the estimates of the decoherence rates and Zeno times, based on the constant readouts which align with one of the eigenvalues of $\hat{A}$, become inconclusive. Therefore, we propose in Section 3.4.1 a different decoherence mechanism in a free system, while Section 3.4.2 provides a different reason for the Zeno effect in a driven system.

3.4.1 Decoherence of a Free System

First we check whether the statement (ii) of Section 3.3.1 is correct. If $\hat{H}$ commutes with $\hat{A}$, $\langle a_i|\hat{H}|a_j\rangle = E_i\delta_{ij}$, for $|\psi(T;\underline{f})\rangle$ in (3.B.15) we have

$$
\begin{aligned}
|\psi(T;\underline{f})\rangle = {} & \alpha_0 \, \exp(-iE_1K\tau) \prod_{k=1}^{K} G(f_k - a_1) \, |a_1\rangle \\
& + \, \beta_0 \, \exp(-iE_2K\tau) \prod_{k=1}^{K} G(f_k - a_2) \, |a_2\rangle.
\end{aligned}
\tag{3.38}
$$

In the case of a free system, i.e. $E_1 = E_2 = 0$, the density matrix $\rho(T) \equiv \int d\underline{f}\,|\psi(T;\underline{f})\rangle\,\langle\psi(T;\underline{f})|$ yields

$$
\begin{aligned}
\langle a_1|\rho(T)|a_2\rangle = {} & \alpha_0\,\beta_0^* \left[\int df\, G(f - a_1)\, G(f - a_2) \right]^K \\
= {} & \alpha_0\,\beta_0^* \, \exp[-\kappa T|a_1 - a_2|^2/2],
\end{aligned}
\tag{3.39}
$$

where we have evaluated the Gaussian integral, and used (3.29). If $\hat{H} \neq 0$, with $\langle a_i|\hat{H}|a_j\rangle = E_i\delta_{ij}$, the off-diagonal element (3.39) is multiplied by the factor $\exp(-i(E_1 - E_2)T)$, but the conclusion remains the same. The coherence $\langle a_1|\rho(T)|a_2\rangle$ vanishes if $\kappa T = \Delta a_T^2 \gg 1/|a_1 - a_2|^2$, leaving the system in a mixed state

$$
\rho(T) = |a_1\rangle|\alpha_0|^2\langle a_1| + |a_2\rangle|\beta_0|^2\langle a_2|.
\tag{3.40}
$$

Thus, the assumption (ii) of Section 3.3.1 is indeed correct. We still need to see how this is possible. Instead of aligning with one of the eigenvalues of $\hat{A}$, a typical readout would alternate wildly, and give no apparent indication as to the state the system has ended up in. Yet such information must be available since, according to (3.B.15), a given readout uniquely determines the system's final destination.

3.4.1.1 Decoherence by "Sudden Reduction"

To see how this happens, we first resort to a simpler model similar to the one used in [151]. The measuring medium consists of a set of non-Gaussian meters, with $G(f)$ (3.14) having the shape of a *rectangular window* of a width $\Delta f > |a_1 - a_2|$, i.e.

$$
G(f) = \begin{cases} 1/\sqrt{\Delta f}, & \text{for } |f| \leq \Delta f/2, \\ 0, & \text{otherwise.} \end{cases}
\tag{3.41}
$$

Following the derivation discussed in Appendix 3.B.2, the firing of the k-th meter, with the pointer value f_k, transforms the quantum state $|\psi_{k-1}\rangle = \alpha_{k-1}|a_1\rangle + \beta_{k-1}|a_2\rangle$ into (assuming $a_2 > a_1$):

$$|\psi_k\rangle = \begin{cases} \alpha_{k-1}|a_1\rangle/\sqrt{\Delta f}, & \text{if } f_k \in [a_1 - \Delta f/2, a_2 - \Delta f/2] \equiv A, \\ |\psi_{k-1}\rangle/\sqrt{\Delta f}, & \text{if } f_k \in [a_2 - \Delta f/2, a_1 + \Delta f/2] \equiv C, \\ \beta_{k-1}|a_2\rangle/\sqrt{\Delta f}, & \text{if } f_k \in [a_1 + \Delta f/2, a_2 + \Delta f/2] \equiv B. \end{cases} \tag{3.42}$$

Here C is the region where $G(f - a_1)$ and $G(f - a_2)$ overlap, and if f_k happens to lie there, the state before the meter has fired, $|\psi_{k-1}\rangle$, remains unaltered. If f_k falls into the regions A or B, $|\psi_{k-1}\rangle$ is reduced to $|a_1\rangle$, or $|a_2\rangle$, respectively. With no Hamiltonian to rotate the state between the measurements, it will remain the same for the rest of the monitoring. An elementary calculation shows that the probabilities $P(J) \equiv \int_J \langle\psi_k|\psi_k\rangle \, df_k$ to have f_k in a region $J = A, B, C$ are

$$P(A) = |a_1 - a_2||\alpha_{k-1}|^2/\Delta f,$$
$$P(B) = |a_1 - a_2||\beta_{k-1}|^2/\Delta f,$$
$$P(C) = 1 - |a_1 - a_2|/\Delta f. \tag{3.43}$$

As before, we wish to lower the measurements resolution, and increase their number, albeit in a slightly different manner:

$$\tau \to 0, \quad \Delta f \to +\infty, \quad \tau \Delta f = \kappa'^{-1}, \tag{3.44}$$

where κ' is a tunable constant. With $P(A)$ and $P(B)$ extremely small, each meter is now likely to leave the state of the system unchanged. It will, therefore, propagate unaltered until an unlikely fluctuation will put f_k in, say, the region A. After that the system will continue in the state $|a_1\rangle$, and subsequent meters will produce the reading in a very broad interval $[a_1 - \Delta f/2, a_1 + \Delta f/2]$, as illustrated in Figure 3.4. Thus, the reduction of $|\psi_0\rangle$ to $|a_1\rangle$ is achieved instantaneously, but the precise moment at which it occurs is hidden from the viewer by the noise of the readout and, thus, remains unknown without further analysis. It is easy to evaluate the number of measurements and, therefore, the time after which the system will have collapsed into one of the two states almost certainly. From (3.43), the probability to survive in the initial state $|\psi_0\rangle$ after K measurements is

$$P_{surv}(T) = P(C)^K = (1 - \kappa'T|a_1 - a_2|/K)^K \quad \xrightarrow{K \to +\infty} \quad \exp(-\kappa'T|a_1 - a_2|), \tag{3.45}$$

and after waiting for $T \gg \kappa'|a_1 - a_2|$ one can be sure that either region A or B has been hit, the initial state has been reduced, and system's density matrix is given by (3.40).

3.4.1.2 Decoherence by "Random Walk"

A somewhat similar mechanism must be responsible for the decoherence of a system monitored by a set of Gaussian meters (3.12). In this case it is unrealistic to expect a single fluctuation capable of eliminating one of the states from the superposition (3.27). Indeed, for $\Delta f \gg |a_1 - a_2|$ to have, for example, $G(f - a_1) \ll G(f - a_2)$ requires an $f \gg f_0 \equiv \Delta f^2/|a_1 - a_2|$. The probability to have any $f > f_0$ is then expressed in terms of the complimentary error function [148], $P(f > f_0) \sim \text{erfc}(f_0/\Delta f) \approx (\Delta f/f_0) \exp(-f_0^2/\Delta f^2) \sim \exp(-\Delta f^2/|a_1 - a_2|^2)$ and is extremely small. With decoherence by "sudden death" unlikely, we should find another mechanism.

Consider the ratio $\xi_k \equiv |\alpha_k/\beta_k|^2$, such that $\xi_k = 0$ if the particle is in the state $|a_2\rangle$ and $\xi_k = +\infty$, if it is in the state $|a_1\rangle$. By plug (3.12) in (3.38), with $E_1 = E_2 = 0$, we have

$$\xi_K = \exp(-X_K)|\alpha_0/\beta_0|^2, \tag{3.46}$$

where

$$X_K \equiv \frac{2(a_2 - a_1)}{\Delta f^2} \sum_{k=1}^{K} \left(f_k - \frac{a_1 + a_2}{2} \right), \tag{3.47}$$

so that the ratio is determined by the value of the sum X_k. For the system to be ultimately driven into one of the eigenstates of $\hat{A}$, X_k must be a large positive or a large negative number. To show
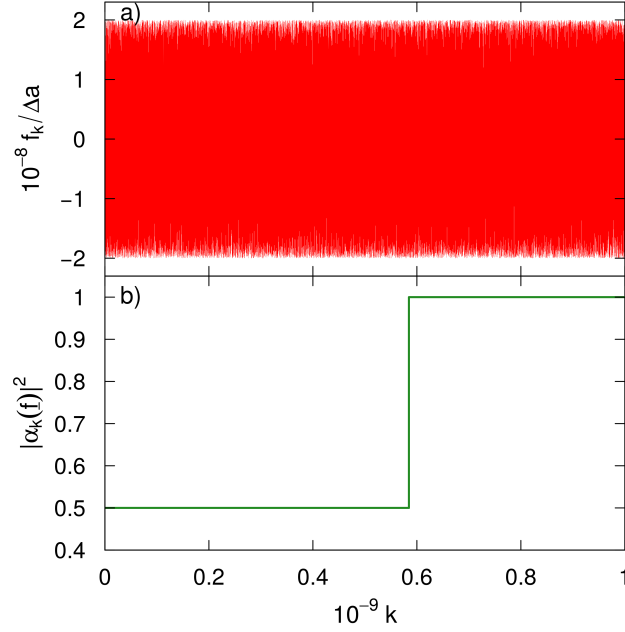
Figure 3.4: Figure (a) shows a randomly chosen readout $f_k/\Delta a$, $\Delta a \equiv a_2 - a_1$, for $K = 10^9$ non-Gaussian meters defined by (3.41) (only 10^5 values are shown). The system is prepared in the initial state $|\psi_0\rangle = (|a_1\rangle + |a_2\rangle)/\sqrt{2}$, with $a_2 = -a_1 = 1$, $\hat{H} = 0$ and $\Delta f/\Delta a = 4 \times 10^8$. Figure (b) provides the probability to find the system in the state $|a_1\rangle$ after k meters have fired.

that this is always the case, we look at the distribution of the random variable X_k. Using (3.38), with $E_1 = E_2 = 0$, we get the probability density function $p(\underline{f})$ of the meter readings $\underline{f} \equiv \{f_1, .., f_K\}$:

$$p(\underline{f}) = \langle \psi(T; \underline{f})|\psi(T; \underline{f})\rangle = |\alpha_0|^2 \prod_{k=1}^{K} G^2(f_k - a_1) + |\beta_0|^2 \prod_{k=1}^{K} G^2(f_k - a_2), \tag{3.48}$$

where $G(f)$ is defined by (3.12). The distribution of the values y assumed by the sum $Y_K(\underline{f}) \equiv \sum_{k=1}^{K} f_k$ can be computed as

$$W_{Y_K}(y) = \int d\underline{f}\, p(\underline{f})\, \delta(Y_K(\underline{f}) - y), \tag{3.49}$$

where $p(\underline{f})$ is given by (3.48) and $\delta(x)$ is the Dirac delta. The expression (3.49) requires the computation of the integrals

$$I_n(y) \equiv \int dx_1 .. dx_K \prod_{k=1}^{K} G^2(x_k - a_n)\, \delta\left(\sum_{k=1}^{K} x_k - y\right), \quad n = 1, 2. \tag{3.50}$$

Given $G(f)$ (3.12), the product $\prod_{k=1}^{K} G^2(x_k - a_n)$ corresponds to the probability density function (PDF) of the random vector $\underline{x} \equiv \{x_1, .., x_K\}$, whose components are independent and normally distributed variables, with mean a_n and standard deviation $\Delta f/\sqrt{2}$, i.e.

$$x_1, .., x_K \overset{\text{ind.}}{\sim} \mathcal{N}(x|a_n, \Delta f/\sqrt{2}), \tag{3.51}$$

where $\mathcal{N}(x|\mu, \sigma)$ is defined by (3.37). Provided that $I_n(y)$ is the PDF of the sum $\sum_{k=1}^{K} x_k$, and

$$x_1, .., x_K \overset{\text{ind.}}{\sim} \mathcal{N}(x|\mu, \sigma) \quad \Rightarrow \quad \sum_{k=1}^{K} x_k \sim \mathcal{N}(x|K\mu, \sqrt{K}\sigma), \tag{3.52}$$

as shown in [152], it follows

113

$$I_n(y) = \mathcal{N}(y|Ka_n, K\Delta a_T/2), \quad n = 1, 2, \tag{3.53}$$

where we have used (3.29). As a result, the distribution $W_{Y_K}(y)$ (3.49) reads

$$W_{Y_K}(y) = |\alpha_0|^2 \mathcal{N}(y|Ka_1, K\Delta a_T/2) + |\beta_0|^2 \mathcal{N}(y|Ka_2, K\Delta a_T/2). \tag{3.54}$$

Given the function

$$x = g(y) \equiv \frac{2(a_2 - a_1)}{\Delta f^2} \left[y - \frac{K(a_1 + a_2)}{2} \right], \tag{3.55}$$

such that $X_K = g(Y_K)$, the distribution $W(x)$ of the values x assumed by $X(T) \equiv X_K$ (3.47) can be found by the *change of variable* formula:

$$W(x) = W_{Y_K}(g^{-1}(x)) \left| \frac{d}{dx}(g^{-1}(x)) \right| = |\alpha_0|^2 \mathcal{N}(x| - 2\kappa T(a_1 - a_2)^2, 2\sqrt{\kappa T}|a_1 - a_2|)$$
$$+ |\beta_0|^2 \mathcal{N}(x|2\kappa T(a_1 - a_2)^2, 2\sqrt{\kappa T}|a_1 - a_2|), \tag{3.56}$$

where we have used (3.29) and g^{-1} denotes the inverse function of g (3.55).

A brief inspection shows that we have a case of two Gaussian random walks with opposite drifts. A walk can be visualised as a process, in which the displacement of a walker at the k-th step consists of a constant "drift" $\pm 2\kappa\tau(a_1 - a_2)^2$ and a random shift y, drawn from a normal distribution $\mathcal{N}(y|0, 2\sqrt{\kappa\tau}|a_1 - a_2|)$. The sum $X(T)$ is then the displacement of the walker at a time T. It is readily seen that the distribution of $X(T)$ consists of two Gaussians moving, as time progresses, in opposite directions, and becoming broader at the same time. The broadening, however, is much slower then the separation, and for $T \gg 1/\kappa(a_1 - a_2)^2$, i.e., for $\Delta a_T \ll |a_1 - a_2|$, the Gaussians are separated completely, as shown in Figure 3.5.

Thus, there are just two possibilities. Either a walk ends far to the right, $X(T) \gg 1$, and leaves the system in the state $|a_2\rangle$ since $\xi(T) \equiv \xi_{T/\tau} \to 0$, or it ends far to the left, $X(T) \ll -1$, and leaves the system in the state $|a_1\rangle$, because $\xi(T) \to +\infty$. The relative frequency, with which both types of the walks occur, is given by the ratio $|\alpha_0|^2/|\beta_0|^2$, in accordance with (3.40).

In summary, for a free system, complete decoherence of an arbitrary pure state (3.27) is indeed achieved for $T \gg 1/\kappa(a_1 - a_2)^2$, but by a mechanism different from the one proposed in [142]. A typical readout does not align with one of the eigenvalues of the measured operator, and remains irregular at all times as shown in Figure 3.6a. To find out into which of the two states the system is driven as a result, we must use all the readings to evaluate the exponent in (3.46), and then see whether the result is a large positive, or a large negative number (see Figure 3.6b). This analysis is easily generalised to systems with any number of states $N > 2$, in which case the large-time distribution of $X(T)$ will be a multi-modal sum of Gaussians. The random walk will choose a single component of the Gaussian mixture, driving the system to the corresponding state. A randomly chosen graph $|\alpha_k|^2 = \xi_0 \exp(-X_k)/[1 + \xi_0 \exp(-X_k)]$ versus k is shown in Figure 3.6c. The irregular patterns, with clearly visible ups and downs, reflect, albeit indirectly, the behaviour of the underlying random walk X_k in Figure 3.6b. As X_k increases, its fluctuations are damped be the factor $\exp(-X_k)$, and the curve $|\alpha_k|^2$ becomes smoother.
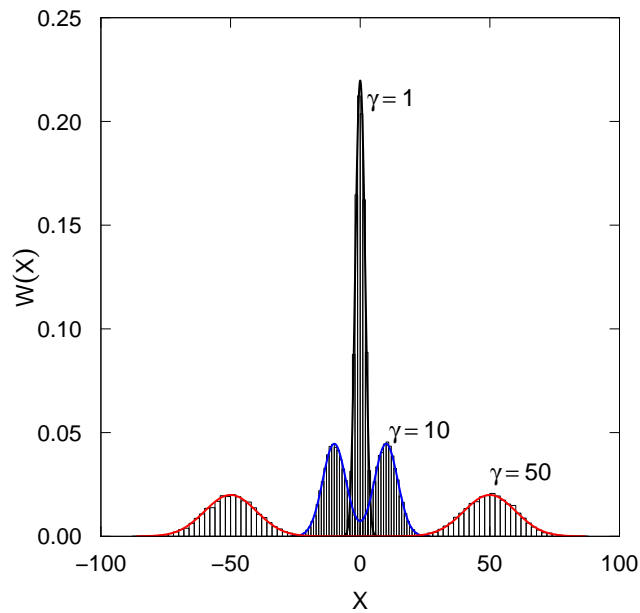
Figure 3.5: The distribution (3.56) of the sum $X(T) \equiv X_K$ (3.47) for different values of the parameter $\gamma = 2\kappa T(a_1 - a_2)^2$. The system is prepared in the initial state $|\psi_0\rangle = (|a_1\rangle + |a_2\rangle)/\sqrt{2}$, with $a_2 = -a_1 = 1$, $\hat{H} = 0$ and $\Delta f/(a_2 - a_1) = 250$. The histograms show the corresponding results of numerical simulations involving 2×10^4 random realisations, obtained with the help of Algorithm 3.1.
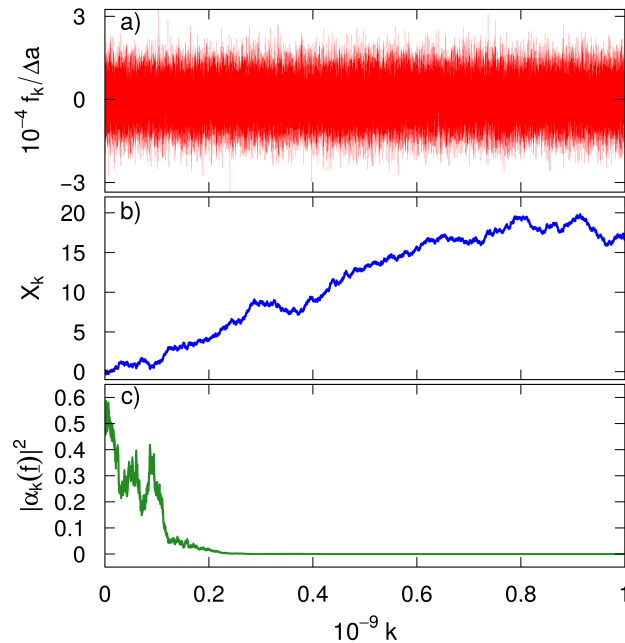
Figure 3.6: (a) A randomly chosen readout $f_k/\Delta a$, $\Delta a \equiv a_2 - a_1$, for $K = 10^9$ Gaussian meters (only 10^5 values are shown). The system is prepared in the initial state $|\psi_0\rangle = (|a_1\rangle + |a_2\rangle)/\sqrt{2}$, with $a_2 = -a_1 = 1$, $\hat{H} = 0$ and $\Delta f/\Delta a = 10^4$. (b) Displacement of the random walker X_k, defined in (3.47). (c) The probability to find the system in the state $|a_1\rangle$ after k meters have fired.

3.4.2 Zeno Effect in a Driven System

This section reconsiders the propositions (I)-(III) of Section 3.3.1. The operator $\hat{A}$, $\hat{A}|a_n\rangle = a_n|a_n\rangle$, is monitored in a two-level system, with Hamiltonian $\hat{H}$:

$$\langle a_1|\hat{H}|a_1\rangle = \langle a_2|\hat{H}|a_2\rangle = 0, \quad \langle a_1|\hat{H}|a_2\rangle = \langle a_2|\hat{H}|a_1\rangle \equiv \omega. \tag{3.57}$$

In the absence of the meters, the probability $P_0(t)$ to start from any initial state $|\psi_0\rangle = \alpha_0|a_1\rangle + \beta_0|a_2\rangle$, with $\langle \psi_0|\psi_0\rangle = 1$, and to return to the state $|\psi_0\rangle$ at time $t > 0$ is given by

$$P_0(t) = |\langle\psi_0|\exp(-i\hat{H}t)|\psi_0\rangle|^2 = \cos^2(\omega t) + (\alpha_0^*\beta_0 + \alpha_0\beta_0^*)^2 \sin^2(\omega t), \tag{3.58}$$

where z^* is the complex conjugate of $z \in \mathbb{C}$. If $(\alpha_0^*\beta_0 + \alpha_0\beta_0^*)^2 \neq 1$, (3.58) shows that the system performs Rabi oscillations with a period $T_R = 2\pi/\omega$. The oscillations (3.58) can be quenched by the *Zeno effect* [127], that corresponds to an artificial freezing of the natural dynamics, obtained by frequent measurements, i.e. $\tau \to 0$. In the Zeno regime, the authors of [142] made the statements (I)-(III), we want to reconsider. The case of the *rectangular* measure G (3.41) is discussed in Section 3.4.2.1. The *Gaussian* measure G (3.12) is considered in Section 3.4.2.2 to revise the propositions (I)-(III).

3.4.2.1 Zeno Effect by "Sudden Reduction"

We start with the simple model (3.41)-(3.44) of Section 3.4.1.1. As before, the reduction of the state to either $|a_1\rangle$ or $|a_2\rangle$ is achieved whenever a rare fluctuation puts an f_k into the regions A or B. A typical time between two fluctuations is of the order of T'_{LR} (LR stands for "level resolution"), where T'_{LR} is the average time after which the first fluctuation occurs,

$$T'_{LR} = -\int_0^\infty t \frac{d}{dt} P_{surv}(t)\, dt = \frac{1}{\kappa'|a_1 - a_2|}. \tag{3.59}$$

What happens to the system between two subsequent reductions depends on the relation between T'_{LR} and the Rabi period T_R. For $T_R \lesssim T'_{LR}$, the system may have a chance to perform a number of Rabi oscillations, as shown in Figure 3.7a. Given $|\psi_0\rangle = |a_1\rangle$ in (3.58), the probability $|\alpha(t, [f])|^2$ to arrive in the state $|a_1\rangle$ at time t will consist of several pieces of regular oscillation $\sim \cos^2(\omega t)$, with arbitrary relative phases. The curve $|\alpha(t, [f])|^2$ becomes discontinuous because of the sudden reductions to either $|a_1\rangle$ or $|a_2\rangle$, caused by the occurrence of a meter reading f_k into the regions A or B (vertical dashed lines in Figure 3.7a).

For $T_R \gtrsim T'_{LR}$, the system would, on average, have no time to complete a single oscillation before it is interrupted by the next reduction, and the curve will typically have an irregular shape shown in Figure 3.7b.

The behaviour is pushed to the limit if $T_R \gg T'_{LR}$. The system state is reduced to either $|a_1\rangle$ or $|a_2\rangle$ with the time scale T'_{LR} way faster than the time scale T_R of the Rabi oscillations. In other words, the probability $|\alpha(t, [f])|^2$ is continuously forced to the values 0 or 1 by the frequent reductions, destroying the natural oscillations. The curve $|\alpha(t, [f])|^2$ takes the characteristic form of telegraph noise [153] shown in Figure 3.7c. In this regime, the system spends, on average, a duration T^{stay} in $|a_1\rangle$, then it makes a sudden transition to spend a similar amount of time in $|a_2\rangle$, as shown in Figure 3.7c. The time T^{stay} can be evaluated by noting that after free evolution during T'_{LR}, the probability for the system to have changed its state is

$$|\langle a_i|\exp(-i\hat{H}T'_{LR})|a_j\rangle|^2 \approx |\langle a_i|1 - i\hat{H}T'_{LR}|a_j\rangle|^2 = \omega^2 T'_{LR}{}^2, \quad j \neq i. \tag{3.60}$$

The system succeeds in changing its state after approximately $n_{att} \approx 1/\omega^2 T'_{LR}{}^2$ attempts, and

$$T^{stay} \approx n_{att} T'_{LR} = \frac{T_R^2}{4\pi^2 T'_{LR}}. \tag{3.61}$$

Thus, the Zeno regime is reached as $T_R/T'_{LR} \to \infty$, and the system remains in one state for any finite time t.
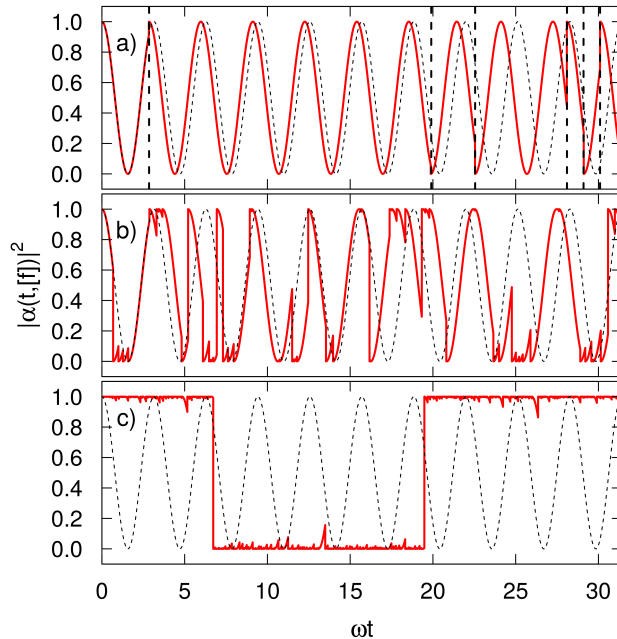
Figure 3.7: Probabilities $|\alpha(t, [f])|^2$ versus t for a randomly chosen set of readouts $[f]$. A "driven" system, with $\hat{H}$ given by (3.57), is monitored for $0 \le t \le T$, $\omega T = 25$, by $K = 10^9$ *rectangular* meters (3.41). The system's initial state is $|\psi_0\rangle = |a_1\rangle$, and $T'_{LR}/T_R =$ a) 0.5, b) 0.08, and c) 0.008. The dashed lines show the Rabi oscillations of the system with no meters present. The vertical dashed lines in (a) indicate the moments the system's state is suddenly reduced to $|a_1\rangle$ or $|a_2\rangle$.

3.4.2.2   Zeno Effect by "Random Walk"

In general, it is impossible to consider separately the system evolution driven by $\hat{H}$ (3.57) and the Gaussian pointers (3.12), as was done in Section 3.4.1.2. The rest of the analysis will have to be performed numerically by taking advantage of the designed Algorithm 3.1.

The results, shown in Figures 3.8 and 3.9, are broadly similar to those presented in Figure 3.7. Following [142], we can introduce a time T_{LR}, similar to T'_{LR} in (3.59),

$$T_{LR} = 1/\kappa(a_1 - a_2)^2, \tag{3.62}$$

and study the evolution of the system's state as function of T_{LR}/T_R.

For $T_R \sim T_{LR} \ll T$, the system performs regular oscillations which gradually get out of phase with the uncoupled Rabi oscillations (Figure 3.8a). For $T_R \gtrsim T_{LR}$, the curve $|\alpha(t, [f])|^2$ is highly irregular (Figure 3.8b). For $T_R \gg T_{LR}$, the system is near a Zeno regime, and the $|\alpha(t, [f])|^2$ curve has a telegraph noise shape (Figure 3.9b), although we cannot easily evaluate the typical duration of T^{stay}, as done in Section 3.4.2.1.

Figure 3.9c shows that each time the system changes the state, the corresponding random walk changes direction. With evolutions of the system and the pointers intertwined, we are unable to say whether the change of the system state affects the direction of the walk, or if the change of direction causes the system to alter its state. As in Section 3.4.2.1, the Zeno regime is reached when $T^{stay} \to \infty$, and the system remains in one state for any finite t.

In summary, for $T_{LR} \ll T_R \ll T$, we do have a Zeno effect, although the conclusions (I)-(III) of [142] must be modified as follows:

(I') The measurement outputs $f(t)$ that are close to one of the constant curves $f(t) = a_1$ and $f(t) = a_2$ are by far not the most probable ones. A typical readout will look like the ones shown in Figure 3.9a.

(II') The probability of a readout being close to a_1 or a_2 is negligible. An analysis of the evolutions,

induced by these constant readouts, does not explain the mechanism of the Zeno effect, since such scenarios will never occur in practice.

(III') Even with most readouts not close to a_1 or a_2, the Rabi oscillations are quenched, and final state is the eigenstate $|a_1\rangle$ or $|a_2\rangle$.
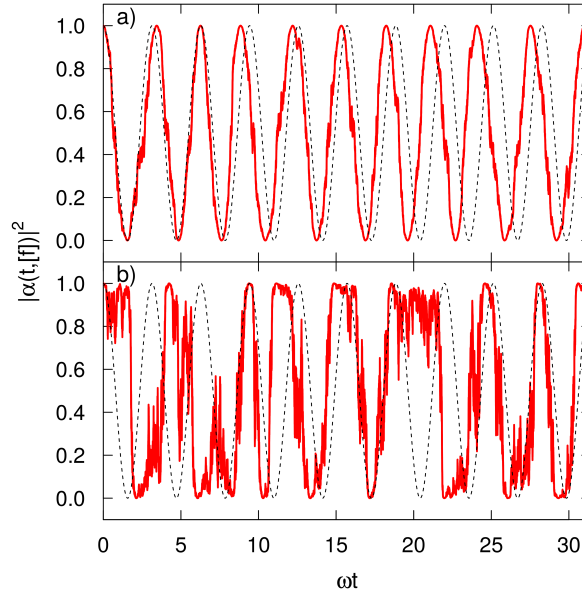
Figure 3.8: Probabilities $|\alpha(t, [f])|^2$ vs. t for a randomly chosen set of readouts $[f]$. A "driven" system, with $\hat{H}$ (3.57), is monitored for $0 \leq t \leq T$, $\omega T = 10\pi$, by $K = 10^9$ Gaussian meters (3.12). The initial state is $|\psi_0\rangle = |a_1\rangle$, and $T_{LR}/T_R =$ a) 0.4; and b) 0.03. The dashed lines show the Rabi oscillations of the system with no meters present.
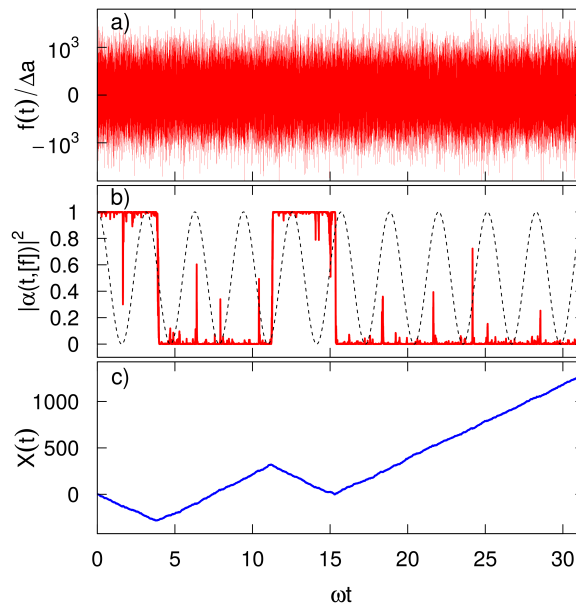
Figure 3.9: a) A randomly chosen readout $f(t)/\Delta a$, $\Delta a \equiv a_2 - a_1$, $a_2 = -a_1 = 1$, for $K = 10^9$ (only 10^5 shown) Gaussian meters (3.12). b) Corresponding probability $|\alpha(t, [f])|^2$ vs. t for a system driven by $\hat{H}$ (3.57). The initial state is $|\psi_0\rangle = |a_1\rangle$, and $T_{LR}/T_R =$0.002. The dashed lines show the Rabi oscillations of the system with no meters present. c) Displacement of the random walker (3.47).

3.5   Conclusions & Discussion

The chapter focuses on the stochastic simulation of continuous quantum measurements. In Appendix 3.B, we provide the basic mathematical formalism, starting from the Hamilton equations for a classical meter. A classical system can be accurately monitored, without any perturbation of the natural dynamics, as shown in Appendix 3.B.1. However, it is not possible to do the same in the case of quantum systems. The equations modelling a single quantum meter are discussed in Appendix 3.B.2, showing that the meter readings affect the state of the coupled quantum system. The derivation is extended in Appendix 3.B.3 to the case of K identical impulsive quantum meters, performed at uniform intervals with length $\tau > 0$. The continuous measurements are reached in the limit $K \to +\infty$ and $\tau \to 0$, as suggested in [131]. Different regimes of the taken observations can be characterised by their accuracy and the corresponding influence on the system dynamics.

On the basis of the equations derived in Appendix 3.B, Section 3.2 designs the stochastic model and the corresponding Monte Carlo (MC) method to simulate the continuous quantum measurements. The probabilistic model is described by (3.7) and the MC method is summarised in Algorithm 3.1. Quantities of interest can be approximated by statistics computed on the drawn samples with size $S \geq 1$. The simulation method is validated through comparison with the available analytical solution (3.17) of the expected meter reading $F(\tau)$, as shown in Figure 3.1a. The order $O(S^{-1/2})$ of the convergence rate is confirmed in Figure 3.1b, using the analytical formula (3.26) for the density matrix $\rho(t_k)$. The MC method also verifies the non-Markovian behaviour of the quantum meters, as shown in Figure 3.2.

The MC method helps us in reconsidering the conclusions of the seminal paper on continuous fuzzy measurements [142] for a large number of impulsive meters of accuracy Δf, imposing a Gaussian restriction on the Feynman paths of a two-level system, as summarised in Section 3.3.1. In Section 3.3.2, we show that, for a fixed period of monitoring, T, as the number of meters, K, increases, typical readouts f_k become highly irregular, and do not align with one of the eigenvalues of the measured quantity, as suggested in [142]. The same behaviour of the meter readings is observed when decoherence of an initial state is achieved (Figure 3.6a), or Zeno effect is imposed on the system (Figure 3.9a). Thus, a different description of the decoherence process and the Zeno effect is required, and we present it in Section 3.4, using a fully tractable non-Gaussian model as a guide.

In particular, for a system prepared in a pure state (3.27), in the case its Hamiltonian $\hat{H}$ does not facilitate transitions between the eigenstates of the measured quantity $\hat{A}$, decoherence can be linked to a fictitious random walk, which is bound to lead to one of two outcomes, which, in turn, determine the final state of the system. More precisely, we have shown that for $\Delta a_T = \Delta f / \sqrt{2/K} \ll |a_1 - a_2|$, the restriction imposed on the paths in (3.30) does not limit the readouts $f(t)$, to the classes $(i = 1, 2)$

$$f(t) \in \mathcal{F}_i, \quad \mathcal{F}_i \equiv \left\{ f(t) \,:\, T^{-1} \int_0^T (f(t) - a_i)^2 \, dt \lesssim \Delta a_T^2 \right\}, \tag{3.63}$$

as proposed in [142]. Given (3.54), the distribution of $K^{-1} \sum_{k=1}^{K}(f_k - a_i)$ shows that, in the limit (3.29), a readout f would belong to one of the two classes

$$f(t) \in \mathcal{F}_i', \quad \mathcal{F}_i' \equiv \left\{ f(t) \,:\, \left[T^{-1} \int_0^T (f(t) - a_i) \, dt \right]^2 \lesssim \Delta a_T^2 \right\}. \tag{3.64}$$

Condition (3.64) is weaker than (3.63) and it allows a typical readout fluctuating on the scale $\Delta f \to +\infty$, rather than aligning with an eigenvalue a_i, as it would do if (3.63) were true. To find out in which of the two eigenstates our monitoring has left the system, we would need to evaluate the (finite) sum $\sum_{k=1}^{K} f_k / K$, in order to see whether its value is closer to a_1 and a_2. However, this procedure would become problematic in the limit $K \to \infty$, since then each term of the sum can be arbitrary large.

The random walk analogy remains useful also in a case of a driven system, subject to Rabi oscillations. For such a system, a typical readout is highly irregular (see Figure 3.9a) even in a near-Zeno regime, where Rabi oscillations of the system's state are replaced by a telegraph noise (Figure 3.9b). In this case, as seen in Figure 3.9c, the corresponding random walk changes direction every time the system

jumps from one state to the other. The two evolutions should be considered together, and it is difficult to say whether it is the walker, which causes the system to change its state, or the system, which causes the walker to change direction. The derived results have been published in:

1. D. Sokolovski, S. Rusconi, S. Brouard, and E. Akhmatskaya. Reexamination of continuous fuzzy measurement on two-level systems. Phys. Rev. A, 95:042111, 2017.

Using the stochastic framework described in this chapter, we plan further to analyse the behaviour of distinguishable and identical particles (bosons), trapped in a double well potential, and to study ensembles of frequently observed two-level systems as detectors for the appearance of the Zeno effect.

Appendix

3.A Basic Principles of Elementary Quantum Mechanics

This appendix provides some basic knowledge of quantum mechanics. In particular, we present in Appendix 3.A.1 the role of the operators associated with measurable quantities of a quantum system. The illustrative example of the momentum operator is discussed. Commuting operators are characterised in Appendix 3.A.2, focussing on the case of the measured operator commuting with the Hamiltonian of the quantum system. Appendix 3.A.3 summarises the Born postulates and the thought experiment of the Schrödinger's cat. The entanglement phenomenon is also explained, outlining the difference between product and entangled states. In Appendix 3.A.4, we present the definition and some properties of the probability amplitude, applying the concept in the example of the Young double-slit experiment. Finally, Appendix 3.A.5 discusses the density operator, explaining the difference between pure and mixed states. The physical meaning of the density matrix entries is explained in the example of the stochastic model (3.7).

3.A.1 Measurable Quantities

Given a quantum system in the Hilbert space H, over the complex set $\mathbb{C}$, any measurable quantity $x \in \mathbb{R}$, or *observable*, is associated with a Hermitian (self-adjoint) operator $\hat{X} : H \to H$, whose eigenvalues correspond to the possible outcomes of the observable x. The quantum state or *wave-function* $|x\rangle \in H$ provides the state of the system, in case the observable x is measured. The set $X \equiv \{|x\rangle\}_{x \in \mathbb{R}}$ establishes a complete orthonormal basis of H, i.e. $\hat{1}|\psi\rangle = |\psi\rangle$, $\forall |\psi\rangle \in H$, with $\hat{1} \equiv \int |x\rangle \langle x| \, dx$, and $\langle x|y\rangle = \delta(x - y)$, for any $|x\rangle$ and $|y\rangle \in X$, with $\delta(x)$ the Dirac delta. Any quantum state of the system can be written as *superposition*, or linear combination, of the basis elements, i.e. $|\psi\rangle = \int \psi(x) |x\rangle \, dx$, $\psi(x) \equiv \langle x|\psi\rangle$, $\forall |\psi\rangle \in H$.
The operator $\hat{X}$ can be defined such that the wave-functions $|x\rangle \in X$ correspond to its eigenvectors:

$$\hat{X} \equiv \int dx \, |x\rangle \, x \, \langle x|. \tag{3.A.1}$$

From previous definitions, it easily follows $\hat{X}|x\rangle = x|x\rangle$. In addition, it is possible to verify that the operator $\hat{X}$ is Hermitian. For any $|v\rangle$ and $|w\rangle \in H$, we have $\langle X_v|w\rangle = \langle v|X_w\rangle$, where $|X_v\rangle \equiv \hat{X}|v\rangle \in H$ and $|X_w\rangle \equiv \hat{X}|w\rangle \in H$.
An illustrative example is given by the momentum operator $\hat{\lambda} : H \to H$. It corresponds to the operator associated with the momentum λ of a particle with position f. Consider the operator $\hat{K} : H \to H$ defined as $\hat{K} \equiv -i\partial_f$, with i the imaginary unit. First, we show that operator $\hat{K}$ is Hermitian. For any

$$|\psi_n\rangle \equiv \int \psi_n(f) |f\rangle \, df \in H, \quad \psi_n(f) \equiv \langle f|\psi_n\rangle \in \mathbb{C}, \quad n = 1, 2, \tag{3.A.2}$$

we have:

$$\langle \psi_1|K_2\rangle = -i \int \psi_1^*(f) \, \partial_f \psi_2(f) \, df = i \int \partial_f \psi_1^*(f) \, \psi_2(f) \, df =$$
$$= \int (-i\partial_f \psi_1(f))^* \, \psi_2(f) \, df = \langle K_1|\psi_2\rangle, \tag{3.A.3}$$

where $|K_n\rangle \equiv \hat{K}|\psi_n\rangle \in H$, for $n = 1, 2$, and z^* is the complex conjugate of $z \in \mathbb{C}$. Then, we consider the spectrum of operator $\hat{K}$:

$$-i\partial_f \psi(f) = k\psi(f), \quad \psi(f) \equiv \langle f|\psi\rangle \in \mathbb{C}, \quad |\psi\rangle \equiv \int \psi(f)\,|f\rangle\,df \in H. \quad (3.A.4)$$

It follows

$$\psi(f) \propto \exp(ikf) = \cos(kf) + i\sin(kf). \quad (3.A.5)$$

The eigenfunction $\psi(f)$ is proportional to ($\propto$) a plane wave with wavelength $l = 2\pi/k$. By De Broglie formula $\lambda = 2\pi\hbar/l$, we have $\lambda = k$, if $\hbar = 1$. In other words, the eigenvalue k of the operator $\hat{K} = -i\partial_f$ is given by the momentum λ of the particle with position f. Given $\hbar = 1$, the Hermitian operator $-i\partial_f$ corresponds to the momentum operator $\hat{\lambda}$, expressed in the position f coordinate, whose eigenfunctions $\langle f|\lambda\rangle$ are proportional to $\exp(i\lambda f)$.

3.A.2 Commuting Operators

The operators $\hat{A}, \hat{B} : H \to H$ on the Hilbert space H are commuting in the case the commutator

$$[\hat{A}, \hat{B}] \equiv \hat{A}\hat{B} - \hat{B}\hat{A} = 0. \quad (3.A.6)$$

The definition (3.A.6) can be generalised. In particular, the operators $\hat{A}$ and $\hat{B}$ commute if and only if

$$f(\hat{A})g(\hat{B}) - g(\hat{B})f(\hat{A}) = 0, \quad (3.A.7)$$

for any function f and g. Two operators are commuting if and only if they share the same eigenvectors. Given $\hat{A} : H \to H$, $\hat{A}|a\rangle = a|a\rangle$, commuting with the operator $\hat{B} : H \to H$, we have that $\hat{B}|a\rangle$ must be an eigenvector of the operator $\hat{A}$ relative to the eigenvalue a:

$$\hat{A}\hat{B}|a\rangle = \hat{B}\hat{A}|a\rangle = a\hat{B}|a\rangle. \quad (3.A.8)$$

In other words, $\hat{B}|a\rangle$ must differ from $|a\rangle$ only by a constant factor b, i.e. $\hat{B}|a\rangle = b|a\rangle$, showing that $|a\rangle$ is an eigenvector of the operator $\hat{B}$ with corresponding eigenvalue b.
Given the operators $\hat{A}, \hat{B} : H \to H$ with the same eigenvectors, i.e. $\hat{A}|x\rangle = a_x|x\rangle$ and $\hat{B}|x\rangle = b_x|x\rangle$, it is possible to show that $\hat{A}$ and $\hat{B}$ commute. In the complete basis of the eigenvectors $|x\rangle$, we have

$$(\hat{A}\hat{B} - \hat{B}\hat{A})|\psi\rangle = \int \psi(x)\,(\hat{A}\hat{B} - \hat{B}\hat{A})\,|x\rangle\,dx = \int \psi(x)\,(a_x b_x - a_x b_x)\,|x\rangle\,dx = 0, \quad \forall|\psi\rangle \in H, \quad (3.A.9)$$

where $\psi(x) = \langle x|\psi\rangle$.
Then, we consider the observable x, represented by the operator $\hat{X} : H \to H$, of a quantum system in the Hilbert space H. The quantum state $|\psi(t)\rangle \in H$ is driven by the Hamiltonian $\hat{H}$ ($\hbar = 1$):

$$i\partial_t|\psi(t)\rangle = \hat{H}|\psi(t)\rangle, \quad |\psi(0)\rangle = |\psi_0\rangle. \quad (3.A.10)$$

Provided the quantum state $|\psi(t)\rangle \in H$, the n-th order moment of the observable x is given by

$$\mathbb{E}[x^n] \equiv \int x^n\,p(x)\,dx = \langle\psi(t)|\hat{X}^n|\psi(t)\rangle, \quad (3.A.11)$$

since $p(x) = \langle\psi(t)|x\rangle\langle x|\psi(t)\rangle$, see Appendix 3.A.3 for further explanations. Expression (3.A.11) leads to

$$\partial_t\,\mathbb{E}[x^n] = \partial_t\langle\psi(t)|\hat{X}^n|\psi(t)\rangle = (\partial_t\langle\psi(t)|)\,\hat{X}^n|\psi(t)\rangle + \langle\psi(t)|\hat{X}^n\,(\partial_t|\psi(t)\rangle) =$$
$$= \left(\langle\psi(t)|\hat{H}i\right)\hat{X}^n|\psi(t)\rangle + \langle\psi(t)|\hat{X}^n\left(-i\hat{H}|\psi(t)\rangle\right) = i\langle\psi(t)|[\hat{H}, \hat{X}^n]|\psi(t)\rangle, \quad (3.A.12)$$

where $[\hat{H}, \hat{X}^n] \equiv \hat{H}\hat{X}^n - \hat{X}^n\hat{H}$. If the operators $\hat{H}$ and $\hat{X}$ commute, the observable x is a conserved quantity, being any order moment constant in time. If the interest is in the observable dynamics, one should assume $[\hat{H}, \hat{X}] \neq 0$, as often done in the chapter.

3.A.3 Born Postulates

Let $|\Psi\rangle \in H$ be the state of a system, composed by the compound of $K \geq 1$ quantum systems, living in the Hilbert spaces $H_1, .., H_K$, i.e. $H \equiv H_1 \otimes .. \otimes H_K$. We consider the *observable* $\varphi \in \mathbb{R}$ and the corresponding quantum state $|\varphi\rangle \in H_1 \otimes .. \otimes H_k$, $1 \leq k \leq K$, as explained in Appendix 3.A.1. The *Born Postulates* can be summarised by the following statements.

- (i) The quantum state $|\psi(\varphi)\rangle \equiv \langle\varphi|\Psi\rangle$ expresses the state of the subsystem living in the Hilbert space $H_{k+1} \otimes .. \otimes H_K$. In the case $k = K$, $\langle\varphi|\Psi\rangle \in \mathbb{C}$ is defined as the *probability amplitude* to find the quantum system in the state $|\varphi\rangle \in H$, being its state $|\Psi\rangle \in H$.

- (ii) The function $p(\varphi) \equiv \langle\Psi|\varphi\rangle\langle\varphi|\Psi\rangle : \mathbb{R} \to \mathbb{R}^+$ provides the *probability density function* to measure observable $\varphi \in \mathbb{R}$, corresponding to the quantum state $|\varphi\rangle \in H_1 \otimes .. \otimes H_k$, $1 \leq k \leq K$.

- (iii) After measuring the observable $\varphi_0 \in \mathbb{R}$, the quantum systems collapse to the states $|\varphi_0\rangle \in H_1 \otimes .. \otimes H_k$, $|\psi(\varphi_0)\rangle \equiv \langle\varphi_0|\Psi\rangle \in H_{k+1} \otimes .. \otimes H_K$ and $|\varphi_0\rangle|\psi(\varphi_0)\rangle \in H$.

The collapse of the wave-function allows us discussing the thought experiment of the *Schrödinger's cat*. A cat is placed in a box, together with a radioactive atom. If the atom decays, a mechanism is prepared to kill the cat. Before opening the box, the cat's fate is tied to the wave-function of the atom, which is in a superposition of decayed and undecayed states. Thus, the cat must itself be in a superposition of dead and alive states, before the observer opens the box, "observes" the cat, and "collapses" its wave-function to either the dead or the alive state.

The Born postulates can also explain a curious phenomenon, known as *entanglement*. Quantum entanglement occurs when two systems are generated, or interact, in ways such that the quantum state of each system cannot be described independently of the other. Even when the systems are separated by a large distance, the two systems must be described as a whole. To explain such phenomenon, we provide the following example.

Consider two quantum systems living in the separable Hilbert spaces H_a and H_b, with orthonormal complete basis $\{|a_n\rangle\}_{n=1,2}$ and $\{|b_n\rangle\}_{n=1,2}$ respectively. The quantum state $|\Psi\rangle = |a_1\rangle|b_2\rangle + |a_2\rangle|b_1\rangle \in H_a \otimes H_b$ is prepared and the systems are separated by a large distance. Suppose to find the first system in the state $|a_1\rangle \in H_a$. The second system must be in the state $\langle a_1|\Psi\rangle = |b_2\rangle \in H_b$. Despite the two systems are very far, the second system is forced to be in state $|b_2\rangle$, just because the first system is in state $|a_1\rangle$. As a result, each system cannot be fully described without considering the other and they must be considered as a whole. The reason lies in the way how state $|\Psi\rangle$ is built. The quantum state $|\Psi\rangle$ is not a *product state*, because it cannot be factorised as a product of states of its single constituents. Thus, it corresponds to an *entangled state*, that must be described as a whole.

3.A.4 Probability Amplitudes

Given $|\psi\rangle \in H$ the state of a quantum system, living in the Hilbert space H, the *probability amplitude* to find the system in state $|\varphi\rangle \in H$ is computed as $\langle\varphi|\psi\rangle \in \mathbb{C}$. In the case the system evolves without been measured, or observed, the following laws apply.

- (i) The probability density function for the occurrence of an event is the square of the absolute value of the corresponding probability amplitude.

- (ii) If there exist mutually exclusive alternatives in which an event might occur, the probability amplitude for the event is given by the sum of probability amplitudes of the distinct alternatives.

- (iii) In the case an event is composed by a succession of sub-events, then the probability amplitude for the complete event is the product of the sub-events amplitudes.

(*iv*) Any product state of a composite quantum system has probability amplitude equal to the product of the amplitudes of the states of constituent subsystems.

If an experiment is performed to decide between mutually exclusive alternatives, the probability of each alternative is given by the squared modulus of the corresponding amplitude. However, it is not possible to sum the amplitudes of the mutually exclusive alternatives.

The concept is better understood by means of the Young double-slit experiment. Electrons are fired against a plate pierced by two parallel slits. The experiment investigates the probability distribution of detecting electrons on a large screen placed behind the plate. Intuition suggests computing the probability of interest as the sum of the probabilities to pass through one of the two slits. However, if one assumes this law to be true, the observed interference pattern on the screen cannot be understood. The correct explanation is provided by probability amplitudes. Let $\psi_i \in \mathbb{C}$ be the amplitude for an electron to pass through the slit $i = 1, 2$. The amplitude for pass through either slit is given by $\psi = \psi_1 + \psi_2 \in \mathbb{C}$ and the corresponding probability is given by $P = |\psi|^2 = |\psi_1|^2 + |\psi_2|^2 + \psi_1^* \psi_2 + \psi_2^* \psi_1$, with z^* the complex conjugate of $z \in \mathbb{C}$. The term $\psi_1^* \psi_2 + \psi_2^* \psi_1$ is called the interference term and it would be missing, if we had added the probabilities $|\psi_1|^2$ and $|\psi_2|^2$. The interference term is capable of explaining the observed pattern on the screen, not understandable by the real probabilities. In the case a detector is placed to observe in which slit each electron goes through, the interference pattern on the screen is destroyed and the probabilities $|\psi_1|^2$ and $|\psi_2|^2$ can be added, yielding $P = |\psi_1|^2 + |\psi_2|^2$.

3.A.5 Density Operator

The density operator can be understood as the observer knowledge of the quantum system. Given the state vector $|\psi\rangle$ belonging to the Hilbert space H, the density operator is defined as

$$\rho \equiv |\psi\rangle\langle\psi|. \tag{3.A.13}$$

The density operator should be used when the quantum state inherits a certain uncertainty, with respect to some observables. Given the state vector $|\psi(x)\rangle \in H$ depending on the observable x, the density operator

$$\rho \equiv \sum_x p_x |\psi(x)\rangle\langle\psi(x)| \tag{3.A.14}$$

models a quantum system found in the state $|\psi(x)\rangle$ with probability p_x. Equivalently, the density operator can represent an ensemble of identical systems in different states. The form (3.A.13) of the density operator indicates a *pure state* of the quantum system, while (3.A.14) corresponds to a *mixed state*.

The physical content of the density operator appears by computing the elements ρ_{xy} of the *density matrix*, with respect to the complete orthonormal basis X:

$$\rho_{xy} = \langle x|\rho|y\rangle, \quad \forall |x\rangle, |y\rangle \in X. \tag{3.A.15}$$

To analyse these matrix elements, we assume the simple form $\rho = |\psi\rangle\langle\psi|$ (3.A.13) of the density operator, though the arguments easily generalise to arbitrary density operators. As discussed in Appendix 3.A.3, the diagonal element ρ_{xx} provides the probability of being in the state $|x\rangle \in X$:

$$\rho_{xx} = \langle x|\psi\rangle\langle\psi|x\rangle = |\langle x|\psi\rangle|^2. \tag{3.A.16}$$

The off-diagonal elements ρ_{xy}, $\forall x \neq y$, are referred as *coherences*, since they give information about the relative phase of the states $|x\rangle$ and $|y\rangle \in X$. Provided the state vector

$$|\psi\rangle = \sum_x c_x |x\rangle \in H, \quad c_x = |c_x| \exp(i\phi_x) \in \mathbb{C}, |x\rangle \in X, \tag{3.A.17}$$

the coherence

$$\rho_{xy} = \langle x|\psi\rangle\langle\psi|y\rangle = |c_x c_y| \exp[i(\phi_x - \phi_y)] \tag{3.A.18}$$

accounts for the difference in phase of the states $|x\rangle$ and $|y\rangle \in X$. The coherence between different states enables their interference, making them indistinguishable, as stated by *Feynman's Uncertainty Principle* (FUP): interfering routes cannot be told apart, and should be considered as one single real route. On the other hand, it is possible to distinguish incoherent states, because they are not able to interfere.

The role of the entries of the density matrix $\rho(t_k)$ (3.9) is particularly clear in the example of the stochastic model (3.7). In the orthonormal basis of the eigenvectors $|a_n\rangle$ of the operator $\hat{A}$, $\hat{A}|a_n\rangle = a_n|a_n\rangle$, the element of row i and column j of the density matrix $\rho(t_k)$ (3.9) can be written as

$$\langle a_i|\rho(t_k)|a_j\rangle = \int p(f_k)\,\langle a_i|\varphi(f_k)\rangle\,\langle\varphi(f_k)|a_j\rangle\,df_k \ \in \mathbb{C}. \tag{3.A.19}$$

By plugging $|\varphi(f_k)\rangle$ (3.7) in (3.A.19), we have

$$\langle a_i|\rho(t_k)|a_j\rangle = \Theta_{i,j}\,c_i(t_k)\,c_j^*(t_k), \quad \Theta_{i,j} \equiv \int G(f - a_i)\,G(f - a_j)\,df \geq 0. \tag{3.A.20}$$

In the Markovian regime explained in Section 3.2.3, the real-valued measure $G(f)$, with $\int G^2(f)\,df = 1$, is narrow enough to satisfy the condition (3.20). The diagonal element $\langle a_i|\rho(t_k)|a_i\rangle$ provides the probability $|c_i(t_k)|^2$ to find the quantum system in the eigenstate $|a_i\rangle$, whereas the assumption (3.20) imposes $\langle a_i|\rho(t_k)|a_j\rangle \approx 0$, $\forall i \neq j$. The negligible coherences reflect the destruction of the interference among the system states. As a result, it is possible to recognise the travelled paths by the narrow measure $G(f)$ (3.20).

If (3.20) does not hold, the supports of the densities $G(f - a_i)$ and $G(f - a_j)$, $i \neq j$, are overlapping, as discussed in Section 3.2.3. The factor $\Theta_{i,j}$ in (3.A.20) accounts for the amount of overlap. A broad measure $G(f)$ implies big values of $\Theta_{i,j}$. The strong coherence $\langle a_i|\rho(t_k)|a_j\rangle \propto \Theta_{i,j}$ allows the interference among the system states, making them indistinguishable by the broad measure $G(f)$, as specified by the FUP.

3.B   Basic Mathematics of Continuous Quantum Measurements

This appendix presents a brief overview of the mathematical formalism used to analyse continuous quantum measurements. In particular, we describe the measurements apparatus (meter) coupled with the observed system. Appendix 3.B.1 reviews the Hamilton equations for a classical meter. As shown in Appendix 3.B.1, it is possible to monitor a classical system without perturbing its evolution. However, the same is not true for quantum systems. Appendix 3.B.2 discusses the equations modelling a single quantum meter, showing that the observations affect the state of the coupled quantum system. In Appendix 3.B.3, we extend the derivation to the case of K identical impulsive von Neumann quantum meters, coupled with a given quantum system. According to the spreading of the meters measure distribution, different regimes can be characterised.

3.B.1   Classical Meter

Let the system of interest, S, be a classical particle with mass m, position x, momentum p and Hamiltonian $h(x,p) = \frac{p^2}{2m} + V(x)$. Suppose we are interested in a certain quantity (dynamical variable) $A(x,p)$, which cannot be measured by a direct inspection. One possible strategy consists of building an apparatus, whose direct inspection can provide the value of A. We can use a second particle, with mass M, position f and momentum λ, to play the role of the pointer P. We couple P to the system S so that the total Hamiltonian $\hat{H}$ takes the form

$$\hat{H} = h(x,p) + \frac{\lambda^2}{2M} + g\,\lambda\,A(x,p), \tag{3.B.1}$$

where the time dependent variable $g(t)$ models the way how the pointer observation is performed. The coupled systems can be tuned in such a way that the displacement of the pointer would be equal to the desired quantity A. For a massive pointer, $M \to \infty$, the second term in the R.H.S. of (3.B.1) may be neglected, and the equations of motion of the composite system become

$$\begin{cases} \dot{x} & = \partial_p \hat{H} = \frac{p}{m} + g\,\lambda\,\partial_p A(x,p), \\ \dot{f} & = \partial_\lambda \hat{H} = g\,A(x,p), \\ \dot{p} & = -\partial_x \hat{H} = -\frac{dV(x)}{dx} - g\,\lambda\,\partial_x A(x,p), \\ \dot{\lambda} & = -\partial_f \hat{H} = 0. \end{cases} \quad (3.B.2)$$

The pointer's momentum is conserved, and setting $\lambda(0) = 0$, we also have $\lambda(t) = 0$, $\forall t \in \mathbb{R}^+$. Equation (3.B.2) leads to:

$$\dot{x} = \frac{p}{m}, \quad \dot{p} = -\frac{dV(x)}{dx}, \quad \dot{f} = g\,A(x,p). \quad (3.B.3)$$

The first two equations in (3.B.3) correspond to the Hamilton equations of the particle with mass m, not perturbed by the presence of the pointer. Note that this would not be the case, if $\lambda(0) \neq 0$. Then, we also have

$$f(t) - f(0) = \int_0^t g(s)\,A(x(s), p(s))\,ds, \quad \forall t \in \mathbb{R}^+. \quad (3.B.4)$$

Setting $f(0) = 0$ and choosing $g(t) = c\,\delta(t - t_0)$, where $\delta(x)$ is the Dirac delta, yields

$$f(t) = A(x(t_0), p(t_0)), \quad (3.B.5)$$

where the constant c is selected unitary. The final displacement $f(t)$ of the pointer returns the desired value $A(x(t_0), p(t_0))$.

3.B.2 Quantum Meter: Von Neumann Measurements

In the following we will be interested in measurements performed on a quantum system in N-dimensional Hilbert space, with finite N. To analyse the work of a quantum (von Neumann [126]) measurement of an operator $\hat{A}$, with the eigenvalues and eigenvectors a_n and $|a_n\rangle$, $n = 1, .., N$, respectively, we need to find a quantum analog of the equations of motion (3.B.2).

The evolution of the composite system $S + P$, prepared at $t = 0$ in the product state (ψ is for the system, and G is for the pointer, which we continue to consider very heavy),

$$|\Psi(0)\rangle = |\psi(0)\rangle |G\rangle, \quad |\psi(0)\rangle = \sum_n c_n(0)|a_n\rangle, \quad |G\rangle = \int G(f)\,|f\rangle\,df, \quad (3.B.6)$$

is governed by the Schrödinger Equation (SE)

$$i\partial_t |\Psi(t)\rangle = \left[\hat{h} + g\,\hat{\lambda}\,\hat{A}\right] |\Psi(t)\rangle, \quad (3.B.7)$$

where $\hat{h}$ is the system's Hamiltonian operator, $\hat{\lambda}$ is the operator representing the pointer's momentum, and $g(t)$ is defined analogously to (3.B.1). Normalisation of the two initial states implies

$$\langle \psi(0)|\psi(0)\rangle = \sum_{n=1}^N |c_n(0)|^2 = 1, \quad \text{and} \quad \langle G|G\rangle = \int |G(f)|^2\,df = 1. \quad (3.B.8)$$

Now we set the clock as in the classical case, ensuring first that the pointer is pointing at zero. This would require $G(f) = \delta(f)$, which is impossible, since $\langle G|G\rangle$ in (3.B.8) will then be infinite. So we must choose $G(f)$ to be peaked around zero with some finite width $\Delta f > 0$. Secondly, we want the pointer momentum to be zero, in order to avoid perturbing the system's evolution, as proposed in Appendix 3.B.1. But then we run into difficulty with the Heisenberg's Uncertainty Principle (UP). The pointer state $|G\rangle$ can be written as superposition of the eigenstates $|\lambda\rangle$ of the momentum operator $\hat{\lambda}$:

$$|G\rangle = \int \tilde{G}(\lambda)\,|\lambda\rangle\,d\lambda, \quad |\lambda\rangle = (2\pi)^{-1/2} \int \exp(i\lambda f)\,|f\rangle\,df, \quad (3.B.9)$$

where $\tilde{G}(\lambda) \equiv \langle\lambda|G\rangle$ is the probability amplitude of the pointer momentum λ and $\langle f|\lambda\rangle \propto \exp(i\lambda f)$, as shown at the end of Appendix 3.A.1 ($\hbar = 1$). Equation (3.B.9) provides the amplitude $G(f) \equiv \langle f|G\rangle$ to measure the pointer position f:

$$G(f) = (2\pi)^{-1/2} \int \tilde{G}(\lambda) \exp(i\lambda f) \, d\lambda. \tag{3.B.10}$$

It is a well known property of the Fourier transform (3.B.10) that a narrow $G(f)$ implies a broad $\tilde{G}(\lambda)$ and vice versa. In other words, a precise choice of the pointer position, $\Delta f \to 0$, implies the impossibility to set accurately its momentum and vice versa (UP).

Thus, the best we can do is to require that the *average* position of the pointer is zero, $\langle f(0)\rangle \equiv \int f|G(f)|^2 df = 0$, or $|G(f)| = |G(-f)|$. By setting the pointer to zero more accurately, we will inevitably perturb the system more. The best we can do is to ensure that the *average* pointer momentum is zero, $\langle \lambda(0)\rangle \equiv \int \lambda|\tilde{G}(\lambda)|^2 d\lambda = 0$, i.e. $|\tilde{G}(\lambda)| = |\tilde{G}(-\lambda)|$, or $G(f) \in \mathbb{R}$, $\forall f \in \mathbb{R}$. These two requirements stipulate our choice of $G(f)$ as a symmetric real function, whose width Δf determines both the accuracy of the measurement, and the inevitable perturbation the measurement produces on the system.

Finally, we are interested in an *impulsive* von Neumann measurement. The choice of $g(t) = c\,\delta(t - t_0)$ allows neglecting $\hat{h}$ in (3.B.7). The system state $\langle f|\Psi(t)\rangle$ is evolved by the Schrödinger Equation (SE)

$$i\partial_t \langle f|\Psi(t)\rangle = g\,\hat{\lambda}\,\hat{A}\,\langle f|\Psi(t)\rangle, \quad \text{for } t \in [t_0 - \varepsilon, t_0 + \varepsilon], \tag{3.B.11}$$

with infinitesimal $\varepsilon > 0$. The initial condition corresponds to the system state just before the meter firing:

$$\langle f|\Psi(t_0 - \varepsilon)\rangle = G(f)|\psi(t_0 - \varepsilon)\rangle, \quad G(f) = \langle f|G\rangle, \quad |\psi(t_0 - \varepsilon)\rangle = \sum_n c_n(t_0)|a_n\rangle. \tag{3.B.12}$$

Just after the measurement, the system state $\langle f|\Psi(t_0 + \varepsilon)\rangle$ becomes *entangled* with the pointer ($\hat{\lambda} = -i\partial_f$, as shown in Appendix 3.A.1),

$$\langle f|\Psi(t_0 + \varepsilon)\rangle \approx \exp(-i\hat{\lambda}\hat{A})\langle f|\Psi(t_0 - \varepsilon)\rangle = \sum_n c_n(t_0)|a_n\rangle \exp(-\partial_f a_n)G(f) =$$
$$= \sum_n G(f - a_n)c_n(t_0)|a_n\rangle = G(f - \hat{A})|\psi(t_0 - \varepsilon)\rangle, \tag{3.B.13}$$

where we have used the expansion (3.B.10) of $G(f)$ and the equality $y(\hat{X})|x\rangle = y(x)|x\rangle$ for the operators $\hat{X} = \hat{A}$ and $\hat{X} = \partial_f$, $\hat{X}|x\rangle = x|x\rangle$, with the corresponding definitions of the function $y(x)$. The constant c is chosen unitary.

By the Born postulate (*ii*) in Appendix 3.A.3, the final probability distribution of the pointer positions is given by

$$p(f) \equiv \langle\Psi(t_0 + \varepsilon)|f\rangle\langle f|\Psi(t_0 + \varepsilon)\rangle = \sum_n |c_n(t_0)|^2\, G^2(f - a_n), \tag{3.B.14}$$

and we can define a measurement which can be considered *accurate*. Namely, we consider a measurement accurate, if $\Delta f \ll |a_n - a_m|$ and $G(f - a_n)\,G(f - a_m) \approx 0$, $\forall f \in \mathbb{R}$, $\forall m \neq n$, as discussed for the Markovian regime in Section 3.2.3. Such a measurement produces a result $f \approx a_n$, and leaves the system in a state $|a_n\rangle$, with a probability $|c_n(t_0)|^2$. In the opposite limit, $\Delta f \gg |a_n - a_m|$, and $G(f - a_n) \approx G(f - a_m)$, $\forall f \in \mathbb{R}$, $\forall m \neq n$, the measurement is "weak" or "fuzzy". A fuzzy measurement perturbs the system only slightly, but provide little information about the value of $\hat{A}$.

3.B.3 Multiple Quantum Meters: Sequential Measurements

Ultimately, we want to study a quantum system subjected, for a period of time T, to an impulsive von Neumann measurement of Appendix 3.B.2 every $\tau = T/K$ units of time. There will, therefore, be K pointers, all prepared in the same state $G(f_k)$, and a measurement readout $\underline{f}$ will consist of K values f_k. Between the measurements at $t_k = k\tau$ and $t_{k+1} = (k+1)\tau$ the system will evolve with an evolution operator $\hat{U}(\tau) = \exp(-i\hat{H}\tau)$. The results of Appendix 3.B.2 are easily generalised to such sequential measurements.

If a readout $\underline{f}$ has been recorded, the (unnormalised) state of the system at $t = T$ is given by

$$|\psi(T, \underline{f})\rangle = \prod_{k=1}^{K} G(f_k - \hat{A}) \exp(-i\hat{H}\tau)|\psi_0\rangle, \tag{3.B.15}$$

where $|\psi_0\rangle \in H$ is the initial condition of the measured system. By the Born postulate (ii) in Appendix 3.A.3, the probability distribution of the readout $\underline{f}$ is given by

$$P(T, \underline{f}) = \langle\psi(T, \underline{f})|\psi(T, \underline{f})\rangle, \tag{3.B.16}$$

so that at $t = T$ the system is described by a density operator

$$\rho(T) = \int df_1...f_K \, |\psi(T, \underline{f})\rangle \, \langle\psi(T, \underline{f})|. \tag{3.B.17}$$

By plugging $G(f_k - \hat{A}) = \sum_{m_k} |a_{m_k}\rangle G(f_k - a_{m_k})\langle a_{m_k}|$ into (3.B.15), it is possible to obtain the amplitude $\langle a_n|\psi(T; \underline{f})\rangle$ to arrive in the state $|a_n\rangle$ at time $t = T$, by previously passing through a sequence of states (a path) $\{|a_{m_1}\rangle, |a_{m_2}\rangle, .., |a_{m_{K-1}}\rangle\}$

$$\langle a_n|\psi(T; \underline{f})\rangle = \sum_{m_1,..,m_{K-1}} F_n(m_1,..,m_{K-1}) \prod_{k=1}^{K} G(f_k - a_{m_k}), \tag{3.B.18}$$

where $F_n(m_1,..,m_{K-1}) \equiv \langle a_n| \exp(-i\hat{H}\tau)|a_{m_{K-1}}\rangle\langle a_{m_{K-1}}|..|a_{m_1}\rangle\langle a_{m_1}| \exp(-i\hat{H}\tau)|\psi_0\rangle$.

Two limiting cases should be distinguished. In the absence of meters, the paths are *virtual*, and the probability to find the system in $|a_n\rangle$ at $t = T$ is given by

$$P_n(T) \equiv |\langle a_n|\psi(T; \underline{f})\rangle|^2 = \left| \sum_{m_1,..,m_{K-1}} F_n(m_1,..,m_{K-1}) \right|^2. \tag{3.B.19}$$

The same result is obtained for highly inaccurate meters, $\Delta f \gg |a_n - a_m|$, where all G's are so broad that $G(f_k - a_m) \approx G(f_k)$.

Highly accurate meters, with $\Delta f \ll |a_n - a_m|$, completely destroy interference between the virtual parts, turning them into N^K *real* routes, travelled with the probabilities $P_n(T, \underline{f}) = |F_n(m_1,..,m_{K-1})|^2$. The probability to reach $|a_n\rangle$, regardless of what the meters read, is now the sum of all such probabilities, and we have

$$P_n(T) = \sum_{m_1,..,m_{K-1}} |F_n(m_1,..,m_{K-1})|^2. \tag{3.B.20}$$

Conclusions & Major Results

We conclude the Thesis by summing up objectives, modelling frameworks, tools, methodologies and major achievements for each chapter. Table C.1 provides a schematic view of the developed lines of research.

Chapter 1 aims to understand the reasons behind the inconsistencies between the classical kinetics predictions and experimental evidence in Controlled Radical Polymerization (CRP). We develop the methodology which explains such discrepancies, and provides the accurate prediction of experimental observations. The key idea of this methodology is to assume non-Markovian kinetics and introduce delays among the competitive processes in CRP.

To prove this idea, we propose the Stochastic Simulation Algorithm (SSA) as a possible modelling framework, being able to introduce non-Markovian dynamics in the evolution of the considered reactions.

We show that the introduction of delays significantly changes the statistics of the polymer chains growth. The equations, and the corresponding properties, derived for predicting Markovian growth, differ significantly from those describing a non-Markovian regime.

We also explain how to simulate the delayed growth, by formulating suitable implementations of the Stochastic Simulation Algorithm. In addition, we propose an approximated methodology using Linear Exponential distributions to embed the delays caused by chemical reactions. The approximated method enhances the simulation speed, especially for big sample sizes, still being able to reproduce the results of the other methods, guaranteeing a reasonable accuracy.

Since our objective is to explain the reduction in relative frequencies of propagations and backbitings (branching fractions) experimentally observed in CRP, we concentrate on simulation of relative frequencies of constrained events. Thus, we propose a Monte Carlo (MC) approach for the evaluation of relative frequencies of constrained events in stochastic processes. We also derive a significantly more efficient analytical formula for computing the frequencies of interest.

The methods are then applied to the evaluation of branching fractions in the CRP. With the derived approaches we were also able to prove that memoryless models are not able to explain the experimentally observed reduction of the branching fraction, and thus only models with delays should be applied for study of CRP.

We investigate the performance and accuracy of the proposed methodologies on the example of CRP of acrylic monomers. We demonstrate that the analytical approach is free of statistical errors, and thus guarantees more accurate estimations, than those provided by MC simulations. In addition, the method is significantly (an order of the sample size $\geq 10^4$) faster than the MC approach.

Finally, Chapter 1 presents an SSA-based method for simulating the CRP process in agreement with the available experimental data. First, we discuss a choice of the delayed distributions to be used in the Monte Carlo method and in the analytical approach for the computation of the branching fraction in CRP. The Linear Exponential density is chosen to account for the required delays, as motivated before. The parameters of the given distributions are defined by an optimisation routine, maximising the fitting to available experimental data of the simulated branching fractions. Then, we formulate the SSA-based method for CRP modelling, which takes advantage of the available experimental data. Algorithm 1.8 summarises the method, and uses the Linear Exponential densities, with the optimised values of the parameters. The algorithm can potentially be used for a systematic study of all properties of the simulated system.

In conclusion, we were able to explain the inconsistencies between the classical kinetics predictions

and experimental evidences in the CRP. Assuming non-Markovian kinetics and introducing delays among the competitive processes, we can provide the accurate prediction of such experimental observations. As shown in Section 1.7, the agreement between predicted and experimental branching fractions validates our non-Markovian model for CRP of acrylic monomers.

The objective of Chapter 2 is to develop a modelling framework allowing for a fast and accurate prediction of Multi-phase Polymers Morphology (MPM). To do so, we derive a Population Balance Equations (PBE) based model for the distribution of the expected size of the polymer clusters, contributing to the morphology of interest. Then, we aim to develop an accurate and efficient methodology for the solution of the proposed model. The speed of the predictive simulations technique should be high enough for enabling on-the-fly recommendations for technological conditions in the synthesis of new multi-phase morphologies.

The introduced PBE model accounts for the mechanisms driving the considered reaction: aggregation, growth, nucleation and phase-transition. Under the assumptions of [45] summarised in Section 2.1.2, we derive the chemical rates of the processes involved in the development of *latex* particles morphology. Aiming to search for the most efficient approach for solving the derived PBE, we also introduce the Models I-III of Section 2.2.1, which use less advanced chemical rates, but can be viewed as coarse approximations to the addressed process.

Since the *latex* particles rates lead to computationally intractable quantities, we propose a novel and automatic procedure for reducing the PBE model to dimensionless variables. In particular, Algorithm 2.1 summarises the steps needed for finding optimal scaling factors leading to a dimensionless PBE with computationally tractable parameters. The proposed optimisation scheme is not computationally demanding, provided one makes the use of an efficient built-in optimisation routine. The validation of the scaling procedure is carried out using the *latex* particles model, and results in reducing the ratio between maximal and minimal parameters values from 10^{57} (original) to 10^5 (dimensionless). Then, we provide an analysis of the addressed PBE model (2.25). We show that the solution $m(v,t)$ of (2.25) must be non-negative. We also characterise the time evolution of the zero- and first-order moments of the distribution $m(v,t)$. Then, the asymptotic behaviour of $m(v,t)$ is discussed for $v \to +\infty$ and a fixed time $t \in \mathbb{R}^+$.

Section 2.3 is devoted to the design of an accurate and efficient methodology for integrating the PBE (2.25). We develop three approaches belonging to the classes of methods revised in Section 2.3.1: the Stochastic Simulation Algorithm (SSA), the Generalised Method Of Characteristics (GMOC) and the Laplace Transform Technique (LTT). In addition, we propose the Laplace Induced Splitting Method (LISM) which does not fit into any described class and is based on the idea which, to our knowledge, has never been explored in the numerical methods for solving PBE. More specifically, we combine a splitting integration scheme with Laplace induced analytical solutions derived for simplified PBEs, composing the PBE of interest.

In order to judge the performance of the derived approaches for realistic settings, we employ the rate functions modelling the morphology of *latex* particles. In the tests of Section 2.4, the parameters of Models I-III assume the orders of magnitude achieved by the dimensionless counterparts of the *latex* particles rates.

Although LTT provides high levels of precision and speed for the tested models, its applicability is limited by the assumptions we made. Our numerical experiments show that the SSA is a robust integration technique, but computational inefficiencies make the approach not competitive for solving the addressed PBE system. In the performed experiments, the GMOC ensures good accuracy and efficiency of the simulation. However, the LISM outperforms the GMOC in computational speed by up to a factor of two orders of magnitude, while achieving the same accuracy in all tested cases.

On the basis of the performed experiments, we conclude that the developed LISM methodology is a promising technique for prediction of multi-phase polymers morphology in systems of many particles.

Chapter 3 aims to model and analyse the behaviour of measurements performed on quantum systems. In particular, we consider frequent observations, continuous in the limit, such as Continuous Fuzzy Measurements (CFM). By their very nature, continuous quantum measurements are not amenable to

an analytical treatment, but are well suited for numerical simulations. Thus, we propose a stochastic model and a Monte Carlo (MC) method to study the dynamics of the observations. The measurements behaviour is described through the knowledge of the distribution of their outcomes.

Quantities of interest can be approximated by MC estimators computed on the drawn samples with size $S \geq 1$. The simulation method is validated through comparison with the available analytical solution (3.17) of the expected meter reading (3.11). The order $O(S^{-1/2})$ of the convergence rate is confirmed, using the analytical formula (3.26) for the density matrix (3.9).

Different measurement regimes are characterised by their accuracy and the corresponding influence on the system's dynamics. In particular, accurate measurements lead to the Markovian behaviour of the meters, but affect the natural dynamics of the quantum system. On the other hand, imprecise observations result in a non-Markovian regime of the meters. The natural evolution is unaltered, but very little is known about the actual state of the system. We provide the proof and the validating tests for the Markovian and non-Markovian behaviour of the quantum measurements. Both regimes can be successfully simulated using the designed MC method.

The MC method helped us in reconsidering the Mensky's theory on CFM [142] for a large number of impulsive meters of accuracy Δf, imposing a Gaussian restriction on the Feynman paths of a two-level system. In the case of the system in a superposition of the eigenstates of a variable $\hat{A}$, the authors of [142] suggested that two things should happen if the CFM monitoring is performed:

(i) the system's pure state will be turned into a density matrix, diagonal in the chosen representation (decoherence);

(ii) every readout will eventually align with one of the eigenvalues of $\hat{A}$, indicating the eigenstate into which the system is driven as a result of being monitored.

We show that while the authors of [142] are correct in their analysis of the decoherence process, they fail to correctly describe the properties of the observed readouts. The fallacy is in neglecting the density of states available to the readouts $f_1, .., f_K$ in a K-dimensional space. While a constant readout does have the largest statistical weight, it is vastly outnumbered by highly irregular ones, which will be observed in almost every run of the experiment. This is even more true in the limit $K \to \infty$, $\Delta f \to \infty$, where the chance of obtaining an almost constant (or, indeed, a smooth) readout curve is virtually null.

We show that, for a fixed period of monitoring, T, as the number of meters, K, increases, typical readouts f_k become highly irregular, and do not align with one of the eigenvalues of the measured quantity, as suggested in [142]. The same behaviour of the meter readings is observed when decoherence of an initial state is achieved, or Zeno effect is imposed on the system. Thus, a different description of the decoherence process and the Zeno effect is required.

For a system prepared in a pure state, in the case its Hamiltonian $\hat{H}$ does not facilitate transitions between the eigenstates of the measured quantity $\hat{A}$, decoherence can be linked to a fictitious random walk, which is bound to lead to one of two outcomes, which, in turn, determine the final state of the system.

The random walk analogy remains useful also in a case of a driven system, subject to Rabi oscillations. For such a system, a typical readout is highly irregular even in a near-Zeno regime, where Rabi oscillations of the system's state are replaced by a telegraph noise. In this case, the corresponding random walk changes direction every time the system jumps from one state to the other. The two evolutions should be considered together, and it is difficult to say whether it is the walker, which causes the system to change its state, or the system, which causes the walker to change direction.

In conclusion, the methodologies developed within this Thesis have been inspired by some particular applications and unresolved issues. However, the proposed novel approaches can be applied to a broad range of physical, chemical and biological systems. Our results have been presented in (i) four scientific papers published in the high impact journals [1, 2, 3, 4] and (ii) eight invited talks delivered in International Conferences, as reported in Contributions & Developed Software.

	Chapter 1 CRP	Chapter 2 MPM	Chapter 3 CFM
Application	Controlled Radical Polymerization (CRP)	Multi-phase Polymers Morphology (MPM)	Continuous Fuzzy Measurements (CFM)
Objective	Quantitative Modelling of CRP	On-the-fly Prediction of MPM	Modelling & Analysis of CFM
Modelling Framework	▷ Stochastic Simulation Algorithm (SSA) [Section 1.2.1]	▷ Population Balance Equations (PBE) [Section 2.2.1] ▷ SSA [Section 2.3.2]	▷ Stochastic Model [Section 3.2.1]
Analytical Treatment	▷ Derivation of Density Distributions for Modelling Polymers Growth: ○ *Markovian Growth*, Distribution (1.19) of Monomers Attachment ○ *Non-Markovian Growth*, Distributions (1.27)-(1.28) of Monomers Attachment	▷ Analysis of Solution of PBE (2.25) [Section 2.2.3]: ○ Non-Negativity ○ First-Orders Moments ○ Asymptotic Behaviour ▷ Laplace Transformed Solutions (LTS) of PBE (2.25) for Models I-III [Section 2.3.4]	▷ Analysis of *Markovian* and *Non-Markovian Regimes* of Quantum Measurements [Section 3.2.3] ▷ Proof & Analysis of [Section 3.3.2]: ○ Density of Available States for CFM ○ Fallacy of CFM Convergence Predicted by Mensky's Theory
Numerical Treatment	▷ SSA-based Methods for Simulating Delayed Growth [Section 1.3.5] ▷ Linear Exponential Approximation of Delayed Distributions [Section 1.3.5.4]	▷ Development of Numerical Methodologies for Solving PBE (2.25) [Section 2.3]: ○ *Stochastic* [SSA] ○ *Discretization* [GMOC] ○ *LTS Inversion* [LTT] ○ *Splitting* [LISM]	▷ Monte Carlo (MC) Method [Algorithm 3.1] for Simulating: ○ Quantum System Dynamics ○ Measurements Distributions
Computed Properties	▷ Polymers Mean Length (1.30) for Delayed Growth [Figure 1.2] ▷ Relative Frequencies of Constrained Events: ○ MC [Section 1.4] ○ Analytical [Section 1.5] ▷ Branching Fractions in CRP: ○ MC [Algorithm 1.5] ○ Analytical [Algorithm 1.6]	▷ Characteristic Constants θ, Scaled Parameters λ and Rates of PBE (2.14)-(2.17) for *Latex* Particles Model [Table 2.1] ▷ Distributions of Expected Size of Polymers Agglomerates for Models I-III [Fig. 2.3-2.7] ▷ Rates for *Latex* Particles: ○ Derivation [Appendix 2.A] ○ Scaling To Dimensionless Variables [Table 2.C.1]	▷ Density Matrix (3.9): ○ MC Estimator (3.10) ○ Analytical Solution (3.26) ▷ Expected Measurements (3.11): ○ MC Estimator (3.11) ○ Analytical Solution (3.17)
Parameter Estimation	▷ Tuning Parameters of Delayed Distributions w.r.t. Experimental Data [Algorithm 1.7]	▷ Optimal Scaling of PBE Parameters to Dimensionless and Computationally Tractable Values [Algorithm 2.1]	
Tests & Analysis	▷ Prediction of Branching Fractions in CRP: ○ Accuracy [Fig. 1.8a, 1.9a] ○ Efficiency [Fig. 1.8b, 1.9b]	▷ Comparative Analysis of Developed Numerical Methodologies: ○ Accuracy [Fig. 2.4-2.7] ○ Efficiency [Tab. 2.2-2.5]	▷ Analysis of Mensky's Theory on CFM [Section 3.4]: Decoherence and Zeno Effect by Random Walk
Major Result	Stochastic Approach for Modelling CRP in Agreement with Experiments [Algorithm 1.8]	Computationally Efficient PBE-based Framework for MPM Prediction using LISM methodology	Re-examination of Mensky's Theory on CFM

Table C.1: Outline of the Thesis: objectives, modelling frameworks, tools, methodologies and results.

Contributions & Developed Software

Controlled Radical Polymerization

CRP

Publications & Presentations

S. Rusconi, E. Akhmatskaya, D. Sokolovski, J.M. Asua. *Study on Controlled Radical Polymerization.* Workshop on Dynamical Systems and Applications, BCAM, Bilbao, Spain, 2013.

Abstract: Controlled radical polymerization (CRP) is a process to form polymers by successive monomers additions. This growing process is mainly made by three events: propagation, if the next monomer is linearly added to the chain, backbiting, when the free radical changes its position and a new branch will start growing perpendicular to the previous one, and termination, if the chain stops to grow. We have proposed a model describing the CRP process and offered two different approaches for solving it: Partial Differential Equations solutions (PDE) and stochastic simulation algorithm based on Monte Carlo estimations (MC). In this presentation, the model and the two approaches are summarized and their benefits as well as drawbacks are discussed. The future developments with the focus on the real applications are outlined.

S. Rusconi, E. Akhmatskaya, D. Sokolovski, J.M. Asua. *Mathematical Modeling of Chemical Reactions Kinetics.* IV Workshop Quantum Days in Bilbao, BCAM, Bilbao, Spain, 2014.

Abstract: Chemical Reactions Kinetics (CRK) mostly consists in the study of chemical processes evolution. In this presentation, a stochastic memoryless kinetics model is summarized. Then, we introduce the Controlled Radical Polymerization (CRP) process and we explain why the memoryless model is not the proper tool to correctly describe this phenomenon. We propose a modification of the model, with the loss of the memoryless property. The modified models provides a good fit of existing experimental data provided by the Basque Center for Macromolecular Design and Engineering (POLYMAT).

N. Ballard, S. Rusconi, E. Akhmatskaya, D. Sokolovski, J. C. de la Cal, J. M. Asua. *Impact of Competitive Processes on Controlled Radical Polymerization.* Macromolecules, 47(19):6580-6590, 2014.

Abstract: The kinetics of radical polymerization have been systematically studied for nearly a century and in general are well understood. However, in light of recent developments in controlled radical polymerization many kinetic anomalies have arisen. These unexpected results have been largely considered separate, and various, as yet inconclusive, debates as to the cause of these anomalies are ongoing. Herein we present a new theory on the cause of changes in kinetics under controlled radical polymerization conditions. We show that where the fast, intermittent deactivation of radical species takes place, changes in the relative rates of the competitive reactions that exist in radical polymerization can occur. To highlight the applicability of the model, we demonstrate that the model explains well the reduction in branching in acrylic polymers in RAFT polymerization. We further show that such a theory may explain various phenomena in controlled radical polymerization and may be exploited to design precise macromolecular architectures.

S. Rusconi, E. Akhmatskaya, D. Sokolovski, J.M. Asua. *Modelling of Delayed Processes in Controlled Radical Polymerization.* LAMA - Laboratorie de Mathématiques, Univeristé de Savoie, Le Bourget-du-Lac, France, 2015.

Abstract: The normal practice in modelling of Controlled Radical Polymerization (CRP) is to apply Monte Carlo based stochastic simulation algorithms assuming the processes to be Markovian. We argue that such an approach overlooks the delayed nature of some processes involved in CRP and do suggest the methodology that overcomes this deficit. The proposed methodology offers the analytical representations for the probability density functions corresponding to the delayed processes as in the cases when the amount of delay is known exactly as it is unknown. Moreover, to improve the accuracy and efficiency of our modelling approach for computation of branching fraction in CRP, we replace the random walk Monte Carlo with the analytical solution. The comparison of the novel methodology with the traditional simulation methods and the experimental data is provided.

D. Sokolovski, S. Rusconi, E. Akhmatskaya, J. M. Asua. *Non-markovian models of the growth of a polymer chain.* Proc. R. Soc. A, 471(2180), 2015.

Abstract: Using simple exactly solvable models, we show that event-dependent time delays may lead to significant non-Poisson effects in the statistics of polymer chain growth. The results are confirmed by stochastic simulation of various growth scenarios. Our interest in mathematical aspects of non-Markovian growth arises from recent successful application of delayed probability density functions in stochastic modelling of controlled radical polymerization.

S. Rusconi, E. Akhmatskaya, D. Sokolovski, N. Ballard, J. C. de la Cal. *Relative frequencies of constrained events in stochastic processes: An analytical approach.* Phys. Rev. E, 92:043306, 2015.

Abstract: The stochastic simulation algorithm (SSA) and the corresponding Monte Carlo (MC) method are among the most common approaches for studying stochastic processes. They relies on knowledge of inter-event probability density functions (PDFs) and on information about dependencies between all possible events. Analytical representations of a PDF are difficult to specify in advance, in many real life applications. Knowing the shapes of PDFs, and using experimental data, different optimization schemes can be applied in order to evaluate probability density functions and, therefore, the properties of the studied system. Such methods, however, are computationally demanding, and often not feasible. We show that, in the case where experimentally accessed properties are directly related to the frequencies of events involved, it may be possible to replace the heavy Monte Carlo core of optimization schemes with an analytical solution. Such a replacement not only provides a more accurate estimation of the properties of the process, but also reduces the simulation time by a factor of order of the sample size (at least $\approx 10^4$). The proposed analytical approach is valid for any choice of PDF. The accuracy, computational efficiency, and advantages of the method over MC procedures are demonstrated in the exactly solvable case and in the evaluation of branching fractions in controlled radical polymerization (CRP) of acrylic monomers. This polymerization can be modeled by a constrained stochastic process. Constrained systems are quite common, and this makes the method useful for various applications.

Developed Software

Computation of Branching Fractions in Controlled Radical Polymerization.
Program Name: Optimise
Author: S. Rusconi
License: N/A
Programming Language: C++
Operating System: Linux
Description: The package provides the implementation of Analytical Solution and Monte Carlo method for computation of branching fractions in Controlled Radical Polymerization (CRP). The solution is computed for the case of Linear Exponential kernels. Different optimisation algorithms are

implemented for searching optimal parameters to achieve the best fit to available experimental data of branching fractions.

Multi-phase Polymers Morphology

Publications, Presentations & Preprints

S. Rusconi, E. Akhmatskaya, D. Sokolovski, D. Dutykh, J.M. Asua, S. Hamzehlou. *Dynamic Development of Particles Morphology.* **UCSB - University of California, Santa Barbara, USA, 2015.**

S. Rusconi, E. Akhmatskaya, D. Dutykh, D. Sokolovski, J. M. Asua. *Mathematical Modelling of Polymers Particles Production.* **Minisymposium Success Stories of Spanish Industrial Mathematics with Industry, ICIAM 2015, Beijing, China, 2015.**
Astract: We present the novel stochastic approach for polymers particles production modelling and numerical simulations amenable to high performance computing. The goal is to enable on-the-fly recommendations for technological conditions in polymerization processes. The focus is on algorithms for prediction of particle morphology development. The work has been done in collaboration with Basque Center for Macromolecular Design and Engineering (POLYMAT), partner of a consortium of companies including some of the major producers of dispersed polymers.

S. Rusconi, E. Akhmatskaya, D. Sokolovski, D. Dutykh, J.M. Asua, S. Hamzehlou. *Mathematical Modeling of Chemical Reactions at Basque Center for Applied Mathematics.* **Workshop on Mathematical Technology Transfer: CTA- IMUS-math-in, Sevilla, Spain, 2015.**

R. Bacsa, W. Bacsa, M.C. Schwarzwälder, V. Cregan, M. Fernández-Pendás, S. Fernandez-Mendez, B. Florio, A. Marquina, I. Moyles, T. Myers, H. Ribera Ponsa, S. Rusconi, S. Serna, C. Vázquez-Cendón. *Synthesis of Monodisperse Spherical Nanocrystals.* **ESGI report [107], Centre de Recerca Matemàtica, Barcelona, Spain, 2016.**
Abstract: Nano-particles, small units of matter with dimensions in the range 1-100 nm, exhibit many advantageous size-dependent magnetic, electrical, chemical and optical properties, which are not observed at the micro-scale or bulk. These properties are extremely sensitive to particle size, and thus the ability to produce mono-disperse particles is critical. Due to its ease of use and flexibility, precipitation of nano-particles from solution is one of the most widely used synthesis method. The main disadvantage of this method is that the relationship between particle growth and system conditions is not fully understood. In practice, the optimal reaction conditions are usually ascertained empirically or intuitively. In this report we consider several different applied mathematical techniques to explain nano-particle growth via the precipitation method. In particular, we describe the impact of size focussing and defocussing (or Ostwald ripening) on the evolution of the nano-particle size distribution.

S. Rusconi, E. Akhmatskaya, D. Dutykh, J.M. Asua, S. Hamzehlou. *Prediction of Polymers Particles Morphology Development: Models and Methods.* **Fourth International Congress on Multiphysics, Multiscale, and Optimization Problems, BCAM, Bilbao, Spain, 2016.**

Developed Software

Dynamic Development of Particles Morphology.
Program Name: DDPM
Author: S. Rusconi

License: N/A
Programming Language: C++ & Matlab
Operating System: Linux
Description: The aim of this package is to implement various numerical algorithms for simulation of the dynamic development of polymers particles morphology. The implemented routines provide estimations for the density functions of the particles volume.

Continuous Fuzzy Measurements

CFM

Publications & Presentations

D. Sokolovski, S. Rusconi, S. Brouard, E. Akhmatskaya. *Reexamination of continuous fuzzy measurement on two-level systems.* Phys. Rev. A, 95:042111, 2017.

Abstract: Imposing restrictions on the Feynman paths of the monitored system has in the past been proposed as a universal model-free approach to continuous quantum measurements. Here we revisit this proposition and demonstrate that a Gaussian restriction, resulting in a sequence of many highly inaccurate (weak) von Neumann measurements, is not sufficiently strong to ensure proximity between a readout and the Feynman paths along which the monitored system evolves. Rather, in the continuous limit, the variations of a typical readout become much larger than the separation between the eigenvalues of the measured quantity. Thus, a typical readout is not represented by a nearly constant curve, correlating with one of the eigenvalues of the measured quantity $\hat{A}$, even when decoherence or Zeno effect is achieved for the observed two-level system, and does not point directly to the system's final state. We show that the decoherence in a "free" system can be seen as induced by a Gaussian random walk with a drift, eventually directing the system towards one of the eigenstates of $\hat{A}$. A similar mechanism appears to be responsible for the Zeno effect in a driven system, when its Rabi oscillations are quenched by monitoring. Alongside the Gaussian case, which can only be studied numerically, we also consider a fully tractable model with a "hard wall" restriction and show the results to be similar.

S. Rusconi , D. Sokolovski, E. Akhmatskaya. *Stochastic Simulation of Continuous Quantum Measurements.* LAMA - Laboratorie de Mathématiques, Univeristé de Savoie, Le Bourget-du-Lac, France, 2017.

Developed Software

Weak Measurements of Quantum Particles Trapped in a Double Well Potential.
Program Name: meter
Author: S. Rusconi
License: N/A
Programming Language: C++
Operating System: Linux
Description: The package provides the implementation of Monte Carlo algorithms for simulation of the behaviour of a meter measuring a quantum system. The considered system describes the dynamics of quantum particles trapped in a double well potential. The developed routine allows estimating the outcomes of the performed measurements and the density matrix, describing the state of the monitored quantum system.

Acknowledgements

Bibliography

[1] N. Ballard, **S. Rusconi**, E. Akhmatskaya, D. Sokolovski, J. C. de la Cal, and J. M. Asua. Impact of Competitive Processes on Controlled Radical Polymerization. *Macromolecules*, 47(19):6580–6590, 2014.

[2] D. Sokolovski, **S. Rusconi**, E. Akhmatskaya, and J. M. Asua. Non-markovian models of the growth of a polymer chain. *Proc. R. Soc. A*, 471(2180), 2015.

[3] **S. Rusconi**, E. Akhmatskaya, D. Sokolovski, N. Ballard, and J. C. de la Cal. Relative frequencies of constrained events in stochastic processes: An analytical approach. *Phys. Rev. E*, 92:043306, 2015.

[4] D. Sokolovski, **S. Rusconi**, S. Brouard, and E. Akhmatskaya. Reexamination of continuous fuzzy measurement on two-level systems. *Phys. Rev. A*, 95:042111, 2017.

[5] N. M. Ahmad, F. Heatley, and P. A. Lovell. Chain transfer to polymer in free-radical solution polymerization of n-butyl acrylate studied by NMR spectroscopy. *Macromolecules*, 31(9):2822–2827, 1998.

[6] C. Plessis, G. Arzamendi, J. R. Leiza, H. A. S. Schoonbrood, D. Charmot, and J. M. Asua. Seeded semibatch emulsion polymerization of n-butyl acrylate. Kinetics and structural properties. *Macromolecules*, 33(14):5041–5047, 2000.

[7] C. Plessis, G. Arzamendi, J. R. Leiza, H. A. S. Schoonbrood, D. Charmot, and J. M. Asua. Modeling of seeded semibatch emulsion polymerization of n-BA. *Industrial & Engineering Chemistry Research*, 40(18):3883–3894, 2001.

[8] J. Vandenbergh and T. Junkers. Macromonomers from AGET activation of poly(n-butyl acrylate) precursors: Radical transfer pathways and midchain radical migration. *Macromolecules*, 45(17):6850–6856, 2012.

[9] A. N. F. Peck and R. A. Hutchinson. Secondary reactions in the high-temperature free radical polymerization of butyl acrylate. *Macromolecules*, 37(16):5944–5951, 2004.

[10] A. Ratkiewicz and T. N. Truong. Kinetics of the C-C Bond Beta Scission Reactions in Alkyl Radical Reaction Class. *The Journal of Physical Chemistry A*, 116(25):6643–6654, 2012.

[11] N. Ballard, J. C. de la Cal, and J. M. Asua. The role of chain transfer agent in reducing branching content in radical polymerization of acrylates. *Macromolecules*, 48(4):987–993, 2015.

[12] G. Moad and D. H. Solomon. *The Chemistry of Radical Polymerization*. Elsevier, 2nd edition, 2006.

[13] N. M. Ahmad, B. Charleux, C. Farcet, C. J. Ferguson, S. G. Gaynor, B. S. Hawkett, F. Heatley, B. Klumperman, D. Konkolewicz, P. A. Lovell, K. Matyjaszewski, and R. Venkatesh. Chain transfer to polymer and branching in controlled radical polymerizations of n-butyl acrylate. *Macromolecular Rapid Communications*, 30(23):2002–2021, 2009.

[14] N. Ballard, M. Salsamendi, J. I. Santos, F. Ruipérez, J. R. Leiza, and J. M. Asua. Experimental evidence shedding light on the origin of the reduction of branching of acrylates in ATRP. *Macromolecules*, 47(3):964–972, 2014.

[15] K. Liang and R. A. Hutchinson. The effect of hydrogen bonding on intramolecular chain transfer in polymerization of acrylates. *Macromolecular Rapid Communications*, 32(14):1090–1095, 2011.

[16] A. Agirre, J. I. Santos, A. Etxeberria, V. Sauerland, and J. R. Leiza. Polymerization of n-butyl acrylate with high concentration of a chain transfer agent (CBr4): detailed characterization and impact on branching. *Polymer Chemistry*, 4:2062–2079, 2013.

[17] Y. Reyes and J. M. Asua. Revisiting chain transfer to polymer and branching in controlled radical polymerization of butyl acrylate. *Macromolecular Rapid Communications*, 32(1):63–67, 2011.

[18] D. Konkolewicz, S. Sosnowski, D. R. D'hooge, R. Szymanski, M. F. Reyniers, G. B. Marin, and K. Matyjaszewski. Origin of the Difference between Branching in Acrylates Polymerization under Controlled and Free Radical Conditions: A Computational Study of Competitive Processes. *Macromolecules*, 44(21):8361–8373, 2011.

[19] T. Junkers, S. P. S. Koo, T. P. Davis, M. H. Stenzel, and C. Barner-Kowollik. Mapping Poly(butyl acrylate) Product Distributions by Mass Spectrometry in a Wide Temperature Range: Suppression of Midchain Radical Side Reactions. *Macromolecules*, 40(25):8906–8912, 2007.

[20] S. P. S. Koo, T. Junkers, and C. Barner-Kowollik. Quantitative Product Spectrum Analysis of Poly(butyl acrylate) via Electrospray Ionization Mass Spectrometry. *Macromolecules*, 42(1):62–69, 2009.

[21] M. Gaborieau, S. P. S. Koo, P. Castignolles, T. Junkers, and C. Barner-Kowollik. Reducing the Degree of Branching in Polyacrylates via Midchain Radical Patching: A Quantitative Melt-State NMR Study. *Macromolecules*, 43(13):5492–5495, 2010.

[22] D. T. Gillespie. Exact stochastic simulation of coupled chemical reactions. *The Journal of Physical Chemistry*, 81(25):2340–2361, 1977.

[23] D. T. Gillespie. Stochastic Simulation of Chemical Kinetics. *Annu. Rev. Phys. Chem.*, 58(1):35–55, 2007.

[24] Y. T. Yeh, L. Yang, M. Watson, N. D. Goodman, and P. Hanrahan. Synthesizing open worlds with constraints using locally annealed reversible jump MCMC. *ACM Trans. Graph.*, 31(4):1–11, 2012.

[25] D. T. Gillespie. A general method for numerically simulating the stochastic time evolution of coupled chemical reactions. *Journal of Computational Physics*, 22(4):403–434, 1976.

[26] Y. Cao, H. Li, and L. R. Petzold. Efficient formulation of the stochastic simulation algorithm for chemically reacting systems. *The Journal of Chemical Physics*, 121(9):4059–4067, 2004.

[27] M. A. Gibson and J. Bruck. Efficient exact stochastic simulation of chemical systems with many species and many channels. *The Journal of Physical Chemistry A*, 104(9):1876–1889, 2000.

[28] D. T. Gillespie. Approximate accelerated stochastic simulation of chemically reacting systems. *The Journal of Chemical Physics*, 115(4):1716–1733, 2001.

[29] P. Langevin. On the Theory of Brownian Motion. *C. R. Acad. Sci.*, 146:530–533, 1908.

[30] Y. Cao, D. T. Gillespie, and L. R. Petzold. Efficient step size selection for the tau-leaping simulation method. *The Journal of Chemical Physics*, 124(4):044109, 2006.

[31] Y. Cao, D. T. Gillespie, and L. R. Petzold. Avoiding negative populations in explicit Poisson tau-leaping. *The Journal of Chemical Physics*, 123(5):054104, 2005.

[32] M. Rathinam, L. R. Petzold, Y. Cao, and D. T. Gillespie. Stiffness in stochastic chemically reacting systems: The implicit tau-leaping method. *The Journal of Chemical Physics*, 119(24):12784–12794, 2003.

[33] Y. Cao, D. T. Gillespie, and L. R. Petzold. The slow-scale stochastic simulation algorithm. *The Journal of Chemical Physics*, 122(1):014116, 2005.

[34] F. A. Haight. *Handbook of the Poisson distribution.* John Wiley and Sons, 1967.

[35] J. A. Nelder and R. Mead. A simplex method for function minimization. *The Computer Journal*, 7(4):308–313, 1965.

[36] M. Mitchell. *An Introduction to Genetic Algorithms.* The MIT Press, 1996.

[37] J. E. L. Joensson, H. Hassander, L. H. Jansson, and B. Toernell. Morphology of two-phase polystyrene/poly(methyl methacrylate) latex particles prepared under different polymerization conditions. *Macromolecules*, 24(1):126–131, 1991.

[38] L. J. González-Ortiz and J. M. Asua. Development of Particle Morphology in Emulsion Polymerization. 1. Cluster Dynamics. *Macromolecules*, 28(9):3135–3145, 1995.

[39] L. J. González-Ortiz and J. M. Asua. Development of Particle Morphology in Emulsion Polymerization. 2. Cluster Dynamics in Reacting Systems. *Macromolecules*, 29(1):383–389, 1996.

[40] L. J. González-Ortiz and J. M. Asua. Development of Particle Morphology in Emulsion Polymerization. 3. Cluster Nucleation and Dynamics in Polymerizing Systems. *Macromolecules*, 29(13):4520–4527, 1996.

[41] J. M. Asua and E. Akhmatskaya. *Dynamical modelling of morphology development in multiphase latex particles. European Success Stories in Industrial Mathematics.* Springer, 2011.

[42] E. Akhmatskaya and J. M. Asua. Dynamic modeling of the morphology of latex particles with in situ formation of graft copolymer. *Journal of Polymer Science Part A: Polymer Chemistry*, 50(7):1383–1393, 2012.

[43] E. Akhmatskaya and J. M. Asua. Dynamic modeling of the morphology of multiphase waterborne polymer particles. *Colloid and Polymer Science*, 291(1):87–98, 2013.

[44] A.V. Lubnin, D. Malaba, V. Stanislawczyk, and G.D. Calhoun. Water dispersions of non-uniform polyurethane particles, 2009. US Patent 7,582,698.

[45] S. Hamzehlou, J. R. Leiza, and J. M. Asua. A new approach for mathematical modeling of the dynamic development of particle morphology. *Chemical Engineering Journal*, 304(C):655–666, 2016.

[46] D. Ramkrishna. *Population Balances: Theory and Applications to Particulate Systems in Engineering.* Academic Press, 2000.

[47] M. V. Smoluchowski. Drei Vorträge über Diffusion, Brownsche Molekularbewegung und Koagulation von Kolloidteilchen. *Zeitschrift fur Physik*, 17:557–585, 1916.

[48] C. d. S. Batista, E. N. Macêdo, and J. N. N. Quaresma. Solution of a general population balance equation by the Laplace transform technique. *Proceedings of ENCIT*, 2010.

[49] D. Bertin, I. Cotabarren, J. Piña, and V. Bucalá. Population balance discretization for growth, attrition, aggregation, breakage and nucleation. *Computers & Chemical Engineering*, 84(C):132–150, 2016.

[50] M. H. Holmes. *Introduction to the foundations of applied mathematics*. Springer, 2009.

[51] S. Kirkpatrick, C. D. Gelatt, and M. P. Vecchi. Optimization by Simulated Annealing. *Science*, 220(4598):671–680, 1983.

[52] V. Černý. Thermodynamical approach to the traveling salesman problem: An efficient simulation algorithm. *Journal of Optimization Theory and Applications*, 45(1):41–51, 1985.

[53] The Mathworks, Natick, Massachusetts. *Optimization Toolbox User's Guide*, 2017.

[54] A. H. Alexopoulos, A. I. Roussos, and C. Kiparissides. Part I: Dynamic evolution of the particle size distribution in particulate processes undergoing combined particle growth and aggregation. *Chemical Engineering Science*, 59(24):5751–5769, 2004.

[55] A. H. Alexopoulos and C. Kiparissides. Part II: Dynamic evolution of the particle size distribution in particulate processes undergoing simultaneous particle nucleation, growth and aggregation. *Chemical Engineering Science*, 60(15):4157–4169, 2005.

[56] A. I. Roussos, A. H. Alexopoulos, and C. Kiparissides. Part III: Dynamic evolution of the particle size distribution in batch and continuous particulate processes: A Galerkin on finite elements approach. *Chemical Engineering Science*, 60(24):6998–7010, 2005.

[57] D. Meimaroglou, A. I. Roussos, and C. Kiparissides. Part IV: Dynamic evolution of the particle size distribution in particulate processes. A comparative study between Monte Carlo and the generalized method of moments. *Chemical Engineering Science*, 61(17):5620–5635, 2006.

[58] L. A. Spielman and O. Levenspiel. A Monte Carlo treatment for reacting and coalescing dispersed phase systems. *Chemical Engineering Science*, 20(3):247–254, 1965.

[59] B. H. Shah, D. Ramkrishna, and J. D. Borwanker. Simulation of particulate systems using the concept of the interval of quiescence. *AIChE Journal*, 23(6):897–904, 1977.

[60] D. Ramkrishna. Analysis of population balance IV: The precise connection between Monte Carlo simulation and population balances. *Chemical Engineering Science*, 36(7):1203–1209, 1981.

[61] E. Debry, B. Sportisse, and B. Jourdain. A stochastic approach for the numerical simulation of the general dynamics equation for aerosols. *Journal of Computational Physics*, 184(2):649–669, 2003.

[62] F. E. Kruis, A. Maisels, and H. Fissan. Direct simulation Monte Carlo method for particle coagulation and aggregation. *AIChE Journal*, 46(9):1735–1742, 2000.

[63] M. Smith and T. Matsoukas. Constant-number Monte Carlo simulation of population balances. *Chemical Engineering Science*, 53(9):1777–1786, 1998.

[64] V. Saliakas, C. Kotoulas, D. Meimaroglou, and C. Kiparissides. Dynamic evolution of the particle size distribution in suspension polymerization reactors: A comparative study on Monte Carlo and sectional grid methods. *The Canadian Journal of Chemical Engineering*, 86(5):924–936, 2008.

[65] F. Jahanzad, S. Sajjadi, and B. W. Brooks. Comparative Study of Particle Size in Suspension Polymerization and Corresponding Monomer-Water Dispersion. *Industrial & Engineering Chemistry Research*, 44(11):4112–4119, 2005.

[66] G. M. Hidy. On the theory of the coagulation of noninteracting particles in Brownian motion. *Journal of Colloid Science*, 20(2):123–144, 1965.

[67] M. J. Hounslow. A discretized population balance for continuous systems at steady state. *AIChE Journal*, 36(1):106–116, 1990.

[68] M. J. Hounslow, R. L. Ryall, and V. R. Marshall. A discretized population balance for nucleation, growth, and aggregation. *AIChE Journal*, 34(11):1821–1832, 1988.

[69] R. Bleck. A fast, approximative method for integrating the stochastic coalescence equation. *Journal of Geophysical Research*, 75(27):5165–5171, 1970.

[70] S. Kumar and D. Ramkrishna. On the solution of population balance equations by discretization - I. A fixed pivot technique. *Chemical Engineering Science*, 51(8):1311–1332, 1996.

[71] S. Kumar and D. Ramkrishna. On the solution of population balance equations by discretization - II. A moving pivot technique. *Chemical Engineering Science*, 51(8):1333–1342, 1996.

[72] S. Kumar and D. Ramkrishna. On the solution of population balance equations by discretization - III. Nucleation, growth and aggregation of particles. *Chemical Engineering Science*, 52(24):4659–4679, 1997.

[73] S. Sarra. The Method of Characteristics with applications to Conservation Laws. *Journal of Online Mathematics and Applications*, 3, 2003.

[74] F. Gelbard and J. H. Seinfeld. Exact solution of the general dynamic equation for aerosol growth by condensation. *Journal of Colloid and Interface Science*, 68(1):173–183, 1979.

[75] A. W. Mahoney and D. Ramkrishna. Efficient solution of population balance equations with discontinuities by finite elements. *Chemical Engineering Science*, 57(7):1107–1119, 2002.

[76] M. Kostoglou and A. J. Karabelas. Evaluation of zero order methods for simulating particle coagulation. *Journal of Colloid and Interface Science*, 163(2):420–431, 1994.

[77] M. Kostoglou and A. J. Karabelas. Evaluation of numerical methods for simulating an evolving particle size distribution in growth processes. *Chemical Engineering Communications*, 136(1):177–199, 1995.

[78] M. Nicmanis and M. J. Hounslow. A finite element analysis of the steady state population balance equation for particulate systems: aggregation and growth. *Computers & Chemical Engineering*, 20(1):S261–S266, 1996.

[79] J. D. Lister, D. J. Smit, and M. J. Hounslow. Adjustable discretized population balance for growth and aggregation. *AIChE Journal*, 41(3):591–603, 1995.

[80] A. Mesbah, H. J. M. Kramer, A. E. M. Huesman, and P. M. J. Van den Hof. A control oriented study on the numerical solution of the population balance equation for crystallization processes. *Chemical Engineering Science*, 64(20):4262–4277, 2009.

[81] C. W. Gear and L. R. Petzold. ODE methods for the solution of differential/algebraic systems. *SIAM Journal on Numerical Analysis*, 21(4):716–728, 1984.

[82] R. David, J. Villermaux, P. Marchal, and J. P. Klein. Crystallization and precipitation engineering - IV. Kinetic model of adipic acid crystallization. *Chemical Engineering Science*, 46(4):1129–1136, 1991.

[83] P. Marchal, R. David, J. P. Klein, and J. Villermaux. Crystallization and precipitation engineering - I. An efficient method for solving population balance in crystallization with agglomeration. *Chemical Engineering Science*, 43(1):59–67, 1988.

[84] G. Madras and B. J. McCoy. Time evolution to similarity solutions for polymer degradation. *AIChE Journal*, 44(3):647–655, 1998.

[85] A. Alexiadis, M. Vanni, and P. Gardin. Extension of the method of moments for population balances involving fractional moments and application to a typical agglomeration problem. *Journal of Colloid and Interface Science*, 276(1):106–112, 2004.

[86] S. Qamar, G. Warnecke, M. P. Elsner, and A. Seidel-Morgenstern. A Laplace transformation based technique for reconstructing crystal size distributions regarding size independent growth. *Chemical Engineering Science*, 63(8):2233–2240, 2008.

[87] Z. Pinar and T. Öziş. An observation on the periodic solutions to nonlinear physical models by means of the auxiliary equation with a sixth-degree nonlinear term. *Communications in Nonlinear Science and Numerical Simulation*, 18(8):2177–2187, 2013.

[88] Z. Pinar, A. Dutta, G. Bény, and T. Öziş. Analytical solution of population balance equation involving aggregation and breakage in terms of auxiliary equation method. *Pramana*, 84(1):9–21, 2015.

[89] Z. Pinar, A. Dutta, G. Bény, and T. Öziş. Analytical solution of population balance equation involving growth, nucleation and aggregation in terms of auxiliary equation method. *Appl. Math. Inf. Sci.*, 9(5):2467–2475, 2015.

[90] A. M. Cohen. *Numerical Methods for Laplace Transform Inversion.* Springer, 2007.

[91] J. Harold. Bromwich's work on Operational Methods. *Journal of the London Mathematical Society*, s1-5(3):220–224, 1930.

[92] F. R. de Hoog, J. H. Knight, and A. N. Stokes. An improved method for numerical inversion of Laplace transforms. *SIAM Journal on Scientific and Statistical Computing*, 3(3):357–366, 1982.

[93] A. Talbot. The accurate numerical inversion of Laplace transforms. *IMA Journal of Applied Mathematics*, 23(1):97–120, 1979.

[94] W. T. Weeks. Numerical inversion of Laplace transforms using Laguerre functions. *J. ACM*, 13(3):419–429, 1966.

[95] M. Hazewinkel. *Laguerre polynomials. Encyclopedia of Mathematics.* Springer, 2001.

[96] R. Schapery. Approximate methods of transform inversion for viscoelastic stress analysis. *Proceedings of the Fourth US National Congress on Applied Mechanics*, 2:1075–1085, 1962.

[97] B. Davies and B. Martin. Numerical inversion of the Laplace transform: a survey and comparison of methods. *Journal of Computational Physics*, 33(1):1–32, 1979.

[98] K. L. Kuhlman. Review of inverse Laplace transform algorithms for Laplace-space numerical approaches. *Numerical Algorithms*, 63(2):339–355, 2013.

[99] L. Brančík. Programs for fast numerical inversion of Laplace transforms in MATLAB language environment. *Proceedings of the 7th Conference MATLAB'99*, pages 27–39, 1999.

[100] K. E. Atkinson. *An Introduction to Numerical Analysis.* Wiley, 1989.

[101] J. R. Macdonald. Accelerated convergence, divergence, iteration, extrapolation, and curve fitting. *Journal of Applied Physics*, 35(10):3034–3041, 1964.

[102] O. Rodríguez Hernández and J. M. López Fernández. A semiotic reflection on the didactics of the Chain rule. *The Mathematics Enthusiast*, 7(2):321–332, 2010.

[103] W. E. Schiesser. *The Numerical Method of Lines.* Academic Press, 1991.

[104] B. Fornberg. Generation of finite difference formulas on arbitrarily spaced grids. *Mathematics of Computation*, 51(184):699–706, 1988.

[105] M. Hazewinkel. *Simpson formula. Encyclopedia of Mathematics.* Springer, 2001.

[106] T. Delin and C. Zheng. On A General Formula of Fourth Order Runge-Kutta Method. *Journal of Mathematical Science & Mathematics Education*, 7(2):1–10, 2012.

[107] R. Bacsa, W. Bacsa, M. C. Schwarzwälder, V. Cregan, M. Fernández-Pendás, S. Fernandez-Mendez, B. Florio, A. Marquina, I. Moyles, T. Myers, H. Ribera Ponsa, **S. Rusconi**, S. Serna, and C. Vázquez-Cendón. Synthesis of monodisperse spherical nanocrystals. ESGI report, Centre de Recerca Matemàtica, Barcelona, 2016.

[108] W. T. Reid. *Riccati Differential Equations*. Academic Press, London, 1972.

[109] J. Bernoulli. *Explicationes, Annotationes & Additiones ad ea, quae in Actis sup. de Curva Elastica, Isochrona Paracentrica, & Velaria, hinc inde memorata, & paratim controversa legundur; ubi de Linea mediarum directionum, alliisque novis*. Acta Eruditorum, 1695.

[110] G. E. Andrews, R. Askey, and R. Roy. *Special functions. Encyclopedia of Mathematics and its Applications*. Cambridge University Press, 1999.

[111] S. Wolfram. *An elementary introduction to the Wolfram language*. Wolfram Media Inc., 2015.

[112] B. Gaviraghi, M. Annunziato, and A. Borzì. Analysis of splitting methods for solving a partial integro-differential Fokker-Planck equation. *Applied Mathematics and Computation*, 294:1–17, 2017.

[113] M. Magdziarz, A. Weron, and K. Weron. Fractional Fokker-Planck dynamics: Stochastic representation and computer simulation. *Phys. Rev. E*, 75:016708, 2007.

[114] H. Risken. *The Fokker-Planck Equation: Methods of Solution and Applications*. Springer, 1989.

[115] G. Strang. On the construction and comparison of difference schemes. *SIAM Journal on Numerical Analysis*, 5(3):506–517, 1968.

[116] M. S. Milgram. The generalized integro-exponential function. *Mathematics of Computation*, 44(170):443–458, 1985.

[117] J. C. Robinson. *An Introduction to Ordinary Differential Equations*. Cambridge University Press, 2004.

[118] J. Pearson. Computation of Hypergeometric Functions. Master's thesis, Worcester College, University of Oxford, 2009.

[119] The Mathworks, Natick, Massachusetts. *Symbolic Math Toolbox User's Guide*, 2002.

[120] R. I. McLachlan and G. R. W. Quispel. Splitting methods. *Acta Numerica*, 11:341–434, 2002.

[121] J. Geiser. *Decomposition Methods for Differential Equations: Theory and Applications*. Chapman & Hall, 2009.

[122] G. I. Marchuk. *Methods of Numerical Mathematics*. Springer, 1981.

[123] C. C. Miller. The Stokes-Einstein Law for Diffusion in Solution. *Proceedings of the Royal Society of London A: Mathematical, Physical and Engineering Sciences*, 106(740):724–749, 1924.

[124] D. W. van Krevelen and P. J. Hoftyzer. *Properties of polymers: correlations with chemical structure*. Elsevier, 1972.

[125] L. F. Shampine and M. W. Reichelt. The MATLAB ODE Suite. *SIAM Journal on Scientific Computing*, 18(1):1–22, 1997.

[126] J. Von Neumann. *Mathematical Foundations of Quantum Mechanics*. Princeton Univ. Press., 1996.

[127] B. Misra and E. C. G. Sudarshan. The zeno's paradox in quantum theory. *Journal of Mathematical Physics*, 18(4):756–763, 1977.

[128] M. A. Nielsen and I. L. Chuang. *Quantum Computation and Quantum Information*. Cambridge University Press, 2000.

[129] T. A. Brun. A simple model of quantum trajectories. *American Journal of Physics*, 70(7):719–737, 2002.

[130] K. Jacobs and D. A. Steck. A straightforward introduction to continuous quantum measurement. *Contemporary Physics*, 47(5):279–303, 2006.

[131] C. M. Caves. Quantum mechanics of measurements distributed in time. a path-integral formulation. *Phys. Rev. D*, 33:1643–1665, 1986.

[132] F. Verstraete, A. C. Doherty, and H. Mabuchi. Sensitivity optimization in quantum parameter estimation. *Phys. Rev. A*, 64:032111, 2001.

[133] R. Ruskov and A. N. Korotkov. Entanglement of solid-state qubits by measurement. *Phys. Rev. B*, 67:241305, 2003.

[134] V. P. Belavkin. *Information, Complexity and Control in Quantum Physics*. Springer-Verlag, 1987.

[135] S. Pilgram, A. N. Jordan, E. V. Sukhorukov, and M. Büttiker. Stochastic Path Integral Formulation of Full Counting Statistics. *Phys. Rev. Lett.*, 90:206801, 2003.

[136] M. A. Buice and J. D. Cowan. Field-theoretic approach to fluctuation effects in neural networks. *Phys. Rev. E*, 75:051919, 2007.

[137] M. I. Dykman, E. Mori, J. Ross, and P. M. Hunt. Large fluctuations and optimal paths in chemical kinetics. *The Journal of Chemical Physics*, 100(8):5735–5750, 1994.

[138] M. D. Srinivas. Quantum theory of continuous measurements and its applications in quantum optics. *Pramana*, 47(1):1–23, 1996.

[139] C. Wunderlich and C. Balzer. Quantum Measurements and New Concepts for Experiments with Trapped Ions. *Advances In Atomic, Molecular, and Optical Physics*, 49(C):293–372, 2003.

[140] M. Mensky. Quantum Restrictions on Measurement of Electromagnetic Field. *Annalen der Physik*, 500(3):215–221, 1988.

[141] M. Mensky. *Quantum Measurements and Decoherence*. Springer, 2000.

[142] J. Audretsch and M. Mensky. Continuous fuzzy measurement of energy for a two-level system. *Phys. Rev. A*, 56:44–54, 1997.

[143] M. Mensky. Decoherence and the theory of continuous quantum measurements. *Physics-Uspekhi*, 41:923–940, 1998.

[144] M. Bauer, D. Bernard, and A. Tilloy. Computing the rates of measurement-induced quantum jumps. *J. Phys. A: Math. Theor.*, 48(25):1–15, 2015.

[145] A. Tilloy, M. Bauer, and D. Bernard. Spikes in quantum trajectories. *Phys. Rev. A*, 92:052111 1–7, 2015.

[146] M. Bauer, D. Bernard, and A. Tilloy. Zooming in on quantum trajectories. *J. Phys. A: Math. Theor.*, 49(10):1–9, 2016.

[147] J. Rice. *Mathematical Statistics and Data Analysis*. Cengage Learning, 3rd edition, 2012.

[148] M. Abramowitz and I. A. Stegun. *Handbook of Mathematical Functions*. Applied Mathematics Series, 1964.

[149] W. Bryc. *The Normal Distribution: Characterizations with Applications*. Springer-Verlag, 1995.

[150] M. K. Simon. *Probability Distributions Involving Gaussian Random Variables*. Springer, 2002.

[151] M. Mensky. Quantum restrictions for continuous observation of an oscillator. *Phys. Rev. D*, 20:384–387, 1979.

[152] B. Eisenberg and R. Sullivan. Why is the Sum of Independent Normal Random Variables Normal? *Mathematics Magazine*, 81(5):362–366, 2008.

[153] S. Gurvitz, A. Aharony, and O. Entin-Wohlman. Temporal evolution of resonant transmission under telegraph noise. *Phys. Rev. B*, 94:075437, 2016.